# Développement d'un outil pour l'optimisation du dimensionnement et de la gestion des systèmes multi-sources avec batteries : application aux tours de télécommunication (OSETTA)

________________________________________,

Date de Soutenance:
06 mai 2025

Thèse de Doctorat
Spécialité : Génie Électrique

Présentée et Soutenue Publiquement Par :

SOUFIANE GHAFIRI

**Jury :**

**Évaluateurs :**

| | | |
|---|---|---|
| M. Jérôme BOSCHE | Professeur des Universités, Université de Picardie Jules Verne | Président |
| M. Serge PIERFEDERICI | Professeur des Universités, Université de Lorraine | Rapporteur |
| Mme Manuela SECHILARIU | Professeure des Universités, Alliance Sorbonne Université-UTC | Rapporteuse |
| M. Minh TA CAO | Professeur associé, Université de Sherbrooke | Examinateur |
| M. Sousso KELOUWANI | Full Professor, Université du Québec à Trois-Rivières | Examinateur |
| Mme Gwénaëlle HAMON | Professeure associée, Université de Sherbrooke | Rapporteuse |

**Encadrants :**

| | | |
|---|---|---|
| M. Arnaud DAVIGNY | Enseignant Chercheur, Junia Lille | Invité |
| M. Maxime DARNON | Directeur – CNRS, Université Jean Monnet - Saint-Étienne | Invité |

**Directeurs :**

| | |
|---|---|
| M. Abbes DHAKER | Professeur, Junia Lille |
| M. João Pedro TROVÃO | Professeur, Université de Sherbrooke |

Université de Lille - Université de Sherbrooke - L2EP - Institut Interdisciplinaire d'Innovation Technologique (3IT)

# Acknowledgements

Throughout this academic journey, I have been blessed with intellectual fortitude, unwavering perseverance, and exceptionally supportive circumstances that enabled me to successfully complete this scholarly endeavor. The privilege of achieving such an intellectual milestone under these auspicious conditions is not lost on me.

I wish to express my most profound gratitude to my doctoral thesis directors, Prof. Dhaker Abbes and Prof. João Pedro Trovao, who provided unwavering support throughout this academic journey. Your consistent availability and attentiveness have been instrumental to my research progress. Our substantive discussions have significantly expanded my intellectual horizons and refined my critical reasoning capabilities.

I am particularly appreciative of your dual role—not merely as academic supervisors, but as professional mentors who guided my intellectual and professional growth with exceptional insight and commitment. Your mentorship extends beyond traditional academic boundaries, offering profound wisdom that reaches far beyond the immediate scope of doctoral research.

To my co-supervisors, Dr. Maxime Darnon and Dr. Arnaud Davigny, I extend my deepest appreciation for your profound insights and contributions to this research endeavor. Your detailed feedback and penetrating reflections shaped the trajectory of this project. I am deeply grateful to have you both as integral members of my advisory team. Your collective expertise significantly enriched the academic experience, providing nuanced perspectives that elevated the research's intellectual rigor. Dr. Arnaud Davigny, your meticulously detailed feedback offered critical refinement to my work. Dr. Maxime Darnon, your incisive questioning challenged and ultimately strengthened my research methodology.

I would like to extend my sincere appreciation to the jury members for undertaking the evaluation of this research work. My gratitude goes to Prof. Jérôme Bosche for chairing the jury, to Prof. Manuela Sechilariu and Prof. Serge Pierfederici as reviewers, and to

Prof. Sousso Kelouwani, Prof. Gwénaëlle Hamon, and Prof. Minh Ta Cao as examiners. Though I await your feedback, I am confident that your expertise will provide valuable insights that will enhance my understanding of microgrids, their subsystems, strategies, design methodologies, and optimization approaches, and guide my future work in energy systems research.

Throughout these years, I was fortunate to collaborate between two esteemed laboratories: L2EP and e-TESC Lab, where I encountered remarkable individuals who made this experience more enriching. At Junia, I would like to thank Willy, Mhammed, Abderrahman, Amira, and Adrien. At e-TESC, I wish to express my gratitude to Marouane, Clarissa, Chi, Van Thang, An Toan, Duong, and Philippe. Furthermore, I extend my sincere appreciation to each person who made this journey joyful, even through the simple gesture of a morning smile.

I extend my sincere appreciation to the funding organizations and institutions that made this research possible. I am grateful to the Canada Research Chairs Program, the Natural Sciences and Engineering Research Council of Canada (NSERC), Bell, and STACE for their partial funding and support of the SAFE-TELECOM project. I also wish to acknowledge LN2, the International Research Laboratory jointly operated by Université de Sherbrooke (Canada) and CNRS, École Centrale de Lyon, INSA Lyon, and Université Grenoble Alpes (France), for its collaborative support. My thanks further extend to the Fonds de Recherche du Québec – Nature et Technologies (FRQNT) for its financial support to LN2, and to the Hauts-de-France region for its direct financial support of this thesis.

Finally, I wish to express my profound gratitude to my beloved family—my mother and father—for their unwavering support during challenging times. I am deeply appreciative of your faith in my decisions, dreams, and aspirations. My heartfelt thanks extend to my brother Nouamane, who has consistently been by my side, offering invaluable counsel, engaging in meaningful dialogues, and generously sharing your philosophical insights and wisdom.

# Résumé

L'industrie des télécommunications fait face à un double défi : élargir l'accès au numérique tout en réduisant son empreinte environnementale. Actuellement, ce secteur représente 3 % de la consommation énergétique mondiale et génère environ 430 $MtCO_2$ par an, soit 1 % des émissions mondiales. Une transformation de son infrastructure énergétique est donc essentielle, d'autant plus que les stations de base, qui assurent la connectivité des réseaux, sont responsables de 57 % de la consommation électrique du secteur.
Parallèlement, l'accès à Internet demeure inégalement réparti, en particulier dans des pays comme le Canada, où la fracture numérique reste préoccupante. En 2022, seulement 64 % des ménages ruraux canadiens disposaient d'une connexion Internet de 50/10 Mbps, contre plus de 99 % dans les zones urbaines. La situation est encore plus critique dans les communautés autochtones vivant dans les réserves, où seulement 41,53 % bénéficient d'un accès à la 5G et 42,9 % à une connexion de 50/10 Mbps. Ce retard en matière de connectivité freine le développement socio-économique de ces régions et souligne l'urgence d'une infrastructure télécoms plus accessible et durable.
Cependant, l'approvisionnement énergétique du secteur repose encore largement sur des sources conventionnelles. Actuellement, 46 % de l'énergie consommée provient de sources renouvelables, tandis que 43% sont issus du réseau électrique conventionnel et 11 % sont produits par des générateurs diesel. Malgré cette part d'énergies renouvelables, moins de 1 % est généré directement sur site, les opérateurs privilégiant les accords d'achat d'électricité. Ce modèle pose des défis importants, notamment face à la croissance prévue des sites en réseau instable ou hors réseau, dont le nombre devrait augmenter de 22 % d'ici 2030, atteignant 109 000 sites en réseau instable et 24 000 sites hors réseau.
Conscients de ces enjeux, les grands opérateurs de télécommunications ont fixé des objectifs ambitieux : réduire leurs émissions de 50 % d'ici 2030 et atteindre la neutralité carbone à l'horizon 2050, tout en poursuivant leurs efforts pour combler la fracture numérique. Dans cette optique, des solutions de nanoréseaux émergent comme une alternative prometteuse pour alimenter les infrastructures situées dans des zones à faible connectivité. En combinant panneaux photovoltaïques, batteries LFP (Lithium-Fer-Phosphate) et générateurs diesel, ces systèmes permettent d'optimiser l'intégration des énergies renouvelables tout en réduisant la dépendance aux combustibles fossiles.
Toutefois, ces initiatives se heurtent à des contraintes géographiques et climatiques, en particulier dans les régions où l'irradiation solaire est inférieure à 3,5-5 kWh/m$^2$/jour, limitant ainsi le potentiel d'exploitation de l'énergie solaire. Surmonter ces obstacles nécessitera des innovations technologiques et une planification adaptée aux réalités locales afin de garantir une transition énergétique efficace et inclusive.
C'est dans ce contexte que s'inscrit ce projet de recherche, qui s'aligne avec la vision des grands opérateurs canadiens tels que Rogers et Bell Canada, ayant annoncé leur engagement à réduire leurs émissions de 50 % d'ici 2030, en prenant 2019 comme année de référence. Afin d'atteindre cet objectif, ces opérateurs ont commencé à déployer des stations alimentées par des énergies renouvelables pour fournir l'électricité aux infrastructures situées dans les zones éloignées.
L'objectif principal de ce projet est le développement d'un outil permettant aux opérateurs télécoms d'optimiser le dimensionnement et la gestion des nanoréseaux hybrides (associant panneaux photovoltaïques, batteries et générateurs diesel) pour alimenter les stations de base dans ces régions isolées. L'approche adoptée se concentre à la fois sur le dimensionnement optimal du système et sur sa gestion en minimisant les coûts économiques et environnementaux.
L'un des aspects novateurs de cette recherche réside dans l'intégration des panneaux photovoltaïques bifaciaux, une technologie émergente qui devrait représenter environ 20 % du marché mondial du photovoltaïque d'ici 2030, contre seulement 5 % en 2020, avec une capacité installée estimée à 100 GW. Ces modules offrent un rendement supérieur de 10 à 20 % par rapport aux panneaux monofaciaux

classiques grâce à leur capacité à capter la lumière réfléchie par le sol et les surfaces environnantes, optimisant ainsi la production énergétique des stations hors réseau.
Un autre défi majeur abordé par cette recherche est l'impact de l'accumulation de neige sur la production des panneaux solaires. Selon les conditions météorologiques, l'enneigement peut entraîner une réduction du rendement énergétique allant de 3,5 % à 100 %. Il est donc essentiel d'intégrer ces effets dans la modélisation et la gestion des nanoréseaux afin de garantir une alimentation énergétique fiable, même en conditions hivernales sévères.

Les contributions de cette recherche se déclinent en trois axes principaux :

1. Modélisation détaillée du système afin de mieux comprendre les interactions entre les différentes sources d'énergie et la consommation des stations de base.

2. Optimisation de la gestion énergétique, prenant en compte les incertitudes liées à la production des nanoréseaux et à la demande énergétique des stations de base.

3. Coordination entre la modélisation et la gestion énergétique grâce à une optimisation conjointe, visant à maximiser l'intégration des sources renouvelables.

À l'issue de cette étude, un outil de dimensionnement optimisé pour les systèmes hybrides sera développé, facilitant la planification et la gestion énergétique des stations de base alimentées par nanoréseaux.
En atteignant ces objectifs, ce projet contribuera directement aux politiques de réduction des émissions de gaz à effet de serre et à l'ambition de neutralité carbone d'ici 2050. Il constitue ainsi une avancée stratégique pour le secteur des télécommunications, en conciliant l'expansion du numérique et la transition énergétique.

# Abstract

The telecommunications industry faces a dual challenge: expanding digital access while reducing its environmental footprint. Currently, this sector accounts for 3% of global energy consumption and generates approximately 430 $MtCO_2$ per year, representing 1% of global emissions. Transforming its energy infrastructure is therefore essential, especially since base stations, which ensure network connectivity, are responsible for 57% of the sector's electricity consumption. At the same time, Internet access remains unevenly distributed, particularly in countries like Canada, where the digital divide remains a concern. This connectivity gap hinders the socio-economic development of these regions and underscores the urgency of a more accessible and sustainable telecom infrastructure.

At the same time,Internet access remains unevenly distributed, particularly in countries like Canada, where the digital divide remains a concern. In 2022, only 64% of rural Canadian households had an Internet connection of 50/10 Mbps, compared to more than 99% in urban areas. The situation is even more critical in Indigenous communities living on reserves, where only 41.53% have access to 5G and 42.9% to a 50/10 Mbps connection.

However, the sector's energy supply still largely relies on conventional sources. Currently, 46% of the energy consumed comes from renewable sources, while 43% is supplied by the conventional power grid, and 11% is produced by diesel generators. Despite this share of renewable energy, less than 1% is generated directly on-site, as operators favor power purchase agreements. This model presents significant challenges, especially given the anticipated growth in sites located in unstable or off-grid networks, whose numbers are expected to increase by 22% by 2030, reaching 109,000 unstable grid sites and 24,000 off-grid sites. Aware of these issues, major telecommunications operators have set ambitious targets: reducing their emissions by 50% by 2030 and achieving carbon neutrality by 2050 while continuing efforts to bridge the digital divide. In this context, nanogrid solutions are emerging as a promising alternative to power infrastructure in low-connectivity areas.

By combining photovoltaic panels, LFP (lithium iron phosphate) batteries, and diesel generators, these systems optimize the integration of renewable energy while reducing dependence on fossil fuels. However, these initiatives face geographic and climatic constraints, particularly in regions where solar irradiation is below 3.5 to 5 $kWh/m^2/day$, limiting the potential for solar energy exploitation. Overcoming these obstacles will require technological innovations and planning adapted to local realities to ensure an effective and inclusive energy transition.

This research project is set within this context, aligning with the vision of major Canadian operators such as Rogers and Bell Canada, which have committed to reducing their emissions by 50% by 2030, using 2019 as the reference year. To achieve this goal, these operators have begun deploying renewable energy-powered stations to supply electricity to infrastructure in remote areas. The primary objective of this project is to develop a tool that enables telecom operators to optimize the sizing and management of hybrid nanogrid (combining photovoltaic panels, batteries, and diesel generators) to power base stations in these isolated regions. The chosen approach focuses on both optimal system sizing and management while minimizing economic and environmental costs.

One of the innovative aspects of this research is the integration of bifacial photovoltaic panels, an emerging technology expected to represent approximately 20 % of the global photovoltaic market by 2030, up from just 5% in 2020, with an estimated installed capacity of 100 GW. These modules offer 10–20% higher efficiency than conventional monofacial panels due to their ability to capture light reflected by the ground and surrounding surfaces, thereby optimizing energy production for off-grid stations.

Another major challenge addressed by this research is the impact of snow accumulation on solar panel performance. Depending on weather conditions, snow cover can cause an energy yield reduction ranging from 3.5% to 100%. It is therefore essential to integrate these effects into the modeling and management of nanogrids to ensure a reliable power supply, even in harsh winter conditions. The contributions of this research are structured around three main areas:

1. Detailed system modeling to better understand interactions between different energy sources and base station consumption.
2. Optimization of energy management, considering uncertainties related to nanogrid production and base stations energy demand.
3. Coordination between design and energy management through a joint optimization approach aimed at maximizing the integration of renewable sources.

At the end of this study, an optimized sizing tool for hybrid systems will be developed, facilitating the planning and energy management of base stations powered by nanogrids. By achieving these objectives, this project will directly contribute to greenhouse gas reduction policies and the goal of carbon neutrality by 2050. It thus represents a strategic advancement for the telecommunications sector, balancing digital expansion with energy transition

# Oraganization of the Thesis

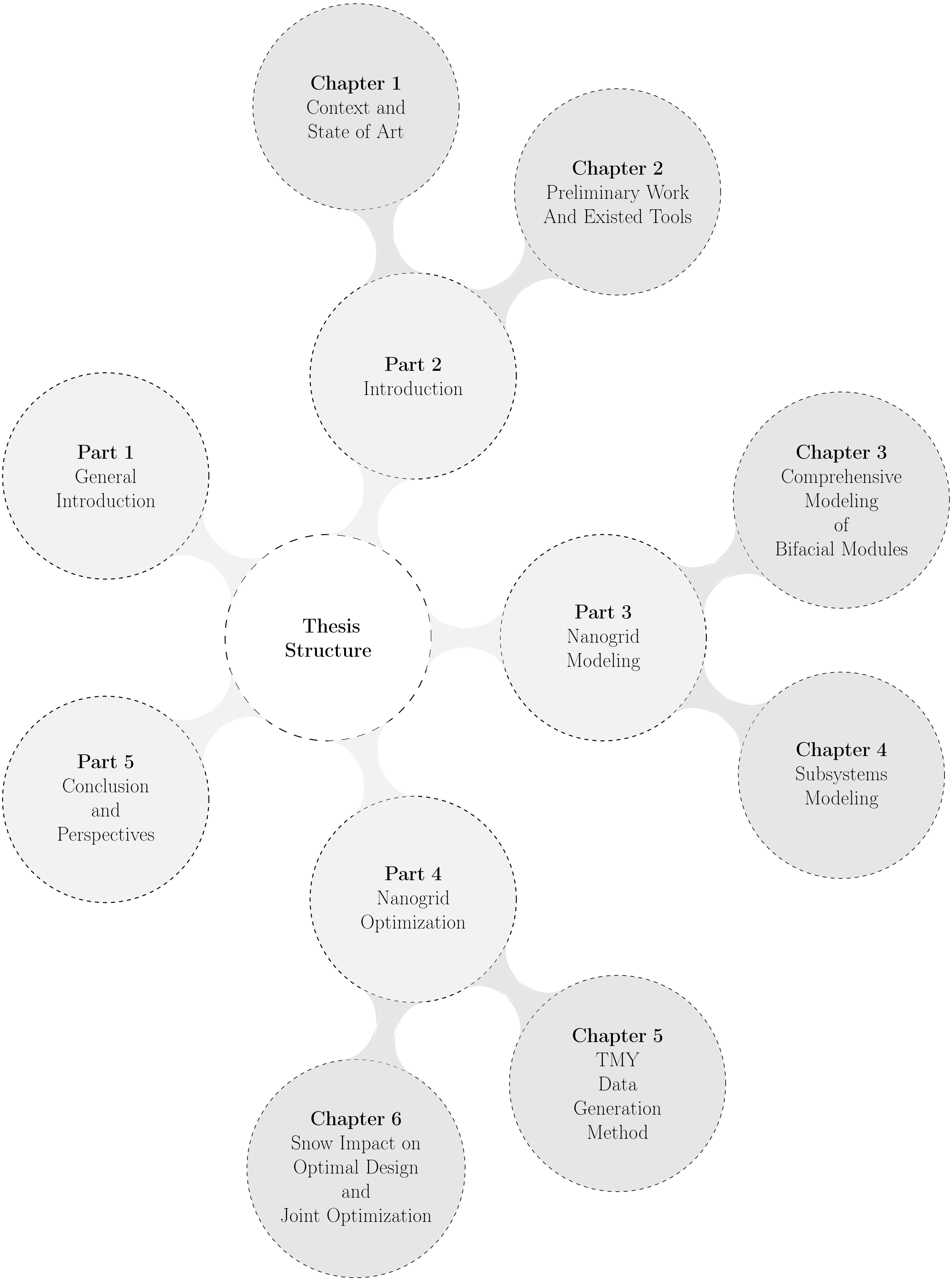

# Contents

# List of Figures

# List of Tables

# Glossary

**AC** Alternating Current. 58

**ANN** Artificial Neural Network. 37

**BTSs** Base Transceiver Stations . 25, 27, 101, 114

**CAPEX** Capital Expenditure. 167, 175

**COV** Coefficient Of interannual Variability. 118

**DC** Direct Current. 58

**DHI** Direct Horizontal Irradiance. 73, 78, 87, 117, 131

**DNI** Direct Normal Irradiance. 78, 87, 117, 126, 131

**EACs** Energy Attribute Certificates. 25

**EARTH** Energy Aware Radio and Network Technologie. 27

**EE** Embodied Energy. 44

**EMR** Energetic Macroscopic Representation. 57, 58

**ESS** Energy Storage System. 27

**GHGs** Greenhouse gases. 27, 29

**GHI** Global Horizontal Irradiance. 62, 78, 87, 121

**GPPAs** Green Power Purchase Agreements. 25, 26

**GSMA** Global System for Mobile Communications . 24, 25

**HOMER** Hybrid Optimization of Multiple Energy Resources. 30, 34, 61–63, 180

**HRES** Hybrid Renewable Energy System. 29–31, 33, 34, 43, 59

**HVAC** Heating, Ventilation, and Air Conditioning. 109, 110, 114

**HVI** Hypervolume Indicator. 173

**LCC** Life Cycle Cost. 43, 44, 141, 143, 146, 149, 160

**LCOE** Levelized Cost of Energy. 30, 64, 141, 143, 145

**LFP** Lithium Iron Phosphate. 64, 103, 167, 174

**LPSP** Loss of Power Supply Probability . 44, 140, 141

**LSTM** Long Short Term Memory. 102

**MCDES** Multi-energy complementary distributed energy system. 43

**MNO** Mobile Network Operators. 27, 54, 100

**MPC** Model Predictive Control. 39

**MPPT** Maximum Power Point Tracking. 78

**NPC** Net Present Cost. 63, 64

**NRMSE** Normalized Root Mean Square Error. 81, 87, 92, 93

**NSGA** Non-dominated Sorting Genetic Algorithm. 144, 164

**OPEX** Operational Expenditure. 24, 28, 33, 139, 175

**PCA** Principal Component Analysis. 126

**PV** Photovoltaic. 26, 34, 69, 117

**RMS** Remote Monitoring System. 28

**SOC** State of Charge. 26, 28

**SOH** State of Health. 28

**TESCOs** nelecom Energy Services Companies. 27

**TMY** Typical Meteorological Year. 118, 119, 131, 182

# List of Symbols

| | |
|---|---|
| $\alpha_0$ | Generator fuel intercept coefficient $[L/kWh]$, with a value of 0.246 $[L/kWh]$ |
| $\alpha_1$ | Generator fuel slope $[L/hr/kW]$, with a value of 0.08145 $[L/hr/kW]$ |
| $\alpha_T$ | Temperature coefficient $[\%/°C]$ |
| $\alpha_{rate}$ | Charging rate of the inverter charger |
| $\alpha_{rate}$ | Output Rate of the Inverter Charger |
| $\beta$ | Solar incidence angle, the angle between the sun's rays and the module's normal [°] |
| $\beta_{CO2_2}$ | Emissions factor (2.4 to 3.5) $[kgCO_2/liter]$ |
| $\delta$ | Declination angle[°] |
| $\eta$ | Bifaciality factor |
| $\eta_{p,stc}$ | Maximum power efficiency under standard test conditions [%] |
| $\gamma$ | Solar absorptance [%] |
| $\mu(\cdot,\cdot)$ | Control Policy |
| $\phi_f$ | Front irradiance $[W/m^2]$ |
| $\phi_r$ | Rear irradiance $[W/m^2]$ |
| $\Phi_t$ | Total received irradiance |
| $\Phi_{ref}$ | Reference Irradiance $[W/m^2]$ |
| $\Phi_{t,noct}$ | Solar irradiance at which $T_{c,noct}$ is defined |
| $\rho$ | Ground's albedo |
| $\tau$ | Solar transmittance [%] |
| $\theta_a$ | Azimuth angle of the sun [°] |
| $\theta_i$ | Angle between the normal and the vector $r_{ij}$ that links two points of the surfaces $S_i$ and $S_j$ [°] |
| $\theta_t$ | Tilt angle [°] |
| $\theta_z$ | Zenith angle [°] |
| $\theta_{aa}$ | Azimuth angle of the array [°] |
| $ACF$ | Actualization Factor |
| $C_u$ | Unit price of the component [$] |
| $C_{comp}$ | Capacity of the component |
| $D$ | Derate Coefficient |
| $d$ | Discount rate |
| $D_f$ | Power Dificit $[W]$ |
| $D_l$ | Linear Damage Due to charging cycles |
| $F_1$ | Circumsolar coefficient |
| $F_2$ | Brightness coefficient |
| $F_{gen,h}$ | Hourly fuel consumption $[L/h]$ |
| $F_{S_i-S_j}$ | View Factor From Surface $S_i$ to surface $S_j$. |
| $h$ | Hour angle [°] |
| $H(\cdot,\cdot,\cdot)$ | The Hamiltonian function |
| $HVI$ | Hypervolume Indicator |

| | |
|---|---|
| $i$ | Inflation rate |
| $i_{bat}$ | Battery current $[A]$ |
| $i_{chr_{in}}$ | Input Current in the Charger Mode $[A]$ |
| $i_{chr_{out}}$ | Output Current in the Inverter Mode $[A]$ |
| $i_{dcdc}$ | Output Current of the Chopper$[A]$ |
| $i_{dcload}$ | BTS DC Load Current $[A]$ |
| $i_{gen}$ | Current of the Diesel Generator $[A]$ |
| $i_{load_{ac}}$ | AC Load Current $[A]$ |
| $i_{mppt}$ | Maximum Output Current of the Bifacial Panels $[A]$ |
| $i_{pv}$ | Bifacial Modules Output Current $[A]$ |
| $k_n$ | Total number of DoD (Depth of Discharge) levels |
| $LCC_{bat}$ | Life Cycle Cost of LFP Batteries [$] |
| $LCC_{gen}$ | Life Cycle Cost of Diesel Generator [$] |
| $LCC_{pv}$ | Life Cycle Cost of Bifacial Modules [$] |
| $N_i$ | Lifespan cycle at amplitude $DoD_i$ |
| $n_i$ | Number of cycles corresponding to the amplitude $DoD_i$ |
| $N_{rep}$ | Number of replacements |
| $P_{gen,h}$ | Hourly generator output $[kW]$ |
| $P_{gen,r}$ | Rated capacity of the generator $[kW]$ |
| $P_{macro}$ | Power consumption of the macro base station $[W]$ |
| $PVF$ | Net Present Worth Factor |
| $r_{ij}$ | Vector linking two points on the surfaces $S_i$ and $S_j$ |
| $S_i, S_j$ | Surfaces involved in the calculation. |
| $T_a$ | Ambient temperature $[°C]$ |
| $T_{a,noct}$ | Ambient temperature at which $T_{c,noct}$ is defined |
| $T_{c,noct}$ | Nominal operating cell temperature $[°C]$ |
| $Thr_{max}$ | Maximum Threshold |
| $Thr_{min}$ | Minimum Threshold |
| $u_{ac}$ | AC Bus Voltage |
| $u_{dc}$ | Tension of the DC Bus $[V]$ |
| $u_{gen}$ | Voltage of the Diesel Generator $[V]$ |

# Introduction Générale

Le dernier rapport du GIEC démontre de manière concluante que les activités humaines sont responsables des changements observés dans le système climatique. Il documente une augmentation de la température de surface mondiale de 1,1°C au-dessus des niveaux de référence préindustriels pendant la période 2011-2020. Ce réchauffement est corrélé à des changements substantiels dans les systèmes océaniques, comme en témoignent les mesures du niveau de la mer montrant une élévation de 0,20 mètre entre 1901 et 2018. Le rythme d'élévation du niveau de la mer démontre un schéma d'accélération clair : progressant de 1,3 mm par an (1901-1971) à 1,9 mm par an (1971-2006), et s'intensifiant davantage à 3,7 mm par an ces dernières années (2006-2018). Le facteur principal qui entraîne ces altérations climatiques systématiques est la concentration atmosphérique accrue de gaz à effet de serre provenant des activités humaines. Les mesures contemporaines indiquent des niveaux historiquement sans précédent de ces gaz, avec des concentrations de dioxyde de carbone atteignant 410 parties par million—une concentration non observée depuis au moins 2 millions d'années.

Les conséquences de ces altérations climatiques se manifestent avec une sévérité croissante à travers les écosystèmes mondiaux et les populations humaines : les écosystèmes font face à des pertes de biodiversité, des événements de mortalité de masse et des dommages irréversibles. Les phénomènes météorologiques extrêmes se sont intensifiés globalement. Environ 3,3 à 3,6 milliards de personnes vivent dans des régions hautement vulnérables, subissant une mortalité accrue, une productivité agricole réduite, une rareté de l'eau, des impacts sur la santé, des pertes économiques et des déplacements, créant des défis en cascade à travers les secteurs et les régions.

La fenêtre d'opportunité pour l'action climatique se referme rapidement. Limiter le réchauffement climatique à 1,5°C nécessite d'atteindre des émissions nettes nulles de $CO_2$ d'ici le milieu du siècle, avec une réduction de 43% des émissions de gaz à effet de serre d'ici 2030 par rapport aux niveaux de 2019. Cela exige l'élimination progressive des combustibles fossiles, l'expansion des sources d'énergie renouvelable (solaire, éolienne, hydraulique) et la réorientation des subventions des combustibles fossiles vers des investissements dans l'énergie propre. Chaque fraction de degré compte dans l'atténuation des pires impacts du changement climatique.

L'industrie des télécommunications représente une part significative de la consommation énergétique mondiale, en faisant un secteur critique pour la transformation vers la durabilité. Reconnaissant ce défi, des chercheurs de deux laboratoires—L2EP et e-TESC Lab—ont initié le projet OSETTA ("Outil pour l'optimisation du dimensionnement et de la gestion des systèmes multi-sources avec batteries: application aux tours de télécommunication") pour aborder la durabilité dans l'infrastructure des télécommunications.

Cette recherche doctorale est un effort collaboratif entre deux institutions : L2EP (Laboratoire d'Électrotechnique et d'Électronique de Puissance) à Lille, France, est un centre de recherche distingué en génie électrique avec des contributions significatives dans les systèmes de contrôle avancés, les machines électriques, les microréseaux, l'électronique de puissance et la conversion d'énergie. Avec 1378 publications indexées Scopus et environ 40 brevets, L2EP démontre un impact scientifique substantiel. Les initiatives de neutralité carbone du laboratoire incluent l'Approche Carbon Care (depuis 2015) pour mesurer et atténuer les émissions liées à la recherche ; le Projet CPER CE2I (2015-2022) développant des convertisseurs d'énergie intelligents tout en compensant les impacts par le reboisement ; et le Projet H2020 PANDA (2018-2021) étendant les principes Carbon Care à travers les collaborations européennes. Le Programme CUMIN transforme le campus de l'Université de Lille en un démonstrateur d'électromobilité, tandis que le Projet MARSHALL crée des systèmes évolutifs de batteries et de piles à combustible pour les véhicules électriques lourds.

Le second laboratoire : e-TESC Lab (electric - Transport, Energy Storage, and Conversion Laboratory) à l'Université de Sherbrooke au Québec, Canada, se concentre sur les véhicules électriques, l'intelligence artificielle, la gestion de l'énergie et les sources d'énergie multiples sous la direction du Professeur João Pedro F. Trovão.

Le Projet OSETTA vise à développer un outil spécialisé conçu pour assister les opérateurs de télécommunications mobiles durant leurs phases de transition, en se concentrant particulièrement sur les stations de base mal desservies et hors réseau. La fonction principale de cet outil est de déterminer les configurations optimales de nanoréseau pour alimenter ces installations de télécommunications éloignées. En fournissant des solutions précises de dimensionnement et de gestion des systèmes énergétiques, le projet cherche à permettre aux entreprises de télécommunications de mettre en œuvre des alimentations durables qui sont à la fois techniquement viables et économiquement efficaces pour des scénarios de déploiement difficiles, en particulier pour les régions avec de faibles niveaux d'irradiance.

*"Our intelligence and our technology have given us unprecedented power to affect the climate, for better or worse. The evidence suggests that we are destabilizing our climate, bringing about climate change of unknown severity. The consequences could be dire for our civilization and for all life on Earth"*

Carl Sagan (1934 - 1996), Billions and Billions

# 1
# Context and State of Art

## Contents

## 1 Context

The global telecommunications industry has emerged as a pioneering sector in addressing climate change, establishing an unprecedented net zero emissions target by 2050. The GSMA's comprehensive 2024 report [1] reveals a complex landscape of energy consumption and carbon mitigation strategies across different regions. Between 2019 and 2022, regional emissions performance demonstrated significant variability: European telecommunications networks achieved a remarkable 53% reduction in emissions per connection, while Chinese networks marginally decreased emissions by only 2%. Concurrently, global electricity demand escalated by 10%, with China contributing a substantial 21% increase, underscoring the critical challenges in decarbonization efforts. The industry's current energy profile is characterized by substantial environmental implications. Telecommunications currently accounts for approximately 3% of global energy consumption, translating to 20-30% of OPEX for individual companies. The sector's carbon footprint is considerable, generating approximately 430 million tons of $CO_2$ annually[2], representing 1% of global emissions in 2021. Network infrastructure, particularly base stations, emerges as the primary energy consumption node, accounting for 57% of total network power requirements (Figure 1.1 ). A significant challenge lies in off-grid and inadequately powered regions, where diesel generators predominate. Approximately 88% of mobile towers in these areas rely on diesel fuel, resulting in an estimated 7,000 kilotons of $CO_2$ emissions in 2020 [3]. Major telecommunications infrastructure providers exemplify this challenge: American Tower, operating over 200,000 sites, consumed 3.6 TWh in 2022, with two-thirds generated from on-site fossil fuels, while IHS Towers' nearly 40,000 towers consumed approximately 4 TWh, with over 90% supplied by diesel generators. Despite these challenges, the industry demonstrates promising momentum toward sustainability. As of 2020, 50% of telecommunications companies (by connection volume) have committed to science-based emission reduction targets, and 31% have engaged in carbon-neutral initiatives [4]. The expanding connectivity landscape and increasing internet subscription rates necessitate innovative, energy-efficient technologies to balance growing digital infrastructure demands with environmental sustainability.

The trajectory towards the 2050 net zero goal requires accelerated, coordinated efforts across technological, operational, and policy domains. Researchers and industry stakeholders must collaborate to develop transformative solutions that minimize carbon emissions while maintaining the critical telecommunications infrastructure supporting global digital connectivity.

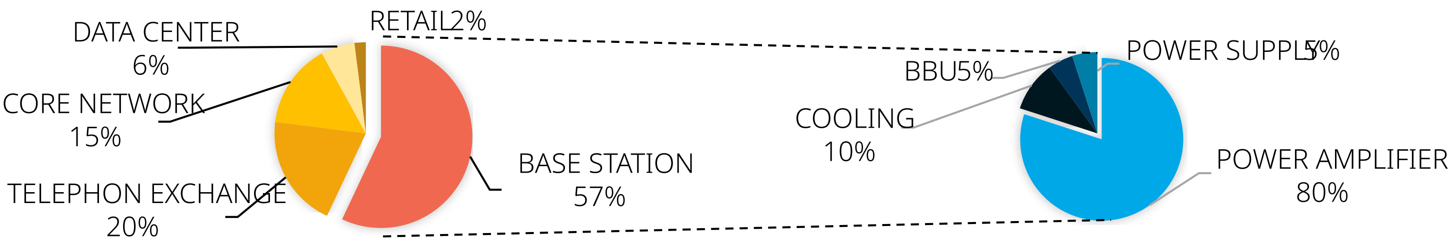


**Figure 1.1:** Power consumption distribution in a wireless network and in a base station

Building upon the previous analysis of the telecommunications sector's energy landscape, this investigation explores strategic approaches to mitigate carbon emissions and enhance network performance. The proposed solutions for improving cellular network sustainability can be systematically categorized into three primary domains of intervention. The first approach focuses on hardware optimization, targeting energy efficiency improvements in critical infrastructure components such as tower transceivers. The second category involves the strategic deployment of renewable energy stations to power mobile towers. This approach represents the most prevalent strategy among mobile operators seeking to reduce their network's carbon footprint. By transitioning from fossil fuel-dependent infrastructure to renewable energy sources, telecommunications companies can significantly decrease their greenhouse gas emissions and contribute to broader climate mitigation efforts. The third solution set concentrates on advanced energy-saving techniques, emphasizing intelligent energy management aligned with dynamic traffic loads. Innovative strategies such as the sleeping mode technique enable networks to optimize power consumption by dynamically adjusting energy usage based on real-time demand, thereby reducing unnecessary energy expenditure during periods of low activity. Given the substantial energy consumption of base stations within telecommunications networks, this research specifically investigates the potential of renewable energy sources for powering infrastructure in bad-grid or off-grid regions. By addressing the unique challenges of these underserved areas, the study aims to demonstrate how technological innovation and sustainable energy solutions can simultaneously enhance connectivity and environmental stewardship.

## 1.1 Adoption of renewable energy solutions in telecom industry

The energy distribution within the telecom industry, as comprehensively analyzed in the GSMA reports, reveals critical insights into the sector's power sourcing strategies. Drawing from a substantial dataset encompassing 750 mobile operators representing 90 percent of global mobile connections across 220 countries, the research highlights significant energy transition dynamics. In 2020, approximately 85% of BTSs relied on conventional grid electricity, with renewable energy accounting for 14% through EACs and GPPAs , and a

mere 1% generated through on-site renewable sources. The subsequent year witnessed a marginal shift, with conventional grid dependency reducing to 81% and an expansion in GPPAs, while maintaining the consistent 1% of on-site renewable generation. By 2023, the landscape further evolved, with non-renewable energy sources declining to 75% and renewable grid-purchased energy rising to 24%, underscoring a gradual but noteworthy progression towards sustainable energy infrastructure in the telecommunications sector (Figure 1.2 ).
Despite the PV panels becoming price-competitive, mobile operators still prefer the option of purchasing renewable electricity with a power purchase agreement from a certified vendor. To ensure a high quality of service, mobile network operators deploy more towers which increases the number of bad-grid and off-grid sites. It is expected that this number will increase by 22% between 2019 and 2030, even though the proportion of the total sites remain stable at around 15%, and the explanation behind this stability is the improvements of connectivity and reliability of grids which reduce the number of bad-grid and off-grid sites.Overall, by 2030, about 557 000 bad-grid and 187 000 off-grid sites are expected to be deployed (Figure 1.3a), representing an attractive opportunity for adopting renewable energy solutions. The idea is to convert sites that rely on diesel power to green stations, as Figure 1.3b shows that by 2030 the penetration rate of renewable energy sources can reach 27%.

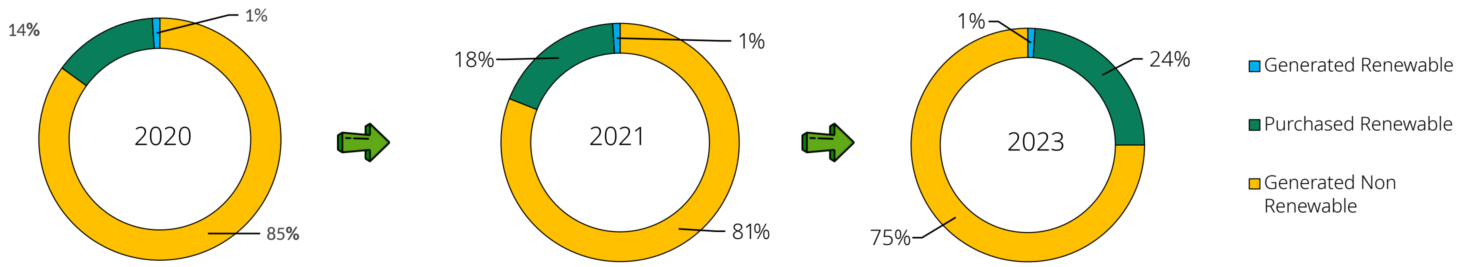


**Figure 1.2:** Adoption of Renewable Energy Sources

In an optimistic scenario, it could rise to 50%. Solar energy represents a promising alternative to diesel generators and grid connections, especially with the drop in solar panel prices and the improvement of their efficiency. Statistically, the prices fall about 80% between 2010 and 2021 [5], whereas the average conversion efficiency of the solar panel goes from 15% to well over 20 %. One of the limitations of using solar panels is the intermittence characteristic of this source. Therefore the necessity to use energy storage systems to achieve the required autonomy and reliability of the station. Still, in isolated regions with low solar irradiance, solar panels must be combined with a diesel generator that works as a backup power source when the SOC of batteries is at its minimum.

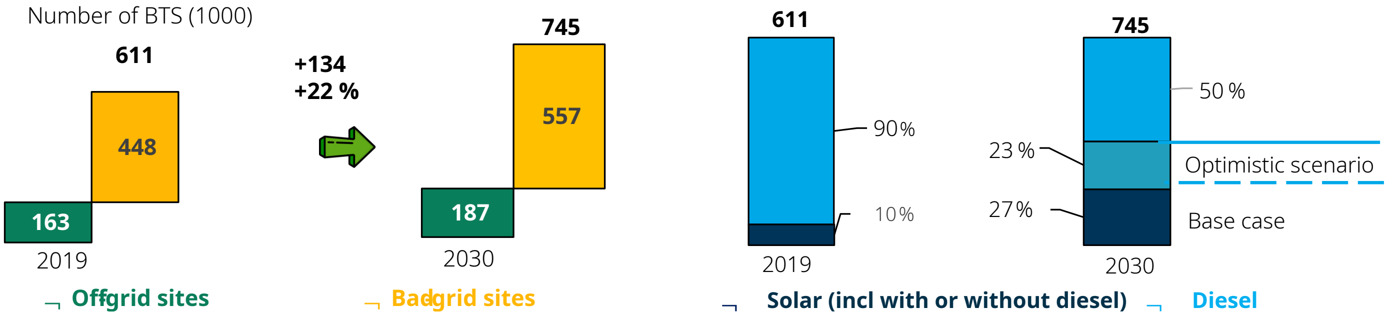

(a) (b)

**Figure 1.3:** (a) Estimation of bad-grid and off-grid towers number (thousand sites) (b) Penetration of renewable energy solutions at bad-grid and off-grid sites (thousand sites) [6]

Batteries or energy storage systems ESS serves for two functions increasing the penetration rate of green power that comes from solar panels and reducing the starts of diesel generators which leads to reducing the diesel consumption, therefore decreasing the GHGs emission.MNOs use mainly lead acid batteries (80% of the existing batteries in BTSs are lead acid batteries [6]) as ESS due to their affordable price, low maintenance cost and their extended operating temperature range. The trend of the market is shifted toward lithium-ion batteries that come with promising features such as high energy density, significant lifespan, and fast recharging performance. There are other viable green alternatives for diesel generators besides solar power, for example, fuel cell technology that requires less technical intervention and offers continuous power production. However, one of the challenges that face MNOs is continuously powering this technology with hydrogen, which implies the implementation of a supply chain. In addition, it is an emerging market. Therefore the capital cost is high. Wind power has the potential, if combined with solar power and ESS, to replace diesel generators, but the reliability system depends strongly on the geographical location of the mobile tower.

Expanding on these technological advancements, the telecommunications industry has initiated several collaborative projects to further develop and implement green energy solutions. These projects aim to address energy efficiency issues and propose a end-to-end solutions from the hardware level to network management. EARTH is a European project launched in January 2010. It is committed to developing new energy-efficient components, deploying innovative green solutions, and strategies to reduce the network's consumption by at least 50%. TESCOs are firms that provide power solution optimization in bad-grid and off-grid areas. The objectives of TESCOs are to minimize energy costs and improve the equipment's lifespan. TESCOs achieve these goals by respecting a set of measures that are listed below:

- Optimal sizing of the PV panels, storage system, and diesel generators.
- Fuel Efficiency improvement of diesel generators with optimal control strategies.
- Reducing OPEX by deploying RMS that monitors essential parameters of the station (SOC, SOH, consumption profile) and faults which reduce unnecessary physical visit.

## 1.2 Net Zero Ambitions and Digital Equity: Analyzing Canada's Telecommunications Infrastructure

In 2025, Canada reaffirmed its commitment to the Paris Agreement, establishing ambitious climate targets to achieve net zero emissions by 2050, with an interim goal of reducing emissions by 40% to 45% by 2030. Despite these commitments, the nation's progress remains modest, with emissions declining by only 9% to date [7], highlighting the significant challenges in transforming the country's energy landscape. The Canadian energy portfolio presents a nuanced picture of sustainable and traditional energy sources. Renewable energy constitutes a substantial portion of the national grid, with hydroelectric power dominating at 58%, complemented by uranium at 13% and solar at 2%. However, fossil fuels continue to play a significant role, with natural gas contributing 15% and coal and coke accounting for 2% of the energy mix. In 2021, the estimated grid emissions reached 76.7 million tons of $CO_2$ equivalent, underscoring the ongoing environmental challenges. The information technology sector emerges as a critical component in this energy ecosystem, consuming between 1.5% and 4% of total energy use. Within this context, the telecommunications industry faces particularly complex challenges, especially in rural and remote regions of Canada. Digital connectivity disparities are most pronounced in Northern Canada and Indigenous communities. As of 2022, only 64% of rural Canadian households had access to 50/10 internet services, compared to over 99% coverage in urban areas. Indigenous communities on reserves experience even more significant connectivity gaps, with merely 41.53% accessing 5G networks and 42.9% having 50/10 internet connection [8]. These statistics reveal a stark digital divide that intersects with broader challenges of energy transition, infrastructure development, and technological equity. Addressing these disparities will require coordinated efforts across government, telecommunications providers, and technology sectors to develop innovative solutions that balance environmental sustainability with comprehensive digital accessibility.

Bell Canada and Rogers Communications, the leading telecom operators in Canada, have committed to near-term science-based targets to reduce their emissions. Their goal is to decrease direct emissions (Scope 1), indirect emissions (Scope 2), and supply chain emissions (Scope 3) [1]. Scope 1 emissions include those from diesel generators powering telecommunication towers. Both operators aim to reduce Scope 1 and 2 GHGs emissions by 50% by 2030 and achieve net-zero emissions by 2050, using 2019 as the base year. Bell Canada has installed nine renewable power stations in the Northwest Territories, generating approximately 130,000 kWh of renewable energy annually [9]. In 2021, Rogers Communications launched a program to provide sustainable off-grid solutions in rural and remote areas without grid access, starting with seven wireless sites [10]. This research aims to align with these initiatives and accelerate the implementation of sustainable telecommunication stations in Canada, thereby extending coverage and reducing the digital divide. By developing a climate-appropriate approach to design and control base stations, this study addresses the gap in research on sustainable telecom infrastructure in Canada.

## 2 Litterature Review

### 2.1 Existing Solutions of HRES for Powering Isolated BTS

The challenge of powering remote base stations while adhering to net-zero emission targets has garnered significant attention within the scientific community, with over 258 publications documented in the SCOPUS[1] database between 1977 and 2022 (Figure 1.4). This growing body of research predominantly focuses on the implementation of HRES as a sustainable alternative to conventional diesel generators .

[1] Comprehensive abstract and citation database of peer-reviewed literature

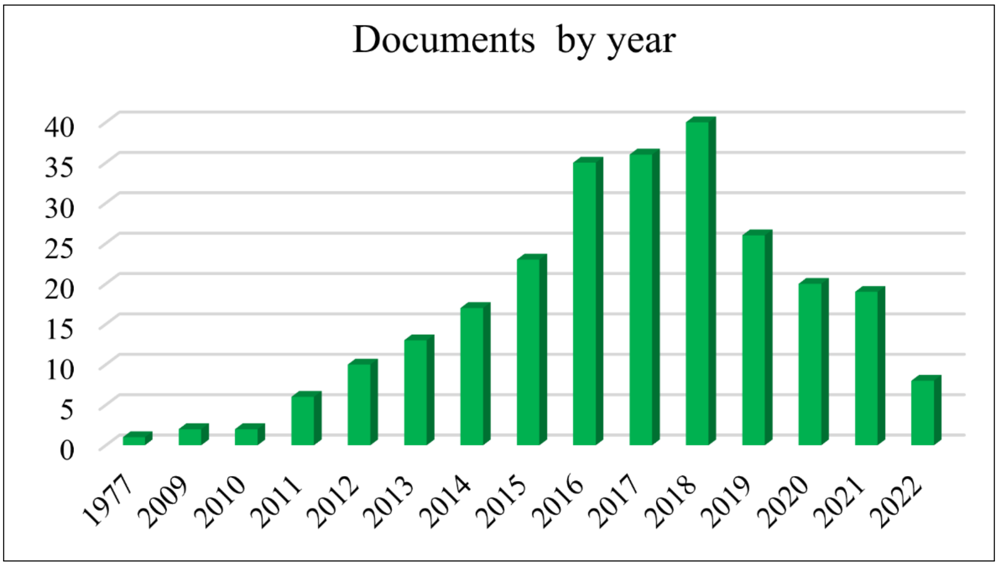


**Figure 1.4:** Publications by year that investigated the subject of renewable sources in base stations Copyright © 2022 Elsevier B.V. All rights reserved. Scopus® is a registered trademark of Elsevier B.V [6]

Studies conducted across various geographical locations have demonstrated the viability of HRES in telecommunications infrastructure. In the Democratic Republic of Congo (DRC), research utilizing HOMER software has established that an integrated system combining wind turbines, photovoltaic (PV) panels, and batteries can fully satisfy energy requirements of the load [11]. The success of these implementations capitalizes on the DRC's equatorial climate, which provides consistent and substantial solar irradiance throughout the year.
Economic feasibility analyses have yielded promising results regarding the financial viability of HRES adoption. The transition from traditional dual diesel generator systems with energy storage to solar-integrated solutions has demonstrated significant cost reductions, with LCOE decreasing from 0.46\$/kWh to 0.18\$/kWh while achieving a remarkable 91% renewable energy contribution [12]. Similar studies in Oman, Ghana, and Nigeria [13], [14], regions characterized by high solar potential with daily irradiance levels between 5.44 and 6 kWh/$m^2$/day [15], have corroborated these findings. By contrast, regions such as Quebec, Canada, exhibit lower solar irradiance ranging from 3.5 to 5 kWh/$m^2$/day [15], highlighting the importance of geographical considerations in HRES optimization.
The widespread adoption of HOMER Pro software, utilized by over 250,000 energy professionals across more than 190 countries [16], has emerged as a standard tool for HRES optimization studies. As illustrated in Table 1.1, we conducted a comprehensive survey to identify studies specifically focused on the application of HRES for supplying Base Transceiver Stations, and the results underscore the widespread use of HOMER Pro in these contexts. While HOMER Pro excels in component sizing optimization, it

is important to note its limitations regarding direct control variable optimization and traditional multi-objective optimization capabilities. Instead, the software employs a prioritization method, optimizing a primary objective function before evaluating additional objectives.

Despite the intermittent nature of renewable resources, research has demonstrated remarkable reliability in hybrid solar and wind power systems supplying base transceiver stations, achieving 99.99% reliability while reducing the levelized unit cost of electricity by 0.34$ [17] . However, the integration of backup power sources, such as diesel generators, microturbines, or grid connections, remains essential for ensuring uninterrupted service delivery. Case studies from various regions have further validated the potential of HRES implementation. In Nigeria's Kaduna state, technical and economic analyses have confirmed the viability of PV/diesel/battery hybrid systems, achieving a 95% renewable energy penetration rate [18]. Similarly, research in South Korea [19] has demonstrated the effectiveness of hybrid systems incorporating PV panels, batteries, and minimal diesel generator backup, providing up to three days of battery autonomy for off-grid installations. This comprehensive body of research underscores the significant potential of HRES in advancing sustainable telecommunications infrastructure while highlighting the importance of geographical considerations and backup power integration in system design and optimization.

| Study | Site Location | Studied Technologies | | | | | | Optimization | | Method - Tool |
|---|---|---|---|---|---|---|---|---|---|---|
| | | PV | WT | DG | BAT | FC | Grid | Design | Strategy | |
| [20], [21] | Pakistan | ✓ | ✓ | ✓ | ✓ | ✗ | ✓ | LCOE, NPC, GHG | LF | Homer Grid |
| [22], [23] | Italy-Denmark | ✓ | ✗ | ✗ | ✓ | ✓ | ✓ | Performance Coefficients | Rule Based | Matlab - Rule Based |
| [24], [25] | China | ✓ | ✗ | ✓ | ✓ | ✓ | ✓ | ✗ | Voltage Regulation | Courtship<br>Learning-based Water Strider Algorithm<br>Improved balanced owl search algorithm |
| [26] | India | ✓ | ✓ | ✓ | ✓ | ✗ | ✗ | COE | Homer | Homer Pro |
| [12] | Saudi-Arabia | ✓ | ✗ | ✓ | ✓ | ✗ | ✗ | LCOE, GHG | Rule Based | Homer Pro |
| [11] | DRC | ✓ | ✓ | ✗ | ✓ | ✗ | ✗ | NPC, GHG, COE | Homer | Homer Pro |
| [27] | Egypt | ✓ | ✓ | ✗ | ✓ | ✗ | ✓ | NPC, RF, LCOE | Homer | Homer Pro |
| [28] | Algeria | ✓ | ✓ | ✗ | ✓ | ✗ | ✗ | LCA | PS | Homer - SIMA Pro |
| [29] | Sudan | ✓ | ✗ | ✓ | ✓ | ✗ | ✗ | COE | Homer | Homer Pro |
| [30] | Denmark | ✓ | ✗ | ✓ | ✓ | ✗ | ✗ | Total Cost, PAF | Rule Based | Convex Optimization - Matlab |
| [31] | Kuwait | ✓ | ✗ | ✓ | ✓ | ✗ | ✗ | NPC | CC, LF | Homer Pro |
| [19] | South Korea | ✓ | ✗ | ✓ | ✓ | ✗ | ✗ | NPC | Homer | Homer Pro |

**Note: BAT**: Batteries, **CE**: Cost of Energy, **FC**: Fuel Cell, **GHG**: Greenhouse Gases, **LCOE**: Levelized Cost of Energy, **LF**: Load Following, **NPC**: Net Present Cost, **PAF**: Power Autonomy Factor, **PV**: Photovoltaic Panel, **PS**: Peak Shaving, **WT**: Wind Turbine.

**Table 1.1:** Survey of Studies on Hybrid Renewable Energy Systems for Telecom Base Station Power Supply.

## 2.2 SWOT analysis

Each hybrid system architecture presents distinct advantages and limitations. Therefore, this subsection is dedicated to a SWOT analysis (Table 1.2) of commonly deployed (HRES) used for powering base stations.

| HRES | S<br>Strengths | W<br>Weaknesses | O<br>Opportunities | T<br>Threats |
|---|---|---|---|---|
| **PV/BAT** | High penetration rate of renewable energies.<br>Low maintenance.<br>Zero carbon emission during the operation | Requires more space.<br>Charging time of batteries.<br>Batteries lifespan | Reduction of panel prices. | High probability of service outage (power intermittency) |
| **PV/FC** | Important penetration rate of renewable energy.<br>Limited maintenance.<br>Doesn't require energy storage systems.<br>Zero carbon emission during the operation | Fuel supply<br>High capital cost<br>Requires Large space | PV panels are decreasing in price.<br>Support R&D to bring down the costs of fuel cells | Electrolyte failure of the fuel cell<br>No ecosystem in place |
| **PV/WT BAT** | High system reliability<br>Zero emissions during the operation | High capital cost<br>Batteries lifespan<br>Geographic dependency (wind speed) | PV panels are decreasing in price. | High probability of service outage |
| **PV/WT FC** | High penetration rate of renewable energies.<br>Low maintenance cost<br>Zero carbon emissions | High capital cost<br>Geographic dependency (wind speed) | PV panels are decreasing in price.<br>Support R&D to bring down the costs of fuel cells | Electrolyte failure of the fuel cell<br>High probability of service outage |
| **PV/DG/ BAT** | High system reliability<br>Low investment cost | GHGs emissions<br>Fuel price and logistics<br>High OPEX<br>Batteries lifespan | PV panels are decreasing in price. | Uncertainty about the fuel price |

**WT** : Wind Turbine, **PV**: Photovoltaic Panel, **BAT** : Batteries, **DG** : Diesel Generator, **FC** : Fuel Cell.

**Table 1.2:** SWOT analysis of common hybrid systems used for powering base stations

### 2.3 Weather Impact on HRES Reliability

Base Stations are critical loads, requiring HRES designed to supply them to demonstrate exceptional reliability and resilience. The operational performance of such systems can be significantly affected by unexpected equipment failures or adverse weather conditions. For example, in 2018, soiling caused an estimated 3–4% reduction in annual photovoltaic energy production, corresponding to economic losses of approximately €3–5 billion. By 2023, these losses were estimated to have increased to 4–5% in energy production, resulting in financial losses of around €4–7 billion [32]. This study focuses on the specific impact of snow soiling on PV modules, particularly in regions prone to significant snowfall. Snow accumulation poses a critical challenge to PV systems by reducing their energy output. Research conducted in Michigan, USA [33], analyzed the effects of snow on PV performance. The study revealed that annual energy losses due to snow ranged between 5% and 12% for elevated, unobstructed modules, with steeper tilt angles resulting in reduced losses. Conversely, obstructed modules experienced energy losses of 29% to 34%, with the tilt angle exerting minimal influence on these losses.Similarly, research conducted in Truckee, California, which experiences an average of 5 meters (200 inches) of snow annually, demonstrated monthly snow-related energy losses reaching 100% for flat, low-profile systems. Annual losses for fixed-tilt systems were reported at 6%, while low-profile systems exhibited losses of 13%, 17%, and 26% for tilt angles of 39°, 24°, and 0°, respectively [34]. Additional studies from Ontario, Canada [35], showed that annual energy yield losses due to snow accumulation reached approximately 3.5%. Further supporting evidence [36]–[39] underscores the importance of considering the effects of snow in the optimal design of PV systems. For PV systems integrated with batteries, snow-related energy losses as high as 100% can result in a complete system failure, reducing reliability to 0%. These findings highlight the critical importance of accounting for snow impact in the design of HRES to ensure reliable operation in snow-prone regions. However, integrating such considerations into standard tools like HOMER Pro remains a complex challenge.

## 3 State of art of the management strategies

Energy management strategies for hybrid energy systems can be classified into three primary methodological frameworks [40], [41] (Figure 1.5).The first category comprises classical rule-based approaches, which leverage human expertise and heuristic knowledge to establish predefined control protocols. While these methods benefit from their straightforward implementation, they may not achieve optimal system performance due to their deterministic nature.

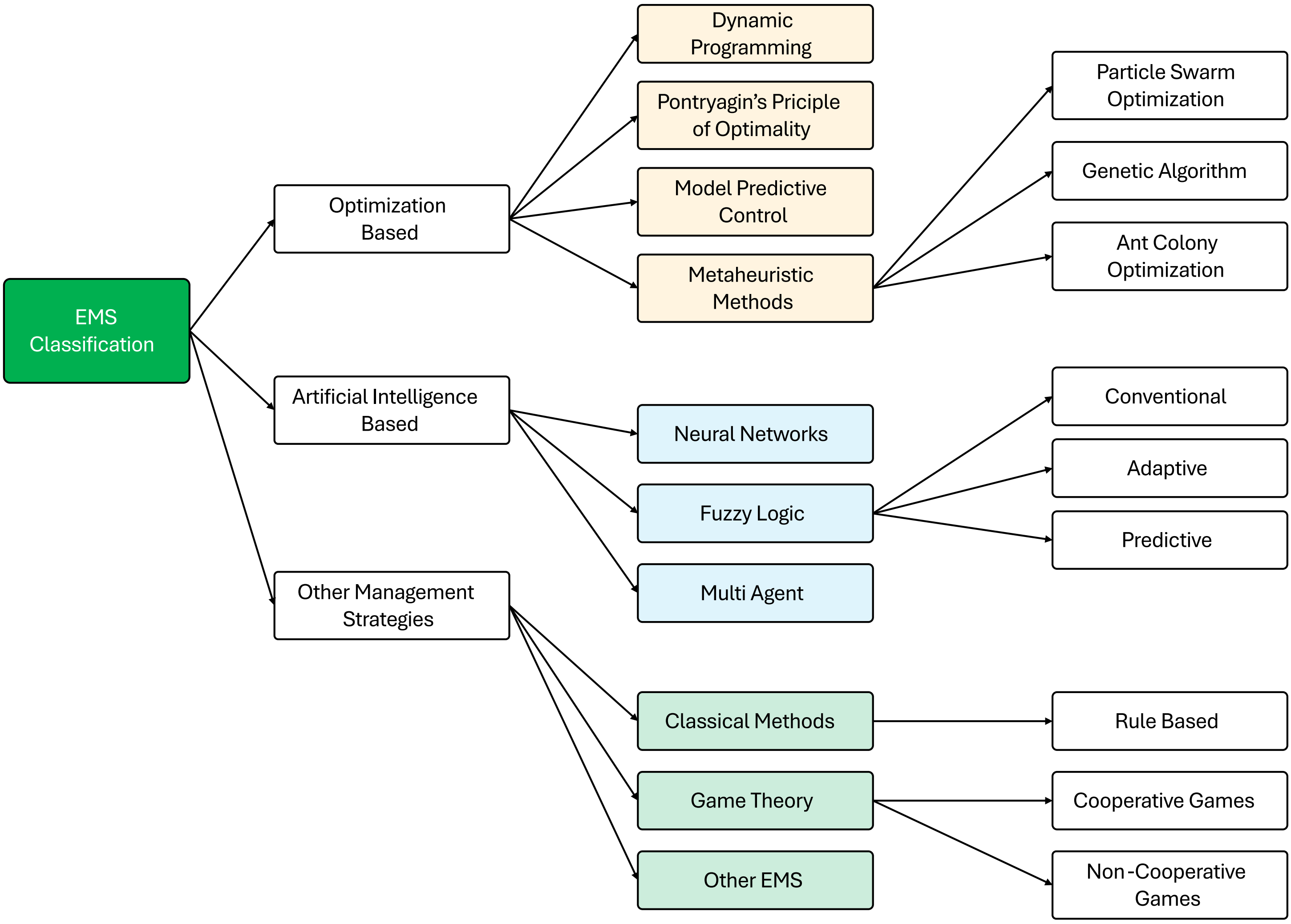


**Figure 1.5:** Energy management strategies

The second category consists of optimization-based methods, which employ mathematical programming techniques to determine control sequences that minimize specified cost functions while satisfying system constraints. These approaches systematically explore the solution space to identify optimal operational parameters, enabling more efficient resource utilization compared to rule-based strategies. The third category encompasses learning-based methods, which utilize machine learning algorithms to address system complexity. These approaches demonstrate particular efficacy in managing non-linear system dynamics and adapting to varying operational conditions through data-driven decision-making processes. Recent research has expanded beyond these traditional categories to incorporate game theory approaches, particularly for multi-agent systems. These methods are especially relevant when managing interactions between multiple system components or stakeholders, though your text appears to be incomplete regarding this aspect.. We will present in detail the common management strategies for Hybrid energy systems in the following.

### 3.0.1 Deterministic rule-based control

It involves implementing predetermined rules and algorithms to determine the optimal control actions for managing energy systems. These rules are typically based on mathematical models, system constraints, and predefined thresholds. Deterministic-based control aims to achieve precise and predictable energy management outcomes by following a set of predetermined guidelines, without incorporating probabilistic or stochastic elements. It provides a structured and rule-driven framework for optimizing energy usage and system performance.

### 3.0.2 Fuzzy logic

Fuzzy logic control is an approach that aims to replicate human thinking by constructing a set of fuzzy rules based on human expertise. This control strategy involves three main steps: fuzzification, inference engine, and defuzzification ( Figure 1.6 ).
Fuzzification: In this step, numerical inputs or variables are transformed into linguistic variables using membership functions. Membership functions define the degree of membership of a value to different fuzzy sets, representing linguistic terms like ”low”, ”medium”, and ”high”. Inference Engine: The inference engine applies fuzzy rules to the fuzzy sets obtained from fuzzification. These rules capture the expert knowledge and define relationships between input variables and output variables. The inference engine evaluates the fuzzy rules and determines the degree to which each rule is activated based on the current input values. Defuzzification: After the fuzzy rules have been evaluated, the defuzzification process converts the fuzzy output variables into crisp values that can be understood by the system. This is done by aggregating the fuzzy sets and finding the most representative crisp value.

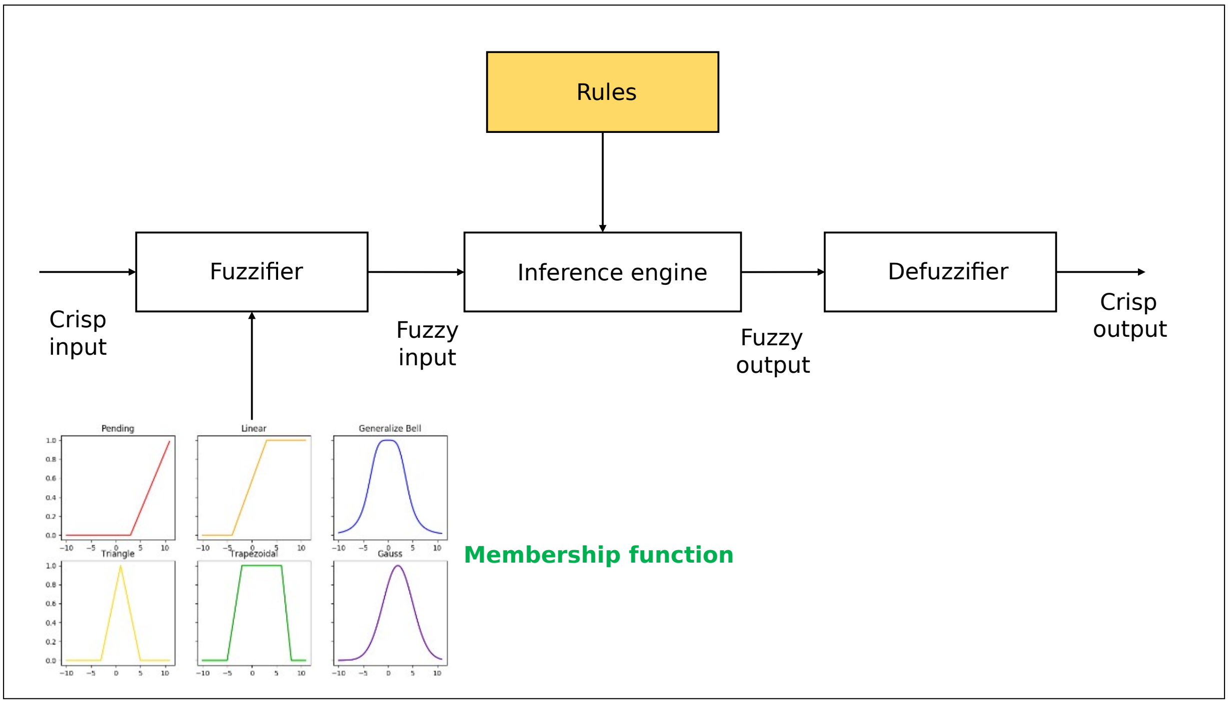


**Figure 1.6:** Block Diagram of Fuzzy Logic Strategy

### 3.0.3 Neural network-based control

Neural network-based control is a strategy for energy management that utilizes artificial neural networksto optimize control actions and decision-making processes. ANNs are computational models inspired by the structure and functioning of biological neural networks in the human brain. In the context of energy management, neural network-based control involves training an ANN using historical data and relevant input variables to learn the relationships and patterns within the data. The trained neural network then predicts the optimal control actions based on the current state of the energy system. The second category of energy management strategies consists of optimization-based methods, which encompass dynamic programming, Pontryagin's minimum principle, model predictive control, and metaheuristic methods. These approaches aim to optimize energy management decisions by leveraging mathematical optimization techniques and algorithms, which don't require any prior information about the system.

### 3.0.4 Dynamic programming

Dynamic programming is a numerical method that finds the global optimal solution by operating backwards in time. Dynamic programming is based on Bellman's principle of optimality. where the optimal control sequence can be expressed as :

$$u_k = \mu^*(x_k, k) = argmin\,(L_k(x_k, u) + Y_{k+1}(f_k(x_k, u_k), u_k))$$

where $Y_{k+1}$ is the cost to go function satrting for $k+1$ to $N$.

$$Y_k(x_k, i) = L_N(x_N, u) + \sum_{k=i}^{N-1} L_k x_k, u_k$$

$L_k$ is the instantaneous cost function.

## Pontraygin's minimum principle

It is a robust method to find the optimal control of a system and probably the one that has received the most attention in recent years. The principle can be formulated as follows :

if $u^*$ is the optimal control of a dynamical system, then the following conditions are satisfied :

$$\begin{aligned}
&\dot{x}^*(t) = \frac{\partial H}{\partial \lambda} = f(x(t)^*, u(t)^*, t) \\
&\dot{\lambda}^*(t) = -\frac{\partial H}{\partial x} = -\frac{\partial L}{\partial x}(x(t)^*, u(t)^*, t) - \left[\frac{\partial f}{\partial x} f(x(t)^*, u(t)^*, t)\right]^T \qquad x(t_0) = x_0 \\
&x(t_f) = x_f \\
&u^*(t) = arg\min_{u \in U}\,(H(u(t)), x(t), \lambda(t)), t))
\end{aligned}$$

### 3.0.5 Model predictive control

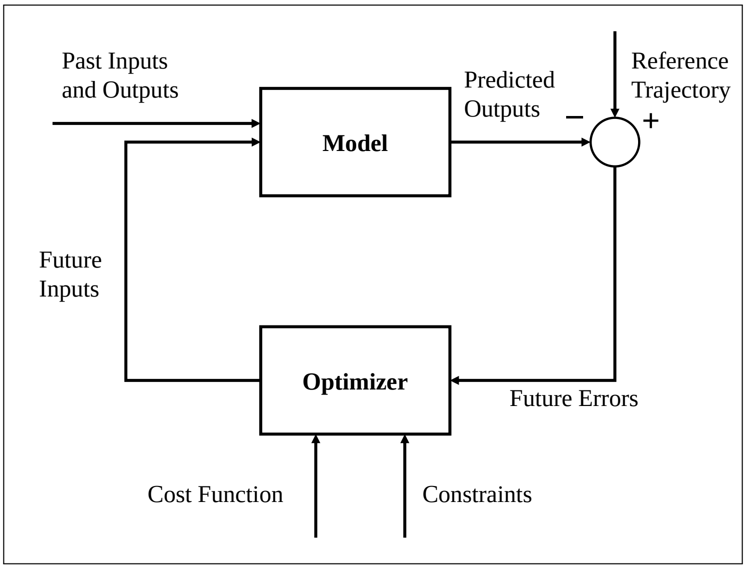


**Figure 1.7:** Basic Structure of Model Predictive Control [42]

Model Predictive Control is an advanced real-time control strategy employed in energy management (Figure 1.7). By utilizing a mathematical model of the system, MPC enables predictive decision-making. It involves solving an optimization problem repeatedly over a specified prediction horizon to determine the optimal control actions. MPC utilizes a dynamic model of the energy system to forecast its future behavior, taking into account the current state and expected disturbances. The control problem is formulated by defining an objective function that encapsulates the desired performance criteria and constraints .

## 3.1 Scientometric Analysis

This section presents a comprehensive scientometric analysis to evaluate the current state of research regarding snow impact on photovoltaic (PV) systems and the integration of management strategies with system design. The analysis aims to identify key contributors and trace scientific developments in these domains. Our investigation focuses on two primary aspects that underscore the novelty of this research: (1) the impact of snow accumulation on PV module performance and (2) the coordination between management strategies and system design. The analysis utilizes the Scopus database, a comprehensive scientific citation indexing service maintained by Elsevier. An initial database query combining the keywords ”PV panels” and ”Impact of snow” yielded 121 published papers(See Figure 1.8). The analysis reveals a significant acceleration in research activity following the publication of the Marion model in 2013, which served as a catalyst for subsequent investigations into snow-related performance impacts on PV systems. The literature addressing snow impact evaluation on PV systems can be categorized into four distinct methodological approaches:

- Rule-based Algorithms: This category encompasses the pioneering Marion model [36], [43] and subsequent derivatives, which establish systematic frameworks for snow impact assessment.
- Empirical Relationship Studies [44] : These investigations derive correlations between snow-induced power losses and meteorological parameters, including ground interference term (GIT), relative humidity (RH), ambient temperature (Tair), and plane of array insolation (POA), using field data from operational PV installations.
- Stochastic Modeling [45]: This approach employs probabilistic methods, particularly Monte-Carlo Simulation (MCS), to estimate electricity generation losses by analyzing actual PV system performance data in conjunction with simulated scenarios.
- Deep Learning Techniques [46]: The most recent category leverages artificial intelligence techniques to quantify the relationship between various snow parameters and solar power generation, offering new insights into complex, non-linear interactions.

This categorization provides a structured framework for understanding the evolution of research methodologies in addressing snow-related impacts on PV system performance.

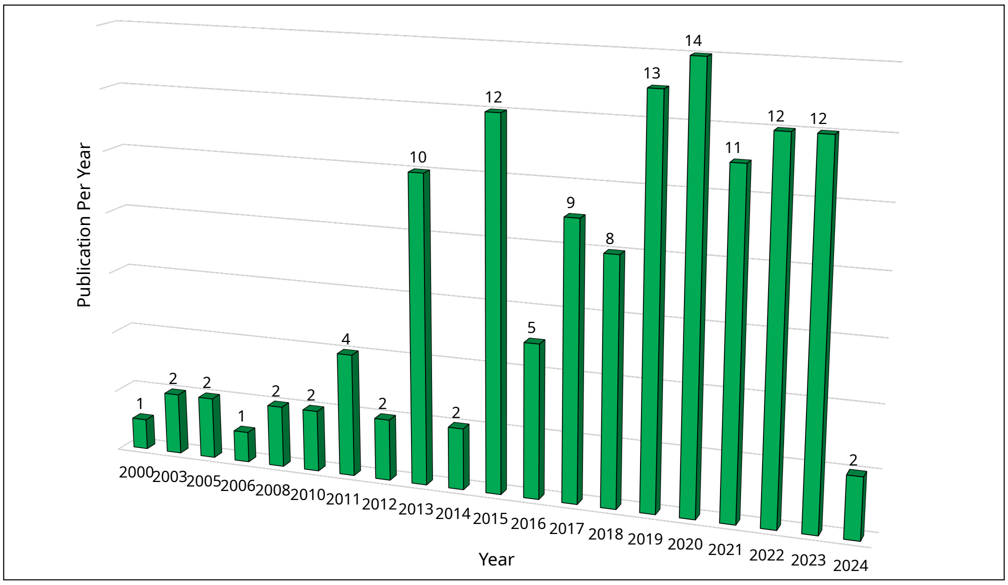


**Figure 1.8:** Publications by year that investigated the subject of Snow Impact on PV Panels Copyright © 2022 Elsevier B.V. All rights reserved. Scopus® is a registered trademark of Elsevier

Further scientometric analysis focused on bifacial PV modules reveals a significant research gap. Between 2017 and 2024, only ten publications addressed the performance of bifacial modules under snowy conditions. Notably, according to the Scopus database, no studies have investigated the integration of bifacial modules within microgrids operating in snow-affected environments, highlighting a fundamental research opportunity. Two pivotal studies have provided significant insights into bifacial module performance in snow-prone regions. The first investigation [47] presented a comparative analysis between conventional bifacial and monofacial modules, revealing substantial performance differentials. Monofacial PV systems exhibited significant snow-related energy losses, averaging 33% during winter periods and 16% annually. In contrast, bifacial systems demonstrated superior performance under severe winter conditions, with winter snow losses limited to 16% and annual losses not exceeding 2% in worst-case scenarios. Most notably, the study documented a 19% bifacial gain compared to monofacial systems during winter operations. The second study elucidated the enhanced snow-shedding capabilities of bifacial PV panels relative to their monofacial counterparts. The research demonstrated that bifacial panels can achieve 10-15% higher electrical energy production through the capture of ground-reflected light, particularly when snow cover increases surface albedo. Furthermore, bifacial panels exhibited accelerated recovery following snowfall events, resuming normal operation more rapidly than monofacial panels, which typically remained snow-covered for extended periods. These encouraging findings provide a strong rationale for investigating the potential deployment of bifacial modules in nanogrid applications, particularly for powering bifacial stations in harsh environments characteristic of Canadian regions. The results underscore the importance of developing accurate power production models that incorporate these snow-related factors, enabling precise sizing and management strategies for nanogrid systems. This research direction addresses a critical gap in the current literature while promising improved system performance in snow-affected environments.

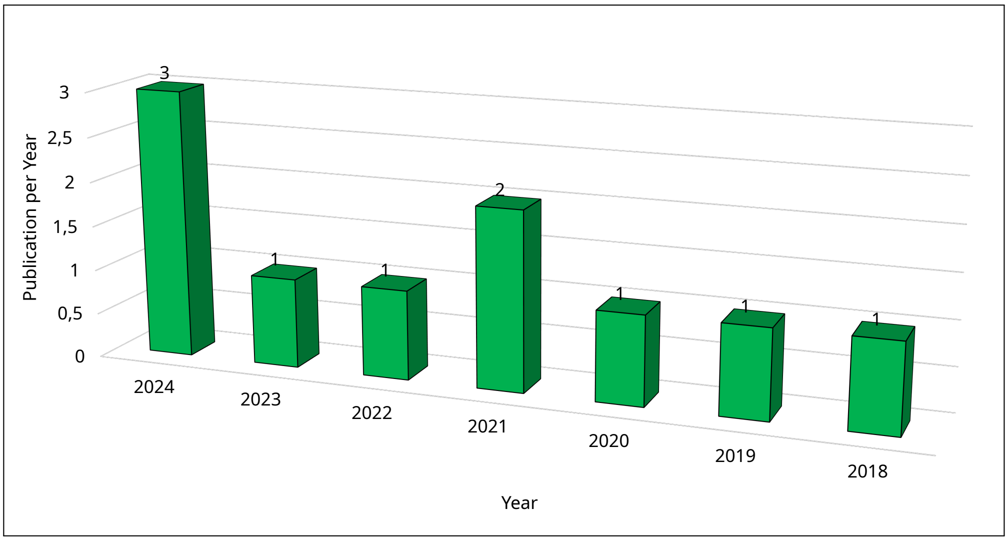


**Figure 1.9:** Publications by year that investigated the subject of Snow Impact on Bifacial PV Modules 

The second aspect of our scientometric analysis examines the integration of design and management strategies through joint optimization approaches in microgrid systems. An investigation of the Scopus database using the keywords "joint optimization", "design and management" and "Microgrids" yielded 246 published papers (Figure 1.10). While not all publications specifically address simultaneous design and management optimization, they reveal distinct methodological frameworks:

- Multi-level Optimization: Decomposes complex problems into hierarchical levels, enabling systematic handling of temporal and spatial scales.
- Bilevel Optimization: Addresses nested optimization problems, typically separating design decisions from operational strategies.
- Multi-step Optimization: Resolves optimization through sequential stages with varying time horizons and decision variables.
- Single-layer Optimization: Tackles design and management simultaneously within a unified framework.

The optimization approaches can be further classified based on their objective function structure: single-objective optimization, which focuses on one specific goal, and multi-objective optimization, which handles competing objectives. In multi-objective cases, the objectives are often consolidated into a single objective function through weighting methods to manage their opposing interests. The significant number of publications and diverse methodological approaches indicate this research domain's growth phase, suggesting opportunities for novel contributions in coordinating design and management strategies, particularly for systems with specific operational constraints such as snow-affected PV installations.

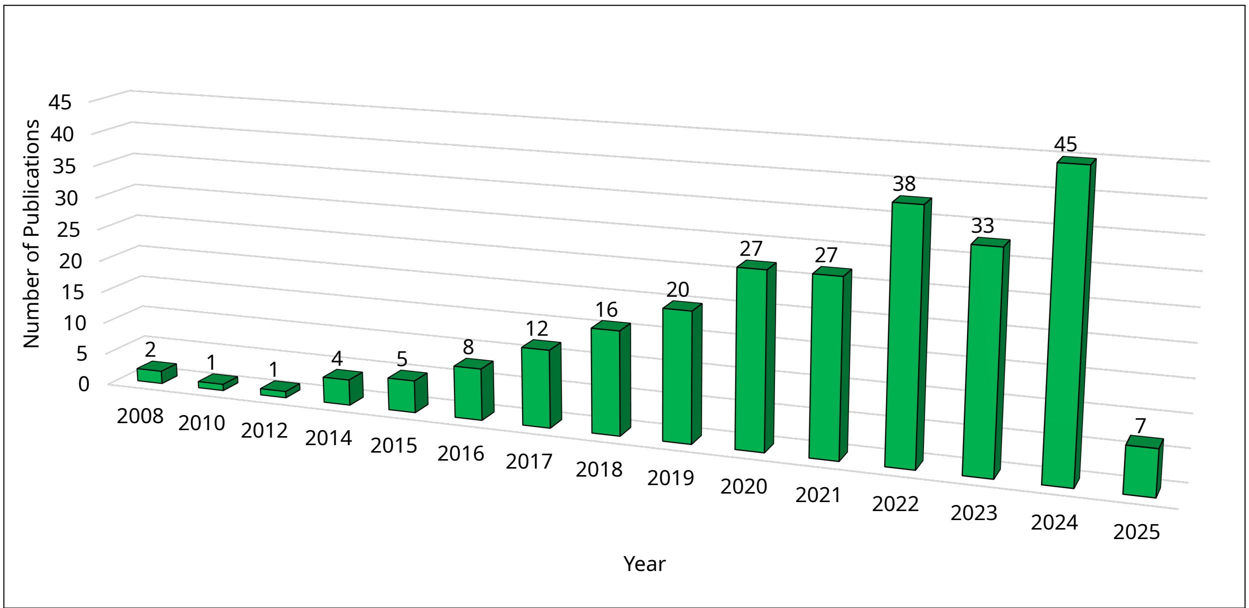


**Figure 1.10:** Publications by year that investigated the subject of Joint Optimization in Microgrids Copyright © 2022 Elsevier B.V. All rights reserved. Scopus® is a registered trademark of Elsevier

# 4 Research Questions

This research project aims to design a MCDES [2] that can achieve high energy efficiency and low carbon emissions. To do so, it requires a collaborative optimization strategy and a life cycle cost that covers all aspects of the system, such as power generation, conversion, storage and consumption.

However, this type of optimization faces two main challenges: the multi-time scales of the system and the uncertainties of the power units, which depend on the variability of renewable sources and the load demand. In this PhD project, we focus on HRES with three power sources and evaluate them based on two cost functions: the LCC that reflects the economic objectives, and the direct carbon emissions that assesses the greenhouse gas emissions.

As mentioned earlier, this problem requires considering two degrees of freedom: the sizing of each sub-system and the management strategy. However, most of the existing research focuses either on the operation [48]–[51] or the design [52]–[56]. For intance, the authors

[2]Multi-energy complementary distributed energy system

of [57] proposed an optimal design of a wind-PV hybrid system with battery storage, taking into account the embodied energy (the energy consumed during the manufacturing process, such as the 1306 MJ/kWp to 1199 MJ/kWp range for PV panels [58]). Similarly, the authors of of [59] presented an optimal sizing of a hybrid PV/Wind/Battery system using a multi-objective optimization problem that considers three objective functions: LCC, EE, and LPSP.

Based on the analysis we have performednd the current state of the art, the main research questions that guide this research project are:

1. What methodologies can be developed to effectively incorporate temporal variations in meteorological parameters into micro-grid design optimization, and how do these seasonal fluctuations affect system performance and reliability?
2. In regions with significant snowfall, what are the critical design considerations for nanogrid systems, and how can snow-related impacts be quantified and integrated into optimization frameworks to ensure robust system performance?
3. How does the energy management strategy impact the optimal design of microgrids, particularly when considering the trade-offs between environmental sustainability, economic viability, and operational efficiency?
4. What approach can enable simultaneous optimization of both system design parameters and management strategy variables in microgrid systems?

## 5 Conclusion

The telecommunications industry is at a turning point, balancing the expansion of digital connectivity with the urgency of sustainable energy adoption. With telecom networks consuming 3% of global energy and base stations accounting for 57% of this demand, optimizing their power systems is crucial. While renewable energy integration has increased from 14% in 2020 to 24% in 2023, significant challenges remain, particularly in off-grid and bad-grid sites where reliance on diesel persists.

In Canada, the digital divide remains stark, with only 64% of rural and 41.53% of Indigenous communities having adequate connectivity. At the same time, major telecom operators have committed to reducing emissions by 50% by 2030, demanding innovative solutions that balance sustainability and reliability.

Our scientometric analysis identified two significant research gaps within the studied literature: the effects of snow on photovoltaic systems and the integrated optimization of design and management strategies that incorporate these snow-related factors. Among 121 studies examining snow impact, only eight publications (2018–2024) specifically investigated bifacial photovoltaic modules under snowy conditions. Additionally, analysis of 246 publications on optimization strategies revealed that joint design and management strategy optimization for microgrids operating under snow-affected conditions represents an underexplored yet promising research domain, with limited studies addressing this integrated approach within the environmental conditions characteristic of the studied regions.

HOMER Pro, a widely used tool for hybrid energy system sizing, lacks key capabilities in this regard—it does not support bifacial PV modeling, joint optimization, or snow impact integration. Our research aims to fill these gaps by developing a comprehensive tool for telecom operators, providing optimal design and management strategies tailored for challenging environments.

The next chapter will introduce the preliminary work of this research, positioning our approach against existing tools like HOMER Pro and highlighting how our methodology addresses its limitations while advancing the field of sustainable telecom infrastructure.

## References for Chapter 1

[1] Jagueneau, Alix. *Mobile Net Zero 2024: State of the Industry on Climate Action*. Accessed via GSMA website. GSMA, 2024. URL: %7Bhttps://www.gsma.com/solutions-and-impact/connectivity-for-good/external-affairs/wp-content/uploads/2024/02/Mobile-Net-Zero-2024-State-of-the-Industry-on-Climate-Action.pdf%7D (visited on 02/10/2025).

[2] GSMA. *Mobile net zero: State of the industry on Climate Action 2022 Report*. June 2022. URL: https://www.gsma.com/betterfuture/resources/mobile-net-zero-state-of-the-industry-on-climate-action-2022-report (visited on 04/03/2025).

[3] GSMA. *Renewable energy for mobile towers: Opportunities for low- and middle-income countries*. Sept. 2020. URL: https://www.gsma.com/mobilefordevelopment/resources/renewable-energy-for-mobile-towers-opportunities-for-low-and-middle-income-countries/.

[4] GSMA. *Mobile net zero: State of the industry on Climate Action 2022 Report*. June 2022. URL: https://www.gsma.com/betterfuture/resources/mobile-net-zero-state-of-the-industry-on-climate-action-2022-report.

[5] GSMA. *Going green: Benchmarking the energy efficiency of Mobile*. June 2021. URL: https://data.gsmaintelligence.com/api-web/v2/research-file-download?id=60621137%20%5C&file=300621-Going-Green-efficiency-mobile.pdf (visited on 04/03/2024).

[6] International Finance Corporation. *Investing in Sustainable Access to Communications:The Role of Telecom Energy Services Companies*. 2021, p. 75. URL: https://www.ifc.org/content/dam/ifc/doc/mgrt/tesco-study-web-9-29-21-final.pdf (visited on 04/03/2025).

[7] Accenture. *Canada's next sustainability frontier: Powering digital transformation with connectivity*. Commissioned by Canadian Telecommunications Association. Canada: Canadian Telecommunications Association, 2023. URL: 'https://canadatelecoms.ca/wp-content/uploads/2023/10/Canadas-Next-Sustainability-Frontier-Powering-Digital-Transformation-with-Connectivity.pdf' (visited on 04/03/2025).

[8] Abdul-Hakim Fuseini, Adam Suleman, Emily Peden, et al. *Navigating Net-Zero*. Policy Lab Brief. Policy Lab Brief. McGill University's Max Bell School of Public Policy, 2024. URL: https://www.mcgill.ca/maxbellschool/files/maxbellschool/telus_navigating_net-zero.pdf (visited on 06/2024).

[9] Bell Canada. *2020 Energy and Greenhouse Gas Report*. June 2021. URL: https://bce.ca/responsibility/key-documents/2020-energy-greenhouse-gas.pdf (visited on 04/03/2025).

[10] Rogers Communications Inc. *2023 Climate Action Report. Available online at the provided URL.* Canada, 2024. URL: https://about.rogers.com/wp-content/uploads/2023-Climate-Action-Report.pdf (visited on 04/03/2024).

[11] Kanzumba Kusakana and Herman Jacobus Vermaak. "Hybrid renewable power systems for mobile telephony base stations in developing countries". In: *Renewable Energy* 51 (Mar. 2013), pp. 419–425. ISSN: 09601481. DOI: 10.1016/j.renene.2012.09.045.

[12] Furqan Asghar, M. Imtiaz Hussain, Fahad Abdullah Alshahrani, et al. "Technoeconomic analysis of standalone hybrid renewable energy systems for telecommunication sector under different climatic conditions in Saudi Arabia". In: *Energy Reports* 11 (June 2024), pp. 4067–4084. ISSN: 23524847. DOI: 10.1016/j.egyr.2024.03.055.

[13] Peter Ozaveshe Oviroh, Tien-Chien Jen, Nosa Idusuyi, et al. "Comparative Energy Cost Analysis of Hybrid System and Diesel Generator in Powering Selected Base Transceiver Stations in Nigeria". In: American Society of Mechanical Engineers, Nov. 2017. ISBN: 978-0-7918-5841-7. DOI: 10.1115/IMECE2017-71212.

[14] David A. Quansah, Saviour K. Woangbah, Emmanuel K. Anto, et al. "TECHNO-ECONOMICS OF SOLAR PV-DIESEL HYBRID POWER SYSTEMS FOR OFF-GRID OUTDOOR BASE TRANSCEIVER STATIONS IN GHANA". In: *International Journal of Energy for a Clean Environment* 18 (1 2017), pp. 61–78. ISSN: 2150-3621. DOI: 10.1615/InterJEnerCleanEnv.2017019537.

[15] Solargis. *Solargis [Tool]*. Version x.x. Accessed: 2025-01-02. URL: https://solargis.com/.

[16] HOMER Energy. *HOMER Pro*. Version 3.16. Accessed: 2025-01-14. Boulder, CO: HOMER Energy by UL Solutions, 2023. URL: https://www.homerenergy.com.

[17] Subodh Paudel, J. N. Shrestha, Fernando J. Neto, et al. "Optimization of hybrid PV/wind power system dfor remote telecom station". In: IEEE, Dec. 2011, pp. 1–6. ISBN: 978-1-4577-1510-5. DOI: 10.1109/ICPES.2011.6156618.

[18] Lanre Olatomiwa, Saad Mekhilef, A. S. N. Huda, et al. "Techno-economic analysis of hybrid PV –diesel–battery and PV –wind–diesel–battery power systems for mobile BTS: the way forward for rural development". In: *Energy Science and Engineering* 3 (4 July 2015), pp. 271–285. ISSN: 2050-0505. DOI: 10.1002/ese3.71.

[19] Mohammed Alsharif and Jeong Kim. “Optimal Solar Power System for Remote Telecommunication Base Stations: A Case Study Based on the Characteristics of South Korea’s Solar Radiation Exposure”. In: *Sustainability* 8 (9 Sept. 2016), p. 942. ISSN: 2071-1050. DOI: 10.3390/su8090942.

[20] Muhammad Bilal Ali, Abdullah Altamimi, Syed Ali Abbas Kazmi, et al. “Techno-economic-environmental optimization of on-grid hybrid renewable energy-electric vehicle charging stations in BTS infrastructure”. In: *Energy Conversion and Management: X* 23 (July 2024), p. 100644. ISSN: 25901745. DOI: 10.1016/j.ecmx.2024.100644.

[21] Muhammad Bilal Ali, Syed Ali Abbas Kazmi, Shahid Nawaz Khan, et al. “Techno-economic assessment and optimization framework with energy storage for hybrid energy resources in base transceiver stations-based infrastructure across various climatic regions at a country scale”. In: *Journal of Energy Storage* 72 (Nov. 2023), p. 108036. ISSN: 2352152X. DOI: 10.1016/j.est.2023.108036.

[22] S. Cordiner, V. Mulone, A. Giordani, et al. “Fuel cell based Hybrid Renewable Energy Systems for off-grid telecom stations: Data analysis from on field demonstration tests”. In: *Applied Energy* 192 (Apr. 2017), pp. 508–518. ISSN: 03062619. DOI: 10.1016/j.apenergy.2016.08.162.

[23] G. Bruni, S. Cordiner, V. Mulone, et al. “Fuel cell based power systems to supply power to Telecom Stations”. In: *International Journal of Hydrogen Energy* 39 (36 Dec. 2014), pp. 21767–21777. ISSN: 03603199. DOI: 10.1016/j.ijhydene.2014.07.078.

[24] Daming Li, Lianbing Deng, Qinglang Su, et al. “Providing a guaranteed power for the BTS in telecom tower based on improved balanced owl search algorithm”. In: *Energy Reports* 6 (Nov. 2020), pp. 297–307. ISSN: 23524847. DOI: 10.1016/j.egyr.2020.01.006.

[25] Maoqing Xie, Leigang Wang, and Hasan Jafari. “Optimal formation of a PEMFC-based telecom tower using Courtship Learning-based Water Strider Algorithm”. In: *Energy Reports* 7 (Nov. 2021), pp. 3225–3237. ISSN: 23524847. DOI: 10.1016/j.egyr.2021.05.051.

[26] Mohammad Junaid Khan, Amit Kumar Yadav, and Lini Mathew. “Techno economic feasibility analysis of different combinations of PV-Wind-Diesel-Battery hybrid system for telecommunication applications in different cities of Punjab, India”. In: *Renewable and Sustainable Energy Reviews* 76 (Sept. 2017), pp. 577–607. ISSN: 13640321. DOI: 10.1016/j.rser.2017.03.076.

[27] Naglaa K. Bahgaat. “Estimation of renewable energy systems for mobile network based on real measurements using HOMER software in Egypt”. In: *Scientific Reports* 13 (1 Oct. 2023), p. 16713. ISSN: 2045-2322. DOI: 10.1038/s41598-023-43877-2.

[28] Saïd Bentouba and Mahmoud Bourouis. “Feasibility Study and Environmental Impact of Using a Photovoltaic System to Secure Relays of Mobile Communication Systems”. In: *Journal of Solar Energy Engineering* 143 (3 June 2021). ISSN: 0199-6231. DOI: 10.1115/1.4048299.

[29] Tasneem Salih, Yaodong Wang, and Marwan Awad Ahmed Adam. “Renewable Micro Hybrid System of Solar Panel and Wind Turbine for Telecommunication Equipment in Remote Areas in Sudan”. In: *Energy Procedia* 61 (2014), pp. 80–83. ISSN: 18766102. DOI: 10.1016/j.egypro.2014.11.911.

[30] Mahshid Javidsharifi, Hamoun Pourroshanfekr, Tamas Kerekes, et al. “Optimum Sizing of Photovoltaic and Energy Storage Systems for Powering Green Base Stations in Cellular Networks”. In: *Energies* 14 (7 Mar. 2021), p. 1895. ISSN: 1996-1073. DOI: 10.3390/en14071895.

[31] Mohammed W. Baidas, Rola W. Hasaneya, Rashad M. Kamel, et al. “Solar-Powered Cellular Base Stations in Kuwait: A Case Study”. In: *Energies* 14 (22 Nov. 2021), p. 7494. ISSN: 1996-1073. DOI: 10.3390/en14227494.

[32] Christian Schill, Anne Anderson, Christopher Baldus-Jeursen, et al. *Soiling Losses – Impact on the Performance of Photovoltaic Power Plants*. Tech. rep. IEA-PVPS T13-21:2022. Paris, France: International Energy Agency, Photovoltaic Power Systems Programme, Dec. 2022. URL: https://iea-pvps.org/wp-content/uploads/2023/01/IEA-PVPS-T13-21-2022-REPORT-Soiling-Losses-PV-Plants.pdf.

[33] Negin Heidari, Jephias Gwamuri, Tim Townsend, et al. “Impact of Snow and Ground Interference on Photovoltaic Electric System Performance”. In: *IEEE Journal of Photovoltaics* 5 (6 Nov. 2015), pp. 1680–1685. ISSN: 2156-3381. DOI: 10.1109/JPHOTOV.2015.2466448.

[34] Tim Townsend and Loren Powers. “Photovoltaics and snow: An update from two winters of measurements in the SIERRA”. In: IEEE, June 2011, pp. 003231–003236. ISBN: 978-1-4244-9965-6. DOI: 10.1109/PVSC.2011.6186627.

[35] Rob W. Andrews, Andrew Pollard, and Joshua M. Pearce. “The effects of snowfall on solar photovoltaic performance”. In: *Solar Energy* 92 (June 2013), pp. 84–97. ISSN: 0038092X. DOI: 10.1016/j.solener.2013.02.014.

[36] "Measured and modeled photovoltaic system energy losses from snow for Colorado and Wisconsin locations". In: *Solar Energy* 97 (Nov. 2013), pp. 112–121. ISSN: 0038-092X. DOI: 10.1016/J.SOLENER.2013.07.029.

[37] S. Hosseini, S. Taheri, E. Pouresmaeil, et al. "Analysis of electrical behaviour of PV arrays covered with non-uniform snow". In: *Electronics Letters* 56 (4 Feb. 2020), pp. 192–194. ISSN: 0013-5194. DOI: 10.1049/el.2019.3221.

[38] Abdel Hakim Abou Yassine, Ehsan Khoshbakhtnejad, and Hossein Sojoudi. "Economics of Snow Accumulation on Photovoltaic Modules". In: *Energies* 17 (12 June 2024), p. 2962. ISSN: 1996-1073. DOI: 10.3390/en17122962.

[39] Soufiane Ghafiri, Maxime Darnon, Arnaud Davigny, et al. "A comprehensive performance evaluation of bifacial photovoltaic modules: insights from a year-long experimental study conducted in the Canadian climate". In: *EPJ Photovoltaics* 15 (Sept. 2024), p. 28. ISSN: 2105-0716. DOI: 10.1051/epjpv/2024025.

[40] Pavitra Sharma, Hitesh Dutt Mathur, Puneet Mishra, et al. "A critical and comparative review of energy management strategies for microgrids". In: *Applied Energy* 327 (Dec. 2022), p. 120028. ISSN: 03062619. DOI: 10.1016/j.apenergy.2022.120028.

[41] Fadi Agha Kassab, Rusber Rodriguez, Berk Celik, et al. "A Comprehensive Review of Sizing and Energy Management Strategies for Optimal Planning of Microgrids with PV and Other Renewable Integration". In: *Applied Sciences* 14 (22 Nov. 2024), p. 10479. ISSN: 2076-3417. DOI: 10.3390/app142210479.

[42] Eduardo F Camacho, Carlos Bordons, Eduardo F Camacho, et al. *Model predictive controllers*. Springer, 2007.

[43] Bill Marion, Sara MacAlpine, Chris Deline, et al. "A Practical Irradiance Model for Bifacial PV Modules". In: IEEE, June 2017, pp. 1537–1542. ISBN: 978-1-5090-5605-7. DOI: 10.1109/PVSC.2017.8366263.

[44] Mari B. Øgaard, Bjørn L. Aarseth, Åsmund F. Skomedal, et al. "Identifying snow in photovoltaic monitoring data for improved snow loss modeling and snow detection". In: *Solar Energy* 223 (July 2021), pp. 238–247. ISSN: 0038092X. DOI: 10.1016/j.solener.2021.05.023.

[45] Taehoon Hong, Choongwan Koo, and Minhyun Lee. "Estimating the Loss Ratio of Solar Photovoltaic Electricity Generation through Stochastic Analysis". In: *Journal of Construction Engineering and Project Management* 3 (3 Sept. 2013), pp. 23–34. ISSN: 2233-9582. DOI: 10.6106/JCEPM.2013.3.3.023.

[46] Noman Bashir, David Irwin, and Prashant Shenoy. "DeepSnow". In: ACM, Nov. 2020, pp. 11–20. ISBN: 9781450380614. DOI: 10.1145/3408308.3427620.

[47] Koami Soulemane Hayibo, Aliaksei Petsiuk, Pierce Mayville, et al. “Monofacial vs bifacial solar photovoltaic systems in snowy environments”. In: *Renewable Energy* 193 (June 2022), pp. 657–668. ISSN: 09601481. DOI: 10.1016/j.renene.2022.05.050.

[48] Sameh Mahjoub, Larbi Chrifi-Alaoui, Saïd Drid, et al. “Control and Implementation of an Energy Management Strategy for a PV–Wind–Battery Microgrid Based on an Intelligent Prediction Algorithm of Energy Production”. In: *Energies* 16.4 (2023). Cited by: 3; All Open Access, Gold Open Access. DOI: 10.3390/en16041883. URL: https://www.scopus.com/inward/record.uri?eid=2-s2.0-85153675634%20%5C&doi=10.3390%2fen16041883%20%5C&partnerID=40%20%5C&md5=8224aed47c8a25dd68890f3247172d0d.

[49] Azim Heydari, Meysam Majidi Nezhad, Farshid Keynia, et al. “A combined multi-objective intelligent optimization approach considering techno-economic and reliability factors for hybrid-renewable microgrid systems”. In: *Journal of Cleaner Production* 383 (2023). Cited by: 7. DOI: 10.1016/j.jclepro.2022.135249.

[50] Salam J. Yaqoob, Husam Arnoos, Mohammed A. Qasim, et al. “An optimal energy management strategy for a photovoltaic/li-ion battery power system for DC microgrid application”. In: *Frontiers in Energy Research* 10 (2023). Cited by: 1; All Open Access, Gold Open Access. DOI: 10.3389/fenrg.2022.1066231.

[51] Muhyaddin Rawa, Yusuf Al-Turki, Khaled Sedraoui, et al. “Optimal operation and stochastic scheduling of renewable energy of a microgrid with optimal sizing of battery energy storage considering cost reduction”. In: *Journal of Energy Storage* 59 (2023). Cited by: 2. DOI: 10.1016/j.est.2022.106475.

[52] Rajendran Joseph Rathish, Krishnan Mahadevan, Senthil Kumaran Selvaraj, et al. “Multi-objective evolutionary optimization with genetic algorithm for the design of off-grid PV-wind-battery-diesel system”. In: *Soft Computing* 25.4 (2021). Cited by: 13, pp. 3175–3194. DOI: 10.1007/s00500-020-05372-y. URL: https://www.scopus.com/inward/record.uri?eid=2-s2.0-85093981958%20%5C&doi=10.1007%2fs00500-020-05372-y%20%5C&partnerID=40%20%5C&md5=6fb842fe86720c4563305c0699e17ecf.

[53] Fahd A. Alturki, Abdullrahman A. Al-Shamma’a, Hassan M. H. Farh, et al. “Optimal sizing of autonomous hybrid energy system using supply-demand-based optimization algorithm”. In: *International Journal of Energy Research* 45.1 (2021). Cited by: 40; All Open Access, Bronze Open Access, pp. 605–625. DOI: 10.1002/er.5766. URL: https://www.scopus.com/inward/record.uri?eid=2-s2.0-85089288200%20%5C&doi=10.1002%2fer.5766%20%5C&partnerID=40%20%5C&md5=83b9086d677a504d58ffacd4b3c0e419.

[54] Khaled Khezzane, Mamadou Lamine Doumbia, and Farid Khoucha. "Multi-objective Sizing of Hybrid Generation Energy System for Remote Area Using Genetic Algorithm". In: Cited by: 2. 2021. DOI: 10.1109/EVER52347.2021.9456645.

[55] Aamir Mehmood, Long Zhang, and Jingzheng Ren. "A multi-stage optimisation-based decision-making framework for sustainable hybrid energy system in the residential sector". In: *Sustainable Futures* 6 (2023). Cited by: 0; All Open Access, Gold Open Access. DOI: 10.1016/j.sftr.2023.100122. URL: https://www.scopus.com/inward/record.uri?eid=2-s2.0-85169802526%20%5C&doi=10.1016%2fj.sftr.2023.100122%20%5C&partnerID=40%20%5C&md5=0e4f7ee23543728e9e44f0a7685c4a9b.

[56] Xi Chen, Zhongbing Liu, Pengcheng Wang, et al. "Multi-objective optimization of battery capacity of grid-connected PV-BESS system in hybrid building energy sharing community considering time-of-use tariff". In: *Applied Energy* 350 (2023). Cited by: 0. DOI: 10.1016/j.apenergy.2023.121727. URL: https://www.scopus.com/inward/record.uri?eid=2-s2.0-85169837101%20%5C&doi=10.1016%2fj.apenergy.2023.121727%20%5C&partnerID=40%20%5C&md5=5cba39726ee2f87ffe84d35e406c78db.

[57] Dhaker Abbes, André Martinez, and Gérard Champenois. "Life cycle cost, embodied energy and loss of power supply probability for the optimal design of hybrid power systems". In: *Mathematics and Computers in Simulation* 98 (Apr. 2014), pp. 46–62. ISSN: 03784754. DOI: 10.1016/j.matcom.2013.05.004.

[58] Giuseppe Todde, Lelia Murgia, Isaac Carrelo, et al. "Embodied Energy and Environmental Impact of Large-Power Stand-Alone Photovoltaic Irrigation Systems". In: *Energies* 11 (8 Aug. 2018), p. 2110. ISSN: 1996-1073. DOI: 10.3390/en11082110.

[59] Dhaker ABBES, André MARTINEZ, Gérard CHAMPENOIS, et al. "MULTI-OBJECTIVE DESIGN OPTIMIZATION OF A HYBRID PV-WIND-BATTERY SYSTEM". In: (). URL: https://www.da-engineering.com/wp-content/uploads/2015/01/MULTI-OBJECTIVE-DESIGN-OPTIMIZATION-OF-A-HYBRID-PV-WIND-BATTERY-SYSTEM.pdf (visited on 04/03/2025).

*"If I have seen further it is by standing on the shoulders of giants"*

Isaac Newton (1643 - 1727), Letter to Robert Hooke

# 2

# Preliminary Work And Existing Tools

## Contents



## 1 Introduction

Building upon the literature review and identified research gaps, this chapter aims to provide a comprehensive analysis of the studied nanogrid architecture. The investigation encompasses three main aspects: First, we examine the structural composition and operational principles of the studied nanogrids. Second, we analyze the preliminary investigations conducted within our laboratory . Third, we evaluate existing market tools and their capabilities in nanogrid design and optimization. Particular emphasis is placed on assessing the limitations of current solutions through systematic simulation studies. These simulations are performed using HOMER Pro, which represents the industry-standard software for microgrid and nanogrid modeling. This methodological approach enables a critical evaluation of existing tools' constraints and highlights areas requiring further development.

## 2 Architecture of The Studied Nanogrid

### 2.1 Dorval Lodge Site

Drawing from the SWOT analysis findings in Chapter 1 and aligned with the MNO partner objectives, this research identifies an optimal nanogrid configuration for powering base stations. The selected architecture combines three key components: bifacial photovoltaic (PV) modules, lithium iron phosphate (LFP) batteries, and a diesel generator backup system. This configuration has been successfully implemented at a remote base transceiver station (BTS) in Dorval Lodge, Quebec, Canada where it powers two 4G antennas. (See Figure 2.1). The installation site presents significant environmental challenges, particularly extreme weather conditions characterized by heavy snowfall and low temperatures, which demand robust and reliable energy solutions. The selection of each system component was driven by specific performance requirements and environmental considerations: The photovoltaic system utilizes bifacial modules, which capture solar energy from both front and rear surfaces. This technology is particularly advantageous in snowy environments like Dorval Lodge, where high ground reflectivity enhances rear-side energy production. Research demonstrates that bifacial modules can increase annual energy yield by up to 30% compared to traditional monofacial panels, as documented by [1], [2]. For energy storage, LFP batteries were selected based on several crucial advantages: superior thermal stability, cost-effectiveness, extended operational lifespan, and reliable performance in low-temperature conditions when properly thermally managed [3], [4]. Alternative technologies such as fuel cells were considered but ultimately rejected due to their higher maintenance requirements, which could compromise system reliability in this remote, harsh environment [3], [5]. To ensure continuous power availability during periods of limited solar generation or elevated energy demand, the system incorporates a diesel generator as a backup power source. This three-component architecture creates a robust and reliable power supply system specifically engineered to withstand and perform effectively under the challenging environmental conditions characteristic of the Dorval Lodge location.

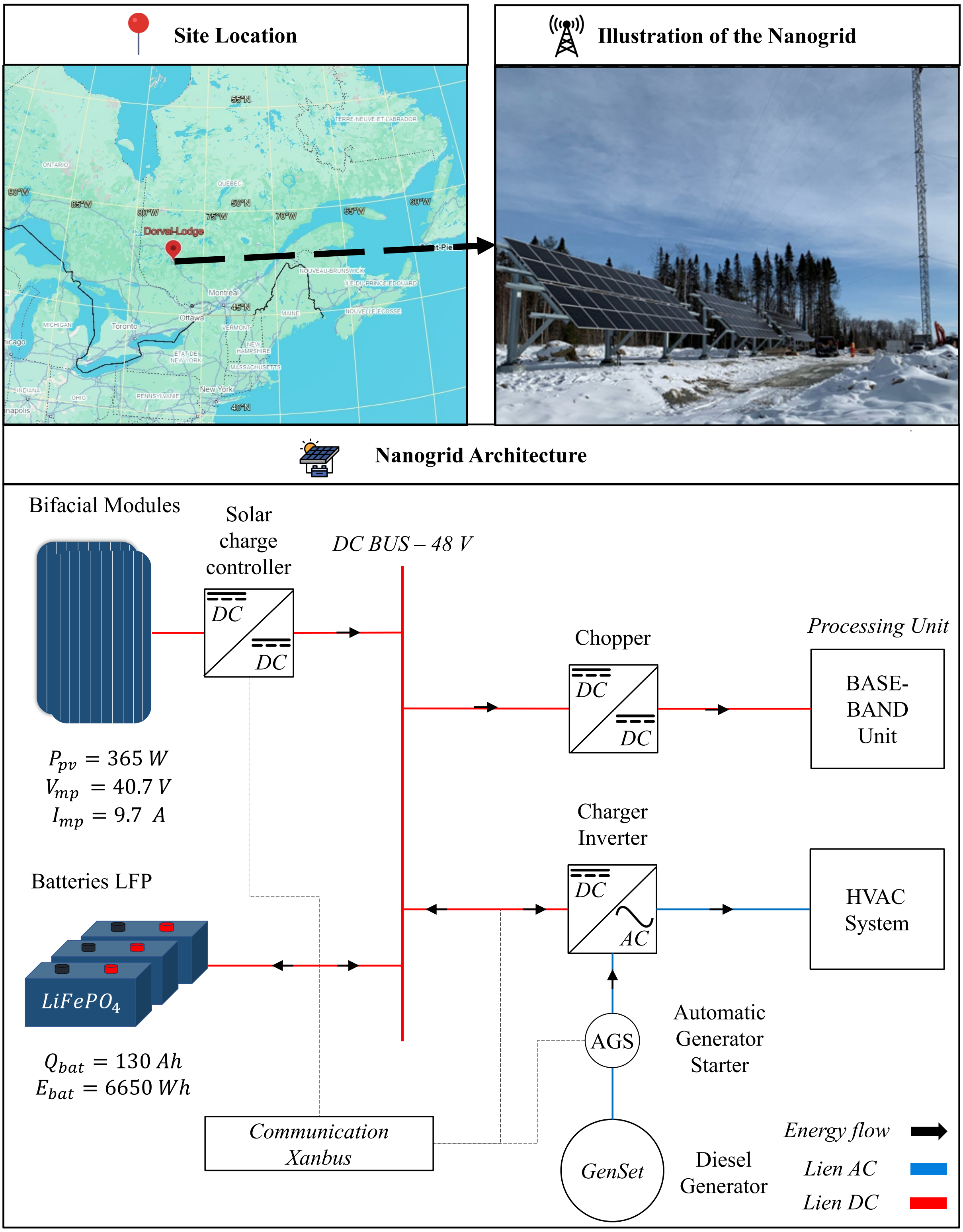


**Figure 2.1:** Geographic Location, Image, and Detailed Architectural Layout of the Proposed Nanogrid Supplying a Base Station at Dorval Lodge, Canada (45.444, -73.769)

## 2.2 Udes Prototype

A second prototype implementation of this nanogrid architecture has been established at the Sherbrooke University Campus, housed within the STACE[1] cube. This installation serves primarily as a research and development facility, providing researchers with convenient access to study and optimize the proposed solution. The campus location was strategically chosen to overcome the logistical challenges posed by the remote Dorval Lodge site, enabling more frequent and detailed experimental work. As illustrated in Figure 2.2, the STACE cube contains two 48V batteries and employs a DC load emulator for telecommunications load simulation. The system is powered by a 7.4 kWp photovoltaic array installed at the UdeS solar park's production area, consisting of 26 PV modules (370Wp each, with 20 currently connected) mounted at a fixed 45-degree tilt. To ensure continuous operation during periods of insufficient solar production (nighttime, cloudy conditions, precipitation), the system is connected to the UdeS electrical grid as a backup power source.

The installation features a programmable active load with bidirectional power capabilities, operating in load (sink) mode to simulate telecommunication antenna power requirements. This active load can both supply and absorb electrical energy, with a maximum power capacity of 18,000 watts in either direction. Its power output can be adjusted between 0 and 18,000 watts and can be monitored and controlled remotely via computer interface. This setup creates a comprehensive research environment that combines practical field implementation with detailed laboratory analysis, complementing the real-world deployment at Dorval Lodge.

[1]Saint-Augustin Canada Electric Inc

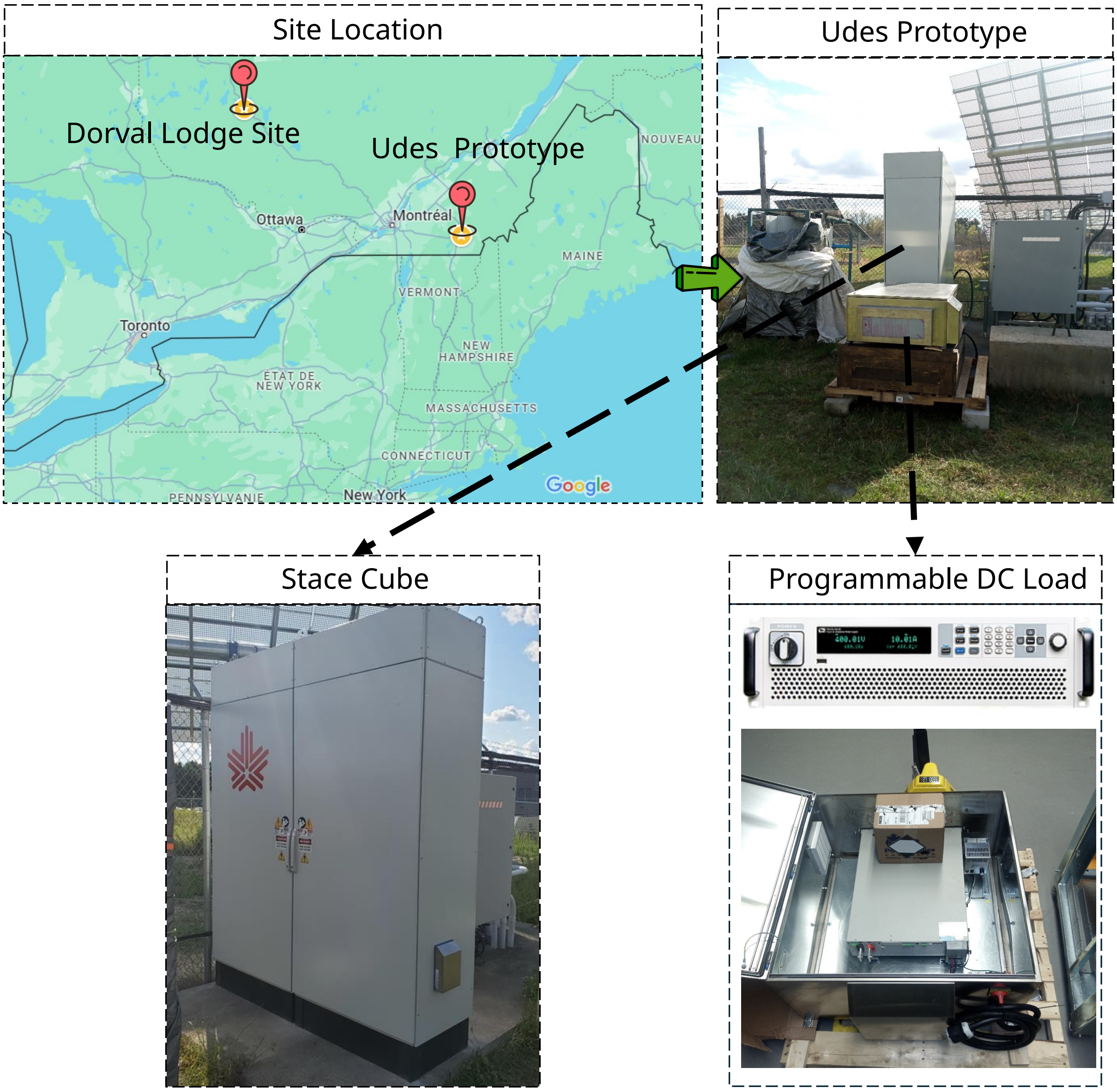


**Figure 2.2:** Geographic Location, Image, and Detailed Architectural Layout of the Udes Prototype Located in 3IT Sherbrooke (45.37, -71.94)

# 3 Nanogrid Representation

## 3.1 Energetic Macroscopic Representation

Previous research preceding this study has primarily focused on the accurate representation of the studied system to enhance its analysis and control. Among the various approaches explored, the EMR was selected for its ability to clearly depict causal relationships and energy exchanges within the system. EMR has been widely recognized in prior studies across diverse applications, showcasing its flexibility and effectiveness. Moreover, it serves as a robust foundation for designing control strategies, particularly when combined with inversion-based control methods, enabling systematic and efficient management of the studied system [6].

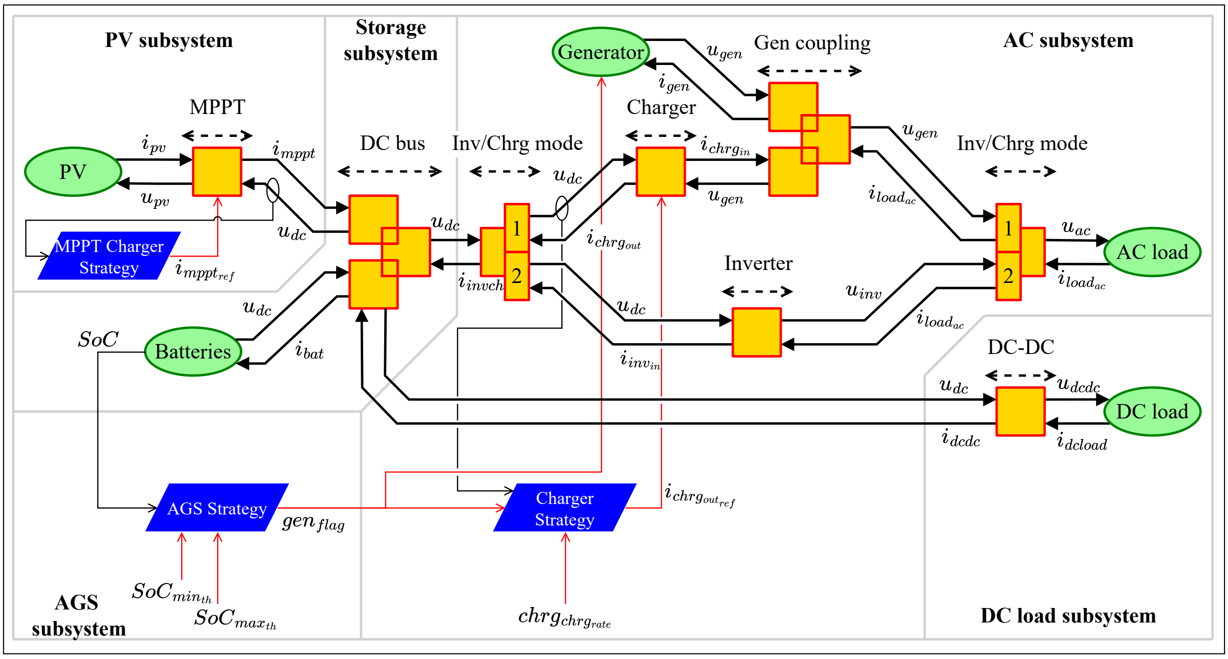


**Figure 2.3:** Energitic Macroscopic Representation of the Proposed Nanogrid [7]

EMR framework incorporates distinct elements to model various components of the energy system. Power generation units, comprising bifacial photovoltaic modules, energy storage systems (batteries), and diesel generators, are depicted as source elements within this representation. The power conditioning units—specifically the Solar Charger, Inverter Charger, and Chopper—are represented as conversion elements. As illustrated in Figure 2.3, the Inverter Charger is uniquely represented by two separate conversion elements, reflecting its dual functionality. The first function activates when batteries reach their minimum state of charge threshold, initiating the charging process. The second function enables DC to AC conversion for supplying alternating current loads. This dual-mode operation necessitates the implementation of a switching mechanism to alternate between inverter and charging modes. The operational strategy governing this switching behavior is implemented within the control elements of the system. Table 2.1 provides a comprehensive inventory of all fundamental EMR elements, including the control components.

| | | | |
|---|---|---|---|
| 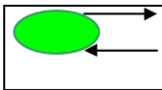 | Source of energy | 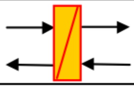 | Element with energy accumulation |
| 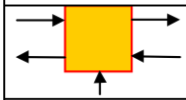 | Electrical converter (without energy accumulation) |  | Control block without controller |
| 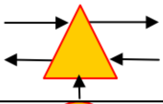 | Mechanical converter (without energy accumulation) | 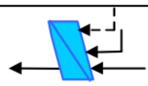 | Control block with controller |
| 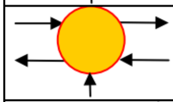 | Electromechanical converter (without energy accumulation) |  | Strategy block |
| 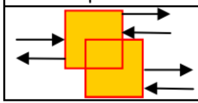 | Coupling devices (for energy distribution) | 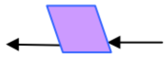 | Estimation block |

**Table 2.1:** EMR Elements (Control Elements Included) [8]

### 3.2 Rule-Based Management Strategy

A straightforward management strategy has been adopted to ensure the reliability of the system, with a primary focus on maintaining the state of charge (SOC) of the batteries. The system operates by activating the diesel generator whenever the SOC falls below a predefined minimum threshold ($Thr_{min}$). Once the SOC is restored to an acceptable level ($Thr_{max}$), the generator is automatically deactivated. This approach effectively balances operational simplicity with system reliability.

## 4 Critical Assessment of Current Software Solutions

A comprehensive benchmarking analysis was performed to evaluate existing market tools designed for sizing HRES. Through systematic assessment, we identified and documented both the capabilities and constraints of each evaluated tool. Our comparative analysis yielded detailed insights into their respective functionalities. The Tables 2.2 and 2.3 summarize the results of the study.

| Competing Software | Advantages | Points to Improve |
|---|---|---|
| HOMER Energy PRO | • A powerful tool for designing and analyzing hybrid electrical systems<br>• Large database of components<br>• Takes battery aging into account<br>• Sizing optimization<br>• Considers user energy management<br>• Parametric analysis<br>• Direct access to site meteorological data<br>• Economic analysis<br>• Wide range of possible configurations<br>• User-friendly graphical interface | • Consideration of the ecological cost of the system<br>• Joint optimization of sizing and energy management<br>• Consideration of regulatory framework<br>• Proposal of intelligent energy management<br>• Include Bifacial Modules<br>• Integrate Snow Impact Model |
| HOMER Quick Start | • Web tool for sizing multi-source systems<br>• Very easy to use<br>• Generic component models<br>• Quick economic analysis | • No consideration of battery aging<br>• Basic energy management<br>• + Previous Points |
| PVsyst | • The reference tool for sizing photovoltaic systems<br>• Bifacial Systems<br>• Snow Model | • Does not support hybrid systems |

**Table 2.2:** Comparison of Energy Software Solutions (Part 1)

| Competing Software | Advantages | Points to Improve |
|---|---|---|
| Sunny Design | • A powerful web tool for sizing multi-source systems<br>• Developed by SMA<br>• Capability to integrate electric vehicles<br>• Several functionalities<br>• High-quality graphical interface<br>• GOLD AWARD 2020 | • No optimization of sizing<br>• No consideration of ecological impact<br>• No Bifacial Modules<br>• No Weather Impact Sensitivity |
| REopt | • Web tool for sizing multi-source systems<br>• Very easy to use<br>• Well-developed services<br>• Generic component models | • No consideration of battery aging<br>• Basic energy management<br>• No consideration of ecological impact |

**Table 2.3:** Comparison of Energy Software Solutions (Part 2)

## 4.1 Preliminary Study Under Homer Pro

This section presents a simulation study of the proposed nanogrid using HOMER Pro, currently the most widely adopted commercial software in the distributed energy systems market. The primary objective is twofold: to evaluate the nanogrid's performance and to identify the software's limitations from an industrial perspective, thereby positioning the unique contributions of this thesis within the broader field. A scientometric review of academic literature reveals that the term "HOMER Pro" appears in the titles of 79 research papers published between 2012 and 2024, with approximately 1,026 mentions across titles, abstracts, and keywords in the Scopus database (Figure 2.4). This significant presence in academic literature underscores both the software's widespread adoption and the ongoing academic discourse regarding its capabilities and limitations. The following section details our HOMER Pro simulation study of the proposed system, focusing on identifying optimal configurations based on economic and environmental criteria. Through this analysis, we aim to highlight both the software's capabilities and its constraints in addressing industrial requirements, thereby establishing the foundation for the novel contributions of this research.

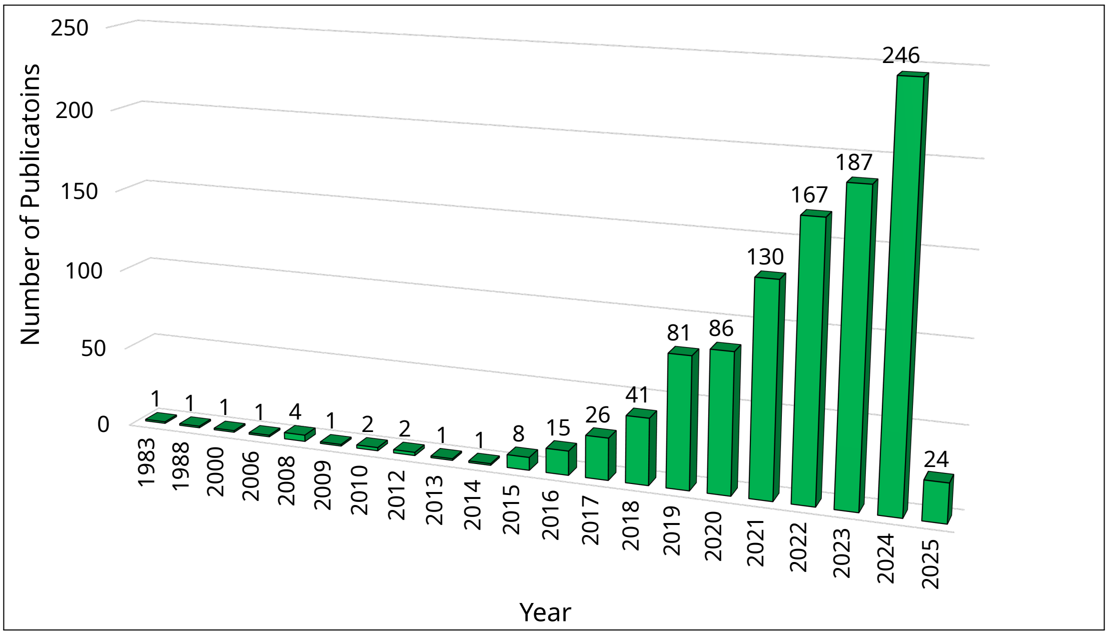


**Figure 2.4:** Publications by year that investigated the subject of Homer Pro Copyright © 2022 Elsevier B.V. All rights reserved. Scopus® is a registered trademark of Elsevier

### **Step 1 :** Defining Load Profile and Energy Resources

The nanogrid simulation is structured through a comprehensive framework encompassing physical components, operational strategies, and economic parameters. The modeling is performed using HOMER Pro, with the objective of accurately representing the existing Dorval Lodge installation. The simulation foundation rests on field data from Dorval Lodge, incorporating both DC and AC load profiles. Environmental conditions are sourced from HOMER Pro's "NASA Prediction of Worldwide Energy Resources" database [9], which provides essential parameters including GHI and temperature variations. The energy system architecture is designed to mirror the existing installation. At its core, the system utilizes a Discover AES 66kWh lithium-ion battery system, whose detailed specifications are presented in Table 2.4.

| Specification | Value |
|---|---|
| Battery Type | Li-Ion |
| Nominal Voltage | 48 V |
| Capital Cost | $6,915 |
| Replacement Cost | $6,915 |
| O&M Cost | $0 /Year |
| Lifetime | 10 Years |
| Nominal Capacity | 7,4 kWh |
| Maximum Capacity | 130 Ah |
| Roundtrip Efficiency | 95% |
| Maximum Charge Current | 1C |

**Table 2.4:** Battery Specifications : AES 42-48-6650 LiFePO4 Solar Stationary Battery Manufacturer Documentation Link

Power generation is managed through a diesel generator configured with standard parameters, featuring a unit cost of 500$/kW and operating with a minimum load ratio of 25%. For solar generation, the system employs a Generic Flat PV configuration operating at 21% efficiency, carefully calibrated to match the performance characteristics of the installed bifacial modules, as HOMER Pro does not directly support bifacial technology. System integration is achieved through a bidirectional converter operating at 95% efficiency, ensuring seamless power flow between components.

The operational dynamics of the system are governed by two distinct dispatch strategies. The Cycle Charging strategy maximizes generator efficiency by operating at full capacity, directing excess power to battery charging. In contrast, The Load Following strategy optimizes generator output to dynamically match primary load demand, providing a more nuanced approach to power management. The economic framework of the simulation incorporates an inflation rate of 4% and a discount rate of 10%. These parameters are fundamental for calculating the NPC, which serves as the primary economic performance indicator for evaluating system configurations and operational strategies. The complete integration of these components and their interactions within the HOMER Pro simulation environment is illustrated in Figure 2.5, providing a visual representation of the system architecture and its interconnections.

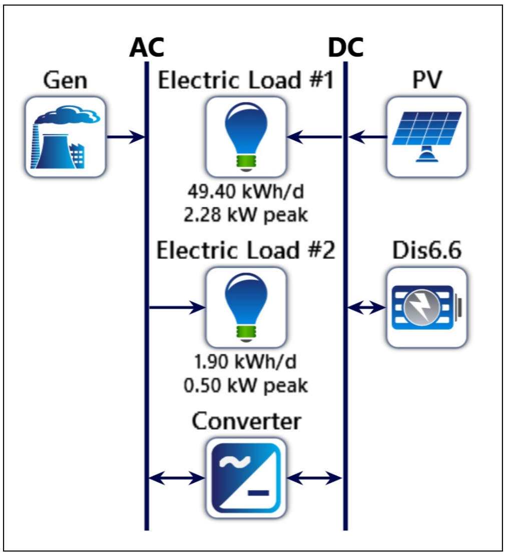


**Figure 2.5:** Homer Pro Schematic of the Nanogrid

### **Step 2 :** Optimization Results

The simulation results from HOMER Pro present a spectrum of solutions, bounded by two distinct scenarios: the most economically optimal and the most environmentally favorable configuration. The economically optimal solution achieves a Net Present Cost (NPC) of 96,689$ with a Levelized Cost of Energy (LCOE) of 0.395$/kWh. This configuration, however, demonstrates limited environmental benefits, producing 10.63 tons of $CO_2$ emissions annually. The renewable energy penetration remains modest at 26%, reflecting minimal investment in renewable infrastructure: a 6.14 kW photovoltaic system paired with a single LFP battery. At the other end of the spectrum, the environmentally optimized solution achieves a remarkable 99.9% renewable energy penetration, though at significantly higher costs. This configuration results in an NPC of 398,972$ and an LCOE of 1.63$/kWh, representing a 313% increase in energy costs compared to the economically optimal solution. The environmental improvements are achieved through substantial renewable infrastructure investment: 54 kW of installed photovoltaic capacity and 20 LFP batteries, while maintaining the same 3.2 kW diesel generator capacity as the economic solution.

### **Step 3 :** Sensitivity Analysis

HOMER Pro's sensitivity analysis capabilities enable a systematic examination of system performance under varying parameters. This analytical tool is particularly valuable for assessing the impact of uncertain variables, including fuel prices, generator minimum load requirements, and economic factors such as inflation and discount rates. In this preliminary investigation, we focused our sensitivity analysis on the renewable energy fraction to evaluate the proposed solution's capabilities. The analysis serves two primary objectives: determining the maximum achievable renewable energy penetration and establishing the corresponding range of NPC across the spectrum of viable solutions generated by HOMER Pro. This approach provides insights into both the technical limitations and economic implications of increasing renewable energy integration within the system. The results of the sensitivity analysis arepresented in Figure 2.6

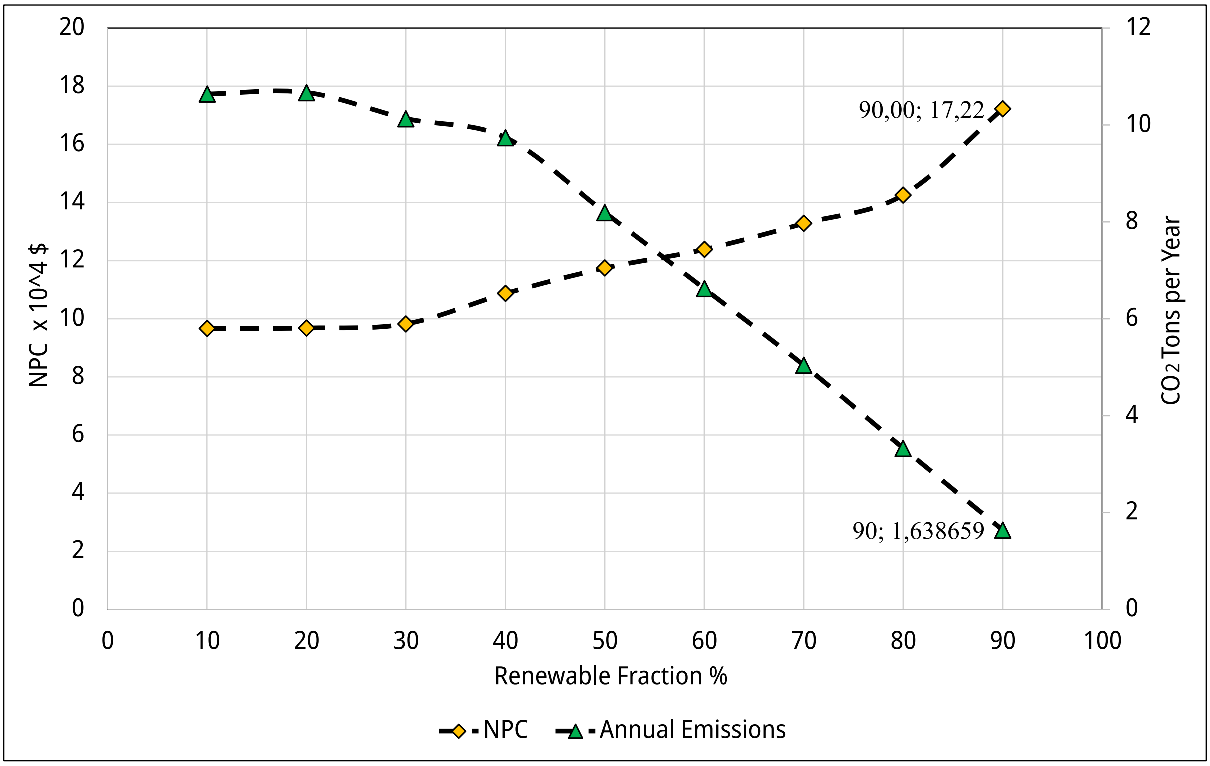


**Figure 2.6:** Sensitivity Analysis Under Homer Pro

## 5 Conclusion

This chapter presents a comprehensive analysis of the studied nanogrid system through three primary dimensions: architectural design, system representation, and software evaluation. The investigation centered on two implementations: the Dorval Lodge site, which demonstrated real-world deployment in harsh conditions, and the STACE cube at Sherbrooke University, which served as a controlled research facility. The system's energy flows and relationships were effectively mapped using the Energetic Macroscopic Representation (EMR) framework, coupled with a rule-based management strategy.

The critical assessment of existing software solutions revealed significant limitations in current market tools. Through detailed benchmarking, HOMER Pro emerged as the industry-standard solution, although with notable constraints. A simulation study conducted using HOMER Pro demonstrated the trade-offs between economic and environmental optimization. Although the software demonstrated that 99% the penetration of renewable energy is theoretically achievable, this finding does not account for several crucial factors.

- The impact of snow accumulation on solar generation
- The performance characteristics of bifacial modules
- Local meteorological variability

These omissions in current software tools highlight the need for more comprehensive modeling approaches. Specifically, the development of accurate subsystem models that incorporate:

- Detailed bifacial module performance under various environmental conditions
- Precise diesel generator operational characteristics
- Local weather impacts, particularly snow accumulation

These findings establish clear directions for the thesis's subsequent contributions, emphasizing the development of more accurate and comprehensive modeling approaches for nanogrid systems operating in challenging environmental conditions.

## References for Chapter 2

[1] Radovan Kopecek and Joris Libal. "Bifacial Photovoltaics 2021: Status, Opportunities and Challenges". In: *Energies* 14 (8 Apr. 2021), p. 2076. ISSN: 1996-1073. DOI: 10.3390/en14082076.

[2] Joshua Stein, Christian Reise, Johanna Castro, et al. *Bifacial Photovoltaic Modules and Systems: Experience and Results from International Research and Pilot Applications*. Apr. 2021. DOI: 10.2172/1779379.

[3] Solomon Evro, Abdurahman Ajumobi, Darrell Mayon, et al. "Navigating battery choices: A comparative study of lithium iron phosphate and nickel manganese cobalt battery technologies". In: *Future Batteries* 4 (Dec. 2024), p. 100007. ISSN: 29502640. DOI: 10.1016/j.fub.2024.100007.

[4] Jia Liu, Xi Chen, Sunliang Cao, et al. "Overview on hybrid solar photovoltaic-electrical energy storage technologies for power supply to buildings". In: *Energy Conversion and Management* 187 (May 2019), pp. 103–121. ISSN: 01968904. DOI: 10.1016/j.enconman.2019.02.080.

[5] Alexandros Arsalis, Panos Papanastasiou, and George E. Georghiou. "A comparative review of lithium-ion battery and regenerative hydrogen fuel cell technologies for integration with photovoltaic applications". In: *Renewable Energy* 191 (May 2022), pp. 943–960. ISSN: 09601481. DOI: 10.1016/j.renene.2022.04.075.

[6] Alain Bouscayrol and Betty Lemaire-Semail. "Energetic macroscopic representation and inversion-based control". In: Elsevier, 2023, pp. 365–375. DOI: 10.1016/B978-0-12-821204-2.00117-3.

[7] Mathieu Blanchard, Abid Ali, Christian Dubuc, et al. "Optimization of Diesel Generator Usage for Multi-Source Nano-Grid". In: IEEE, Aug. 2023, pp. 1–5. ISBN: 979-8-3503-9996-7. DOI: 10.1109/PEDS57185.2023.10246652.

[8] W. Lhomme, P. Delarue, F. Giraud, et al. "Simulation of a Photovoltaic Conversion System using Energetic Macroscopic Representation". In: IEEE, Sept. 2012, DS3e.7-1-DS3e.7–6. ISBN: 978-1-4673-1972-0. DOI: 10.1109/EPEPEMC.2012.6397361.

[9] NASA POWER Project Team. *NASA Prediction Of Worldwide Energy Resources*. https://power.larc.nasa.gov/. Accessed on 2025-02-19. Hampton, VA, USA: NASA Langley Research Center, Jan. 2025.

*"I never satisfy myself until I can make a mechanical model of a thing. If I can make a mechanical model, I can understand it. As long as I cannot make a mechanical model all the way through, I cannot understand."*

William Thomson (1824 - 1907)

# 3

# Comprehensive Modeling of Bifacial Modules: Quantifying Snow's Influence on Energy Yield

## Contents



## 1 Introduction

It has been reported in the literature that the use of bifacial panels can improve the energy yield of power plants by 25-30% [1]. Due to their promising efficiency, bifacial panels have been widely deployed in a variety of applications, such as green roofs, agriculture and highways [2]–[6]. The rated power of bifacial modules is not straightforward to define, since it depends on various factors, such as the nature of the ground, the mounting configuration, and the bifaciality factor. The higher this factor is, the higher the module output power. Current PERC [1] cells' bifaciality factors measure at 0.7, with SHJ cells exhibiting the highest values of up to 0.92 [7]. Accurate estimation of the energy production of PV modules is a crucial part of achieving optimal system sizing [8], as evidenced by a high-Performance Ratio (PR). A study [9] has demonstrated that ignoring soiling effects in the region, PR can be reduced by up to 26%. Furthermore, the validity of this statement was reinforced by [10], which indicated that the monthly losses due to snow coverage in severe climates can reach as high as 100% which reduces significantly the system's performance ratio. Numerous studies have delved into the effects of snowfall on monofacial PV modules. For instance, the authors of one such study [11] discovered that energy losses in PV systems due to snow accumulation could reach up to 90% on a monthly basis and fluctuate between 1% and 12% annually. A comprehensive review [12] paper further corroborates these findings, indicating that while annual electricity generation losses were generally less than 10% in most climates, monthly losses during winter months typically exceeded 25%. Bifacial PV panels, on the other hand, present a unique advantage. They are capable of producing an additional 10-15% of electrical energy by harnessing reflected light from the ground [13],. This capability is particularly pronounced when the albedo is high due to snow cover. This distinctive feature enables bifacial PV panels to recover more swiftly from snowfall events and resume normal operation. In contrast, monofacial PV panels may remain obstructed by snow for extended periods.

Recent studies have examined the accuracy of predicting power production from bifacial solar panels utilizing various methods, such as view factors and the ray-tracing technique. Results demonstrated high accuracy in comparison to field measurements. In [14], a simple model was proposed to consider received irradiance and module temperature. The authors reported an 8% maximum residual error. Validation of this model was conducted with 25 days' data, the model displaying an overestimation of power at higher temperatures. In [15], a model based on the configuration factor was introduced, which calculations focused solely on back-side irradiance. This model was validated using data from a 6-month period. In [16], an electro-thermal model was proposed to assess the energy yield of bifacial modules and their dependence on parameters such as albedo. It was reported that a ground albedo of 0.5 could increase the global bifacial gain by about 20%. To eliminate the effects of snowing, only data from 3 months was used for validation. The purpose of [17] is to evaluate the performance of a range of irradiance tools, by assessing their

[1] Passivated Emitter and Rear Cell

predictions against measurements. In particular, it was shown that the bifacial gain for Fixed-Tilt systems varied between 5.5 - 7.5%, compared with an experimental result of 6%.

This research work differs from previous studies by three significant contributions to the field of bifacial photovoltaic (PV) modules. Firstly, it introduces a power model for bifacial PV modules, capable of estimating power output based on various factors such as irradiance on the front and rear surfaces, cell temperature, and more. Secondly, the model is validated through a year-long experiment involving 12 bifacial PV modules installed at Université de Sherbrooke in Canada. The validation process involves a comparison of the model's results with measured data, evaluated using metrics like the normalized root mean square error and bifacial gain. Lastly, Sensitivity analysis was conducted to examine the model's response to different sources of weather data and reducing the probability of overestimating the power production by considering the impact of snow coverge.

## 2 Estimating the total received irradiance

This section examines the various methods for calculating the total irradiance that bifacial modules receive. The total irradiance may be divided into two parts: the irradiance attained by the module's front surface and the irradiance received by its backside. Direct irradiance, diffuse sky irradiance, ground-reflected irradiance, and reflected irradiance from the surrounding surfaces are typically the four elements of the irradiance absorbed on a tilted surface. Figure 3.1a displays each of these components' origins. This chapter's primary goal is to present an accurate power model of double-sided modules, which necessitates precisely calculating the module's total irradiance. The methods for calculating the front and rear irradiance in earlier studies may be categorized into three groups: view factor approaches, ray tracing simulations, and empirical models. The view factor technique is the most often used strategy in the literature. It is based on the computation of the configuration factor, which is the percentage of light emitted from one surface that reaches the surface under analysis. The view factor is expressed using the equation given, assuming there is no obstruction between the two surfaces and that they are completely visible to one another:

$$F_{S_i-S_j} = \frac{1}{S_i}\int_{S_i}\int_{S_j}\frac{cos(\theta_i)cos(\theta_j)}{\pi r_{ij}^2}dS_idS_j \tag{3.1}$$

Where $\theta_i$ and $\theta_j$ are the angles formed by the normals to the surfaces $S_i$ and $S_j$, respectively, and the vector $r_{i,j}$ that connects two points on the surfaces $S_i$ and $S_j$ . This equation does not have a general analytical solution. As stated in [18], [19], there are only analytical solutions for particular geometries. Under the supposition that the length of the row is significantly greater than its width, the problem of parallel rows of PV panels may be simplified to a 2D problem. The Hotel's cross-string approach is frequently used by researchers to address this problem.

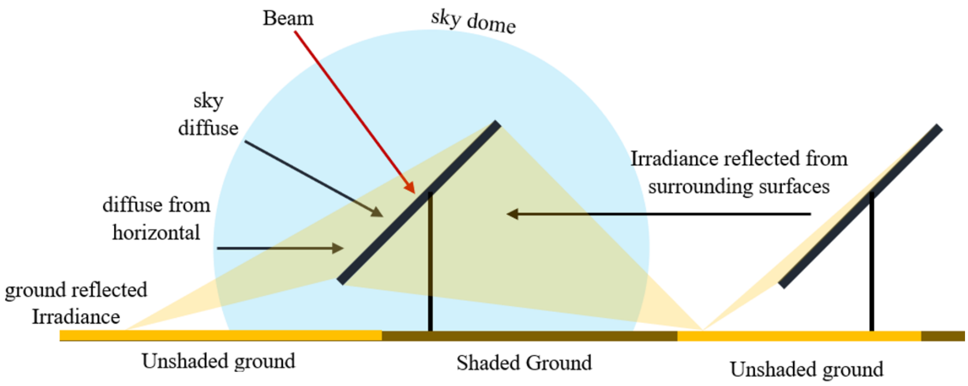


**(a)** Sources of incident irradiance on bifacial module

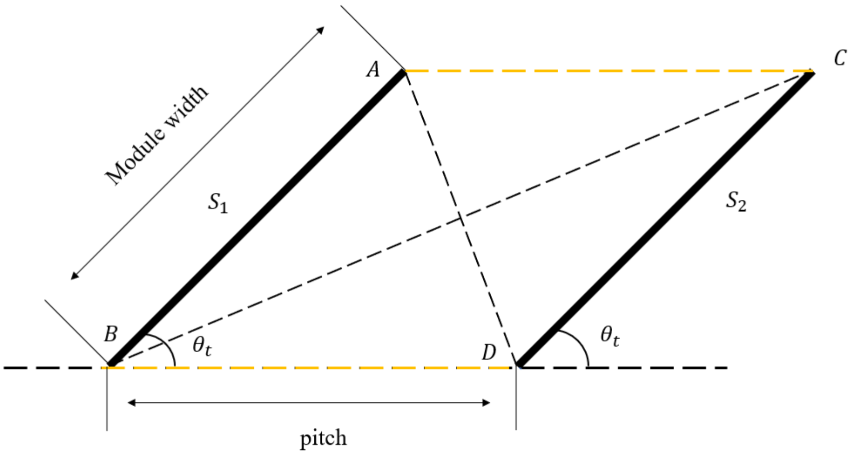


**(b)** Hotel's cross-strings method between two surfaces

**Figure 3.1:** Model reduction to 2-dimensions problem

The hotel's cross-strings approach is used to reduce the configuration factor computation to two dimensions, as illustrated by figure 3.1b, from which the expression for the view factors between two surfaces can be derived. Therefore we express the view factor as follows:

$$F_{S_i-S_j} = \frac{\sum crossed\ strings - \sum uncrossed\ strings}{2\ strings\ in\ S_i} \tag{3.2}$$

$$F_{S_2-S_1} = \frac{(AD+BC)-(BD+AC)}{2DC} \tag{3.3}$$

The total incident irradiance on bifacial modules can be expressed as function of view factors

$$\Phi_t = \Phi_f + \eta \Phi_r \tag{3.4}$$

We suppose that the front irradiance has three components; beam direct, diffuse irradiance and the irradiance reflected from the ground :

$$\Phi_f = \phi_{bf} + \phi_{df} + \phi_{gf} \tag{3.5}$$

$$\Phi_f = \cos(\beta)\ DNI + F_{sky-view}\ DHI + F_{ground-view}\ \rho\ GHI \tag{3.6}$$

$$\beta = cos^{-1}\left(sin(l-\theta_t)sin(\delta) + cos(l-\theta_t)cos(h)\right) \tag{3.7}$$

$$\delta = 23.45\ sin\left[\frac{360}{365}\ (284+n)\right] \tag{3.8}$$

$$h \pm 0.25 * (Number\ of minutes\ from\ local\ solar\ noon) \tag{3.9}$$

$$\phi_{df} = I_{dome} + I_{circumsolar} + I_{horizon} \tag{3.10}$$

$$I_{dome_{iso}} = DHI \frac{1+cos(\theta_t)}{2} \tag{3.11}$$

DNI stands for Direct Normal Irradiance, DHI is the Direct Horizontal irradiance, GHI is the Global Horizontal irradiance, $\rho$ the ground's albedo, while $\beta$ is the solar incidence angle is the angle created by the sun's rays and the module's normal, the equation 3.7 refers to the angle of incidence for a south-facing module in the northern hemisphere, $\delta$ is the declination angle, $h$ is the hour angle $\theta_t$ is the tilt angle.

The azimuth angles of the array and the sun are $\theta_{aa}$ and $\theta_a$, respectively, and $\theta_z$ is the zenith angle.

Numerous methods have been suggested in the literature to estimate the diffuse sky component of the front irradiance since it depends on the sky model. Isotropic models and anisotropic models are the two categories of these models. In the first category, it is assumed that the sky dome's diffuse irradiance intensity is uniform. Whereas, in the anisotropic models the circumsolar and horizon-brightening effects are present as well as the isotropic component [20].The general formula for the sky diffuse component is expressed by 3.10, as cited in [21] the first model of the diffuse irradiance was presented as function of the tilt angle 3.11 and DHI, in this case the view factor of the module to sky is :

$$F_{view-sky} = \frac{1+cos(\theta_t)}{2} \tag{3.12}$$

We may drive a new expression of the $F_{view-sky}$ by using Hotel's cross-string approach;

thereby, from the figure 3.2, we can write :

$$F_{view-sky} = \frac{CD + AC - AD}{2CD} \tag{3.13}$$

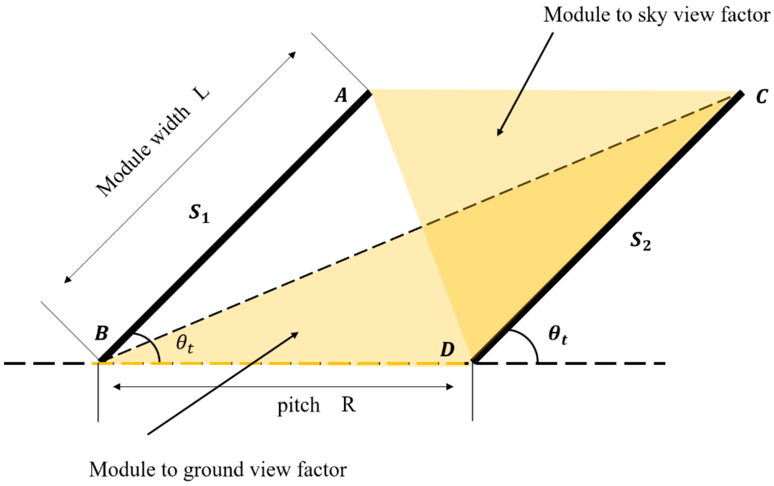


**Figure 3.2:** View factors: module to ground and module to sky

The two most commonly utilized anisotropic models for estimating diffuse irradiance are the [22] and [23] models. The horizon brightening factor is ignored in the first model, which solely considers the circumsolar component. The diffuse component is therefore expressed as follows:

$$\phi_{df} = DHI \left[ \frac{DNI\ cos(\beta)}{E_x\ cos(\theta_z)} + \left(1 - \frac{DNI}{E_x}\right) \frac{1 + cos(\theta_t)}{2} \right] \tag{3.14}$$

Extraterrestrial radiation $E_x$ is the radiation on a horizontal surface sitting on the boundary of the Earth's atmosphere. In terms of the solar constant $E_0$ ($1367 W/m^2$) and the day of the year $n$, it is expressed as follows [24]:

$$E_x = E_0 \left( 1 + 0.033\ cos(\frac{360\ n}{365}) \right) \tag{3.15}$$

The three diffuse irradiance components stated above are all taken into consideration by the Perez model, one of the most common and accurate representations of the sky, which reduces the computation error of the total irradiance received on a tilted surface. Since the authors of [23] provide a simplified version of this model, the sky diffuse component may be expressed as follows:

$$\phi_{df} = DHI\left[\frac{(1+cos(\theta_t)}{2}(1-F_1)+F_1\frac{cos(\beta)}{cos(\theta_z)}+F_2 sin(\theta_t))\right] \tag{3.16}$$

The amount of irradiance that the ground reflects to the module is divided into two terms 3.17: the first term denotes the irradiance that is reflected from the unshaded ground, and the second term specifies the irradiance that is reflected from the shaded ground:

$$\phi_{gf} = \rho GHI\ F_{S2-unshaded} + \rho DHI\ F_{S_2-shaded} \tag{3.17}$$

If we assume the following four assumptions for the first row, we may express the view factor to the ground with the equation 3.18 : the ground is perfectly horizontal, there is no ground shade, the row is indefinitely long, and the ground is a Lambertian reflector (it reflects light evenly in all directions) [25].

$$F_{S1-ground} = \frac{1-cos(\theta_t)}{2} \tag{3.18}$$

Therefore the ground reflected irradiance for the first row under the four hypotheses listed above is:

$$\phi_{gf} = \rho GHI\ \frac{1-cos(\theta_t)}{2} \tag{3.19}$$

We can calculate the total irradiance incident on the rear surface by rotating the module at an angle complementary to beta $(\pi-\theta_t)$ . Similarly, and using the same isotropic model as previously, we may express rear total irradiance as:

$$\Phi_r = DNIcos(aoi) + DHI\frac{1-cos(\theta)}{2} + \rho GHI\frac{1+cos(\theta_t)}{2} \tag{3.20}$$

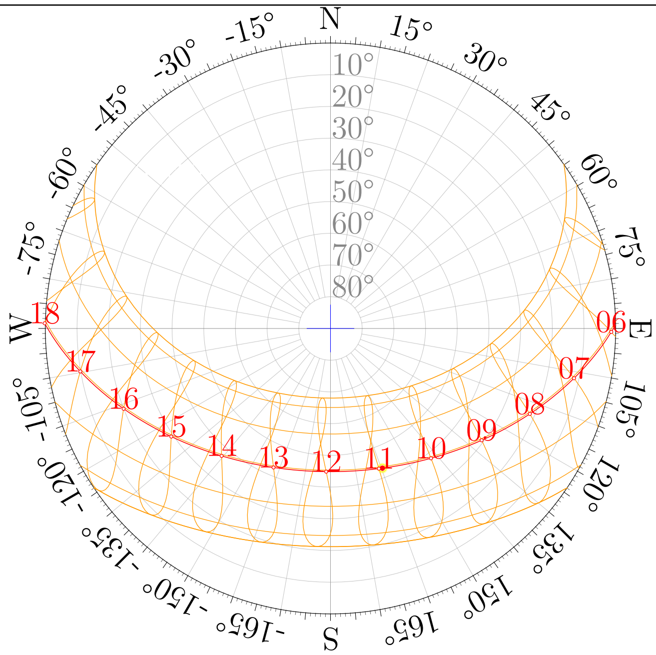


**Figure 3.3:** Sun-Path over the year 2022 seen from Sherbrooke (45.4°lat, -71.8 long)

In addition to diffuse and ground refleced irradiance, the back surface receives beam irradiance, which is primarily determined by two parameters: the latitude coordinate and the orientation of the module; in our example, the PV panels are located in Sherbrooke (45.4° lat, −71.8 long), and they are oriented to the south with an inclination angle of 30° . Figure 3.3 illustrate a simulation of the sun's path, which indicates that when the sun is at the two north quarters , the backside of the module receives direct rays, meaning that the azimuth angle is between $[0°, 90°]$ and $]270\ °, 360°[$, and we can see that this occurs at sunrise and sunset.According to Figure 3.3, the sun enters the northern hemisphere at the start of the Spring season (20 March 2022) and goes back to the southern hemisphere at the beginning of the Fall (23 September 2022).

## 3 Methodology

The power model of the bifacial module is presented in figure 3.4. It is a model that employs two different approaches to estimate the module irradiance; either we can employ the view factor method by using *pvfactors* or the raytracing technique by using *bifacial_radiance*. The module bifaciality coefficient is then multiplied by the rear irradiance and added to the front irradiance. The cell temperature is computed using Homer Pro model. By selecting the irradiance model presented in [26] carefully, one may choose between accuracy and execution speed. For example, *bifacial_radiance* can be used to analyze the irradiance on a specific segment of the module, the influence of the torque tube, or the nature of the ground on panel production. *pvfactors*, on the other hand, enables quick simulations.

The power equation of the bifacial module is expressed as:

$$P_{bif} = P_{mp}\frac{(\Phi_f + \eta\Phi_r)}{\Phi_{ref}}(1 + \alpha_p(T_{cell} - T_{c,stc}))(1 + D) \tag{3.21}$$

Where $\eta$ is the bifaciality factor, $\phi_r$ $[W/m^2]$ and $\phi_f$ $[W/m^2]$ are the rear and front irradiance respectively, $\alpha_p$: temperature coefficient of power, $\Phi_{ref}$: reference irradiance, $P_{mp}$: module maximum power, $T_{c,stc}$: cell temperature at STC, $T_{cell}$: module cell temperature, and $D$ is the derate coefficient.

The cell temperature of the PV module is critical for estimating the power production of the module. The equation used by Homer Pro for estimating the cell temperature is [27]:

$$T_{cell} = \frac{T_a + (T_{c,noct} - T_{a,noct})\ \frac{\Phi_t}{\Phi_{t,noct}}\left(1 - \frac{\eta_{p,stc}(1 - \alpha_T T_{cstc})}{\gamma\tau}\right)}{1 + \frac{\Phi_t(T_{c,noct} - T_{a,noct})\ \alpha_T\eta_{p,stc}}{\Phi_{ref}\ \gamma\tau}} \tag{3.22}$$

Where: $T_a$: ambient temperature, $T_{c,noct}$ nominal operating cell temperature $[°C]$, $T_{a,noct}$ ambient temperature at which $T_{c,noct}$ is defenied, $\Phi_t$ total received irradiance, $\Phi_{t,noct}$ solar irradiance at which $T_{c,noct}$ is defined, $\eta_{p,stc}$: maximum power efficiency under standard test conditions [%], $\alpha_T$ : temperature coefficient $[\%/°C]$, $\tau$ solar transmittance [%], and $\gamma$ solar absorptance[%]. The Homer model sets the value of the product $\gamma\tau$ to 0.9, and the rest of the coefficients are obtained from the module's datasheet.

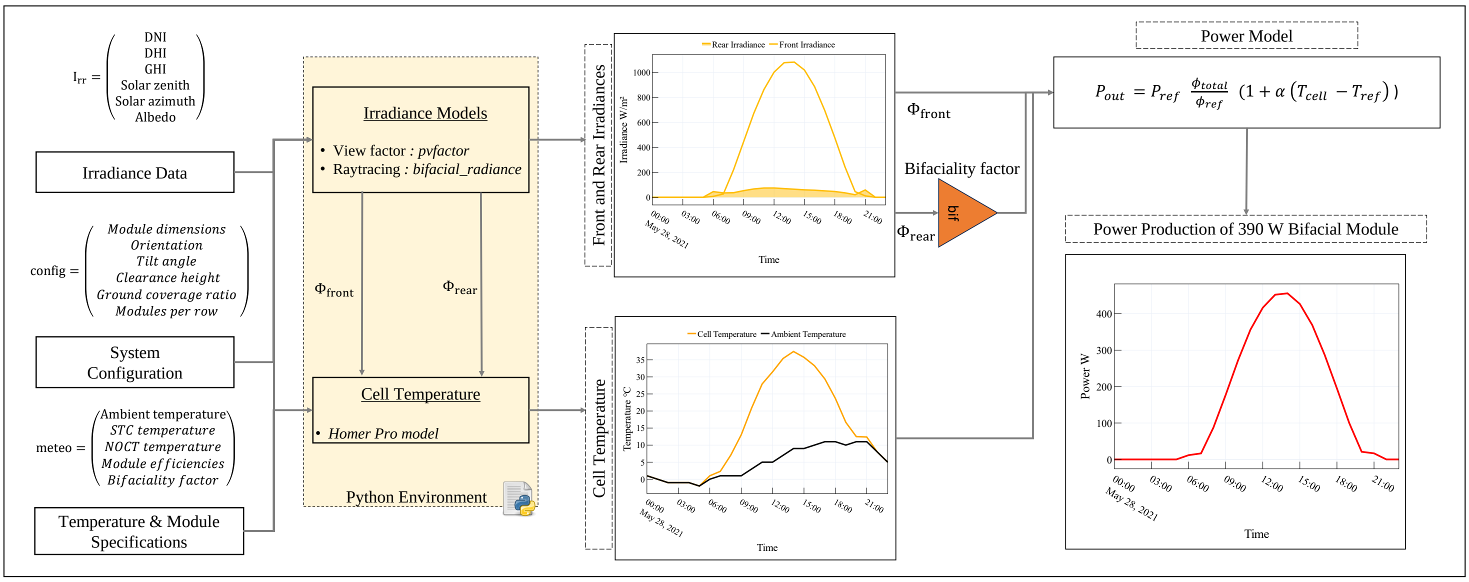


**Figure 3.4:** Model for the power production estimation

The Power production data of 12 PV modules (Figure 3.5a) was collected from Université de Sherbrooke for all seasons of the year 2021, this amount of data will be utilized to evaluate the model under varied weather conditions. The used system is composed of 12 modules mounted at 30° in landscape configuration. We used 390 Wp monocrystalline bifacial modules. The module are connected in a series configuration via SolarEdge power optimizers. These optimizers facilitate MPPT [2] , thereby optimizing the energy extraction from each individual module. Furthermore, they provide the capability to monitor the power and energy output of each module independently. The optimizers exhibit a weighted efficiency of 98.8%, with a peak efficiency reaching as high as 99.5%. The detailed system configuration is summarized in the table below 3.1.

| Parameter | Value |
|---|---|
| Module type | LG390N2T-A5 |
| Cell Type | Monocrystalline / N-type |
| Bifaciality Coefficient | 76 |
| Tilt Angle | 30 |
| Number of rows | 1 |
| Number of modules | 12 |
| Center Height | 2.4 m |
| Surface Azimuth | 180 |
| Ground Coverage Ratio | 0.001 |
| Orientation | Landscape |

**Table 3.1:** System mounting parameters of the modules

The RaZON+ system from Kipp and Zonen is employed to measure two key types of solar irradiance: DNI and DHI. These measurements are crucial as they are used to calculate the GHI. For albedo values, we utilize data provided by Solcast. This data is derived from NASA's Moderate Resolution Imaging Spectroradiometer (MODIS) products, which offer historical albedo data. To cater to specific locations and times, the data undergoes spatial and temporal interpolation. Solcast ensures the accuracy and consistency of this interpolated data by performing bias corrections. The solar Zenith and Azimuth angles is provided by the RaZON+ System, which calculates the solar angles using NREL's Solar Position Algorithm (SPA) [28]. This algorithm enables accurate tracking of the sun's position throughout the day. These parameters, collected on an hourly basis, serve as the foundation for the model depicted in Figure 3.4. The EdgeSolar Optimizer is

[2] Maximum Power Point Tracking

employed to monitor the power output's hourly fluctuations. This data, representing the system's actual performance, is subsequently used as a benchmark to assess the model's precision. By comparing the model's predictions with these real-world measurements, we can evaluate the model's accuracy and make necessary adjustments to improve its predictive capabilities. In order to ensure the quality of our data, we have employed two distinct techniques. The first involves the removal of outliers by imposing limits on the parameter values. For instance, we have set the maximum value of the received irradiance equal to the constant solar irradiance, thereby eliminating any anomalously high readings. The second technique pertains to the handling of missing values. If any parameters required to estimate the power output are missing for a specific hour, we exclude that hour from our dataset. Consequently, our meteorological input data has been reduced from 8760 to 8676 entries, indicating that 84 values have been filtered out due to missing parameters.

**(a)** Installed PV Array on the UdeS Campus

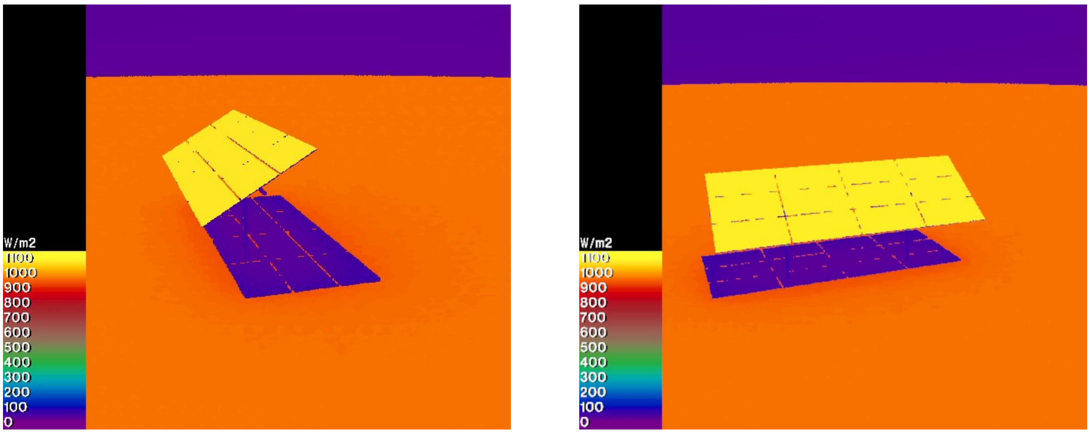


**(b)** Ray Tracing Technique Applied to PV Array: Side View (Left) at 13:00 on 2021-05-28 and Front View (Right) at 14:00 on 2021-05-28

**Figure 3.5:** Raytracing Technique Applied to UdeS PV Array

# 4 Results and Discussions

## 4.1 Ray tracing Technique : bifacial_radiance

The application of ray-tracing technique by the using *bifacial_radiance* [29], presents a significant challenge due to the extensive computational time required, which is not conducive to a comprehensive, hourly analysis over an entire year. In fact, a one-year simulation of our system is projected to require approximately 13 hours of computation on a computer equipped with an Intel® Core™ i5-8265U CPU @ 1.60GHz 1.80 GHz and 8 GB of RAM. To address this issue, we employed code optimization in conjunction with parallel computing, which effectively reduced the execution time to a mere 3 hours. The strategy involves utilizing the measured data as input for the function responsible for calculating the hourly power production [3]. The simulation of a single day is then decomposed according to the number of processors available in our machine. This approach allows for a more efficient use of computational resources, thereby significantly reducing the overall execution time.
As illustrated in Figure 3.5b, we implemented the ray-tracing technique to the given scene, taking into account the mounting parameters of the system. To enhance precision, we configured the *bifacial_radiance* parameter to accommodate nine sensors. This configuration is based on the array's composition, which consists of three rows with four modules each, resulting in three sensors per module. The data acquired from this setup enabled us to conduct a comprehensive analysis of the system and ascertain the power output of each individual module. This rigorous approach ensures a detailed understanding of the system's performance. NRMSE [4] (Equation 3.23) was computed for each individual module over a three-month period corresponding to each of the four seasons in the year 2021, as a measure to evaluate the precision of the power model and quantify its deviation from the experimental data. This error measurement is normalized by the range of the observed values, as shown in the equation below (Equation 3.23). The results are depicted in Figure 3.6.

$$NRMSE = \frac{\sqrt{\frac{1}{N}\sum_{i=1}^{N}\left(P_{meas,i} - P_{est,i}\right)^2}}{P_{meas,max} - P_{meas,min}} \tag{3.23}$$

Where $P_{meas,i}$ and $P_{est,i}$ are the measured and the estimated energy in the hour $i$, and $N$ number of a season days , $P_{meas,max}$ and $P_{meas,min}$ are the maximum and the minimum power respectively.

[3] gendaylit2manual function in *bifacial_radiance*
[4] Normalized Root Mean Square Error

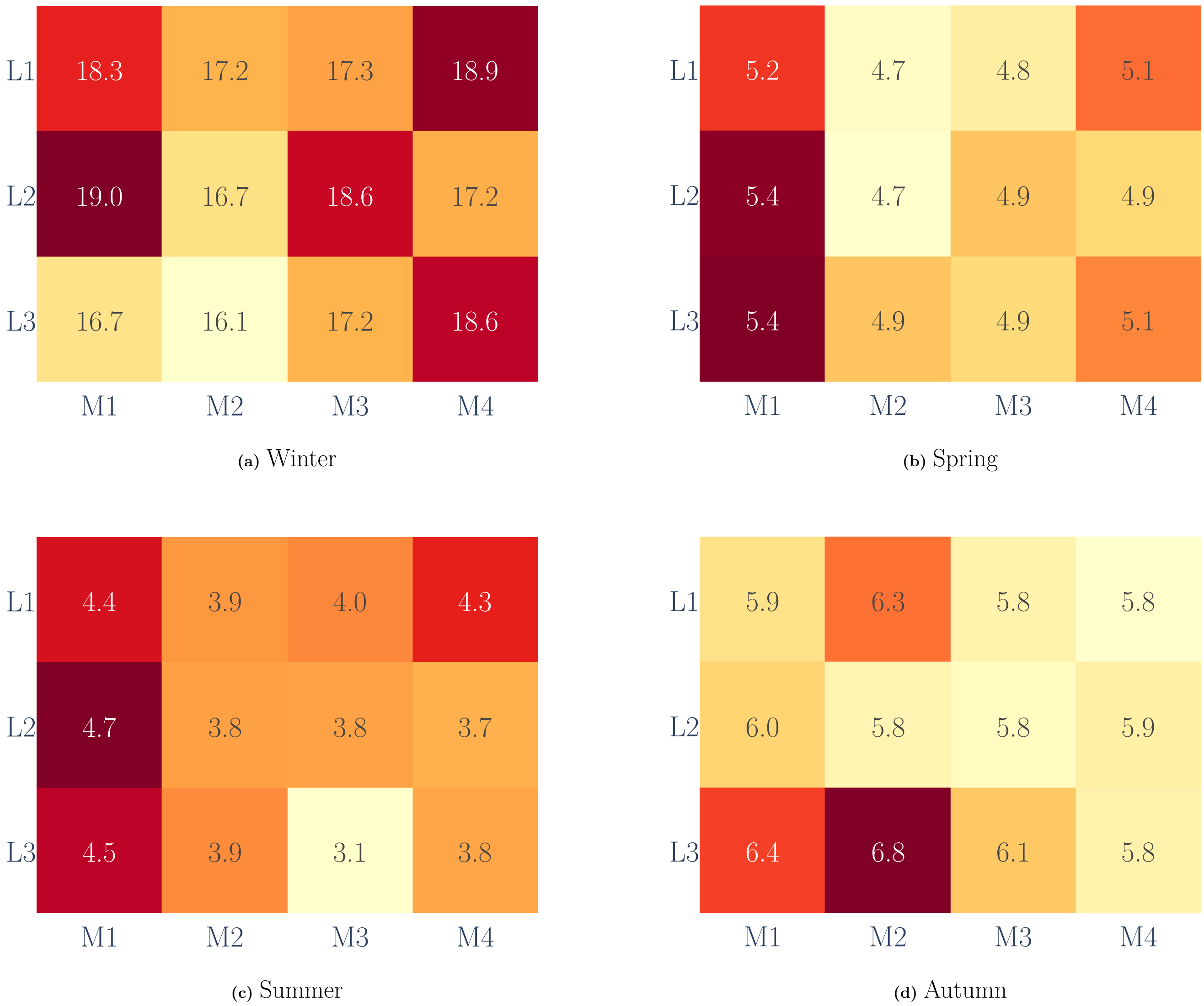


**Figure 3.6:** Seasonal NRMSE [%] for the year 2021

The summer season, with its higher number of clear sky days compared to other seasons, exhibits the lowest NRMSE values. The maximum value for this season is 4.7%, while the minimum value is 3.1%, indicating a commendable degree of accuracy for the model during this period. In the spring season, the NRMSE values range from 4.7% to 5.4%, which is still within an acceptable range. However, during the autumn season, there is a rise in the NRMSE values of each module, with the minimum value being 5.8% and the maximum value reaching 6.8%. The observed augmentation can be attributed to the amplified frequency of cloudy conditions prevalent during this particular season. This is evident from the Table 3.2 showing the monthly fraction of cloudy days. As we analyze the data, we see that the monthly fraction of cloudy days rises from 52% to a significant 72% in December. However, the model's accuracy shows a notable variation during the winter season, with NRMSE values fluctuating between a minimum of 16.1% and a maximum of 19%. Despite the superior quality of the validation data, it's presumed that the main contributor to these significant NRMSE values is the snow coverage. This postulation is based on the geographical location's tendency for winter snowfall, suggesting that the degree of snow coverage during the winter season has a substantial effect on the model's power production.

| Fraction | Jan | Feb | Mar | Apr | May | Jun | Jul | Aug | Sep | Oct | Nov | Dec |
|---|---|---|---|---|---|---|---|---|---|---|---|---|
| Cloudier | 75% | 72% | 66% | 60% | 57% | 52% | 43% | 40% | 43% | 52% | 64% | 72% |
| Clearer | 25% | 28% | 34% | 40% | 43% | 48% | 57% | 60% | 57% | 48% | 36% | 28% |

**Table 3.2:** Monthly Distribution of Cloud Cover and Clear Days: Data Courtesy of WeatherSpark.com

### 4.1.1 Seasonal Bifacial Gain

Snow albedo is the fraction of incoming light or radiation that a surface reflects. It ranges from 0.5 to 0.7 for old snow, but it can surpass 0.9 for freshly fallen snow [30]. As a result, in the winter, the received ground-reflected irradiance increases significantly, as does the bifacial gain. To quantify the additional energy obtained by using bifacial modules versus monofacial modules, we compute the bifacial gain, that represents the ratio of the irradiance received by the back surface to the irradiance received by the front surface. As expressed in the Equation 3.24, we consider the efficiency of the module's backside. This equation is commonly used in the literature, and it is an approximation of the actual value.

$$G_{bif} = \eta \frac{\phi_r}{\phi_f} \tag{3.24}$$

Where $\eta$ is the bifaciality factor, $\phi_r$ $[W/m^2]$ and $\phi_f$ $[W/m^2]$ are the rear and front irradiance respectively.

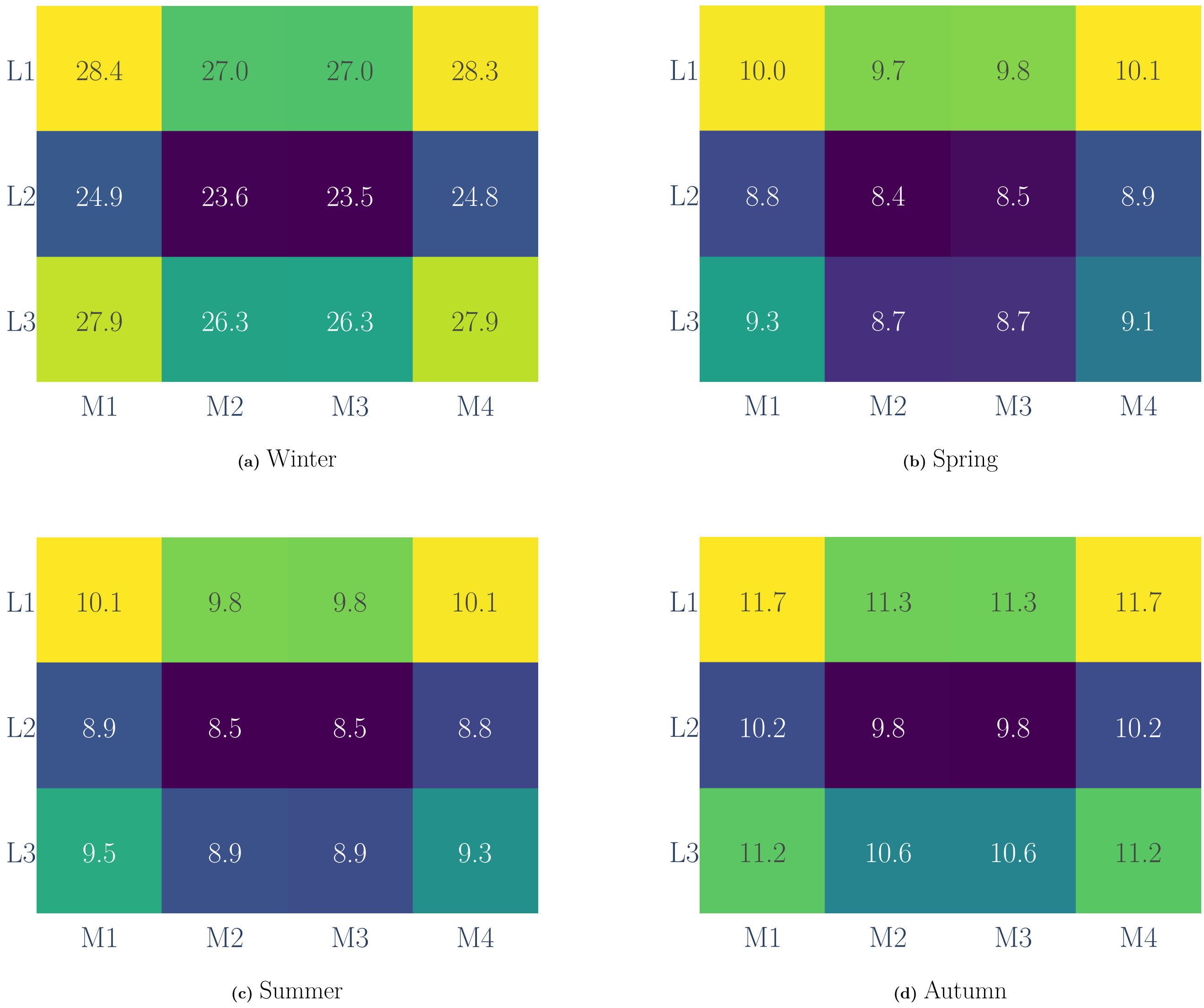


**Figure 3.7:** Seasonal Bifacial Gain [%] of the year 2021 using *bifacial_radiance*

Figure 3.7 illustrates the remarkable advantage of employing bifacial modules with our system configuration. These modules can boost efficiency by as much as 28.4% during winter months, a figure nearly three times the minimum improvement observed in summer, which stands at 9.8%. In terms of seasonal variations, the bifacial gain fluctuates between 8.4% and 10% in spring, 8.5% and 10.1% in summer, and 9.8% and 11.7% in autumn. The increase in autumn is attributable to the rise in albedo values. Upon closer examination, it is evident that the modules located at the bottom and in the center exhibit a lower gain compared to those at the top edges. This discrepancy can be attributed to the shading effect caused by the mounting structure and torque tube for the central modules, and the reduced rear side collection due to lower altitude for the bottom modules. It is important to note that the bifacial gain discussed here is based on modeling and does not account for snow losses. which are known to decrease when photovoltaic (PV) modules are bifacial [10].

## 4.2 View Factor Method : pvfactors

A fast simulation can be reached using *pvfactors* [31]. *pvfactors* assumes that all the modules at the same altitude are similar (2D View Factor model). This assumption, however, limits the ability to study power production variations among adjacent modules with identical mounting properties. It is of significance to note that the Ground Coverage Ratio (GCR) delineated in Table 3.1 aligns with the value utilized for the *pvfactors* model. As *bifacial_radiance* model can accommodate a GCR value of 0. *pvfactors* operates as a view factor model, employing the GCR to compute the spacing required to achieve the desired GCR. This spacing is crucial for accurate modeling THE shading characteristics A GCR value of 0 would result in an error in this context. Consequently, to circumvent this issue, we approximate this value to 0.001.

To validate the model using *pvfactors*, we selected the modules located at the highest point and initiated a simulation spanning one year. Remarkably, the execution time for this simulation was a mere 15 seconds. This swift computation time is particularly advantageous for modeling larger scale photovoltaic (PV) systems or for integrating this model into simulations that necessitate multiple iterations.

The scatter plots depicted in the figure 3.8 illustrate a comparison between the hourly measured power and the estimated power using the *pvfactors* model. We compare the simulation output with the mean power production of the top four modules. Similarly to modeling with *bifacial_radiance*, the PV production is overestimated during the winter season. This overestimation is attributed to the snow effect. The Normalized Root Mean Square Error (NRMSE) peaks at 18.77%, and the coefficient of determination ($R^2$) is 0.35. This suggests that the model moderately fits the experimental data, leaving 65% of the variability unexplained. However, the model aligns well with the measured values during the spring and summer seasons. This is evidenced by the coefficients of determination of 0.97 and 0.98 respectively, and NRMSE values of 4.94% and 3.93%. A minor deviation is observed during the autumn season, with an error of 6.22% and a coefficient of determination of 0.94. This deviation can be associated with the occasional snowy days characteristic of this season, particularly in December.

The performance of the two modeling methods in terms of two factors (Error and execution time) is compared in Table 3.3. We notice that *pvfactors* has almost the same values as *bifacial_radiance* except for the computation time. The model with *pvfactors* shows therefore an interesting advantage for integration into management strategies and optimization problems for hybrid systems or microgrids that require multiple iterations.

However, it is not capable of capturing 3D effects such as the impact of the mounting structure that was clearly visible with *bifacial_radiance*.

| | **Season** | **Pvfactors** | **bifacial_radiance** |
|---|---|---|---|
| **Bifacial Gain** | Winter | 33.11 | 27.67 |
| | Spring | 13.54 | 9.9 |
| | Summer | 13.97 | 9.95 |
| | Autumn | 14.58 | 11.5 |
| **NRMSE %** | Winter | 18.77 | 17.92 |
| | Spring | 4.94 | 4.90 |
| | Summer | 3.93 | 4.12 |
| | Autumn | 6.22 | 5.96 |
| **Execution Time** | | 15 seconds | 3 hours |

**Table 3.3:** Results of the simulation using *pvfactors* and *bifacial_radiance*

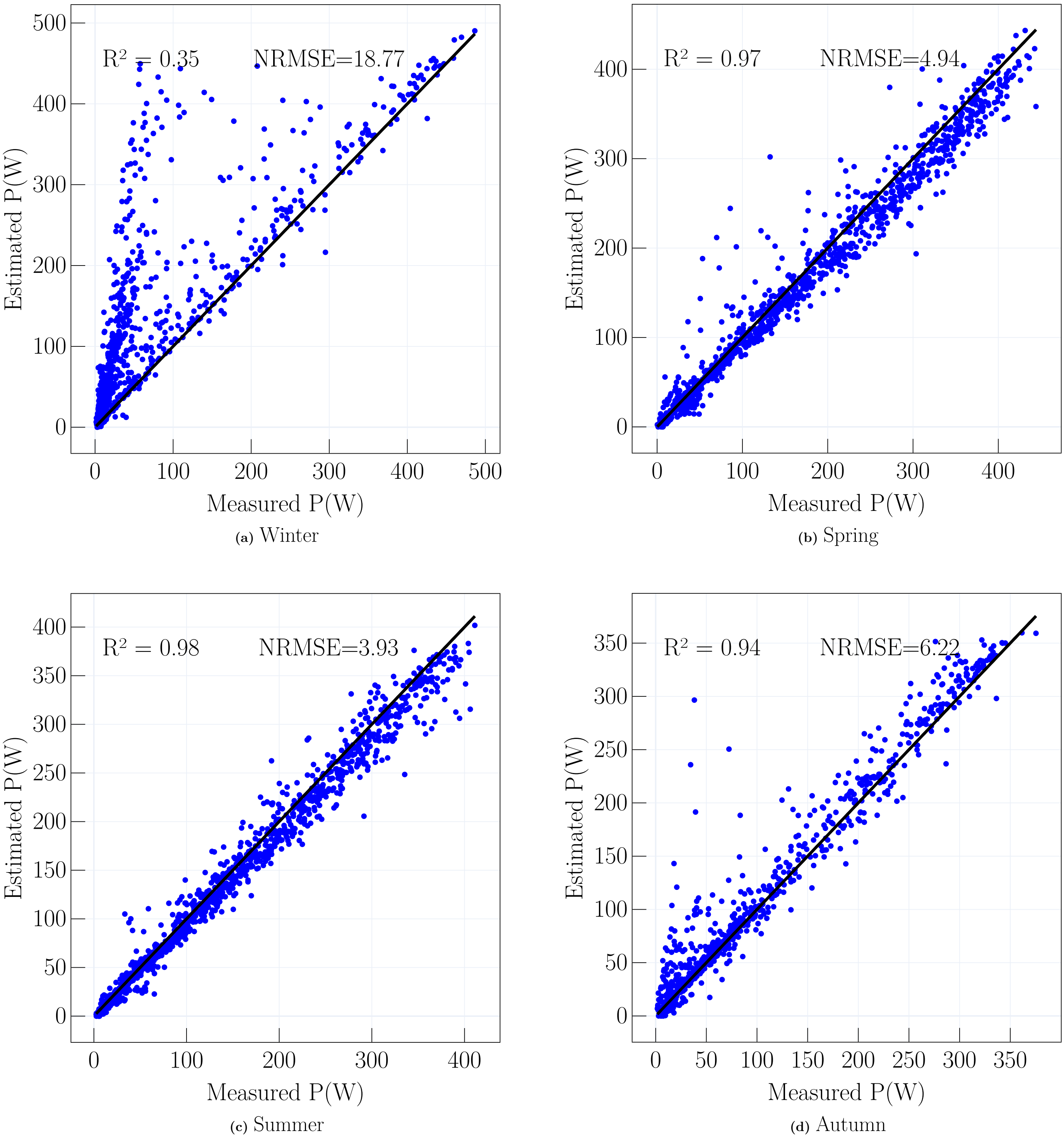


(a) Winter

(b) Spring

(c) Summer

(d) Autumn

**Figure 3.8:** Comparison of Measured and Estimated Power Output Using *pvfactors* (Top Module) and Local Data with Razon+

## 4.3 Sensitivity Analysis

In this section, we examine the sensitivity of the model with respect to input data. As previously noted in section 3, validation of the model was conducted using measured data, except for the albedo parameter. Therefore, this section addresses the accuracy of the model when it is supplied exclusively with weather data obtained from Solcast, which utilizes geostationary weather satellites and weather model data to estimate irradiance components. Various satellite-derived solar irradiance datasets provide historical irradiance time series, such as SOLARGIS, PVGIS, Solar AnyWhere, and METEONORM. Among these, Solcast stands out due to its promising characteristics, including its remarkable precision, which has been demonstrated in the publication [32].

The performance of the model utilizing Solcast irradiation data is detailed in Figure 3.9, with each sub-figure representing a specific season in the year 2021. Significant errors are observed across all seasons. Even in summer, which typically experiences the clearest skies ( Table 3.2 ), the NRMSE [5] is 14.72%, with a coefficient of determination ($R^2$) of 0.71. During spring, the NRMSE is 15.32% with an $R^2$ of 0.71, while autumn exhibits an NRMSE of 17.78% and an $R^2$ of 0.55. As anticipated, winter shows the highest error and greatest discrepancy between measured and estimated values, with an NRMSE of 22.76% and an $R^2$ as low as 0.07.

The elevated error values are attributed to the input data quality. To investigate this, we compared Solcast's historical data with measured data, focusing on four primary parameters impacting power production estimation: DNI, DHI, GHI, and Temperature. We computed the NRMSE for each parameter, summarized in Figure 3.10. The NRMSE values for DNI, DHI, GHI, and Temperature were 36.81%, 24.03%, 30.12%, and 12.81%, respectively.

[5] Normalized Root Mean Square Error

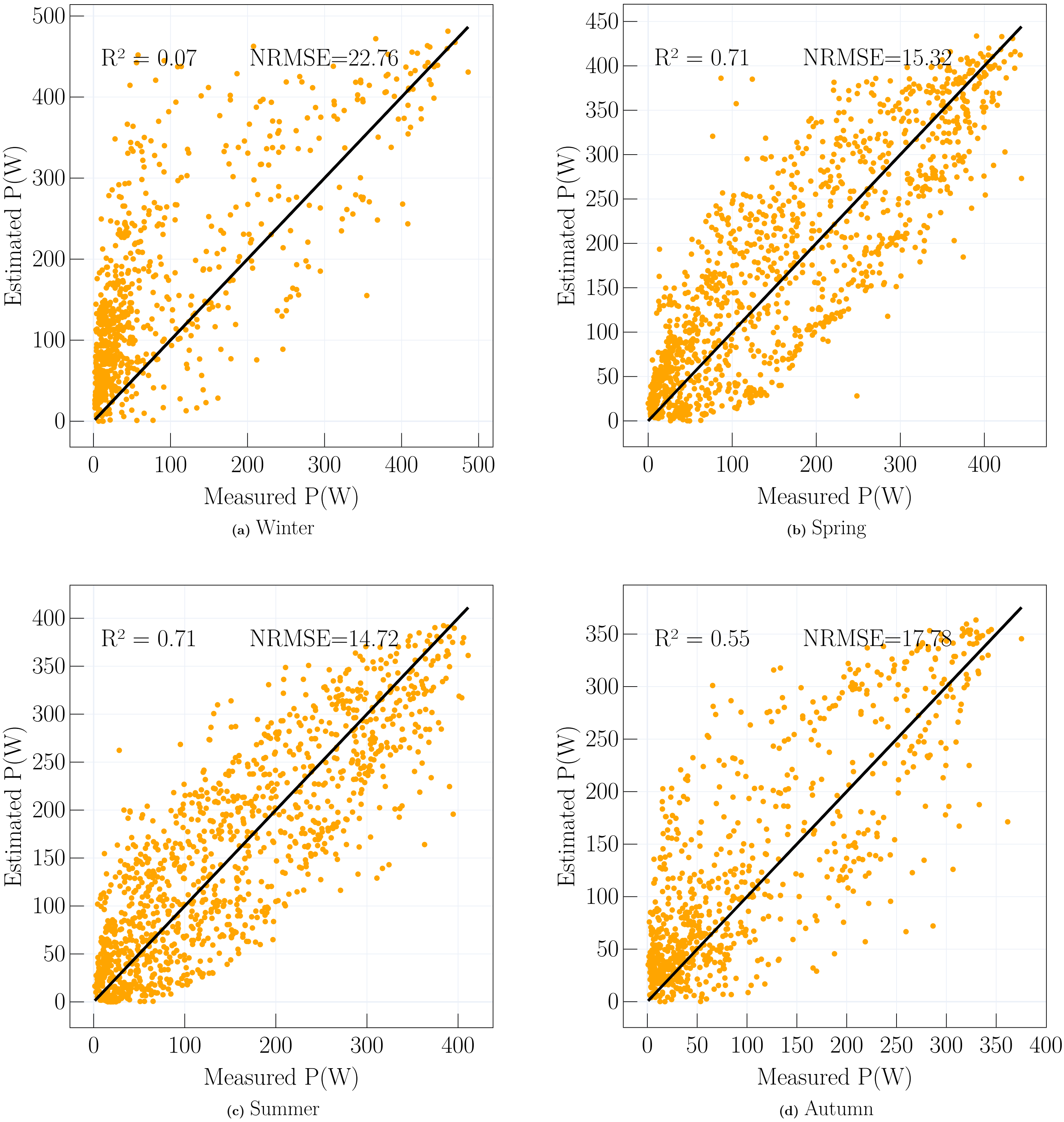


**Figure 3.9:** Comparison of Measured and Estimated Power Output Using *pvfactors* (Top Module) and Solcast Data

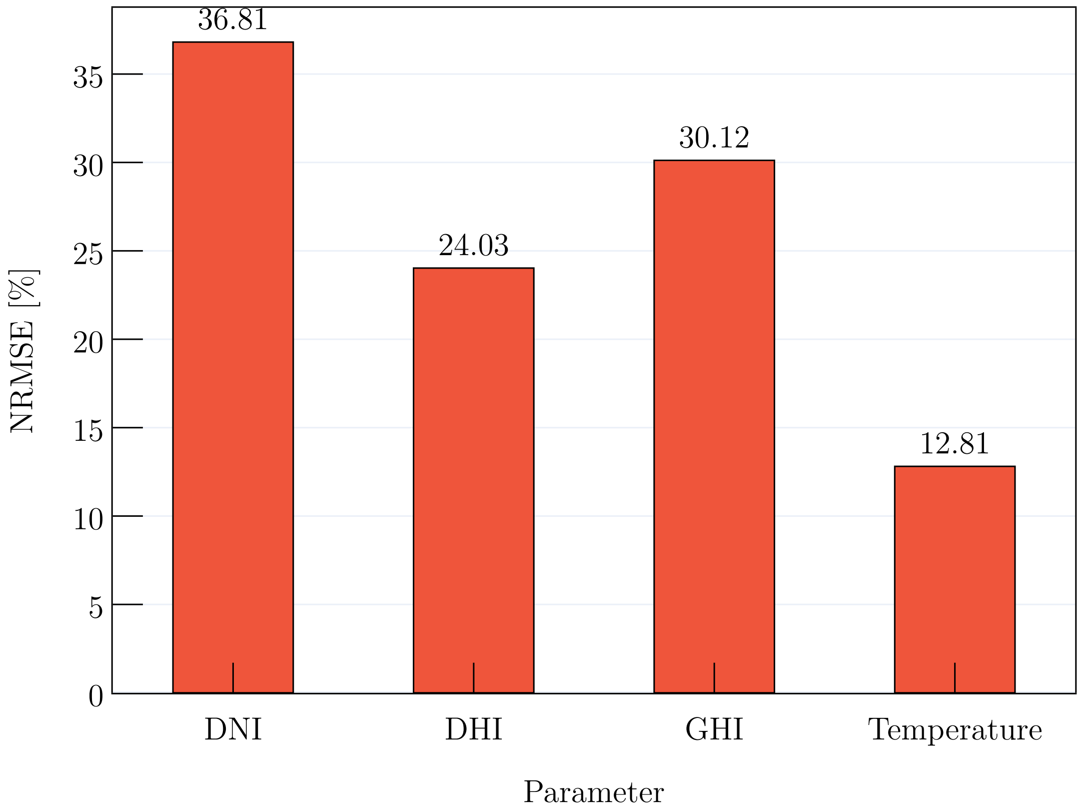


**Figure 3.10:** Discrepancy Between Measured Values and Solcast (Satellite-Derived ): DNI, DHI, GHI, and Temperature

## 4.4 Impact of Snow Coverage

This paper underscores the impact of snow on the energy yield of bifacial panels, a factor that significantly influences the sizing of power systems that utilize these panels. The common sizing methodology employs weather data, predominantly irradiance time series, to project the annual power variation of a single bifacial PV module. Subsequently, an optimization algorithm is used to ascertain the ideal number of modules needed to fulfill specific objectives while complying with load constraints. This method is extensively adopted in various studies and tools, including but not limited to Homer Pro and Pvsyst [33]–[35]. However, in regions prone to heavy snowfall, the power production of PV panels can be considerably diminished due to snow coverage.

To confirm the accumulation of snow on the modules, we have utilized the 'snow on the ground' metric, measured in centimeters. The variations in this specific parameter have been derived from an extensive database managed by a station located in Linexoville, Sherbrooke. In order to validate the presence of snow on the front surface of the module, we have strategically placed a camera directed towards the installed bifacial module. This configuration allows us to visually confirm and track the build-up of snow.

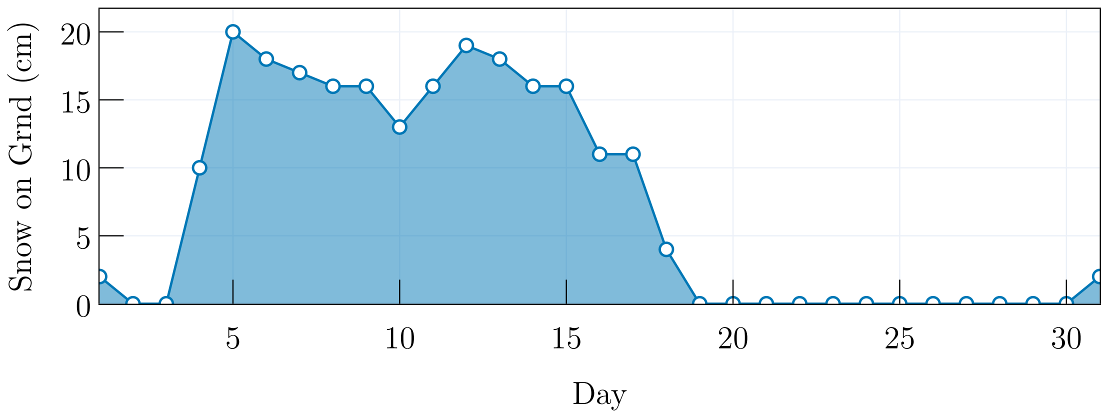


**(a)** December 2023

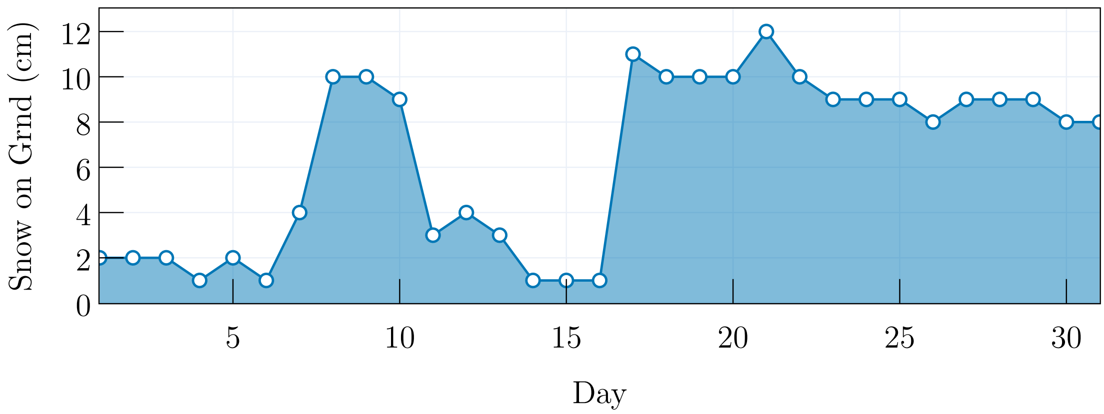


**(b)** January 2024

**Figure 3.11:** Accumulation of Snowfall (in cm) in Sherbrooke

From 3.11 and 3.12, a discernible pattern emerges: when the accumulated snow on the ground reaches or exceeds 2 cm, and the derivative of snow accumulation from the previous day is positive, the solar modules become entirely covered by snow on their front surface. This phenomenon is evident in the data for the four specific days depicted in Figure 3.12 namely, January 20, 2024, January 15, 2024, January 8, 2024, and May 12, 2024.

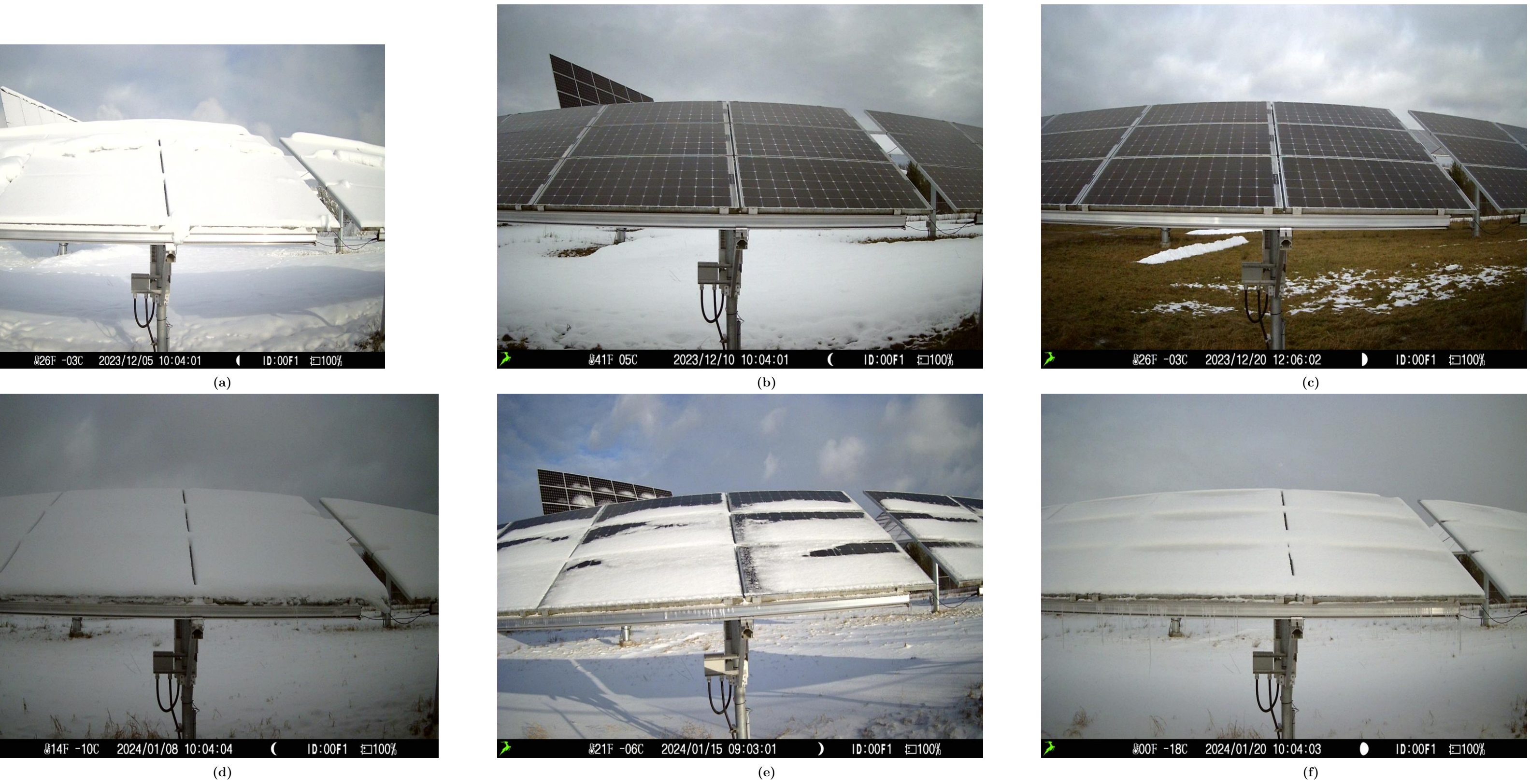


**Figure 3.12:** Bifacial PV String Installation on Sherbrooke Campus: A Photo Series Captured Across Selected Winter Days of 2023-2024

Conversely, it is observed that when the snow accumulation surpasses or equals 2 cm, and the derivative of the accumulation from the preceding day is negative, coupled with a significant temperature escalation, these conditions instigate the activation of the sliding phenomenon. This results in the clearance of the front surface of the bifacial panels. In our photographic series (Figure 3.12), we have documented a day where this phenomenon was observed, specifically on December 10th. On this day, the snow depth was 13 cm, however, there was a notable increase in the daily mean temperature. Starting from December 6th, 2024, the temperature rose from -10 degrees Celsius and reached 5.5 degrees Celsius on December 10th, 2024. This thermal shift appears to have contributed to the observed sliding phenomenon.


(a)

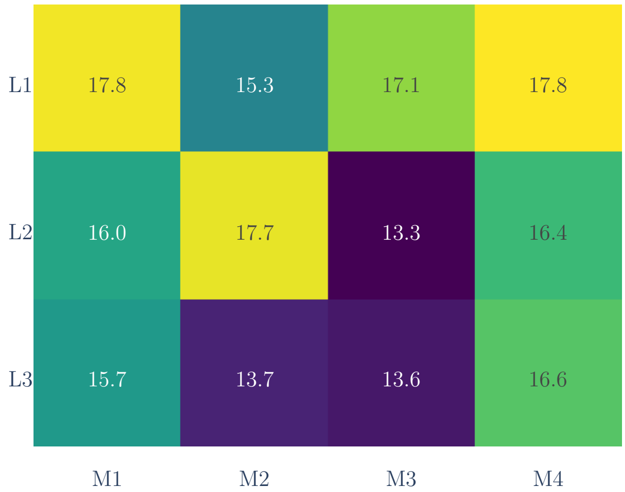


(b)

**Figure 3.13:** Measured Power Output of Fully Snow Covered Front Surface Bifacial Modules on January 8, 2024

Under the full coverage of the front surface all the string of the bifacial panels are masked with the snow. Thus only the rear surface of the bifacial modules generates the power based on the power and the expression of the power production can be expression as follows :

$$P_{bif} = P_{mp}\,\frac{\eta\Phi_r}{\Phi_{ref}}(1+\alpha_p(T_{cell}-T_{c,stc})) \tag{3.25}$$

Figure 3.13 presents a heatmap of the production output for each module, recorded at 12:00 (UTC-5) on January 8, 2024. As depicted in Figure 3.13a, the panels were entirely covered with snow throughout the day. The snow accumulation on the ground was measured to be 10 cm. In the absence of snow coverage, the top modules were estimated to produce approximately 86.6 W. However, the highest observed value was only 17.8 W, indicating a power loss of 79%.

To enhance the modeling of power production during the winter season, we employed Equation 2 under conditions of complete snow coverage. We identified days where the snow depth exceeded 2 cm, and the daily mean and maximum temperatures were strictly below 0°C to ensure the absence of snow sliding phenomena. These conditions were met from January 19, 2021, to February 27, 2021, and again from December 6, 2021.Previously, the NRMSE value for the winter season was 18.77%, with an $R^2$ value of 0.35. After refining the modeling approach to account for the impact of snow, the NRMSE value improved to 9.17%, and the $R^2$ value increased to 0.83, reflecting an improvement of approximately 51.1% in NRMSE and a substantial enhancement in $R^2$.

Despite these improvements, further refinement is possible. As observed in Figure 3.14, there are instances where the power production of bifacial modules is underestimated. This discrepancy may be attributed to undetected snow sliding phenomena.

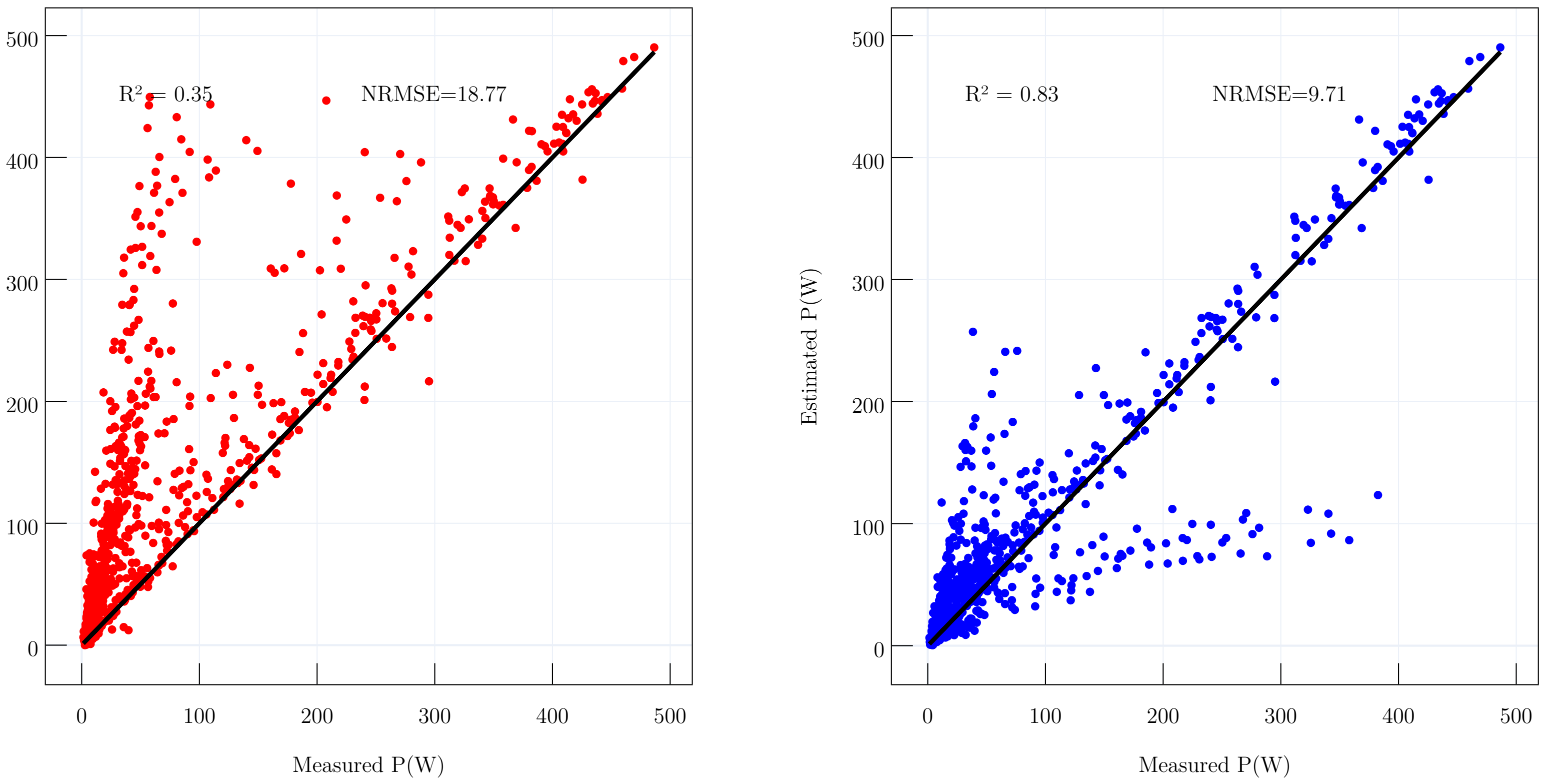


**(a)** Without Considering the Snow Coverage

**(b)** Considering the Snow Coverage

**Figure 3.14:** Refinement of NRMSE Value via Snow Coverage Consideration in Winter Season Modelling

## 5 Conclusion

With their promising energy yield and reasonable manufacturing cost, bifacial panels technology is showing remarkable momentum in the PV market, thus an accurate and fast model of the bifacial panel is necessary for sizing and implementing efficient management strategies for stations that use these modules. This study presents an experimentally validated model of bifacial panels tailored for snow-prone climates, ensuring strict time efficiency. The evaluated model, based on the *pvfactors* , achieves NRMSE of 18.77%, 4.94%, 3.93%, and 6.22% for Winter, Spring, Summer, and Fall, respectively. Remarkably, it accomplishes these results in under 15 seconds for a full year simulation of 2021. In contrast, simulations using the *bifacial_radiance* model are significantly slower, with corresponding NRMSE values of 17.92%, 4.9%, 4.12%, and 5.96% for the same seasons.

The *pvfactors* model strikes a commendable balance between accuracy and execution time across three seasons, with winter being the exception. During winter, the model tends to overestimate power production due to high agreement with clear weather periods, leading to notable discrepancies. Sensitivity analysis using satellite-imagery driven data from Solcast revealed a substantial performance drop, attributed to the data quality. Further investigation, including camera monitoring of the PV arrays, identified snow coverage on the front surface of the modules as the primary cause of poor winter performance. Snow coverage can reduce production by up to 80%, leaving the rear surface as the sole power producer. Incorporating snow depth metrics to estimate snow presence on panel surfaces improved model accuracy by 51%. In summary, the *pvfactors*-based model offers a robust and efficient solution for simulating bifacial panel performance, particularly under varying seasonal conditions, while highlighting areas for improvement in snow-affected regions.

Our experimental work on bifacial solar panels has yielded significant insights into their performance modeling, particularly in snow-prone environments. Building on our validated model and findings, we have developed an open-source tool to facilitate broader adoption and scientific collaboration. This tool, named BifacialPowerEstimator, is now available on GitHub (Figure 3.15). The documentation provides comprehensive details about the tool's features, including required inputs and expected outputs. The repository can be accessed at BifacialPowerEstimator. Having established this accurate modeling framework for bifacial panels, which represent a crucial component of our microgrid system, subsequent chapters will address the remaining subsystems, including the Energy Management System, diesel generator integration, and load profile analysis.

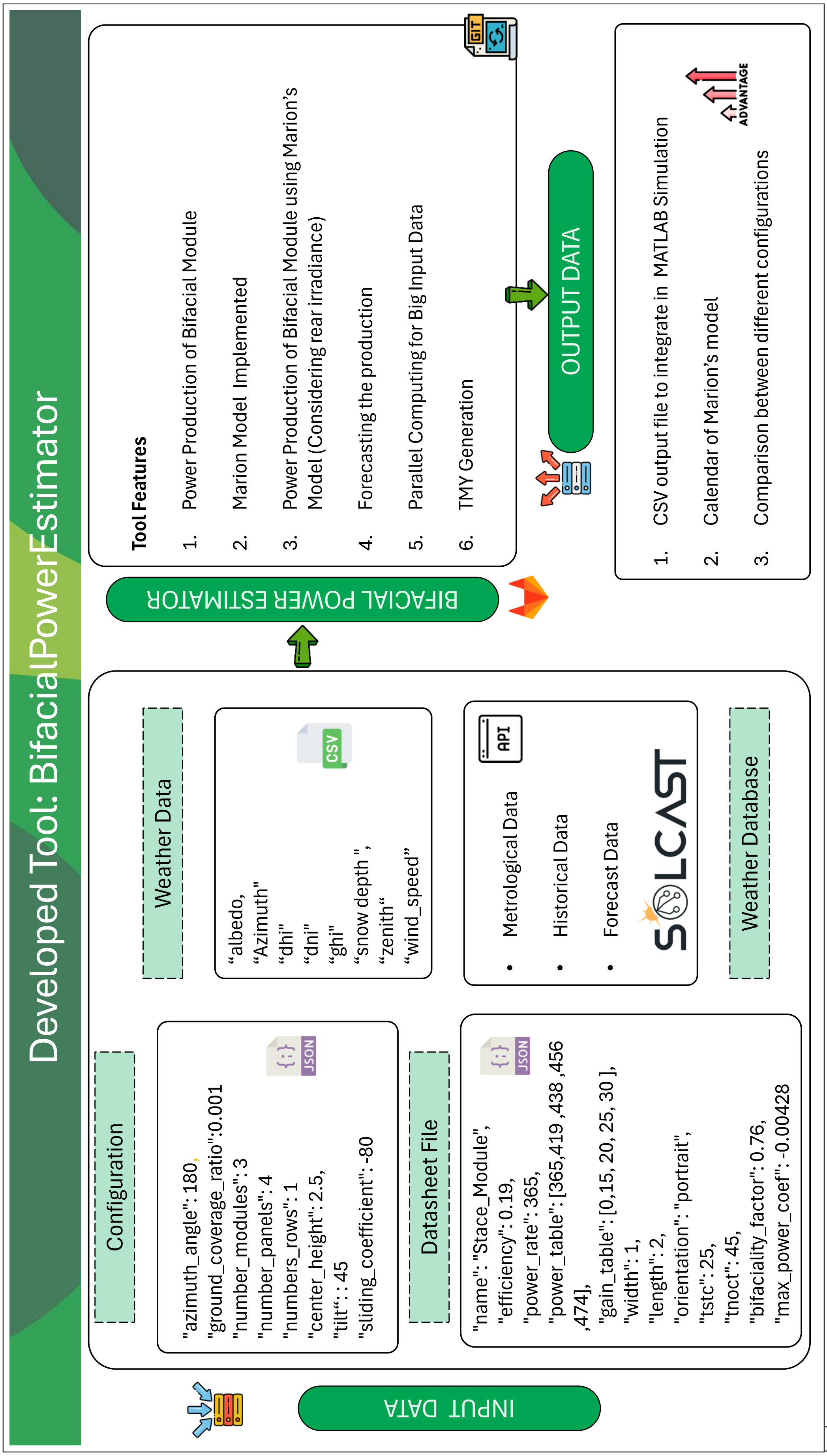


**Figure 3.15:** GitHub Project: BifacialPowerEstimator - A Newly Developed Tool

## References for Chapter 3


[1] Joshua Stein, Christian Reise, Johanna Castro, et al. *Bifacial Photovoltaic Modules and Systems: Experience and Results from International Research and Pilot Applications*. Apr. 2021. DOI: 10.2172/1779379.

[2] Md. Sultan Mahmud, Md. WazedurRahman, M.S. Hossain Lipu, et al. "Solar Highway in Bangladesh Using Bifacial PV". In: IEEE, July 2018, pp. 1–7. ISBN: 978-1-5386-4866-7. DOI: 10.1109/ICSCAN.2018.8541253.

[3] Muhammad Hussnain Riaz, Hassan Imran, Rehan Younas, et al. "The optimization of vertical bifacial photovoltaic farms for efficient agrivoltaic systems". In: *Solar Energy* 230 (Dec. 2021), pp. 1004–1012. ISSN: 0038092X. DOI: 10.1016/j.solener.2021.10.051.

[4] Amaury Martin, Pierre-Philippe Grand, Matthew Hull, et al. "Architecture of symmetrical bifacial perovskite/Si/perovskite PV modules and LCOE comparison in bifacial applications". In: *EPJ Photovoltaics* 14 (Nov. 2023), p. 33. ISSN: 2105-0716. DOI: 10.1051/epjpv/2023025.

[5] Odysseas Alexandros Katsikogiannis, Hesan Ziar, and Olindo Isabella. "Integration of bifacial photovoltaics in agrivoltaic systems: A synergistic design approach". In: *Applied Energy* 309 (Mar. 2022), p. 118475. ISSN: 03062619. DOI: 10.1016/j.apenergy.2021.118475.

[6] Thomas Baumann, Hartmut Nussbaumer, Markus Klenk, et al. "Photovoltaic systems with vertically mounted bifacial PV modules in combination with green roofs". In: *Solar Energy* 190 (Sept. 2019), pp. 139–146. ISSN: 0038092X. DOI: 10.1016/j.solener.2019.08.014.

[7] F. "Markus, H. Michael W. Susanne, and T." Jutta. "International Technology Roadmap for Photovoltaic 2022". In: *ITRPV-VDMA, Tech. Rep.* (2021). URL: https://www.vdma.org/international-technology-roadmap-photovoltaic.

[8] Manoel Henrique Oliveira Pedrosa Filho and Vanusa Alves Teixeira. "Low Cost Electroluminescense Lab Implementation". In: International Solar Energy Society, 2019, pp. 1–7. ISBN: 978-3-9820408-1-3. DOI: 10.18086/swc.2019.16.06.

[9] B. Decker and U. Jahn. "Performance of 170 grid connected PV plants in Northern Germany—Analysis of yields and optimization potentials". In: *Solar Energy* 59 (4-6 Apr. 1997), pp. 127–133. ISSN: 0038092X. DOI: 10.1016/S0038-092X(96)00132-6.

[10] Robert E. Pawluk, Yuxiang Chen, and Yuntong She. "Photovoltaic electricity generation loss due to snow – A literature review on influence factors, estimation, and mitigation". In: *Renewable and Sustainable Energy Reviews* 107 (June 2019), pp. 171–182. ISSN: 13640321. DOI: 10.1016/j.rser.2018.12.031.

[11] "Measured and modeled photovoltaic system energy losses from snow for Colorado and Wisconsin locations". In: *Solar Energy* 97 (Nov. 2013), pp. 112–121. ISSN: 0038-092X. DOI: 10.1016/J.SOLENER.2013.07.029.

[12] "Identifying snow in photovoltaic monitoring data for improved snow loss modeling and snow detection". In: *Solar Energy* 223 (July 2021), pp. 238–247. ISSN: 0038-092X. DOI: 10.1016/J.SOLENER.2021.05.023.

[13] Ajay Singh and Derek Jones. "Snow Shedding properties of Bifacial PV Panels". In: IEEE, June 2022, pp. 0646–0648. ISBN: 978-1-7281-6117-4. DOI: 10.1109/PVSC48317.2022.9938947.

[14] Daniel Riley, Clifford Hansen, Joshua Stein, et al. "A Performance Model for Bifacial PV Modules". In: IEEE, June 2017, pp. 3348–3353. ISBN: 978-1-5090-5605-7. DOI: 10.1109/PVSC.2017.8366045.

[15] Bill Marion, Sara MacAlpine, Chris Deline, et al. "A Practical Irradiance Model for Bifacial PV Modules". In: IEEE, June 2017, pp. 1537–1542. ISBN: 978-1-5090-5605-7. DOI: 10.1109/PVSC.2017.8366263.

[16] Xingshu Sun, Mohammad Ryyan Khan, Chris Deline, et al. "Optimization and performance of bifacial solar modules: A global perspective". In: *Applied Energy* 212 (Feb. 2018), pp. 1601–1610. ISSN: 03062619. DOI: 10.1016/j.apenergy.2017.12.041.

[17] Amir Asgharzadeh, Fatima Toor, Ben Bourne, et al. "A Benchmark and Validation of Bifacial PV Irradiance Models". In: IEEE, June 2019, pp. 3281–3287. ISBN: 978-1-7281-0494-2. DOI: 10.1109/PVSC40753.2019.8981272.

[18] P. Vueghs and P. Beckers. "Presentation of the hemisphere method". In: vol. 53. 2006, pp. 121–130. ISBN: 1845641760. DOI: 10.2495/HT060121.

[19] Lílian Dobrowolski, Carvalho Augusto, Bruno Giacomet, et al. *NUMERICAL METHOD FOR CALCULATING VIEW FACTOR BETWEEN TWO SURFACES*, pp. 2007–269.

[20] K.N. Shukla, Saroj Rangnekar, and K. Sudhakar. "Comparative study of isotropic and anisotropic sky models to estimate solar radiation incident on tilted surface: A case study for Bhopal, India". In: *Energy Reports* 1 (Nov. 2015), pp. 96–103. ISSN: 23524847. DOI: 10.1016/j.egyr.2015.03.003.

[21] John A Duffie and William A Beckman. *Solar engineering of thermal processes*. John Wiley & Sons, 2013.

[22] John E Hay. "Calculation if the solar radiation incident on inclined surfaces". In: *Proceedings first Canadian Solar Radiation Data Workshop, Toronto. Ontario, Canada 1978*. 1978.

[23] Richard Perez, Robert Seals, Pierre Ineichen, et al. "A new simplified version of the perez diffuse irradiance model for tilted surfaces". In: *Solar Energy* 39 (3 1987), pp. 221–231. ISSN: 0038092X. DOI: 10.1016/S0038-092X(87)80031-2.

[24] RJ Stone. "Improved statistical procedure for the evaluation of solar radiation estimation models". In: *Solar energy* 51.4 (1993), pp. 289–291.

[25] Tian Shen Liang, Mauro Pravettoni, Chris Deline, et al. "A review of crystalline silicon bifacial photovoltaic performance characterisation and simulation". In: *Energy & Environmental Science* 12 (1 2019), pp. 116–148. ISSN: 1754-5692. DOI: 10.1039/C8EE02184H.

[26] Soufiane Ghafiri, Maxime Darnon, Arnaud Davigny, et al. "A Comparative Study of Existing Approaches for Modeling the Incident Irradiance on Bifacial Panels". In: *Electrimacs*. Nancy, France, May 2022. URL: https://hal.archives-ouvertes.fr/hal-03831357.

[27] Fouzia Brihmat and Said Mekhtoub. "PV cell temperature/PV power output relationships homer methodology calculation". In: *Conférence Internationale des Energies Renouvelables" CIER'13"/International Journal of Scientific Research & Engineering Technology*. Vol. 1. 02. International Publisher &C. O. 2014, pp. 0–0.

[28] Ibrahim Reda and Afshin Andreas. "Solar position algorithm for solar radiation applications". In: *Solar Energy* 76 (5 Jan. 2004), pp. 577–589. ISSN: 0038-092X. DOI: 10.1016/J.SOLENER.2003.12.003.

[29] Silvana Ayala Pelaez and Chris Deline. "bifacial_radiance: a python package for modeling bifacial solar photovoltaic systems". In: *Journal of Open Source Software* 5 (50 June 2020), p. 1865. ISSN: 2475-9066. DOI: 10.21105/joss.01865.

[30] Harald K. Seidlitz, Stephan Thiel, Andreas Krins, et al. *Solar radiation at the Earth's surface*. 2001. DOI: 10.1016/S1568-461X(01)80071-5.

[31] Marc Abou Anoma, David Jacob, Ben C. Bourne, et al. "View Factor Model and Validation for Bifacial PV and Diffuse Shade on Single-Axis Trackers". In: *2017 IEEE 44th Photovoltaic Specialist Conference (PVSC)*. 2017, pp. 1549–1554. DOI: 10.1109/PVSC.2017.8366704.

[32] Jamie M. Bright. "Solcast: Validation of a satellite-derived solar irradiance dataset". In: *Solar Energy* 189 (Sept. 2019), pp. 435–449. ISSN: 0038092X. DOI: 10.1016/j.solener.2019.07.086.

[33] Linta Khalil, Kamran Liaquat Bhatti, M. Arslan Iqbal Awan, et al. "Optimization and designing of hybrid power system using HOMER pro". In: *Materials Today: Proceedings* 47 (2021), S110–S115. ISSN: 22147853. DOI: 10.1016/j.matpr.2020.06.054.

[34] Ahmad Shah Irshad, Gul Ahmad Ludin, Hasan Masrur, et al. "Optimization of grid-photovoltaic and battery hybrid system with most technically efficient PV technology after the performance analysis". In: *Renewable Energy* 207 (May 2023), pp. 714–730. ISSN: 09601481. DOI: 10.1016/j.renene.2023.03.062.

[35] Dhaker Abbes, André Martinez, and Gérard Champenois. "Life cycle cost, embodied energy and loss of power supply probability for the optimal design of hybrid power systems". In: *Mathematics and Computers in Simulation* 98 (Apr. 2014), pp. 46–62. ISSN: 03784754. DOI: 10.1016/j.matcom.2013.05.004.

*"The scientists of today think deeply instead of clearly. One must be sane to think clearly, but one can think deeply and be quite insane."*

Nicolas Tesla (1856-1943)

# 4

# Modeling of Macrocell BTS, Energy Storage System, and Generator Set

## Contents



## 1 Introduction

This chapter presents comprehensive models for the key components of these nanogrids, providing MNOs with a framework for system analysis and optimization. While our research incorporates actual power consumption data from a dual-antenna macro base station at Dorval Lodge, we recognize that such historical data may not always be available to MNOs. Therefore, we develop detailed theoretical models that can be applied regardless of data availability. Building upon our previous detailed modeling of bifacial photovoltaic modules, our modeling framework encompasses three additional essential subsystems: macro base stations, energy storage systems (specifically $LiFePO_4$ batteries), and diesel generators.

## 2 Macro Base station: power consumption model

In a heterogeneous mobile network, several BTSs are implemented to ensure total zone coverage. These stations have different sizes, coverage areas, and costs. Macro stations are large stations with high towers and antennas; they require space to deploy all the equipment compared with the micro and Pico stations, which are generally installed to cover small to medium areas with dense traffic. Another smaller type of station can be found, which is the Femto station, designed to serve small areas as indoor spaces. The result of [1] measurement shows that the power consumption of the micro station is nearly half lower than the power consumption of the macro station because this later handles more traffic than the other stations. Based on the traffic load dependency [2] divides the components of a macro base into two groups, the first group has a constant power under the assumption that we have a constant heat generation of the equipment inside the cabin, and this group consists of an air conditioner and microwave link. The second group includes all the components whose consumption depends on the traffic load, such as the baseband unit (digital processing), power amplifier, transceivers, and DC-DC converter. From the power flow diagram presented in Figure 4.1, the power consumption of the macro base station can be expressed with this equation:

$$P_{macro} = P_{cooling} + n_{sectors}(P_{rect} + f(n_{tex}(P_{tx} + P_{pa}) + P_{bb}) \tag{4.1}$$

Where $P_{cooling}P_{rect}$, $P_{tx}$,$P_{pa}$ and $P_{sp}$ are the power consumption of air conditioner, rectifier, transceiver, power amplifier which amounts to over than 50% of the total power consumption of BS and baseband unit respectively, $n_{sectors}$ number of sectors served by the BS, and $f$ load factor that varies between 0 (case of no load traffic) and 1 (when the station reaches its maximum capacity ).The maximum power consumption of BS using the EARTH model [3] grows proportionally with the number of transceivers:

$$P_{in} = \frac{n_{tx}(\frac{P_{out}}{\eta_{pa}(1-\sigma_{feed}))} + P_{rf} + P_{bb}))}{((1-\sigma_{dc})(1-\sigma_(ms))(1-\sigma_{cool})} \tag{4.2}$$

Where $P_{out} = P_{max}, n_{tx}$ number of transceivers and represents the loss factors $\sigma = 1 - \eta$. Several studies have examined the power consumption model for macro base stations in the literature. For example, [2] use the same model presented above, but for the load traffic, they propose a linear model that links the load factor with two parameters, which are the received voice and data calls, the coefficient of the linear equation is determined with the measurements of the power consumption, voice and data load. [4] have proposed a multivariate LSTM model to forecast the traffic patterns in the function of temporal and spatial variation, and the mean absolute error was 0.074 and 0.083 for two different locations. EARTH project developed a global energy efficiency evaluation framework for BS [5] with an accurate power consumption model based on statistical models that expect the number and duration of requests received by a station using Poisson distribution. Authors in [6] divided the power consumption of the BS into static and dynamic components, but due to the neglected dynamical part, the power model can be reduced to the statistical one.

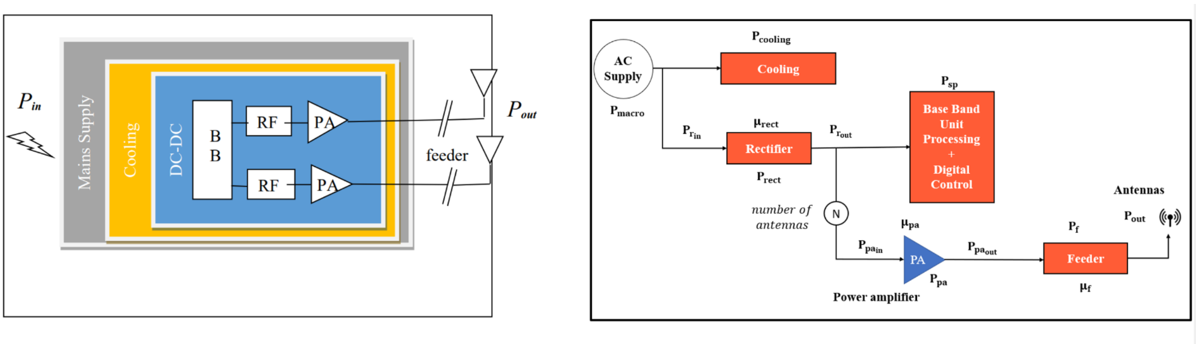


**Figure 4.1:** Typical architecture of base station and Power flow diagram in the macro base station

Figure 4.2 shows the DC load profile, this variation has spatial and temporal components as described in [7]; the author proposed a three-order sinusoid waveform to model the traffic volume received by a macro station. Within the scope of our study , the DC load demonstrates a near-invariant trend throughout the annual cycle. This observation is substantiated by Figure 4.2a , which offers an amplified perspective on the load's fluctuation during the month of February 2021. In order to derive the load profile, we have implemented an approach based on the hourly mean variation. The findings from this methodology are illustrated in 4.2b . We've applied the same approach on the AC load to extract its hourly profile.

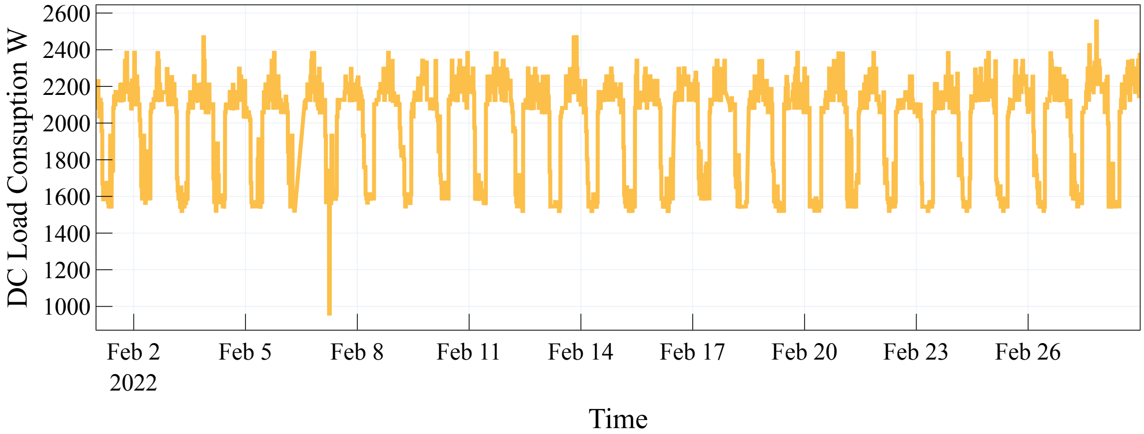


**(a)** February 2022 DC Consumption for the Pair of 4G Antennas

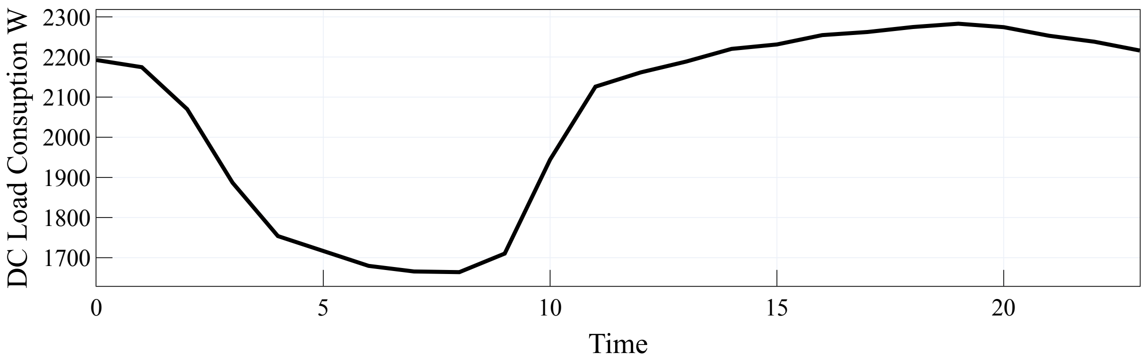


**(b)** HourlyLoad Profile

**Figure 4.2:** DC Load Consumption

## 3 Modeling of the ESS: Batteries $LiFePO_4$

Lead acid batteries have long maintained a dominant market position in the telecommunications industry as the preferred energy storage system for hybrid systems powering Base Stations. This preference can be attributed to their cost-effectiveness, high discharge rate, and established technological maturity. However, a recent trend has emerged, indicating a shift towards the utilization of Lithium-ion batteries, specifically those composed of $LiFePO_4$. This shift is due to the array of promising characteristics exhibited by these power sources, including notably high energy density, prolonged lifespan, non-toxicity (lacking Cobalt-Nickel elements), stability at elevated temperatures, and an enhanced safety profile. It is worth noting that while Lithium titanate batteries outperform LFP in these properties, LFP remains the cost-effective choice for the time being[8]. There are numerous methods to estimate the battery's State Of Charge as presented by the authors of the review [8]. For the sake of reducing the simulation time we have implemented the

Coulomb counting in order to estimate the battery state of charge , the voltage of the battery is deduced from the open circuit voltage variation (Equation 4.4).

$$SOC(t) = SOC_0 + \int_{t_0}^{t} \frac{i_{bat}(t)}{Q_{bat}} dt \tag{4.3}$$

$$V_{bat} = OCV - R_{bat} i_{bat} \tag{4.4}$$

$$OCV = f(SOC) \tag{4.5}$$

Where $SOC_0$ is the initial battery's state of charge, $i_{bat}$ is the battery current, $Q_n$ nominal battery capacity, $OCV$ open circuit voltage, and $R_{bat}$ is the battery's series resistance.

### 3.0.1 Battery Degradation

Battery degradation is predominantly caused by two primary aging phenomena. The first, cyclic aging, is closely linked to the battery's C-rate, depth of discharge, and the number of discharge cycles it undergoes. The second, calendar aging, is primarily affected by the temperature, state of charge (SOC), and duration of storage [9], [10].To quantify the cyclic aging of batteries, the Palmgren–Miner linear damage rule is utilized to account for the accumulation of damage resulting from charge and discharge cycles. The number of cycles is computed using the Rainflow algorithm. Figure 4.4, which represents the number of cycles versus the depth of charge, is used in conjunction with the Palmgren–Miner rule, which states:

$$D_l = \sum_{i=0}^{k_n} \frac{n_i}{N_i} \tag{4.6}$$

Where $n_i$ is the number of cycles that corresponds to the amplitude $DoD_i$, $k_n$ the total number of DOD levels, and $N_i$ lifespan cycle at amplitude $DOD_i$. The depth of discharge levels are determined by processing the state of charge signal after one year of simulation.

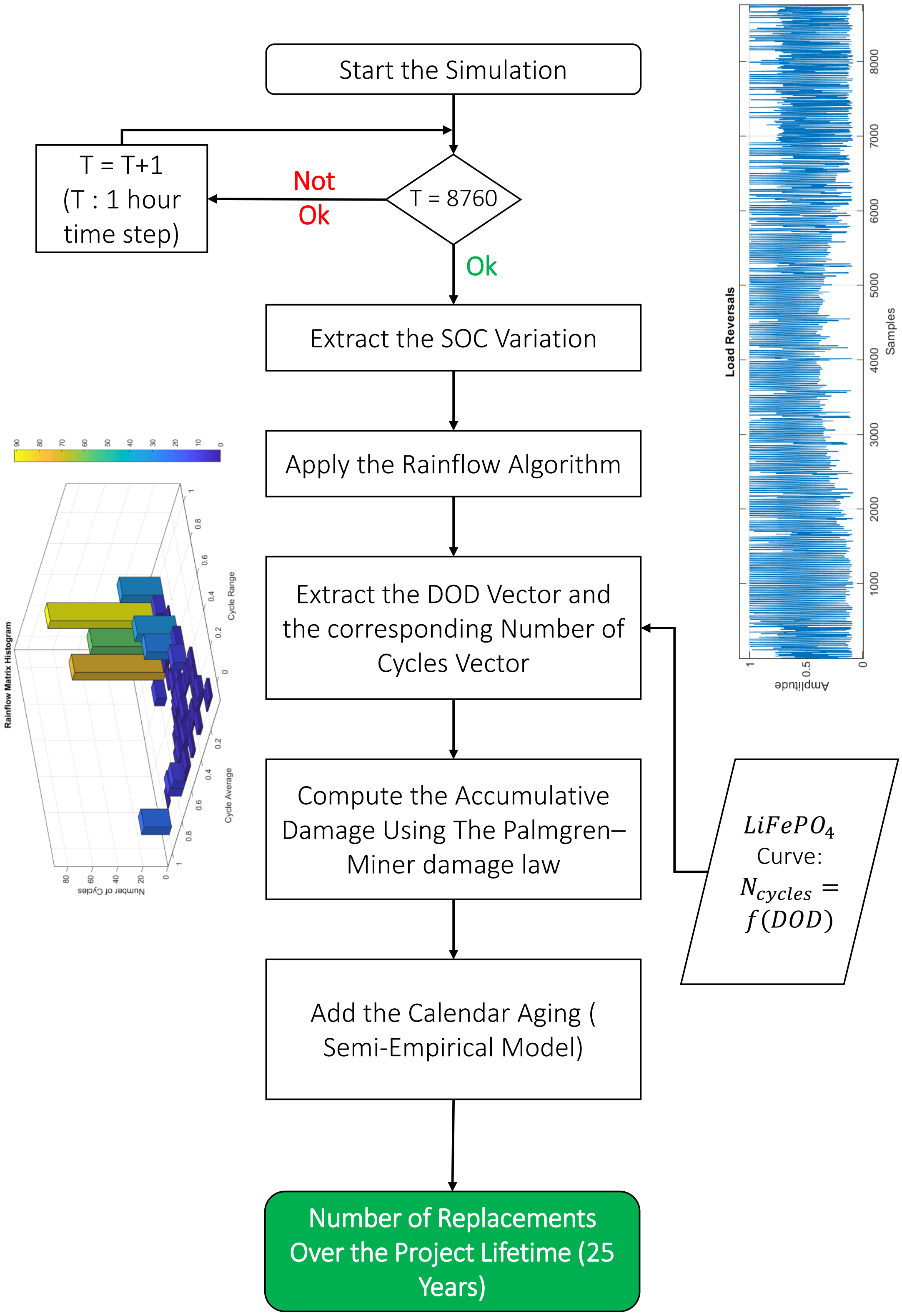


**Figure 4.3:** Flow Chart for Projecting Battery Replacement Frequency

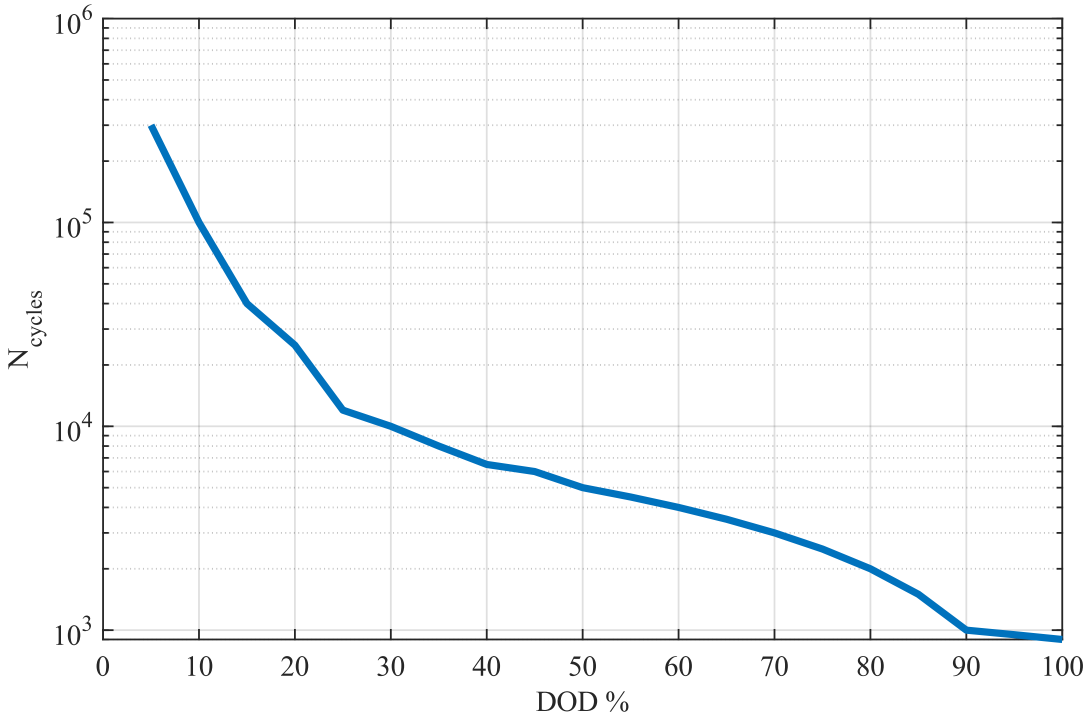


**Figure 4.4:** $LiFePO_4$ Number of Cycles versus the Depth of Discharge (Data from [11])

To estimate the calendar aging, we utilize a semi-empirical model [12], that establishes a relation between the capacity fade and two key parameters: temperature and state of charge. The model's precision is substantiated through a dynamic calendar aging study, conducted under varying temperature and state of charge conditions. The results of this study reveal that the model errors for capacity loss remain consistently below the 2.2% threshold. Therefore the capacity fade due to calendar aging is expressed as :

$$Q_{cal,loss} = k_{soc}\, k_{T_{bat}}\, \sqrt{t} \tag{4.7}$$

$$k_{soc} = 2.8575\,(SOC - 0.5)^3 + 0.60225 \tag{4.8}$$

$$k_T = 0.0012571\ \exp\left(-2059.8\,\left(\frac{1}{T_{bat}} - \frac{1}{298.15}\right)\right) \tag{4.9}$$

$$\frac{dq_{cal}}{dt} = \frac{k_{soc}\, k_{T_{bat}}}{\sqrt{\tilde{t}}} \tag{4.10}$$

Where $T_{bat}$ is the battery temperature, $k_{soc}$ and $k_t$ are coefficients that respectively denote the influence of the state of charge and the temperature on the Battery discharge capacity, $\tilde{t}$ is the virtual time . The Figure 5.1b below illustrates the fluctuations in temperature. The key observation is that during winter, the temperature can plummet to low levels, which may decrease the battery capacity retention [13].

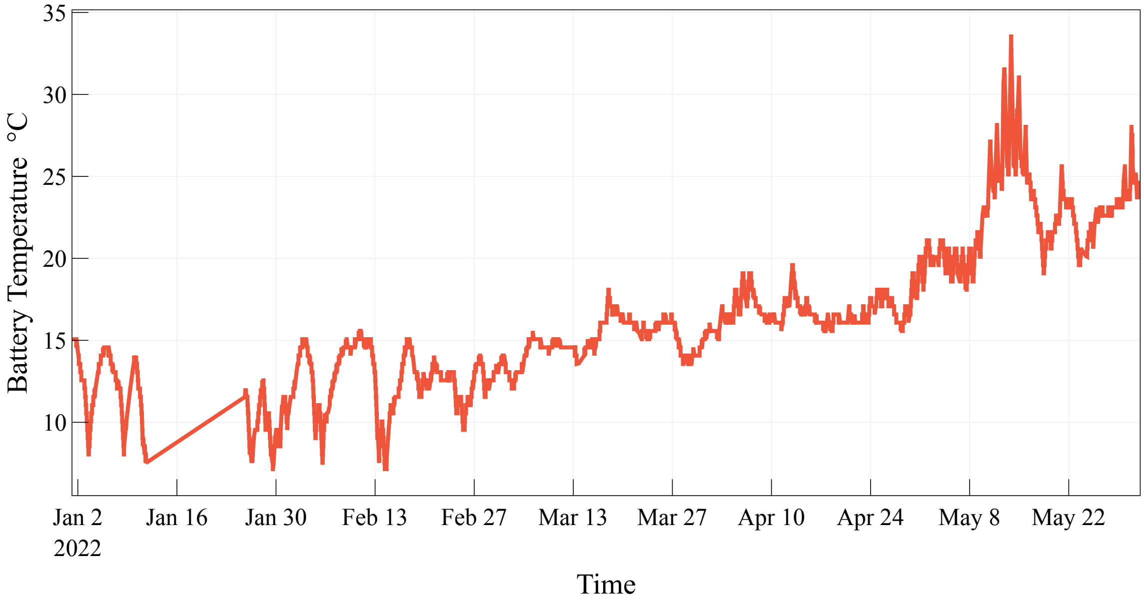


**Figure 4.5:** Battery Temperature Variation

Our hypothesis posits that the battery temperature is influenced by the external temperature Figure 4.6. Consequently, through an examination of our records, we can discern the relationship between the battery temperature and the external temperature Equation 4.11. It is crucial to emphasize that the applicability of the empirical formula is confined to the system under investigation, taking into account the specific type of enclosure and the prevailing climatic conditions.

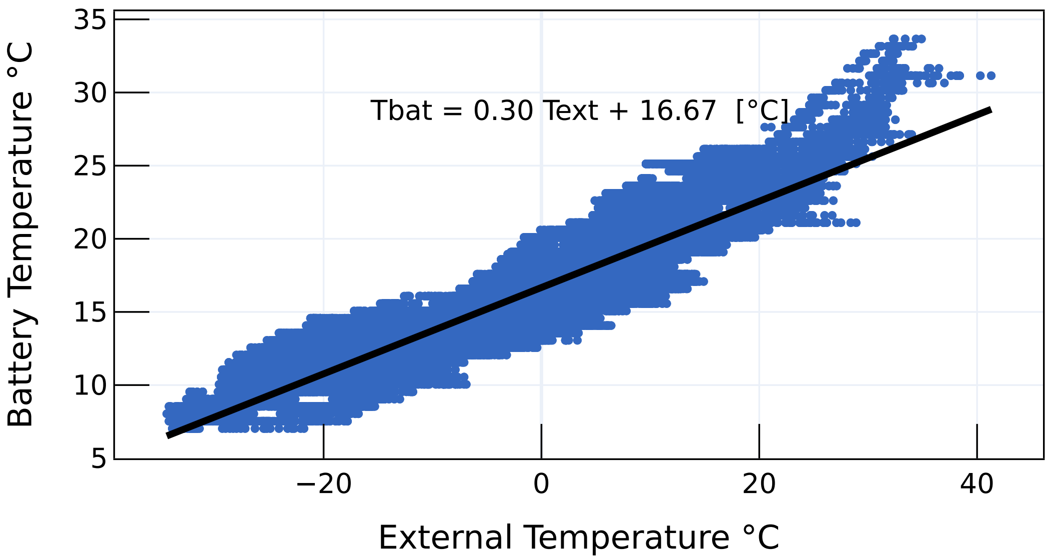


**Figure 4.6:** Example of the Battery Temperature Variation

The equation of the regression line is :

$$T_{bat} = 0.3\, T_{ext} + 16.67 \tag{4.11}$$

Where $T_{ext}$ is the dry bulb temperature in $°C$. The Equation 4.7 is employed to represent static conditions. For dynamic conditions, we utilize its derivative (Equation 4.10) to estimate the change in capacity fade over a specified time. Our methodology involves calculating the monthly loss in discharge capacity. After a one-month period, we compute the calendar aging. In dynamic mode, we substitute actual time with a virtual equivalent. This virtual time or signifies the duration until the same quantity of loss (Qloss) is attained under the newly established storage conditions. Figure 4.7 represents the result of the explained approach. In the current design, our computations indicate that the annual calendar aging is approximately 0.95%. Concurrently, the cyclic aging, after 489 cycles, is around 3.68%. Consequently, the cumulative degradation of the discharge capacity, which we've calculated to be 4.63%, encapsulates the combined effects of both the calendar and cyclic aging processes as summurized in the Table 4.1. The flowchart in Figure 4.3 summarizes the methodology to estimate the replacement frequency of the batteries.

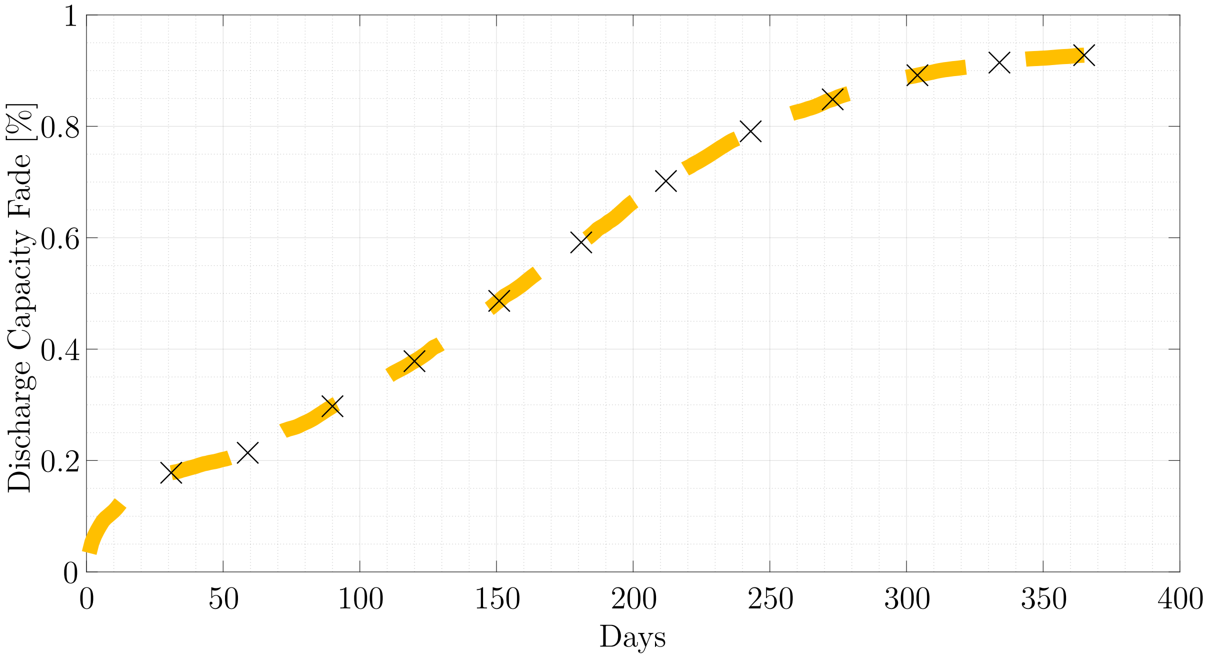


**Figure 4.7:** Estimation of the Yearly Calendar Aging using Semi-emperical Model

| Cycles | Calendar Aging [%] | Cyclic Aging [%] |
|---|---|---|
| 489 | 0.92 | 3.68 |

**Table 4.1:** Summary of the Estimated Cyclic and Calendar Aging for the Current Design

### 3.0.2 Electro-thermal model of batteries

One of the perspectives of this project is to manage the energy consumption of the HVAC system inside the equipment room. The underlying objective is to ensure an optimal operating temperature for the battery, as the external temperature can plummet below 30 degrees. The electro-thermal model in Figure 4.8 is used to control and monitor the variation in the battery's internal temperature. For simplicity, we ignore the diffusion voltages in the electrical model. Therefore, the internal heating of the battery cell is only due to the internal resistance $R_s$.

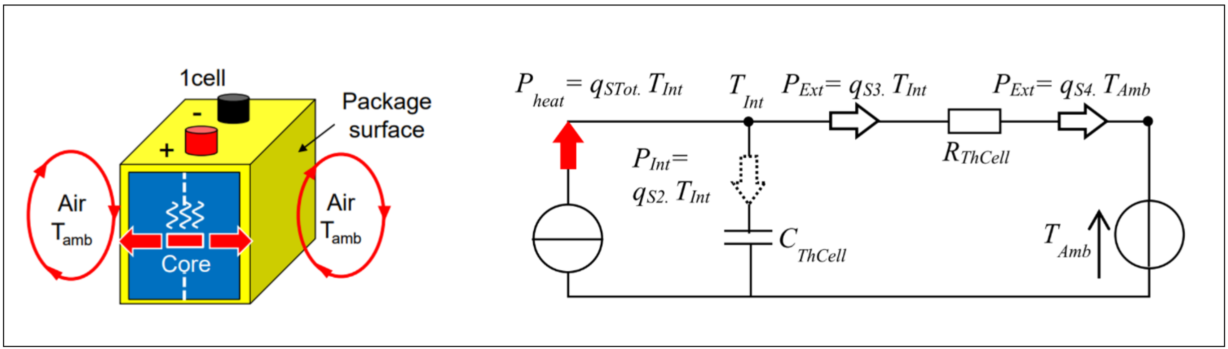


**Figure 4.8:** Thermal model of the battery cell [14]

In the thermal model (above Figure 4.8), we have three unknown parameters. A characterization protocol is defined in [15] to determine the exact value of these parameters to have an accurate estimation. The electrical losses are the source of the cell heating; therefore, we can write:

$$P_{heat} = R_s i_{cell}^2 \tag{4.12}$$

$$P = ST \tag{4.13}$$

$S$ is the entropy flow, in the thermal domain the power is expressed with the Equation 4.13.

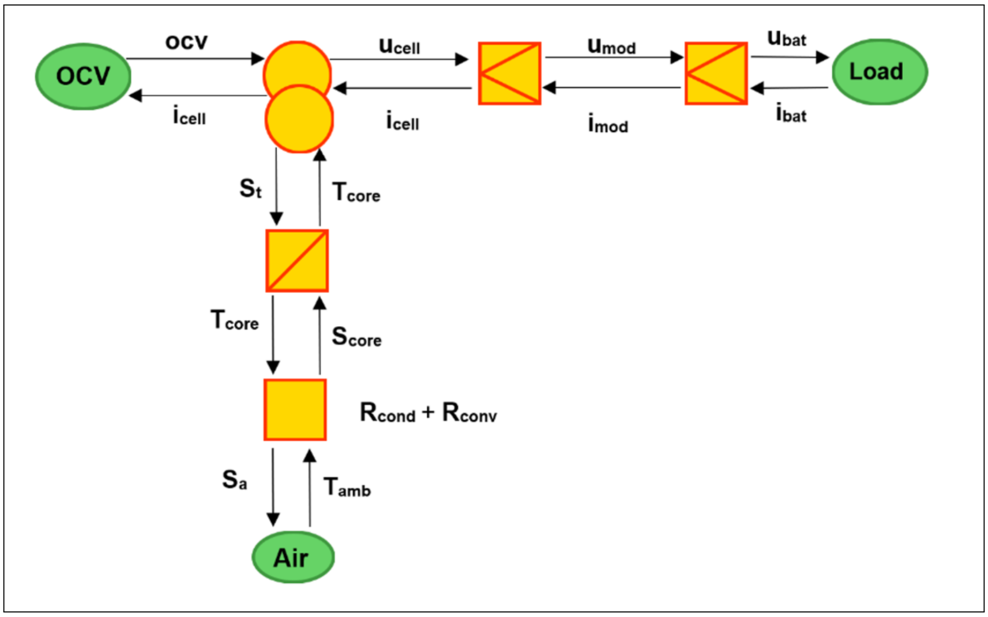


**Figure 4.9:** EMR representation of battery electro-thermal model

To conclude, We assume that the monitoring of the thermal resistance of the battery is not necessary as the HVAC system maintains an optimal operating temperature.

# 4 Modeling of Diesel Generator

In order to accurately assess the efficiency and operational costs of a diesel generator, it is essential to model its fuel consumption. This can be achieved through the use of Equation 4.14, which establishes a direct relationship between three key variables: the generator's hourly output power, its rated power, and the hourly fuel consumption. By applying this equation, it becomes possible to estimate the amount of diesel fuel that the generator will consume during a given operating hour. This information is vital for optimizing the generator's performance, reducing its environmental impact, and minimizing operational expenses.

$$F_{gen,h} = \alpha_0 P_{gen,i} + \alpha_1 P_{gen,r} \tag{4.14}$$

$\alpha_0$ and $\beta_1$ are the coefficients of the fuel curve, their respective values are 0.246 [L/kWh] and 0.08145 [L/kWh] [16], [17]. This equation allows us to calculate the amount of diesel fuel that the generator will use during a specific operating hour, which is vital for enhancing its performance, lowering its environmental impact, and reducing operational expenses.
In order to validate this model we compared its outputs with two values that are indicated in the Generator's datasheet and the Table 4.2 summarizes the results.

| Output Power | Estimated Consumption | Measured Consumption | Relative Error |
|---|---|---|---|
| 20kW (Full Charge ) | 7 L/h | 6.54 L/h | 7% |
| 13.6 kW | 4.97 L/h | 4.6 L/h | 8% |

**Table 4.2:** Validation of the Generator Model

## 4.1 Operation of Diesel Generators: Essential Aspects and Measures

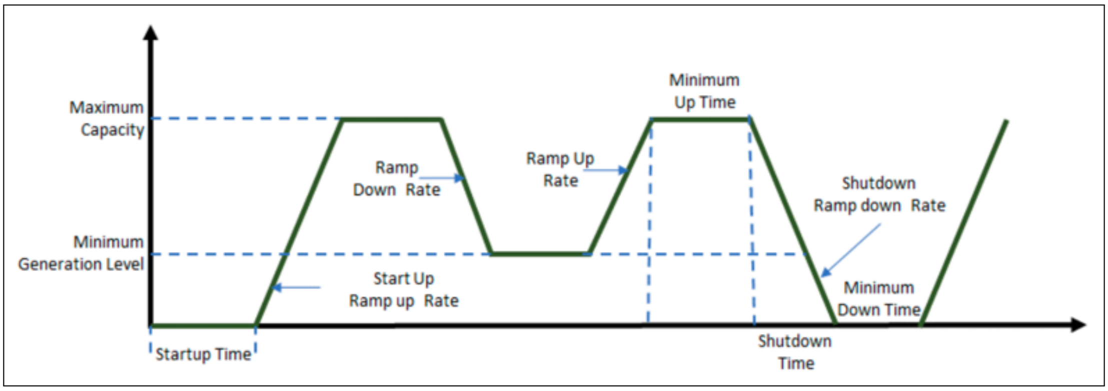


**Figure 4.10:** Flexibility Attributes of Diesel Generator

The paramount factor that determines the performance of the diesel generator is its flexibility (Figure 4.10), which signifies its capacity to responds with both anticipated and unforeseen fluctuations of power system conditions across various temporal scales. The four main parameters that describe the operation of diesel generator are:

- Minimum Generator level: This is the lowest power output that the diesel generator can sustain continuously without compromising its performance. This level depends on the efficiency of the generator, which decreases as the power output declines.
- Ramp rate: This measures how rapidly the generator can adjust its power output to match the demand. A higher ramp rate indicates a more flexible and responsive generator.
- Startup/shutdown time: This is the time required to switch from the non-operational state to the operational state and vice versa. A shorter startup/shutdown time means a lower operational cost and a lower environmental impact.
- Minimum up/down time: This is the minimum duration that the generator must operate or remain idle before it can change its state. This ensures a safe and reliable operation of the diesel generator.

Our model adheres to ISO 8528 standards and utilizes a Prime-rated generator configuration (Figure 4.11). This selection enables sustained annual operation while accommodating specific temporal constraints related to startup and shutdown processes. The operational framework is governed by three fundamental criteria: first, a 30% minimum load requirement is maintained to ensure optimal generator performance; second, the average load factor must not exceed 70%; and third, a defined operational period of 500 hours is followed by a mandatory 4-hour maintenance window. The 500-hour operational cycle aligns with standard oil change intervals and preventive maintenance requirements. This scheduling ensures consistent performance and equipment longevity. The establishment of a 30% minimum load threshold is crucial for several technical reasons. First, it prevents wet stacking, a phenomenon involving the accumulation of unburned fuel in the exhaust system. Operating below the threshold increases the risk of this condition. Second, proper combustion sealing requires adequate operational loads, as insufficient loading leads to incomplete fuel combustion. Third, Diesel Particulate Filter functionality depends on maintaining appropriate operating temperatures, as suboptimal loads prevent the achievement of necessary temperatures, leading to filter blockage. The fourth critical factor relates to emissions management. Complete fuel combustion, achieved through proper loading, delivers several important benefits: it reduces particulate matter emissions, ensures compliance with environmental standards, and enhances overall environmental performance metrics.

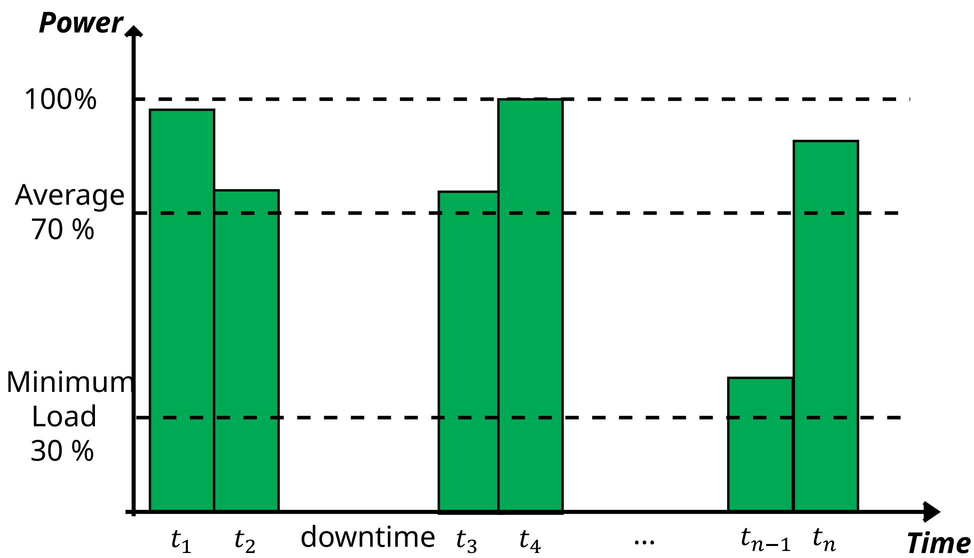


**Figure 4.11:** ISO 8528 standards for Prime Rated Generator

# 5 Conclusion

This chapter establishes a rigorous modeling framework for three key components: the load, represented by the macro base station, and the two main elements of the nanogrid ; the LFP batteries and the diesel generator.

For macro base stations, our power consumption modeling distinguishes between constant components and traffic-dependent elements. By analyzing the Dorval Lodge site data, we derived the hourly load profile using average consumption patterns, providing a practical approach to characterize the consistent temporal variations in DC load, while also developing theoretical models that can be applied regardless of historical data availability. Our energy storage modeling focused on LiFePO4 batteries, revealing 4.63% annual capacity degradation (3.68% cyclic, 0.95% calendar aging for the Installed system). The electro-thermal model establishes a foundation for future HVAC optimization to maintain optimal battery temperatures. The diesel generator model incorporates ISO 8528 standards with 30% minimum load requirements, 70% maximum average load factors, and scheduled maintenance intervals. Fuel consumption calculations demonstrated strong accuracy with 7-8% relative error versus manufacturer specifications.

The next phase of this research will address multi-objective optimization strategies that balance environmental sustainability with economic efficiency. By leveraging these detailed component models, we will develop control algorithms that minimize operational costs and carbon emissions while maintaining the robust reliability essential for BTSs.

## References for Chapter 4


[1] Madhu Dahal, Jagan Shrestha, and Shree Shakya. "Comparison & Measurement of Energy Efficiency of Micro and Macro Base Stationsin Nepal Using Regression Model". In: *Journal of Green Engineering* 7 (Jan. 2018), pp. 505–526. DOI: 10.13052/jge1904-4720.743.

[2] Margot Deruyck, Emmeric Tanghe, Wout Joseph, et al. "Characterization and optimization of the power consumption in wireless access networks by taking daily traffic variations into account". In: *EURASIP Journal on Wireless Communications and Networking* 2012 (Aug. 2012). DOI: 10.1186/1687-1499-2012-248.

[3] Gunther Auer, Vito Giannini, Claude Desset, et al. "How much energy is needed to run a wireless network?" In: *IEEE Wireless Communications* 18.5 (2011), pp. 40–49. DOI: 10.1109/MWC.2011.6056691.

[4] Longbiao Chen, Dingqi Yang, Daqing Zhang, et al. "Deep mobile traffic forecast and complementary base station clustering for C-RAN optimization". In: *Journal of Network and Computer Applications* 121 (Nov. 2018), pp. 59–69. ISSN: 10848045. DOI: 10.1016/j.jnca.2018.07.015.

[5] Gunther Auer, Oliver Blume, and Vito Giannini. *Energy efficiency analysis of the reference systems, areas of improvements and target breakdown*. Dec. 2010, pp. 1–68. URL: https://bscw.ict-earth.eu/pub/bscw.cgi/d71252/EARTH_WP2_D2.3_v2.pdf.

[6] Oliver Arnold, F. Richter, G. Fettweis, et al. "Power Consumption Modeling of Different Base Station Types in Heterogeneous Cellular Networks". In: July 2010, pp. 1–8. ISBN: 978-0201896831.

[7] Shuo Wang, Xing Zhang, Jiaxin Zhang, et al. "An Approach for Spatial-Temporal Traffic Modeling in Mobile Cellular Networks". In: IEEE, Sept. 2015, pp. 203–209. ISBN: 978-1-4673-8422-3. DOI: 10.1109/ITC.2015.31.

[8] M.A. Hannan, M.S.H. Lipu, A. Hussain, et al. "A review of lithium-ion battery state of charge estimation and management system in electric vehicle applications: Challenges and recommendations". In: *Renewable and Sustainable Energy Reviews* 78 (Oct. 2017), pp. 834–854. ISSN: 13640321. DOI: 10.1016/j.rser.2017.05.001.

[9] E. Sarasketa-Zabala, I. Gandiaga, L.M. Rodriguez-Martinez, et al. "Calendar ageing analysis of a LiFePO4/graphite cell with dynamic model validations: Towards realistic lifetime predictions". In: *Journal of Power Sources* 272 (Dec. 2014), pp. 45–57. ISSN: 03787753. DOI: 10.1016/j.jpowsour.2014.08.051.

[10] Madeleine Ecker, Jochen B. Gerschler, Jan Vogel, et al. "Development of a lifetime prediction model for lithium-ion batteries based on extended accelerated aging test data". In: *Journal of Power Sources* 215 (Oct. 2012), pp. 248–257. ISSN: 03787753. DOI: 10.1016/j.jpowsour.2012.05.012.

[11] Yaling Wu, Zhongbing Liu, Benjia Li, et al. "Energy management strategy and optimal battery capacity for flexible PV-battery system under time-of-use tariff". In: *Renewable Energy* 200 (Nov. 2022), pp. 558–570. ISSN: 0960-1481. DOI: 10.1016/J.RENENE.2022.09.118.

[12] Maik Naumann, Michael Schimpe, Peter Keil, et al. "Analysis and modeling of calendar aging of a commercial LiFePO4/graphite cell". In: *Journal of Energy Storage* 17 (June 2018), pp. 153–169. ISSN: 2352152X. DOI: 10.1016/j.est.2018.01.019.

[13] "Temperature effect and thermal impact in lithium-ion batteries: A review". In: *Progress in Natural Science: Materials International* 28 (6 Dec. 2018), pp. 653–666. ISSN: 1002-0071. DOI: 10.1016/J.PNSC.2018.11.002.

[14] Ronan German, Anatole Desreveaux, and Alain Bouscayrol. "Single Cell Electro-Thermal Model for Simulation of an Electric Vehicle". In: IEEE, Aug. 2018, pp. 1–5. ISBN: 978-1-5386-6203-8. DOI: 10.1109/VPPC.2018.8605040.

[15] Ronan German, Seima Shili, Anatole Desreveaux, et al. "Dynamical Coupling of a Battery Electro-Thermal Model and the Traction Model of an EV for Driving Range Simulation". In: *IEEE Transactions on Vehicular Technology* 69 (1 Jan. 2020), pp. 328–337. ISSN: 0018-9545. DOI: 10.1109/TVT.2019.2955856.

[16] Ali M. Eltamaly and Mohamed A. Mohamed. *Optimal Sizing and Designing of Hybrid Renewable Energy Systems in Smart Grid Applications*. 2018. DOI: 10.1016/B978-0-12-813185-5.00011-5.

[17] Chaouki Ghenai and Maamar Bettayeb. "Modelling and performance analysis of a stand-alone hybrid solar PV/Fuel Cell/Diesel Generator power system for university building". In: *Energy* 171 (Mar. 2019), pp. 180–189. ISSN: 03605442. DOI: 10.1016/j.energy.2019.01.019.

*"Not everything that can be counted counts, and not everything that counts can be counted"*

Albert Einstein (1879 - 1955)

# 5

# Refined TMY Data Generation Method

## Contents



## 1 Introduction

The common approach for optimally sizing microgrids, especially those incorporating intermittent renewable energy sources such as PV panels and wind turbines, begins with the meticulous collection and curation of meteorological data. For instance, the estimation of power generation from PV modules is primarily dependent upon three parameters: DNI, DHI and ambient temperature. As a result, the uncertainty associated with the optimal design solutions is fundamentally linked to the uncertainty of these input parameters. We emphasize that numerous recent studies, that aim to attain the optimal sizing of microgrids, employ a consistent hypothesis. This involves either selecting a specific meteorological year [1]–[5] or constructing the average hourly profile [6], [7] of the input parameters. Subsequently, the objective functions spanning the project's lifetime are delineated. Generally, it is presumed that we will observe identical output values of the objective functions for all the years within the project's lifetime horizon. This assumption not only reduces computational time but also yields feasible solutions. It's noteworthy that a considerable degree of parameter variability is lost when the data from a specific year is selected or when only the fluctuation of the average is taken into account. Furthermore, this approach compromises the reliability of the Microgrid, as evidenced [8], The study indicates that by extending the duration of simulation periods, the reliability of Renewable Energy Systems can be significantly enhanced. Moreover, the configurations derived from these extended simulations can demonstrate a robustness that is up to 94% greater than those obtained using a single year of data. The coefficient of interannual variability COV is a statistical measure that is frequently employed to quantify the degree of variability. In the context of solar energy research, the authors of [9] have applied this measure to study the variability of the Global Horizontal Irradiance , a key parameter in solar energy production. Their findings revealed that the COV for the annual average GHI is approximately 3%, indicating a relatively low level of year-to-year variability. However, when they examined the monthly averages, the COV increased to around 5%, suggesting a higher level of variability within each year. It is crucial to emphasize that the observed diversity is profoundly impacted by the ongoing transformations in our climate as demonstrated in the studies [10], [11]. The Typical Meteorological Year (TMY) is a method that captures the enduring variability of weather data for a specific location. The aim is to distill a large amount of weather data, ideally over 30 years [12], [13], into a single year. This year is composed of 12 representative months, known as Typical Meteorological Months (TMMs). Each TMM is selected from a different year and combined to form a complete year. It's important to note that the TMY does not represent extreme conditions. Instead, it reflects the meteorological conditions that are considered typical over a long period[13]. The methodology for constructing the Typical Meteorological Year (TMY) can be broadly classified into three primary categories. Firstly, we have the Stochastic Process Simulation Methods, exemplified by the Monte Carlo method. This approach relies on the generation of random variables to simulate the possible outcomes of a complex process over time. Secondly, we have the Standard Deviation Methods, which include the Danish method [14] and the Weather Year for Energy Calculations (WYEC). These methods focus on the dispersion of a data set and are particularly useful when the

data exhibits a normal distribution. Lastly, we have the Statistical Methods category. Within this category, the most commonly employed method is the Sandia method [15]. This method is renowned for its effectiveness and widespread use in the field [12], [13]. Recent research endeavors have proposed innovative methods to enhance the generation of Typical Meteorological Year TMY data and reduce the average deviation. For instance, the authors of [16] demonstrated that their novel method could decrease the average deviation by 6% when applied to the field of building energy consumption. The novelty of this study lies in the authors' use of an Empirical Mode Decomposition (EEMD) method to filter out abnormal variations in weather data. Consequently, only the low-frequency intrinsic modes were selected in their approach. However, the literature suggests that other methods, such as Variational Mode Decomposition (VMD) [17], [18], offer superior noise resistance, decomposing performance, and stability. Most of the aforementioned methods involve a step where they calculate a short-term component and compare it with a long-term component. The selection criterion for the Typical Meteorological Months (TMMs) is based on the smallest difference between these two components. However, these components are based on weighting factors. While some studies use the weighting factors established by Sandia Model, others assign new weighting factors to each parameter of the dataset [18]–[20]. This discrepancy underscores a lack of consensus regarding the value of meteorological parameter weights when generating TMY data.
This study aims to explore the unutilized potential of applying Principal Component Analysis (PCA) to meteorological parameters. Although the existing literature on this topic is sparse, the method, initially introduced by [21] as the Typical Principal Component Year method (TPCY), has shown to be on par with the Sandia model (TMY). It's noteworthy that the weight assignment in the TPCY method mirrored those utilized in the Sandia model. Our work stands out in its endeavor to extract the TMY that is compatible with microgrids equipped with bifacial modules. The task of estimating the power generation of these systems is intricate and demands a more comprehensive set of meteorological parameters than the standard Global Horizontal Irradiance and ambient temperature used for monofacial modules. A case in point is the albedo, which has a substantial effect on the power production of bifacial panels. The optical bifacial gain can fluctuate between 2.11% and 59.16% as the albedo shifts from 0 to 1 [22]. Another critical parameter, especially in snow-prone climates, is the depth of the snow. The presence of snow can drastically reduce the power production of bifacial panels, potentially causing monthly losses that peak at 100% during winter and annual losses that surpass 30% [23], [24]. Several models [25], [26] incorporate the snow depth parameter to estimate the power production of bifacial panels under snow coverage, highlighting its significance in our study. This research aims to shed light on these overlooked aspects and contribute to the optimal sizing of microgrids that

use bifacial modules.

# 2 Methods

## 2.1 Interannual Variability of the Power Production

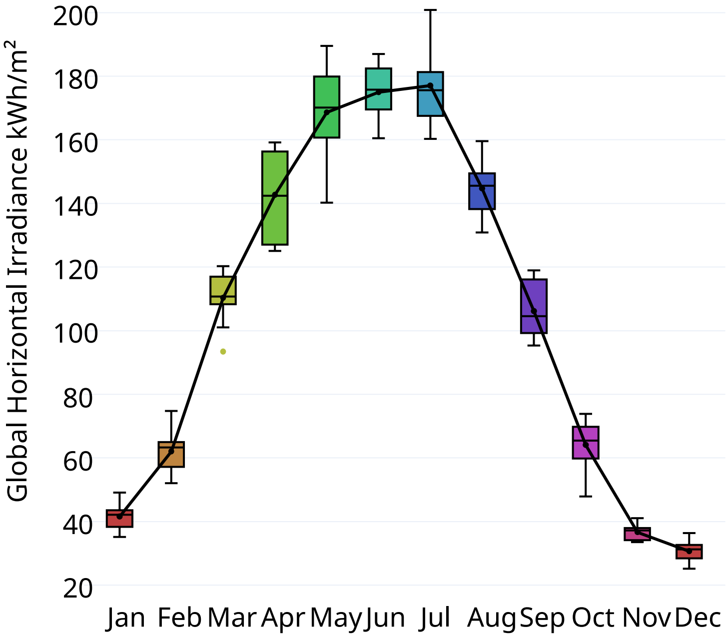


**(a)** Monthly Received Global Horizontal Irradiance GHI at Dorval Lodge. The Monthly Average Values Are Represented with the Black Line.

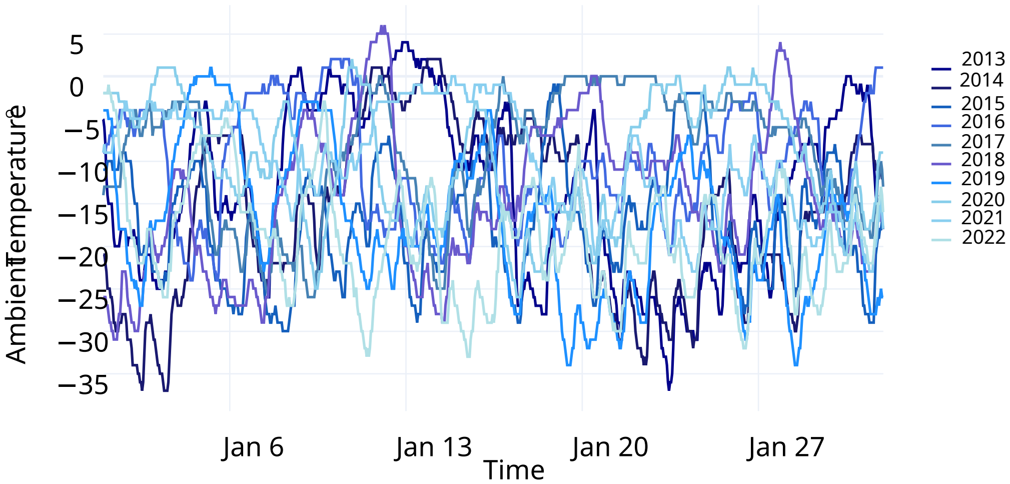


**(b)** Ambient Temperature Variation °$C$ for the Month of January Over a decade (2012-2022)

**Figure 5.1:** Annual Variability of The Meteorological Parameters (a) GHI and (b) Ambient Temperature

The initiation of this section is marked by an emphasis on the repercussions of meteorological data oscillations on the energy yield of bifacial modules. This, in turn, plays a pivotal role in the design of power systems that integrate these modules. Each year is typified by its distinct meteorological traits, such as temperature (Figure. 5.1b) or the monthy received GHI ( Figure 5.1a) . As referenced in the introduction, the methodology of selecting a specific year for the dimensioning of power systems, particularly those that employ bifacial modules, lacks exactitude. This assertion is substantiated by Figure 5.2, which showcases the interannual energy production of the scrutinized Microgrid, composed of 60 bifacial modules (for module specifications, please refer to Tab. 5.1). The energy yield gap can escalate to a maximum of 3.17 MWh, which constitutes approximately 8% (with a fluctuation interval ranging from 7.95% to 8.64%) of the Microgrid's cumulative annual energy production. The meteorological time-series datasets used in this study are sourced from Solcast, a company specializing in high-precision solar energy forecasting and irradiance data services. Solcast's data, which includes real-time, forecast, and historical solar irradiance data, has proven to be more precise compared to other datasets [27], thereby enhancing the accuracy of our study.

| **Parameter** | **Value** |
|---|---|
| Module Name | STA-PV72B SERIES |
| Maximum Power Rating | 365 W |
| Bifacial Factor | 76 % |
| Location | Dorval Lodge |
| Orientation | Portrait |
| Tilt angle | 45 ° |
| Surface Azimuth | 180 ° |
| Height | 2.5 m |
| Number of Rows | 1 |
| Number of Modules | 60 |

**Table 5.1:** Module specifications and system configuration

In our quest to evaluate the power production of bifacial modules and to compute their annual energy yield, we turn to an empirical model, denoted as Equation 5.1 . This model establishes a relationship between power and the total irradiance received. To estimate this total irradiance, we employ a view factor model.

$$P_{bif} = P_{ref}\frac{\Phi_{front} + \beta\Phi_{rear}}{\Phi_{ref}}(1 - \eta(T_{cell} - T_{c,stc})) \tag{5.1}$$

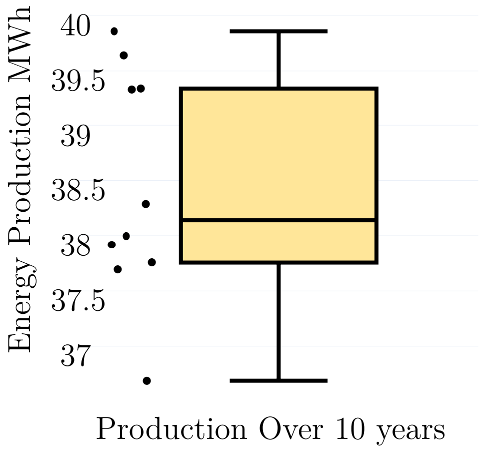


| Year | Energy Production MWh |
|---|---|
| 2013 | 36,68 |
| 2014 | 37,99 |
| 2015 | 39,85 |
| 2016 | 39,63 |
| 2017 | 37,91 |
| 2018 | 37,69 |
| 2019 | 39,32 |
| 2020 | 37,75 |
| 2021 | 39,33 |
| 2022 | 38,28 |

**Figure 5.2:** Impact of Meteorological Data Fluctuations on the Energy Output of the Studied Microgrid (60 Bifacial Modules). Color Scale Based on the Highest Value of Annual Energy (Green).

## 2.2 Principal Component Analysis

The primary aim of this paper is to establish a representative meteorological year by employing Principal Component Analysis. We introduce a novel approach for applying this method to meteorological parameters. To calculate all components of the irradiance received by bifacial modules, it is imperative to consider five meteorological parameters: ambient temperature, Direct Normal Irradiance (DNI), Diffuse Horizontal Irradiance (DHI), Albedo, and Snow Depth. Notably, the latter is utilized to estimate the power output of the Photovoltaic (PV) module under snow coverage conditions.
Let's consider that we have 10 years long data, we construct the matrix for a given parameter $P_j$ for a given month $m_i$ as follows:

$$P_j^{m_i} = \begin{array}{c c} & \begin{array}{ccccc} y_1 & \cdots & y_5 & \cdots & y_{10} \end{array} \\ \begin{array}{c} H_1 \\ \vdots \\ H_5 \\ \vdots \\ H_{end} \end{array} & \begin{pmatrix} p_{[h_1,y_1]} & \cdots & p_{[h_1,y_5]} & \cdots & p_{[h_1,y_{10}]} \\ \vdots & \cdots & \vdots & \cdots & \vdots \\ p_{[h_5,y_1]} & \cdots & p_{[h_5,y_5]} & \cdots & p_{[h_5,y_{10}]} \\ \vdots & \cdots & \vdots & \cdots & \vdots \\ p_{[h_{end},y_1]} & \cdots & p_{[h_{end},y_5]} & \cdots & p_{[h_{end},y_{10}]} \end{pmatrix} \end{array} \tag{5.2}$$

The element $p_{[h_i,y_j]}$ denotes the value of the meteorological parameters at a specific hour, represented by $h_i$, during a particular year, denoted by $y_j$. The concept of Principal Component Analysis involves identifying a new dimensional space that outlines the maximum variance of the matrix (Equation 5.2), using a minimal set of basis vectors $u_i$.

$$\begin{cases} max \sum_{i=1}^{10} (y_i^T u)^2 \\ u^T u = 1 \end{cases} \tag{5.3}$$

By employing the method of Lagrange multipliers, we transform the problem's solution into the task of identifying the eigenvectors of the Covariance Matrix. Subsequently, we sort the principal components according to their eigenvalues $\lambda_i$. The selection process involves choosing those components that contribute to 80% of the cumulative variance. The variance explained by each principal component, denoted as $\sigma_i$, is expressed as follows:

$$\sigma_i = \frac{\lambda_i}{\sum_{i=1}^{10} \lambda_i} \tag{5.4}$$

Each principal component is expressed as a function of the loading factors $e_{i,j}$ :

$$pc_i = \sum_{i=1}^{10} e_i \, y_i \tag{5.5}$$

The correlation between $y_j$ and $pc_i$ is expressed as follows :

$$cor(y_j, pc_i) = e_{i,j} \frac{\sqrt{\lambda_i}}{std_{y_j}} \tag{5.6}$$

Where $std_{y_j}$ is the standard deviation of the vector $y_i$. To construct the representative year, we identify and select the month within a given year that exhibits the highest degree of correlation with the chosen principal components. This process is delineated in Flowchart (Figure 5.3), which provides a comprehensive overview of the steps involved in our proposed methodology.

To select the most representative year for a specific month and a given meteorological parameter, we use the criterion of maximizing $C_{y_i}$, which is the sum of the correlations between the year $i$ and the principal components that explain at least 80% of the cumulative variance, we denote $n$ as the index of the principal component

$$C_{y_i} = \sum_{j=1}^{n} cor(pc_i, y_j) \tag{5.7}$$

However, it is anticipated that we will have a different representative month for each meteorological parameter. Therefore, we assign the same coefficient, in our case 1/5, to each parameter and select the month with the highest sum.

$$S_{y_i} = \sum_{j=1}^{5} \frac{1}{5} C_{y_i} \tag{5.8}$$

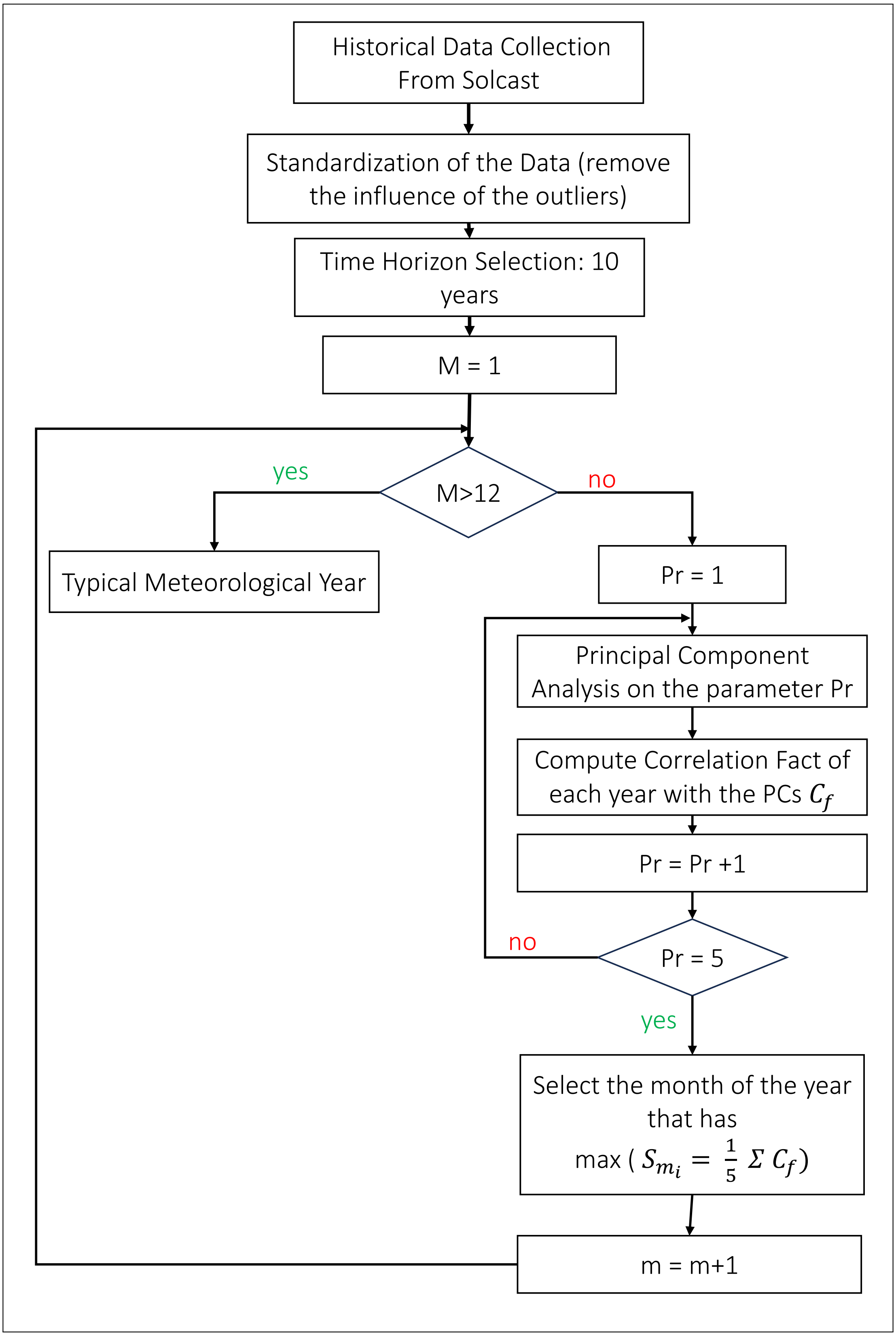


**Figure 5.3:** Flow Chart of The Proposed Methodology

# 3 Results and Discussion

## 3.1 PCA results

We have applied PCA to a set of five parameters. To provide a clearer picture, we've showcased the results of this technique on three key parameters - Temperature, DNI, and Snow depth - specifically for the data collected in January. As depicted in Figure 5.4, applying PCA to the temperature yields 10 principal components. However, we only require the first five components as they capture approximately 80.1% of the temperature variance. The subsequent step involves computing the correlation of each month of the year with these five components, as per Equation (5.6) . Given that we have standardized the dataset, the standard deviation (refer to Flowchart 5.3) is equal to 1. For instance, according to our methodology, the month that best represents the temperature variation is January 2017. For the DNI, we observe that the first component accounts for approximately 39.8% of the variance. The subsequent components contribute less significantly, but we continue until we capture 80% of the variance (Figure 5.5). Consequently, six components are selected, accounting for 82.9% of the variance. The month that best represents the variation in DNI, according to this method, is January 2013. As shown in Figure 5.6, the snow depth parameter can be adequately represented by three components, which account for 88% of the total variance. The first component alone explains 61.4% of the variance, indicating its high importance. The month that best represents the variation in snow depth, January of 2018.

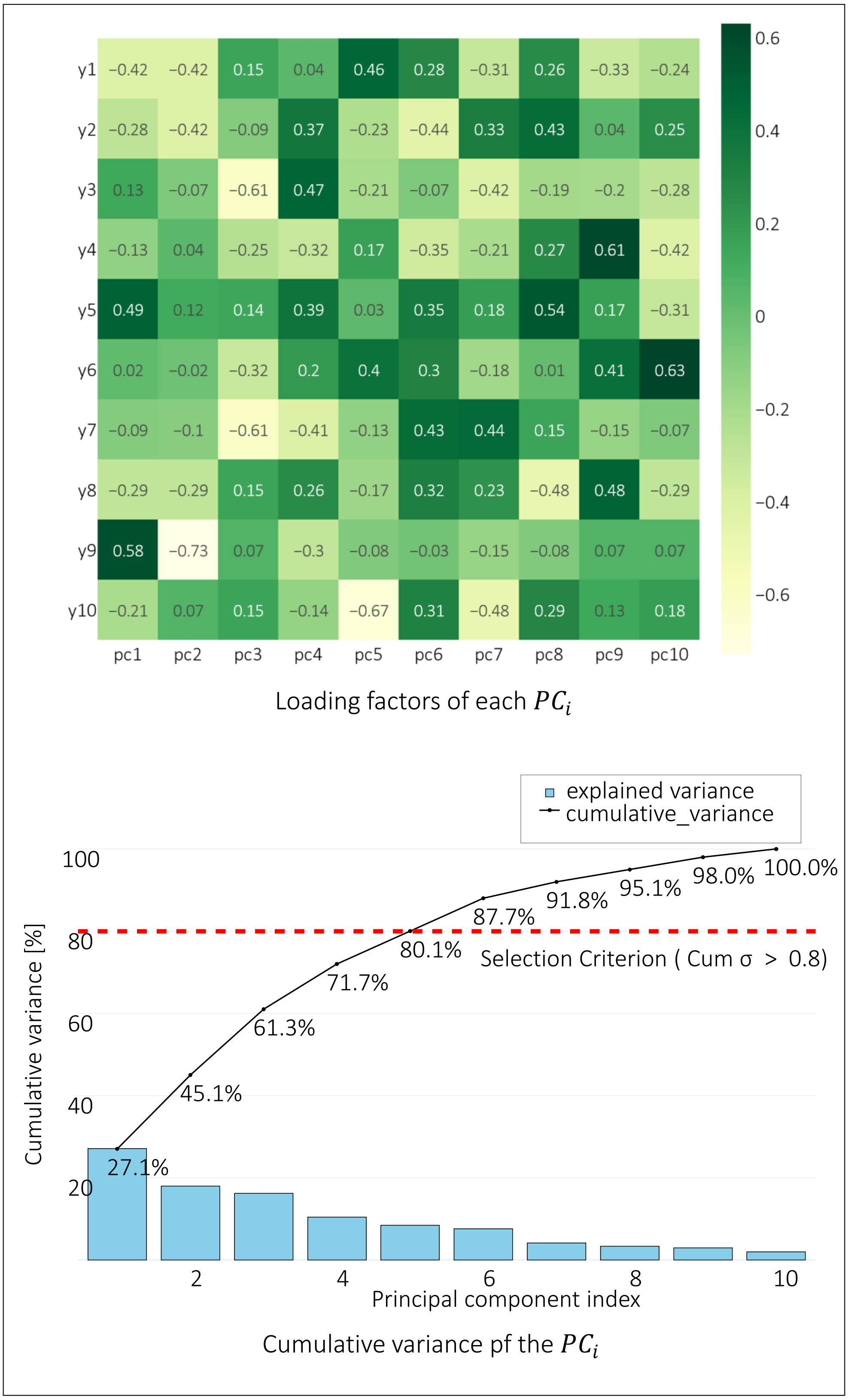


**Figure 5.4:** PCA Applied on the Ambient Temperature °C

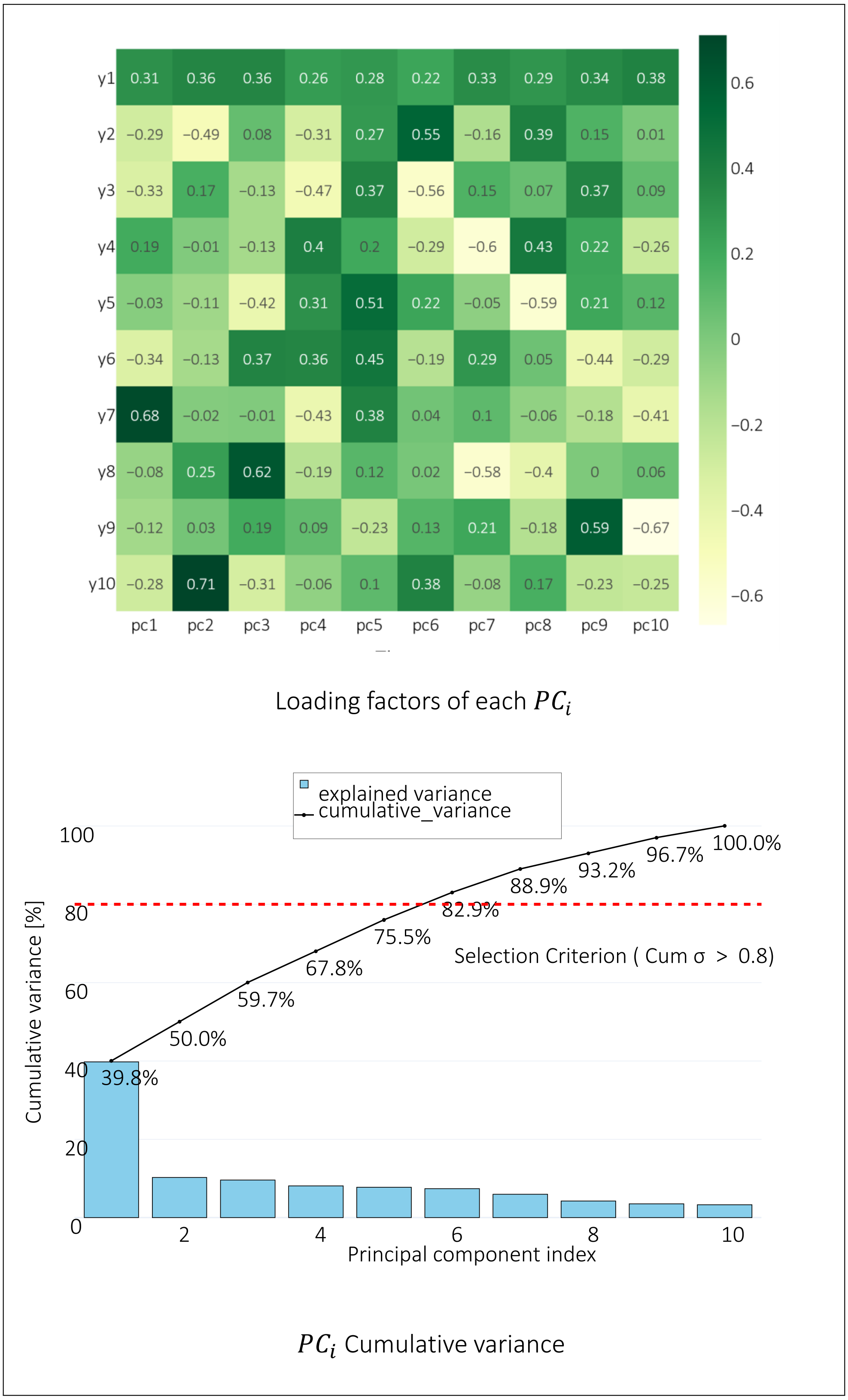


**Figure 5.5:** PCA Applied on the DNI $[W/m^2]$

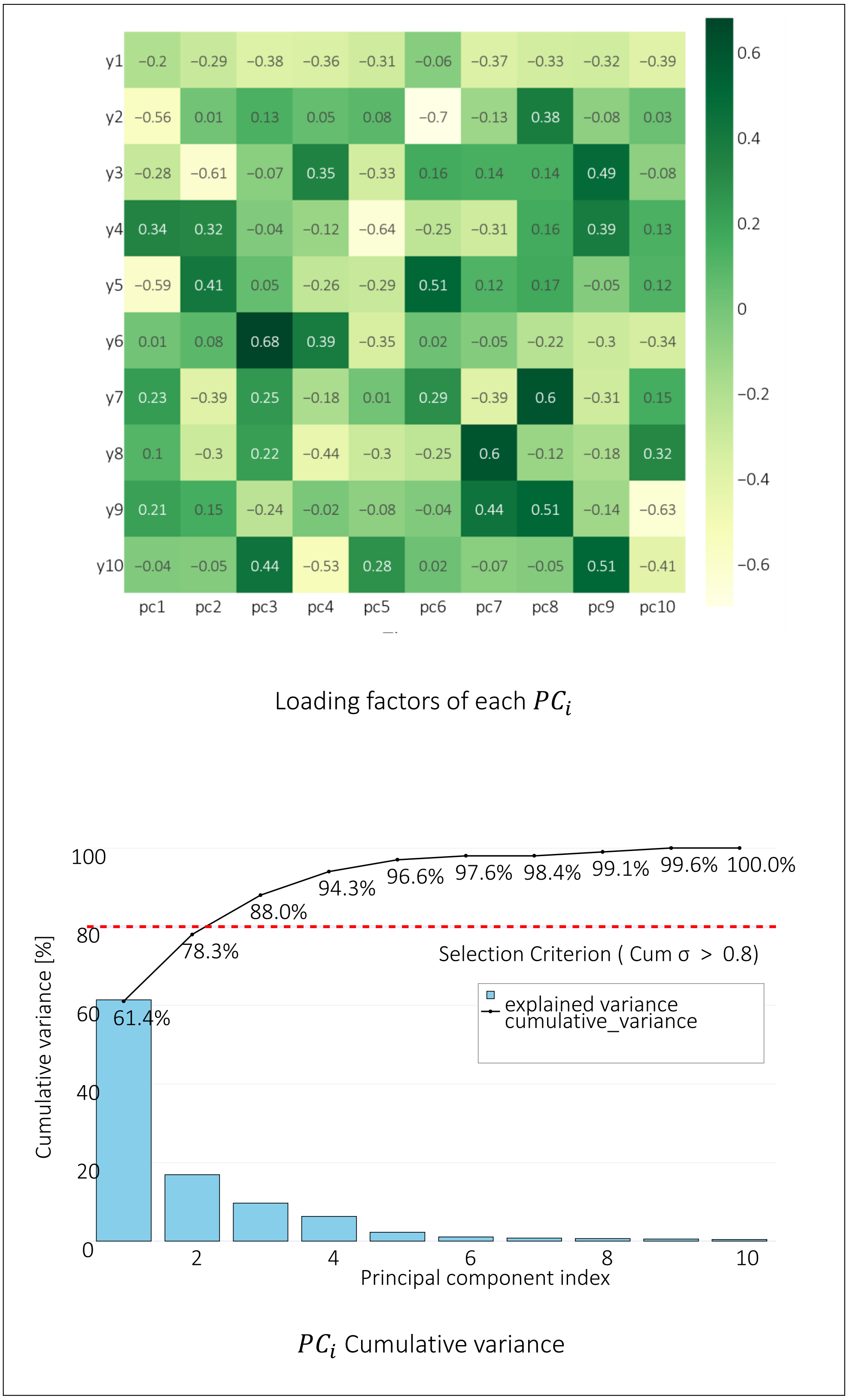


**Figure 5.6:** PCA Applied on the Snow Depth [cm]

## 3.2 Validation

To validate our proposed methodology for generating the Typical Meteorological Year (TMY), we juxtapose it with two established methods from PVSyst: the Sandia method and the NSRDB TMY method (TMY 3). The typical months for each method are delineated in Table 5.2. We proceed to calculate the annual energy yield for a system comprising 60 modules using each of these methods. Our methodology yields an annual energy output of 38.64 MWh. In contrast, the TMY of the Sandia method and the NSRDB TMY method yield 39.52 MWh and 39.32 MWh, respectively. To facilitate a comparative analysis of these results, we employ the z-score metric (Equation 5.9) . This metric quantifies the deviation of a value from the mean of a group of values. The z-scores corresponding to our methodology, the Sandia method, and the NSRDB TMY method are 0.20, 1.10, and 0.89, respectively. These scores are juxtaposed with the interannual energy vector, as illustrated in Figure 5.2.

| TMMs | Proposed Methodology | PVsyst SANDIA | PVsyst NSRDB TMY |
|---|---|---|---|
| January | 2021 | 2013 | 2018 |
| February | 2015 | 2019 | 2014 |
| March | 2013 | 2016 | 2016 |
| April | 2014 | 2020 | 2020 |
| May | 2016 | 2014 | 2016 |
| June | 2013 | 2019 | 2019 |
| Jully | 2013 | 2021 | 2013 |
| August | 2022 | 2016 | 2016 |
| September | 2014 | 2018 | 2018 |
| October | 2013 | 2022 | 2022 |
| November | 2018 | 2013 | 2013 |
| December | 2013 | 2019 | 2019 |

**Table 5.2:** Table of Typical Meteorological Year for Dorval Lodge Over the Decade 2013-2022 With Three Different Methods

$$z = \frac{x - \mu}{S} \tag{5.9}$$

Here $S$ is the standard deviation, $\mu$ is the mean, and $x$ is the value being evaluated. Despite a marginally lower annual energy yield, our methodology aligns more closely with the average interannual energy, as evidenced by its lower z-score. Moreover, our methodology effectively reduces the maximum interannual energy gap from 8% to 5.3%. Conversely, the maximum gaps for the Sandia and NSRDB TMY methods are 7.75% and 7.20%, respectively. This underscores the efficacy of our proposed methodology in providing a more accurate representation of typical meteorological conditions.

## 4 Conclusion

In this chapter, we proposed a methodology that applies principal component analysis to five meteorological variables that influence the power production of bifacial panels: ambient temperature, DNI, DHI, albedo, and snow depth. By selecting the most representative months from a 10-year historical data set based on the correlation between the principal components and the original data, we can generate a TMY data that captures the interannual variability of the meteorological data and reduces the average deviation.

We compared the proposed method with two existing methods from PVSyst: the Sandia method and the NSRDB TMY method (TMY3). We showed that the proposed method yields a lower z-score of 0.20 and a smaller interannual energy gap of 5.3% than the other methods, indicating a closer alignment with the average interannual energy and a higher reliability and accuracy for the optimal sizing and design of microgrids that use bifacial modules. After generating this refined TMY, the next chapter will address the optimization of nanogrid design under this representative year to ensure we've captured the variability of meteorological variables for more accurate results. Before proceeding with optimization, we will conduct a systematic analysis to evaluate the performance of the system under this TMY in terms of both economic and environmental costs. Particularly, the next chapter will focus on how snow accumulation could impact the optimal design of the nanogrid, as snow coverage significantly affects the irradiance received by bifacial panels. This represents a critical aspect often overlooked in traditional TMY approaches but essential for regions with seasonal snow coverage.

## References for Chapter 5


[1] Ahmad Alzahrani, Muhammad Arsalan Hayat, Asif Khan, et al. "Optimum sizing of stand-alone microgrids: Wind turbine, solar photovoltaic, and energy storage system". In: *Journal of Energy Storage* 73 (Dec. 2023), p. 108611. ISSN: 2352-152X. DOI: 10.1016/J.EST.2023.108611.

[2] Daniele Colarossi and Paolo Principi. "Optimal sizing of a photovoltaic/energy storage/cold ironing system: Life Cycle cost approach and environmental analysis". In: *Energy Conversion and Management* 291 (Sept. 2023), p. 117255. ISSN: 0196-8904. DOI: 10.1016/J.ENCONMAN.2023.117255.

[3] "Optimal Sizing of On-site Renewable Resources for Offshore Microgrids". In: (Aug. 2023). DOI: 10.1109/NAPS58826.2023.10318718.

[4] "Multi-objective optimization minimizing cost and life cycle emissions of stand-alone PV–wind–diesel systems with batteries storage". In: *Applied Energy* 88 (11 Nov. 2011), pp. 4033–4041. ISSN: 0306-2619. DOI: 10.1016/J.APENERGY.2011.04.019.

[5] "Multi-objective optimization of campus microgrid system considering electric vehicle charging load integrated to power grid". In: *Sustainable Cities and Society* 98 (Nov. 2023), p. 104778. ISSN: 2210-6707. DOI: 10.1016/J.SCS.2023.104778.

[6] El Manaa Barhoumi. "Optimal design of standalone hybrid solar-wind energy systems for hydrogen-refueling station Case study". In: *Journal of Energy Storage* 74 (Dec. 2023), p. 109546. ISSN: 2352-152X. DOI: 10.1016/J.EST.2023.109546.

[7] Qi Chen, Zhonghong Kuang, Xiaohua Liu, et al. "Optimal sizing and techno-economic analysis of the hybrid PV-battery-cooling storage system for commercial buildings in China". In: *Applied Energy* 355 (Feb. 2024), p. 122231. ISSN: 0306-2619. DOI: 10.1016/J.APENERGY.2023.122231.

[8] Muhammad Shahzad Javed, Jakub Jurasz, Mohammad Guezgouz, et al. "Impact of multi-annual renewable energy variability on the optimal sizing of off-grid systems". In: *Renewable and Sustainable Energy Reviews* 183 (Sept. 2023), p. 113514. ISSN: 1364-0321. DOI: 10.1016/J.RSER.2023.113514.

[9] "Consequences of neglecting the interannual variability of the solar resource: A case study of photovoltaic power among the Hawaiian Islands". In: *Solar Energy* 167 (June 2018), pp. 61–75. ISSN: 0038-092X. DOI: 10.1016/J.SOLENER.2018.03.085.

[10] Shuo Wang, Jinxin Zhu, Gordon Huang, et al. "Assessment of climate change impacts on energy capacity planning in Ontario, Canada using high-resolution regional climate model". In: *Journal of Cleaner Production* 274 (Nov. 2020), p. 123026. ISSN: 0959-6526. DOI: 10.1016/J.JCLEPRO.2020.123026.

[11] Charles Fant, C. Adam Schlosser, and Kenneth Strzepek. "The impact of climate change on wind and solar resources in southern Africa". In: *Applied Energy* 161 (Jan. 2016), pp. 556–564. ISSN: 0306-2619. DOI: 10.1016/J.APENERGY.2015.03.042.

[12] William Marion and Ken Urban. *User's Manual for TMY2s (Typical Meteorological Years) - Derived from the 1961-1990 National Solar Radiation Data Base*. June 1995. DOI: 10.2172/87130.

[13] "Users manual for TMY3 data sets". In: (2008).

[14] Haixiang Zang, Qingshan Xu, Wei Wang, et al. "A step-by-step application of Danish method for generation of typical meteorological years of China". In: *Journal of Renewable and Sustainable Energy* 5 (5 Sept. 2013). ISSN: 19417012. DOI: 10.1063/1.4826193/286279.

[15] I J Hall, R R Prairie, H E Anderson, et al. "Generation of a typical meteorological year". In: (Jan. 1978). URL: https://ntrl.ntis.gov/NTRL/dashboard/searchResults/titleDetail/SAND781096C.xhtml.

[16] Xinying Fan. "A method for the generation of typical meteorological year data using ensemble empirical mode decomposition for different climates of China and performance comparison analysis". In: (2021). DOI: 10.1016/j.energy.2021.122822.

[17] Hui Liu, Guangxi Yan, Zhu Duan, et al. "Intelligent modeling strategies for forecasting air quality time series: A review". In: *Applied Soft Computing* 102 (Apr. 2021), p. 106957. ISSN: 1568-4946. DOI: 10.1016/J.ASOC.2020.106957.

[18] Konstantin Dragomiretskiy and Dominique Zosso. "Variational Mode Decomposition". In: *IEEE Transactions on Signal Processing* 62 (3 Feb. 2014), pp. 531–544. ISSN: 1053-587X. DOI: 10.1109/TSP.2013.2288675.

[19] T. Kershaw, M. Eames, and D. Coley. "Comparison of multi-year and reference year building simulations". In: *http://dx.doi.org/10.1177/0143624410374689* 31 (4 Aug. 2010), pp. 357–369. ISSN: 01436244. DOI: 10.1177/0143624410374689.

[20] I. A. Rahman and J. Dewsbury. "Selection of typical weather data (test reference years) for Subang, Malaysia". In: *Building and Environment* 42 (10 Oct. 2007), pp. 3636–3641. ISSN: 0360-1323. DOI: 10.1016/J.BUILDENV.2006.10.004.

[21] "A new method to develop typical weather years in different climates for building energy use studies". In: *Energy* 36 (10 Oct. 2011), pp. 6121–6129. ISSN: 0360-5442. DOI: 10.1016/J.ENERGY.2011.07.053.

[22] Mohammad Hassan Shahverdian, Hoseyn Sayyaadi, and Ali Sohani. "An optical-based comparative study to detect best configurations for installation of monofacial and bifacial PV technologies". In: *Solar Energy* 266 (Dec. 2023), p. 112184. ISSN: 0038-092X. DOI: 10.1016/J.SOLENER.2023.112184.

[23] "Identifying snow in photovoltaic monitoring data for improved snow loss modeling and snow detection". In: *Solar Energy* 223 (July 2021), pp. 238–247. ISSN: 0038-092X. DOI: 10.1016/J.SOLENER.2021.05.023.

[24] Robert E. Pawluk, Yuxiang Chen, and Yuntong She. "Photovoltaic electricity generation loss due to snow – A literature review on influence factors, estimation, and mitigation". In: *Renewable and Sustainable Energy Reviews* 107 (June 2019), pp. 171–182. ISSN: 13640321. DOI: 10.1016/j.rser.2018.12.031.

[25] "Measured and modeled photovoltaic system energy losses from snow for Colorado and Wisconsin locations". In: *Solar Energy* 97 (Nov. 2013), pp. 112–121. ISSN: 0038-092X. DOI: 10.1016/J.SOLENER.2013.07.029.

[26] Tim Townsend and Loren Powers. "Photovoltaics and snow: An update from two winters of measurements in the SIERRA". In: IEEE, June 2011, pp. 003231–003236. ISBN: 978-1-4244-9965-6. DOI: 10.1109/PVSC.2011.6186627.

[27] Jamie M. Bright. "Solcast: Validation of a satellite-derived solar irradiance dataset". In: *Solar Energy* 189 (Sept. 2019), pp. 435–449. ISSN: 0038092X. DOI: 10.1016/j.solener.2019.07.086.

*"The game of science is, in principle, without end. He who decides one day that scientific statements do not call for any further test, and that they can be regarded as finally verified, retires from the game."*

Karl Popper (1902 - 1994), "The Logic of Scientific Discovery."

# 6
# Nanogrid Optimization

## Contents

# 1 Impact of Snow on the Optimal Design

Following our analysis of meteorological parameter temporal variability through principal component analysis in response to the first research question, we now turn our attention to the second research objective: examining snow's impact on system optimal design. This chapter presents a detailed investigation of this phenomenon and proposes methodological approach to incorporate its effects into the optimization framework.

## 1.1 Optimization Problem Formulation

The aim of this research endeavor is to reduce the economic cost and mitigate the environmental impact of the hybrid system by minimizing two distinct objective functions. These functions include the life cycle cost function, which assesses the economic cost of the system, and the environmental impact function, which evaluates the effect of the system on the environment. To that end, this study solely accounts for one of the prominent greenhouse gases, namely, carbon dioxide that is discharged during the operation of the diesel generator. Moreover, the continuous supply of the base station is a crucial constraint that needs to be fulfilled, which necessitates a reduction of the loss of power supply probability. In the rest of this section, we will present the objective functions that correspond to each sub-system. In continuation of this section, we will introduce the objective functions that pertain to each sub-system. In this study we can reformulate the problem as a multi-objective optimization problem (MOOP) that has two objectives $f_{lcc}$ and $f_{CO_2}$ :

$$
\begin{aligned}
\min_{X_{design}} \quad & (f_{lcc} = LCC_{bat} + LCC_{pv} + LCC_{gen}, \quad f_{CO_2}) \\
\text{s.t.} \quad & 0 \leq LPSP \leq 0.0001\% \\
& 0 < P_{gen,r} \leq P_{gen,max} \\
& Q_{min} \leq Q_{bat} \leq Q_{max} \\
& N_{pv,min} < N_{pv} \leq N_{pv,max} \\
& 0\% \leq SOC \leq 100\% \\
& \frac{P_{bbu}}{\eta_{dc}} + \frac{P_{cool}}{\eta_{inv}} = \epsilon P_{gen} + P_{bif}\eta_{scc} + P_{bat} \\
& \epsilon = \begin{cases} 1 & \text{if} \quad SOC \leq Thr_{min} \; (i_{bat} < 0) \\ 0 & \text{if} \quad Thr_{max} \leq SOC \end{cases}
\end{aligned}
\tag{6.1}
$$

Upon reaching their minimum state of charge, the batteries activate the generator to supply power to the system, irrespective of whether the bifacial panels can generate adequate energy or not. While this implementation strategy is not without its shortcomings, such as an over-reliance on non-renewable energy sources, it does confer a high degree of system reliability. Consequently, the state of charge during the charging phase can be accurately expressed as:

$$SOC(t) = SOC(t-1) + \tfrac{1}{Q_{bat}} \left( \epsilon P_{gen}(t) - \tfrac{P_{bbu}(t)}{\eta_{dc}} - \tfrac{P_{ac}(t)}{\eta_{ac}} + P_{bif}(t)\eta_{scc} \right) \tfrac{1}{u_{dc}} \Delta t \quad (6.2)$$

$$P_{gen}(t) = min\left(C_{rate} i_{max} v_{ac}, P_{gen,r}\right) \quad (6.3)$$

During the discharging process, the batteries are supplying power to the station, working in conjunction with the bifacial panels. Consequently, the state of charge (SOC) is determined by the given expression :

$$SOC(t) = SOC(t-1) + \frac{1}{Q_{bat}} \left( P_{bif}(t)\eta_{scc} - \frac{P_{bbu}(t)}{\eta_{dc}} - \frac{P_{ac}(t)}{\eta_{ac}} \right) \frac{1}{u_{dc}} \Delta t \quad (6.4)$$

### 1.1.1 Life Cycle Cost Function

Within the life cycle cost function of each sub-system, our analysis takes into account three key components: the initial cost, the operating and maintenance expenses, and the replacement cost over the system's lifespan. In regards to the latter, we base our assessment on the expected lifespan of the panels. We started with the bifacial modules, the LCC function associated with this sub-system is :

$$LCC_{bif} = LCC_{bif,i} + LCC_{bif,m} + LCC_{bif,r} \quad (6.5)$$

$$LCC_{bif,i} = 1.3\ C_{u,bif} N_{PV} \quad (6.6)$$

To account for all components apart from the PV modules, which is known as the balance of system (BOS), a 30% markup was incorporated into the cost of PV panels . Considering that each solar converter supports ten bifacial modules, thus the initial cost of the needed converters is :

$$C_{i,scc} = C_{u,scc} \left[ \frac{N_{pv}}{10} \right] \quad (6.7)$$

Assuming that the solar charger will be replaced twice during the project's lifetime, we can calculate the replacement cost of the converter by taking into account the reduction in present value. This can be done by multiplying the acquisition price of the converter by the present worth factor as shown in the equation below:

$$RC = \sum_{j=1}^{N_{rep}} C_u C_{comp} \quad PVF^{\frac{nj}{N_{rep}+1}} \tag{6.8}$$

$$PVF = \left(\frac{1+i}{1+d}\right) \tag{6.9}$$

Thus the LCC function of the bifacial panels with 25 years project lifetime is :

$$LCC_{bif} = 1.3C_{u,bif}P_{bif,r} + C_{i,scc}(1 + PVF^{\frac{25}{3}} + PVF^{\frac{50}{3}}) \tag{6.10}$$

With the same approach we can deduce the LCC function of the energy storage system :

$$LCC_{bat} = Q_{bat}C_{u,bat}(1 + \sum_{j=1}^{N_{rep}} PVF^{\frac{25j}{N_{rep}+1}}) \tag{6.11}$$

To illustrate, let us examine the existing configuration of the system (Table 6.3 ). Here, the State of Health (SOH) scrap value is set at 60%. By employing the currently implemented strategy, it is projected that the batteries will attain their end-of-life phase following a duration of approximately 13 years. Figure 6.1 illustrates the cycle count over a one-year period.

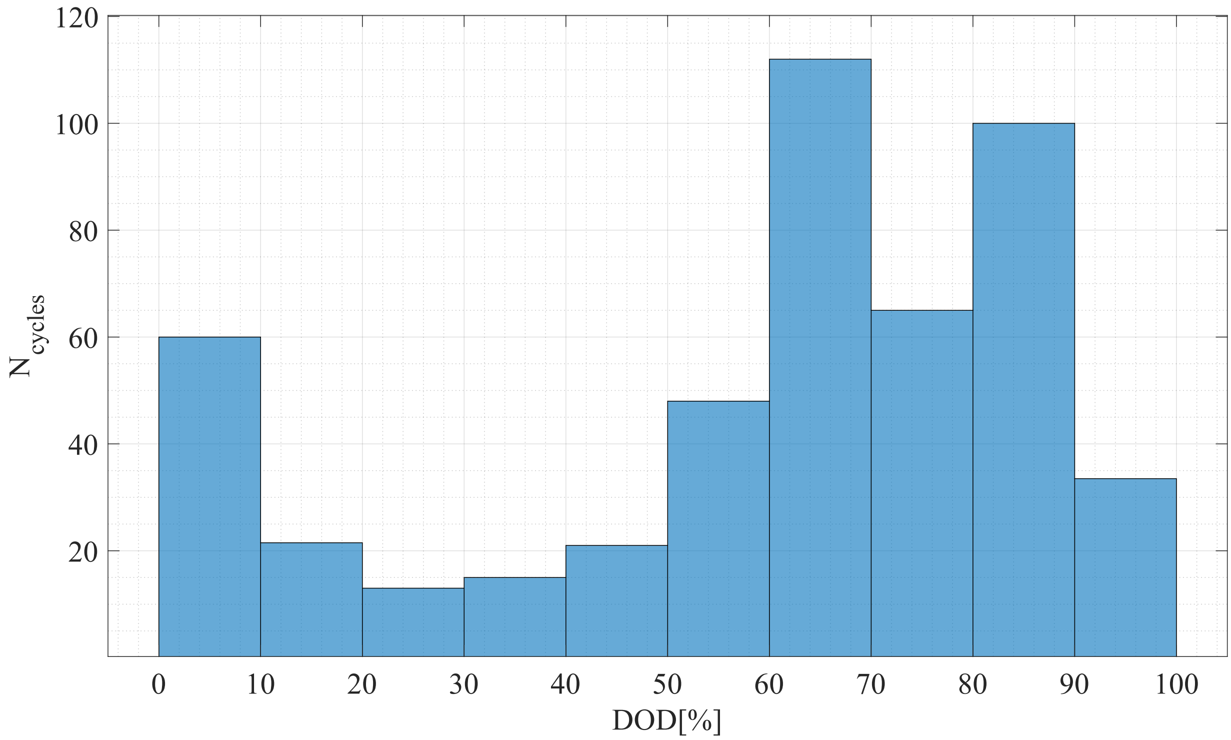


**Figure 6.1:** Number of Cycles versus the Depth of Discharge using the Rainflow Method

The last power source is the diesel generator, over the project lifetime we assume that two replacements will occur. In addition, the OPEX will be accounted for, and the hourly fuel consumption will be the sole origin of such costs. The purchase of diesel fuel is planned for the beginning of each year, the actualization factor is:

$$ACF = PVF * \frac{1 - PVF^n}{1 - PVF} \tag{6.12}$$

Hence, the life cycle cost function of the generator can be determined by this equation :

$$LCC_{gen} = P_{gen} C_{gen,u} (1 + PVF^{\frac{25}{3}} + PVF^{\frac{50}{3}}) + ACF \sum_{i=0}^{8760} (\alpha_0 P_{gen,i} + \alpha_1 P_{gen,r}) \tag{6.13}$$

### 1.1.2 Carbon Emission Function

The objective of this study is to reduce the environmental impact of the hybrid system in the sizing phase, and here we aim to reduce the production of carbon dioxide, we estimate the hourly emission based on the equation of the fuel consumption 4.14, thus the carbon emission can be estimated as follows :

$$f_2 = \alpha_{CO_2} F_{gen,i} \tag{6.14}$$

### 1.1.3 Loss of Power Supply Probability

The use of hybrid systems for supplying telecom base stations is subject to a constraint aimed at guaranteeing high reliability. To this end, we employ the LPSP metric to assess the probability of incurring complete or partial losses over a one-year timeframe. We impose a limit of 0.001% on the LPSP value to ensure the system's reliability meets the required standard.

$$LPSP = \frac{\sum_{t=0}^{8760} D_f(t)}{\sum_{t=0}^{8760} P_{macro}(t)} \tag{6.15}$$

$$d(t) = (P_{macro}(t) - \epsilon P_{gen}(t) P_{bif}(t) \mu_{scc} - P_{bat}(t)) \tag{6.16}$$

$$D_f(t) = \begin{cases} d(t) & \text{if} \quad d(t) \geq 0 \\ 0 & \text{if} \quad d(t) < 0 \end{cases} \tag{6.17}$$

Table 6.1 contains a comprehensive list of all parameter values that are presented in the reformulation of the optimization problem.

| Parameter | Value |
| --- | --- |
| Inflation rate | 4% |
| Discount rate | 10% |
| Fuel price per liter | 1 $ per liter |
| Unit price of the battery | 57 $/Ah |
| Unit price of the bifacial modules | 0.77 $/W |
| Unit price of diesel generator | 500 $/kW |
| Price of solar charge controller | 2,000$ |
| Price of the inverter charger | 8,000$ |
| Price of the diesel generator starter | 200$ |
| Efficiency of the solar charger | 95 % |
| Efficiency of the inverter charger | 93% |
| Efficiency of the chopper | 84% |
| Minimum battery state of charge | 15 % |
| Maximum Battery state of charge | 100 % |

**Table 6.1:** Value of the Parameters used in the Reformulation of the Optimization Problem

### 1.2 Systematic Analysis

After developing our nanogrid model and establishing the objective functions and constraints, we proceed with a comprehensive evaluation of different system architectures using two primary assessment criteria: economic and environmental performance. The economic assessment utilizes the LCOE and LCC metrics, which collectively represent the total expenditure associated with electricity production and distribution throughout the system's operational lifespan. For environmental performance, we measure carbon emissions and wasted renewable energy, which serve as indicators of the system's climate impact and efficiency of resource utilization. Additionally, we incorporate the LPSP as a key metric to evaluate the system's reliability and operational efficiency.
In this systematic analysis, we have maintained constant control variables while methodically varying the design variables. For battery storage, we examine configurations ranging from 0 to 20 batteries, each with a unit capacity of 130 Ah. For the diesel generator component, we investigate rated power outputs spanning from 0 to 100 kW. Similarly, for photovoltaic generation, we consider installations of bifacial modules ranging from 0 to 200 units. To ensure thorough coverage of the design space, we divide each decision variable interval into 100 equidistant points and employ interpolation techniques to characterize the behavior of the objective function across the surfaces between these discrete points.

- **Diesel Generator and Bifacial Modules Topology :**

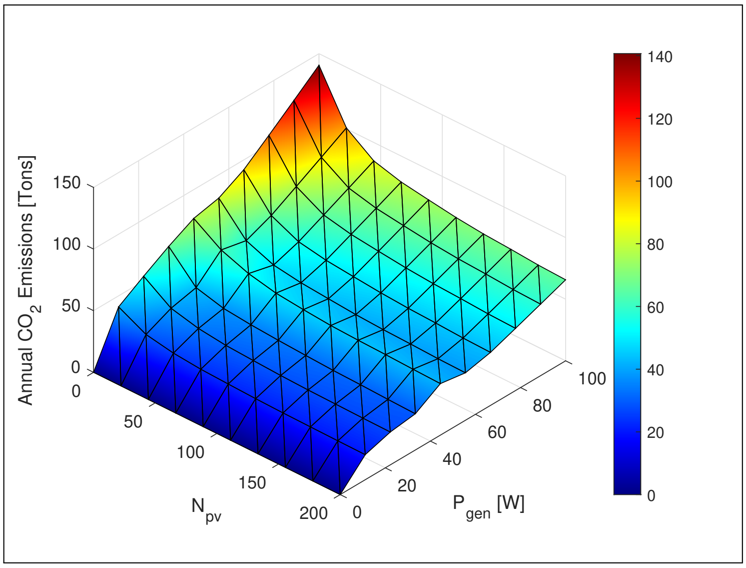


(a) Annual $CO_2$ Emissions

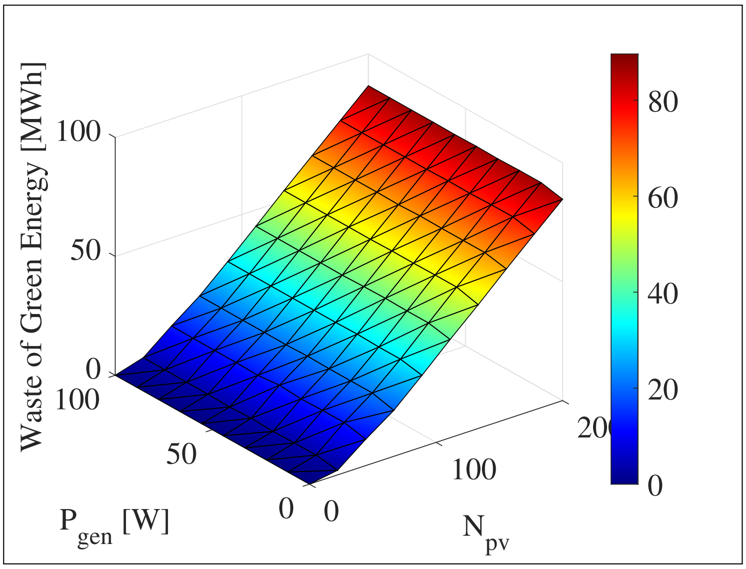


(b) Energy Waste

**Figure 6.2:** Enviromental Performance of The PV/GEN Topology

Regarding the environmental impact of this configuration, several significant observations emerge from our analysis of the environmental function variations. Notably, the quantity of wasted energy demonstrates a proportional relationship with the number of installed bifacial modules. This correlation exists primarily due to the absence of direct storage capacity in the system, resulting in surplus energy that cannot be effectively utilized or stored during periods of high generation (Reached 90MWh for 200 Bifacial Modules, Figure 6.2a). Concurrently, our analysis reveals that carbon emissions increase in direct proportion to the rated power of the diesel generator (Figure 6.2b).

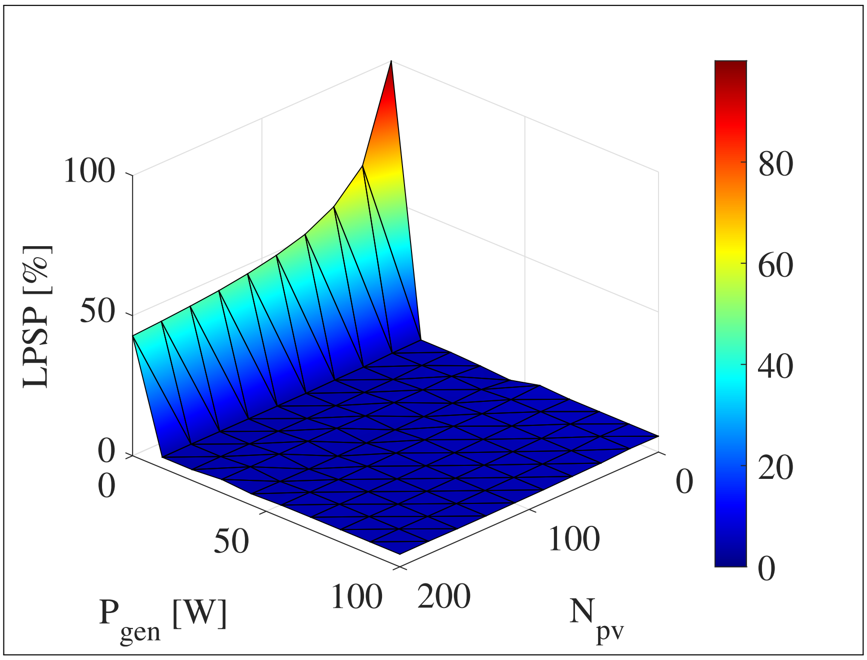


**Figure 6.3:** LPSP [%]

To comprehensively evaluate this configuration, we must assess its reliability performance. By plotting the LPSP variation as a function of the design variables, we identify that the minimum LPSP value achievable with this topology is approximately 3.9% (Figure 6.3). This value significantly exceeds the stringent LPSP constraint established in the previous section, which requires a maximum LPSP of 0.0001%. This substantial disparity indicates that the current configuration falls considerably short of meeting the reliability requirements essential for BTS Stations. Furthermore, we notice from Figure 6.3 that the LPSP exhibits minimal variation for generator capacities exceeding 10kW. This important observation suggests that rather than utilizing the current 20kW rated power diesel generator, a 10kW generator could potentially deliver comparable reliability performance. This finding presents an opportunity for system optimization, potentially reducing both capital expenditure and environmental impact without significantly compromising system reliability. Regarding the economical performance of this topology the maximum value of LCC AND LCOE are 90 $10^4$ \$ and 2.7 $\$/kWh$ respectively.

- **Bifacial Modules and LFP Batteries :**

This configuration represents the most ecological option within our analysis framework, and according to the Homer Pro evaluation presented in the earlier chapter, it could theoretically achieve a renewable energy fraction of 99%. However, our systematic analysis incorporating bifacial modules reveals that the minimum LPSP value attainable with this configuration is approximately 4.5%, as illustrated in Figure 6.4a . This significant discrepancy underscores the necessity of integrating backup power sources such as diesel generators to meet reliability requirements. These findings effectively demonstrate the limitations inherent in the Homer Pro modeling approach. An additional noteworthy observation pertains to the management of surplus renewable energy. Even with the integration of Energy Storage Systems (ESS), the maximum reduction in wasted energy amounts to only 10MWh from a baseline of 80MWh (Figure 6.4b). This modest improvement highlights substantial inefficiencies in the current energy management strategy. Regarding the economical performance of this topology the maximum value of LCC AND LCOE are 32 $10^4$ \$ and 1.32 $\$/kWh$ respectively, this topology represets the most economical and ecological solution.

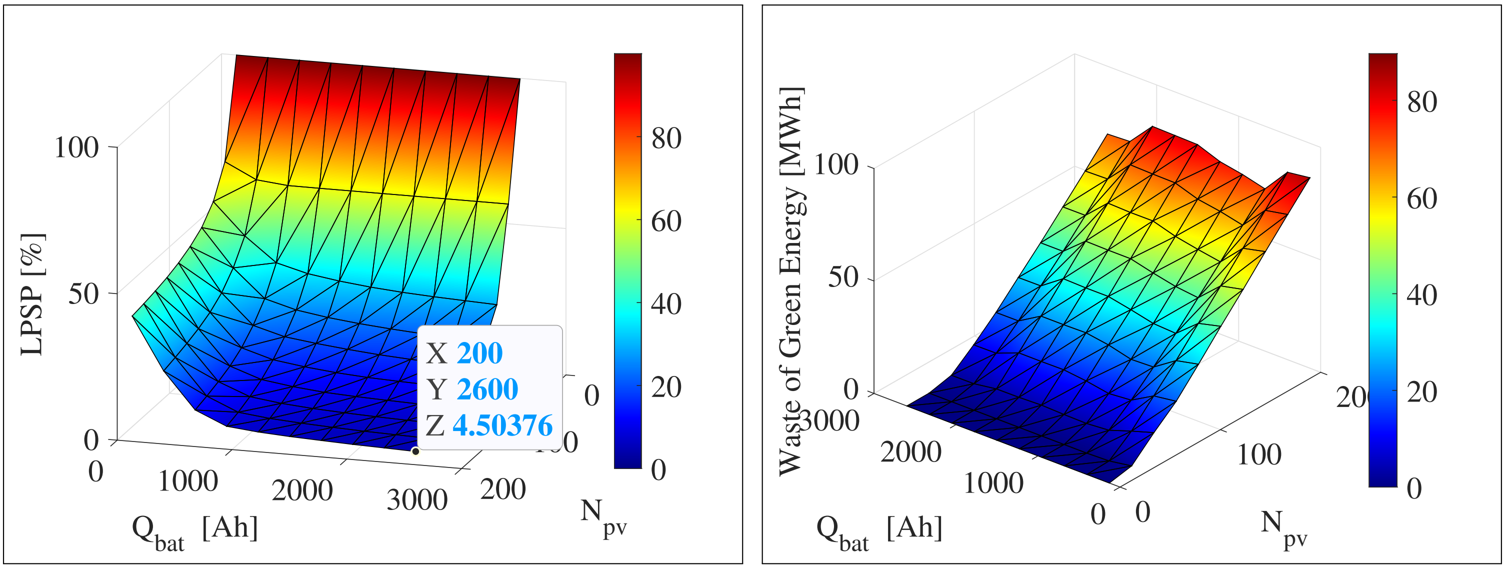


(a) LPSP [%]

(b) Energy Waste MWh per year

**Figure 6.4:** Enviromental Performance and LPSP For The PV/Bat Topology

- **Diesel Generator and LFP Batteries :**

This configuration, integrating diesel generation with battery storage, emerges as the most reliable solution in our systematic analysis, achieving a minimum LPSP of 0% (Figure 6.5a). This perfect reliability score confirms that power supply is consistently maintained without interruption. However, this operational excellence comes with substantial economic implications, as the maximum LCC reaches approximately $66\times10^4$ $\times$with an LCOE of $2.7\$/kWh$. A noteworthy observation from Figure 6.5b is the reduced annual emissions profile compared to the bifacial modules and diesel generator topology previously analyzed. This comparative reduction in emissions presents an interesting counterpoint to the conventional understanding of diesel-based systems. The achievement of 0% LPSP definitively corroborates our proposition regarding the necessity of incorporating diesel generation for meeting stringent reliability requirements.

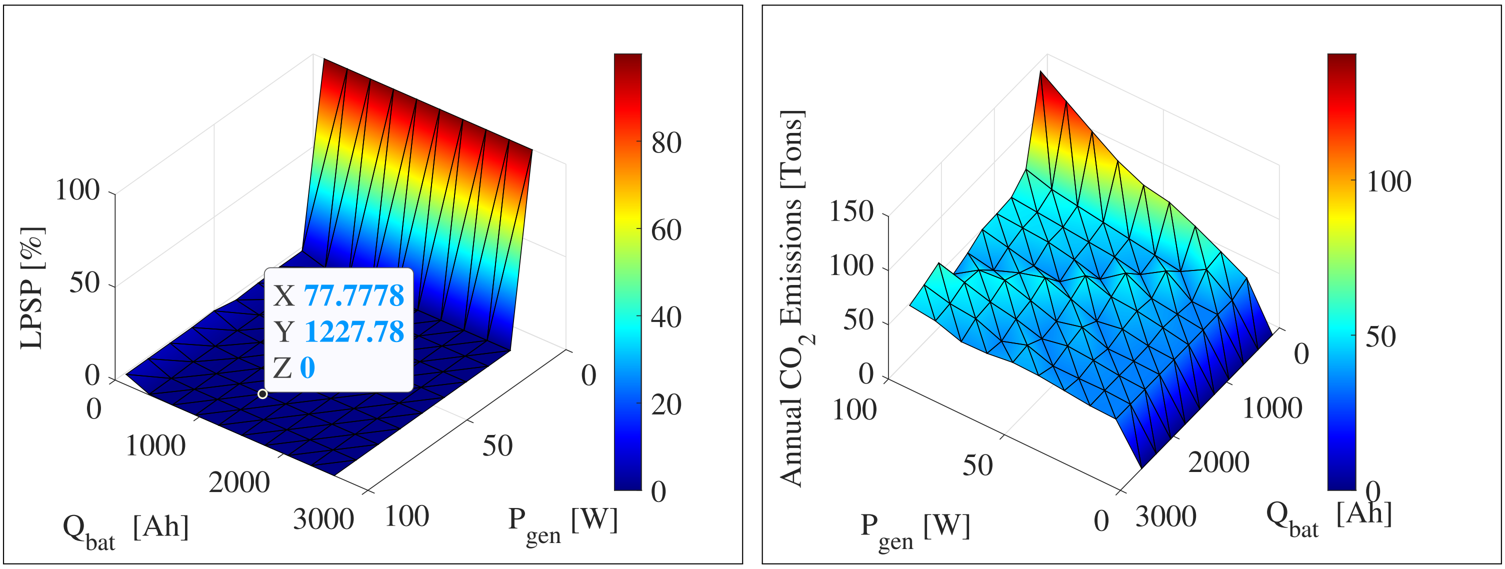


**(a)** LPSP [%]

**(b)** Annual $CO_2$ Emissions

**Figure 6.5:** Annual Emissions and LPSP For The GEN/Bat Topology

## 1.3 Results and Discussion

This section will provide an overview of the optimization results, accompanied by a sensitivity analysis that encompasses the impact of key parameters and their effect on the optimal design of the system under study. Our current challenge involves addressing a continuous optimization problem that is subject to constraints, wherein the objective functions exhibit nonlinear behavior. The initial stage towards solving this problem entails creating a model of the entire system in Matlab Simulink®. Following this, a subsystem is developed to assess the objectives and constraints. Finally, the optimization problem is resolved, and the Pareto Front is plotted by means of the Global Optimization Toolbox®. To address the given problem and attain the global Pareto front, a controlled elitist genetic algorithm, which is a variation of NSGA-II, was employed. Table 6.2 displays the results of the current station design proposed by Homer Pro, with a focus on five parameters that are considered to be representative of the economic and environmental costs associated with the station. The first parameter pertains to the carbon emissions during a one-year period. The second parameter is the LCOE, expressed by the Equation 6.18, which represents the average cost of producing one unit of energy over the system's lifespan. The third parameter is the amount of wasted energy, which is the difference between the potential output of the bifacial panels and the actual consumed energy. The fourth parameter pertains to the probability of a loss of power supply, and the last parameter is the lifespan of the battery, expressed in years.

$$LCOE = \frac{LCC}{25\sum_{i=0}^{8760} \frac{E}{(1+d)^i}} \tag{6.18}$$

| Parameter | Carbon [tons/year] | LCOE [$/kWh] | Wasted Energy [MWh] | LPSP [%] | Battery lifespan [years] |
|---|---|---|---|---|---|
| Value | 8.64 | 0.85 | 14.14 | 0 | 13 |

**Table 6.2:** Simulation Results with the Current System Design

### 1.3.1 Multi-Objective Optimization in Snow-Free Conditions

The multi-objective optimization problem concerns the simultaneous minimization of two objective functions, denoted as $f_1$ and $f_2$. The sought-after solution is a Pareto-optimal set, which constitutes the non-dominated set over the entire feasible design space. Specifically, the Pareto-optimal set encompasses those design solutions that are not inferior to any other solution, in terms of both objective functions. Subsequently, the Pareto-optimal front is established, which denotes the boundary defined by the set of all points mapped from the Pareto-optimal set. In our multi-objective optimization problem, the Pareto front is illustrated in Figure 6.6.

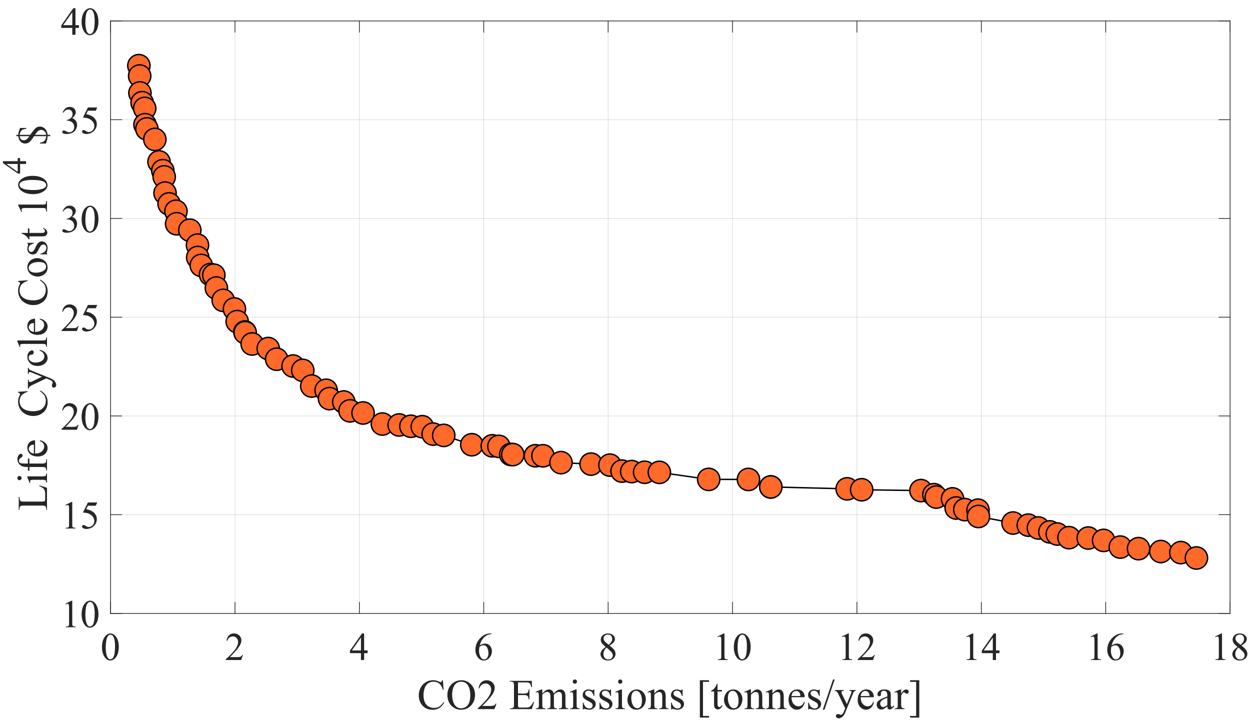


**Figure 6.6:** Pareto Front for the two Objective Functions LCC and $CO_2$

The Pareto fraction was set to 0.85 and the population size to 100, resulting in 85 solutions on the Pareto front. To evaluate the trade-off between economic and environmental costs, two anchor points on the Pareto front were identified and compared to the current design. The first anchor point is characterized by the lowest annual carbon emissions, $CO_2 =$ 0.7 tons/year, with a corresponding life cycle cost of $38.077 \times 10^4$ \$. The second anchor point, located at the bottom right of the Pareto front, represents the optimal economic cost solution, with a total cost of $12.83 \times 10^4$ \$, but this comes with increased carbon emissions of 17.36 tons/year.

According to the Table 6.2, the current hybrid system has an estimated life cycle cost of $20.6 \times 10^4$ and carbon dioxide emissions of 8.64 tons/year. Selecting the first anchor point over the current design results in a significant reduction in carbon emissions by approximately 91.9% (from 8.64 tons/year to 0.7; tons/year), albeit with an increased life cycle cost by approximately 84.8% (from $20.6 \times 10^4$ \$ to $38.077 \times 10^4$ \$). The high LCC for the first anchor point is due to the use of more PV modules (approximately 143) and more batteries (17) to store energy, along with a reduction in the size of the diesel generator to 6kW. Conversely, choosing the second anchor point reduces the life cycle cost by approximately 37.7% (from $20.6 \times 10^4$ \$ to $12.83 \times 10^4$ \$), but increases carbon emissions by approximately 101.0% (from 8.64 tons/year to 17.36 tons/year). This is because the second anchor point reduces the size of the components to 39 PV modules and 2 batteries, while relying more on the diesel generator, which is reduced to 8 kW, thereby increasing the emissions of the nanogrid. The performance of the extremes on the Pareto front has been presented. To identify a balanced trade-off between these solutions, the subsequent section will focus on determining the pareto equilibrium point.

### 1.3.2 Pareto Competitive Equilibrium Point

All points residing on the Pareto front are considered feasible solutions. However, the challenge lies in attaining a consensus between two objectives. In the current scenario, telecom operators desire to minimize their economic expenditure, while being legally obliged to minimize the hybrid system's environmental costs. A resolution can be achieved by identifying a Pareto-competitive equilibrium, characterized by the sole point $\left(\tilde{f}_1, \tilde{f}_2\right)$ that entails an equivalent tradeoff between both objective functions. The authors of the paper [1] have presented an approach based on transforming the Pareto front in order to find a unique compromise design.

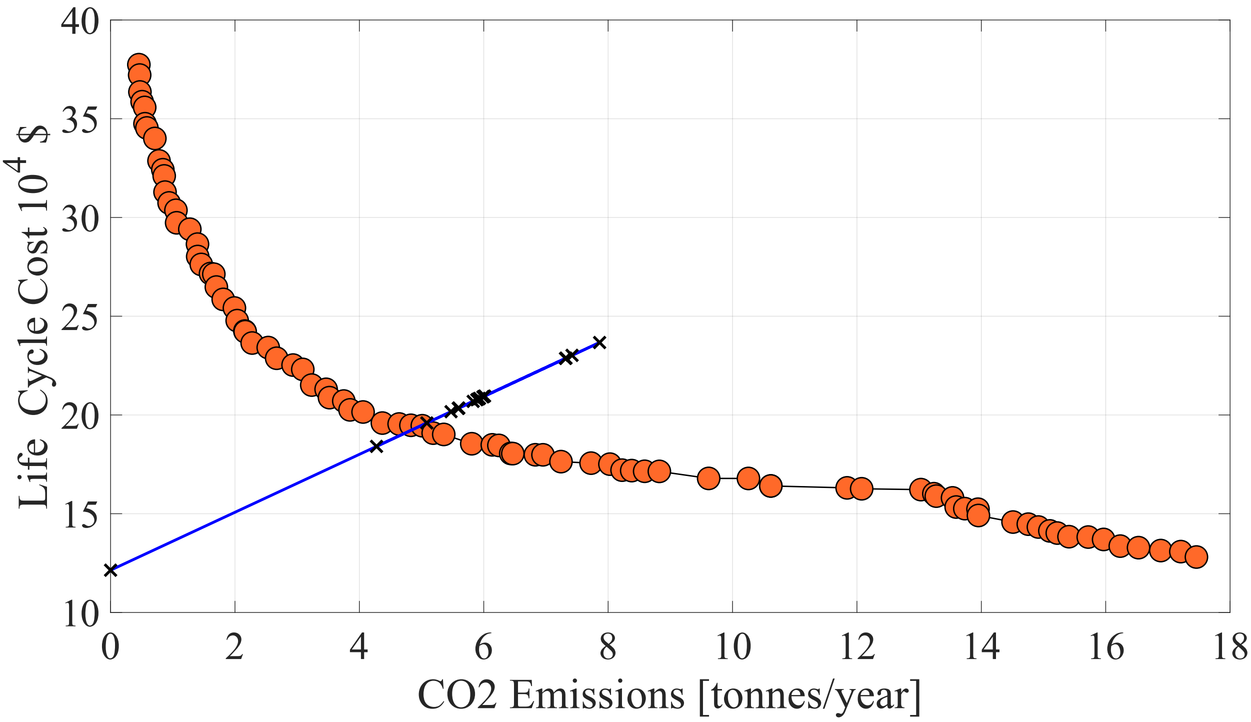


**Figure 6.7:** Optimal Compromise Solution From the Pareto-front

The coordinates that correspond to the unique point of interest can be determined through the application of the ensuing mathematical formulations:

$$\tilde{f}_1 = f_1^{max} - \left(f_1^{max} - f_1^{min}\right)\left(\Delta r_0 + \sqrt{2}/2\right) \tag{6.19}$$

$$\tilde{f}_2 = f_2^{max} - \left(f_2^{max} - f_2^{min}\right)\left(\Delta r_0 + \sqrt{2}/2\right) \tag{6.20}$$

Where $\Delta r_0$ is the radial shift of the Pareto-Front curve :

$$\Delta r_0 = \sqrt{2}\left(0.5 - \left(x_i^* + x_{i+1}^*\right)\left(y_i^* + y_{i+1}^*\right) / \left(x_i^* + x_{i+1}^* + y_i^* + y_{i+1}^*\ \right)\right) \tag{6.21}$$

where the vector index $i$ satisfies the two conditions : $x_i^*/y_i^* \leq 1$ and $x_{i+1}^*/y_{i+1}^* \geq 1$, all points that fulfill the stipulated conditions are identified (represented by the blue line in Figure 6.7). Consequently, the equilibrium point is characterized as the intersection between the aforementioned line and the Pareto frontier.. $x = f_1/f_1^{max}$ and $y = f_2/f_2^{max}$ are the normalized vectors that correspond respectively to the Pareto-front $f_1$ and $f_2$. $x^*$ and $x^*$ are the shifted vectors :

$$x^* = (x + \delta x)/(1 + \delta x) \tag{6.22}$$

$$y^* = (y + \delta y)/(1 + \delta y) \tag{6.23}$$

$\delta x$ and $\delta y$ denote the displacement magnitude along the horizontal x-axis and the vertical y-axis, respectively.

$$\delta x = \sqrt{2}\left(x^{max} - x^{min}\right) - x^{max} \tag{6.24}$$

$$\delta y = \sqrt{2}\left(y^{max} - y^{min}\right) - y^{max} \tag{6.25}$$

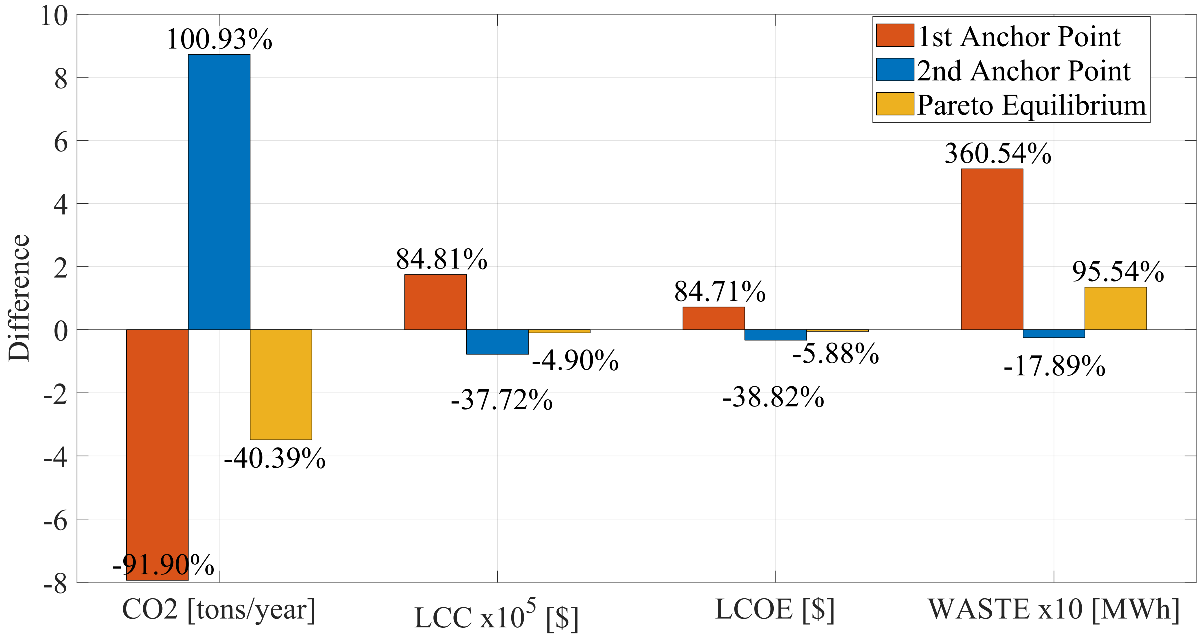


**Figure 6.8:** Performance of the Pareto Equilibrium Point and Two Anchor Points on the Pareto Front

The performance of the Pareto Equilibrium Point was compared to two anchor points. As illustrated in the Figure 6.8, the Pareto front effectively minimizes two objectives: $CO_2$ emissions and LCC , with reductions of 40.4% and 5.9%, respectively. The figure also highlights another critical parameter: the annual total waste of energy produced by bifacial modules. The Minimum $CO_2$ solution, which utilizes more bifacial modules, results in an estimated green energy waste of 360%. This is attributed to the increased use of bifacial modules and the overproduction of the PV array during the summer. Conversely, the second solution reduces energy waste by 17.9% but doubles the emissions of the nanogrid. The Pareto Equilibrium offers a trade-off by increasing energy waste by only 95.5%. The rounded values for decision variables at the Pareto Equilibrium Point are summarized in the table below:

| Generator | Energy Storage System | Bifacial Modules |
|---|---|---|
| 5 kW | 130 x 7 Ah | 365 x 88 W |

**Table 6.3:** Pareto Equilibrium Point: Values of Design Variables

## 1.4 Multi-Objective Optimization Under Snow Conditions

The primary benefit of employing bifacial modules stems from their distinctive capacity to capture irradiance on both sides. As illustrated in Figure 6.9a, the system under examination exhibits the optical gain of the module, which can achieve a noteworthy value of 22.3%. This substantial gain carries the potential to markedly augment the energy yield of the nanogrid. An inference drawn from the figure indicates that the bifacial gain escalates during winter, attributable to the increased albedo of the ground due to snowfall. However, this phenomenon presents a significant challenge as the snowfall obscures the front side of the bifacial modules, thereby diminishing their production. The image 6.9b of the studied system reveals that the modules are occasionally completely covered during winter.

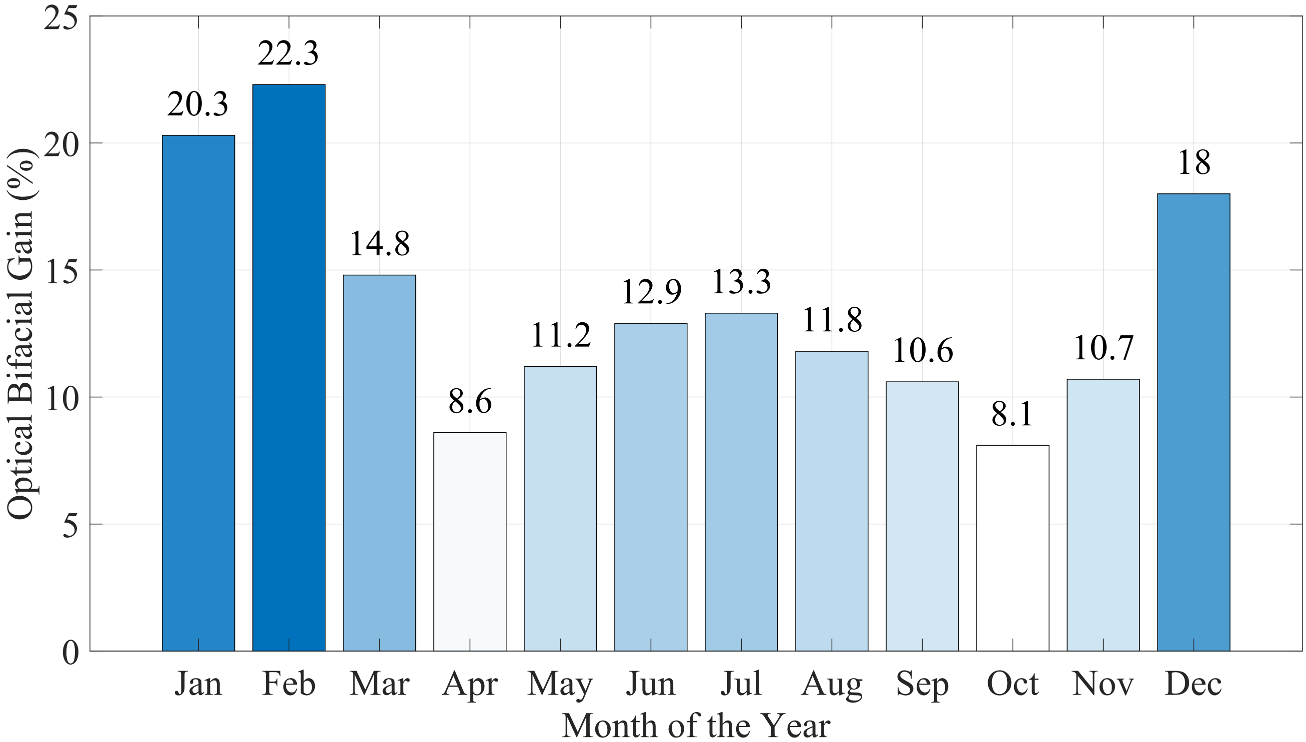


**(a)** Monthly Optical Gain [%]

**(b)** Bifacial Modules at Dorval Lodge Completely Blanketed by Snow

**Figure 6.9:** Installed Bifacial Modules During the Winter Season

To estimate the power production of bifacial modules under snowy conditions, the Marion model is employed [2]. This model has demonstrated reasonable accuracy for systems mounted on the ground. The depth of the snow serves as the meteorological parameter that determines the extent to which the oblique height of the module is covered. Given that the modules are oriented in portrait, if a portion of the front surface is obscured, the module substrings will be covered, resulting in zero output power. In such instances, only the rear side will generate power, thereby capitalizing on the unique capabilities of bifacial modules. Figure 6.10 illustrates the input of the method implemented. It provides a comparison between the actual power production of the bifacial module under snowy conditions and its power production when snow coverage losses are disregarded. The subfigure 6.10b magnifies the power production during the initial ten days of January. During this period, the snow depth fluctuates between 33.8 cm and 38 cm, which accounts for the reduced power production of the bifacial module. The computed annual loss for a single module, approximately 150.6 kWh, represents a significant 23.4% of its total production, excluding the potential influence of snow. This substantial loss will inevitably impact the design parameters of the nanogrid.

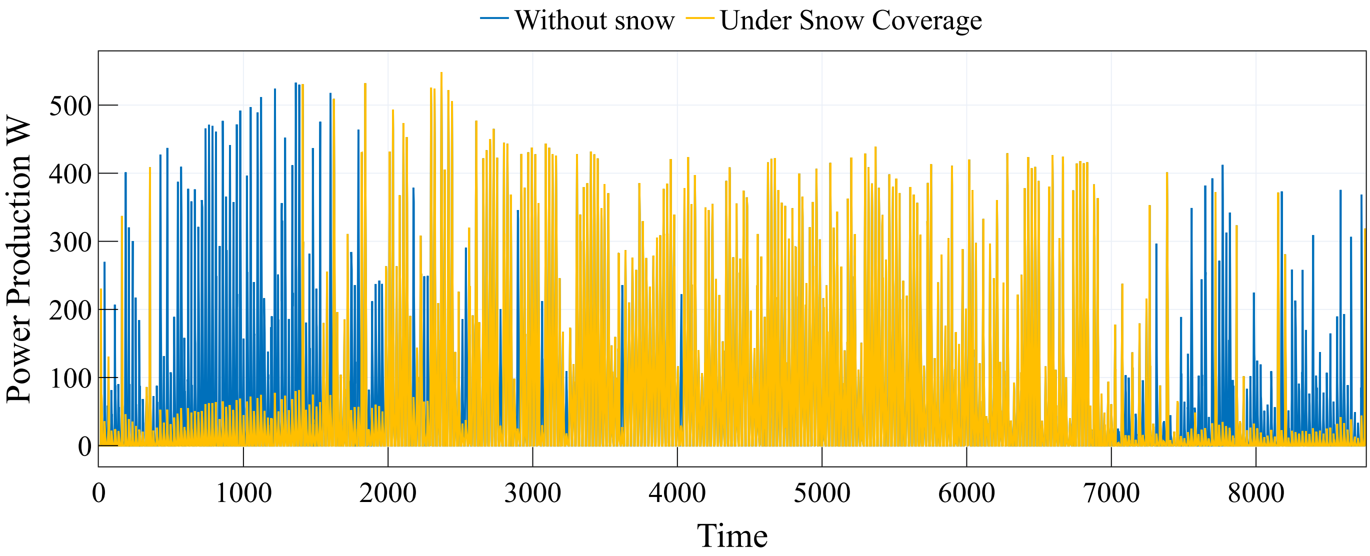


**(a)** Modeling the power production of One Bifacial Module 365 W Located in Dorval Lodge

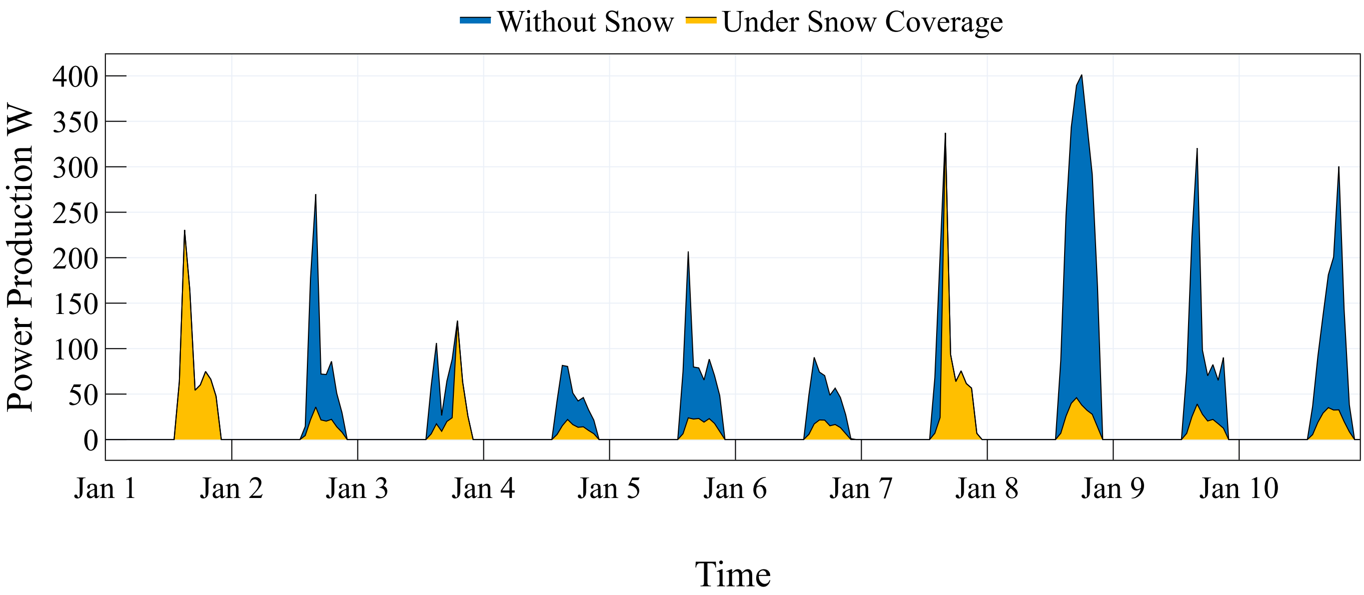


**(b)** Zoom on the Month of January

**Figure 6.10:** Power Production Estimation Under Snow Coverage Using Marion Model

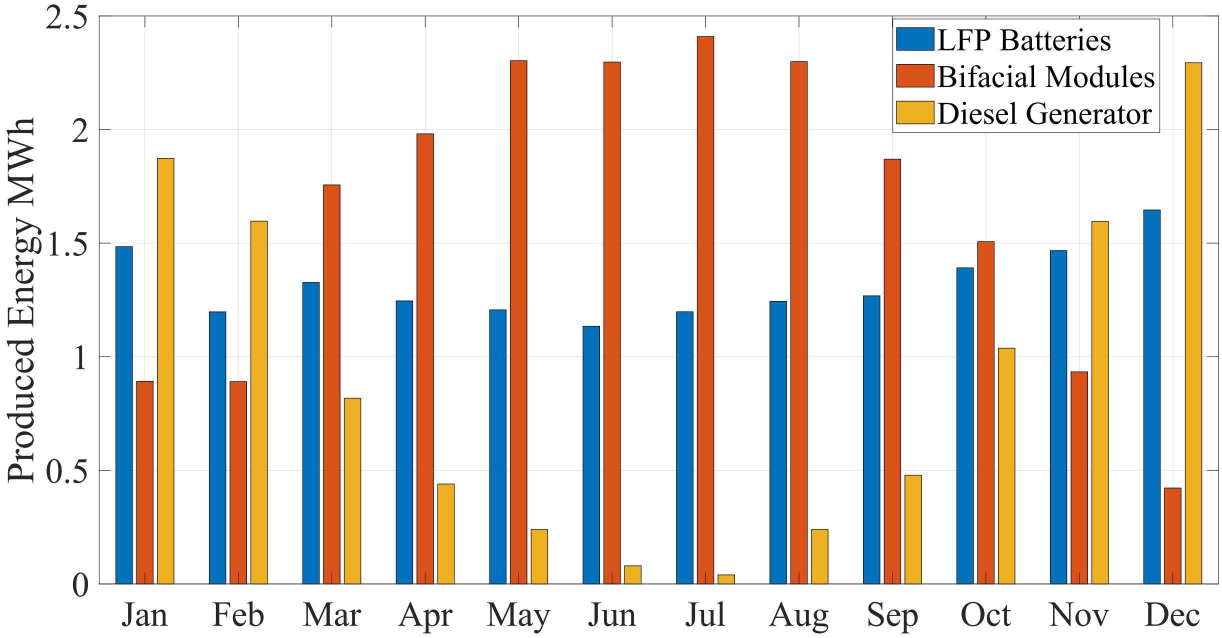


**Figure 6.11:** Monthly Energy Production by Each Sub-System in the Nanogrid, Taking Snowfall into Account

An examination of snowfall influence reveals a significant decline in the power output of the modules during the winter months. As illustrated in Figure 6.11, there is a marked increase in the reliance on the diesel generator during this season. Taking December as a representative example, the energy generated by the bifacial modules is as low as 0.42 MWh. In contrast, the diesel generator produces approximately 2.3 MWh. This represents an increase of 60.8% in comparison to the previously mentioned results, underscoring the substantial impact of winter conditions on the performance of the bifacial modules.

In response to the observed conditions of the nanogrid, we re-engage the optimization algorithm to derive an updated Pareto front. The results from this secondary optimization are illustrated in Figure 6.12. It is observed that the Pareto front has been displaced to the right, a shift primarily driven by the increased reliance on the diesel generator, resulting in elevated $CO_2$ emissions. For instance, the initial anchor point in the first optimization achieved the lowest $CO_2$ emissions, measured at 0.7 tons per year. However, the first anchor point on the updated Pareto front reveals an increase, rising to 3.41 tons per year.

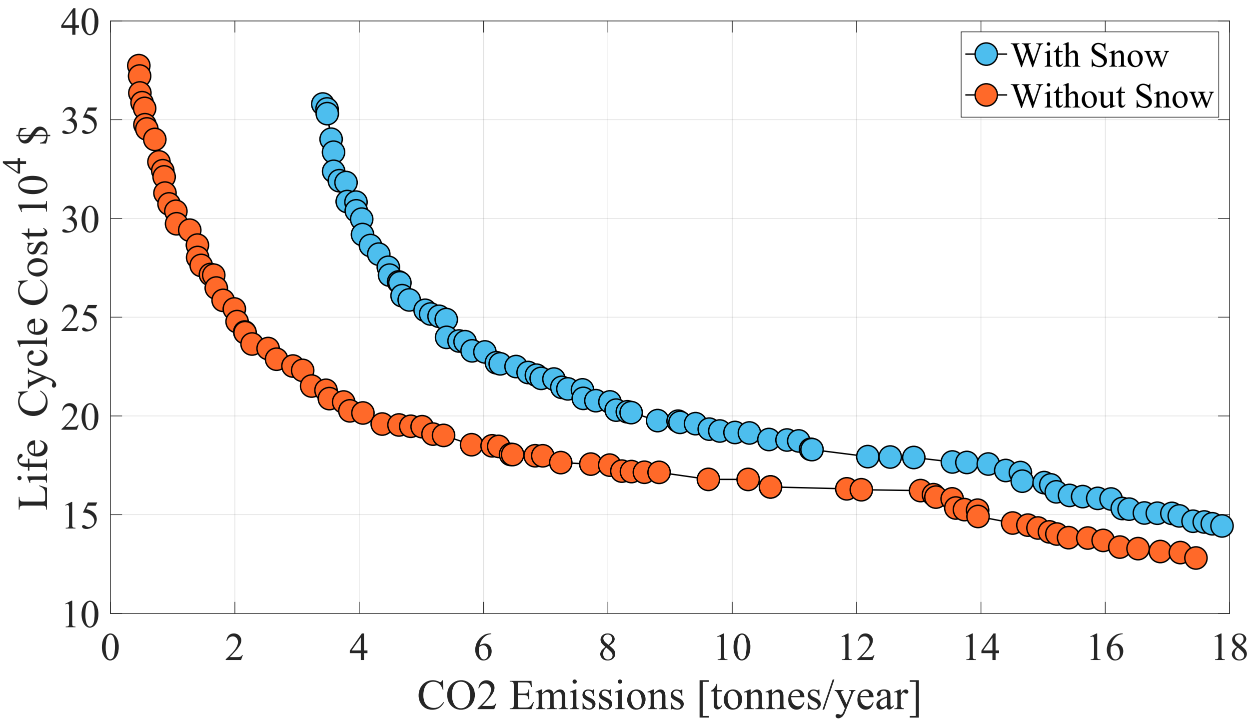


**Figure 6.12:** Impact of the Snow on the Pareto Front

The new Pareto front also contains 85 solutions, matching the original. This consistency is due to maintaining the same algorithm parameters, specifically the Pareto set fraction and population size, across both simulations. To navigate this multitude of potential solutions and identify a singular, optimal choice, we have employed Multi-Criteria Decision Making (MCDM). As illustrated in Figure 6.14, the Pareto competitive equilibrium is discerned at the intersection of the delineated blue line and the Pareto front. The solution in closest proximity to this point of equilibrium, denoted as $p^{\star} = (7.83\ tons/year, 20.68\ 10^4\ \$)$ , corresponds to the design vector $x^{\star} = (5.3kW, 103.7\ modules, 835.02\ Ah)$. This point, therefore, represents our selected solution within the multi-dimensional design space of the nanogrid configuration.

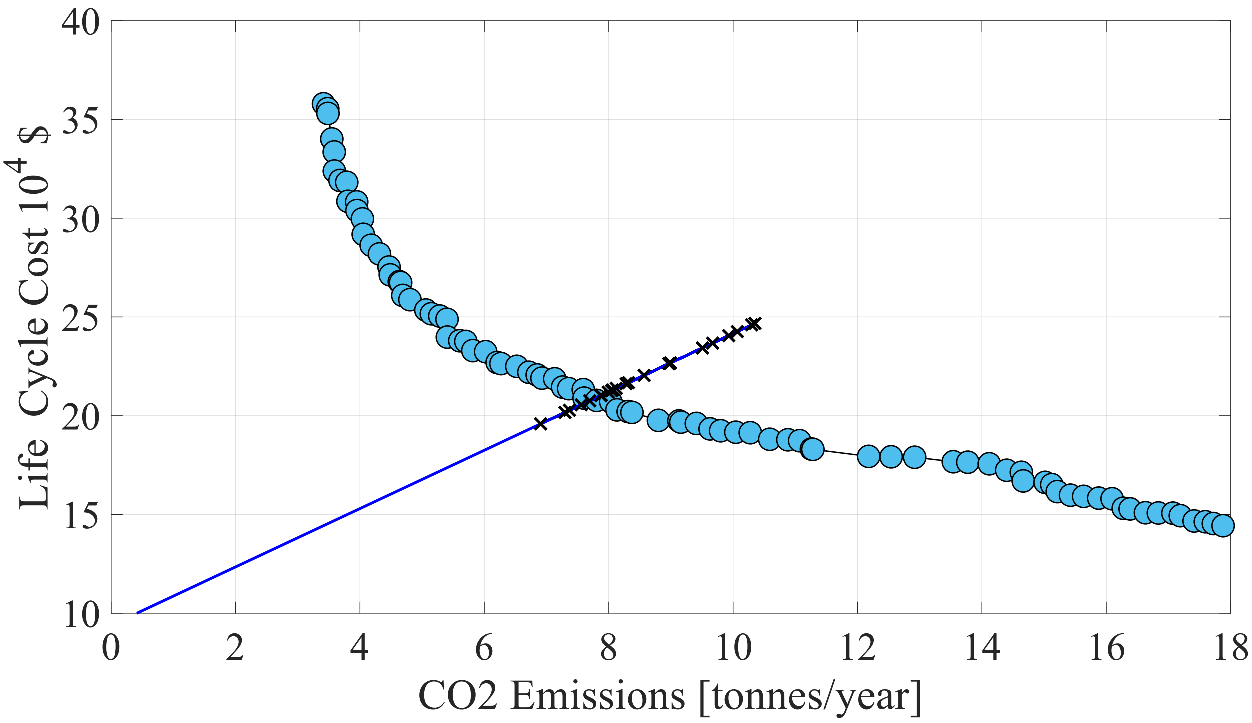


**Figure 6.13:** Pareto Equilibrium Point Under Snow Coverage Conditions

In order to propose a feasible solution that aligns with market standardization, we will incorporate a 6 kW diesel generator, 104 bifacial modules, and 6 batteries into the nanogrid design. Thus new optimal design according to the new Pareto competitive equilibrium point is :

| Generator | Energy Storage System | Bifacial Modules |
|---|---|---|
| 6 kW | 130 x 6 Ah | 365 x 104 W |

**Table 6.4:** Design Variable: Pareto Equilibrium Point

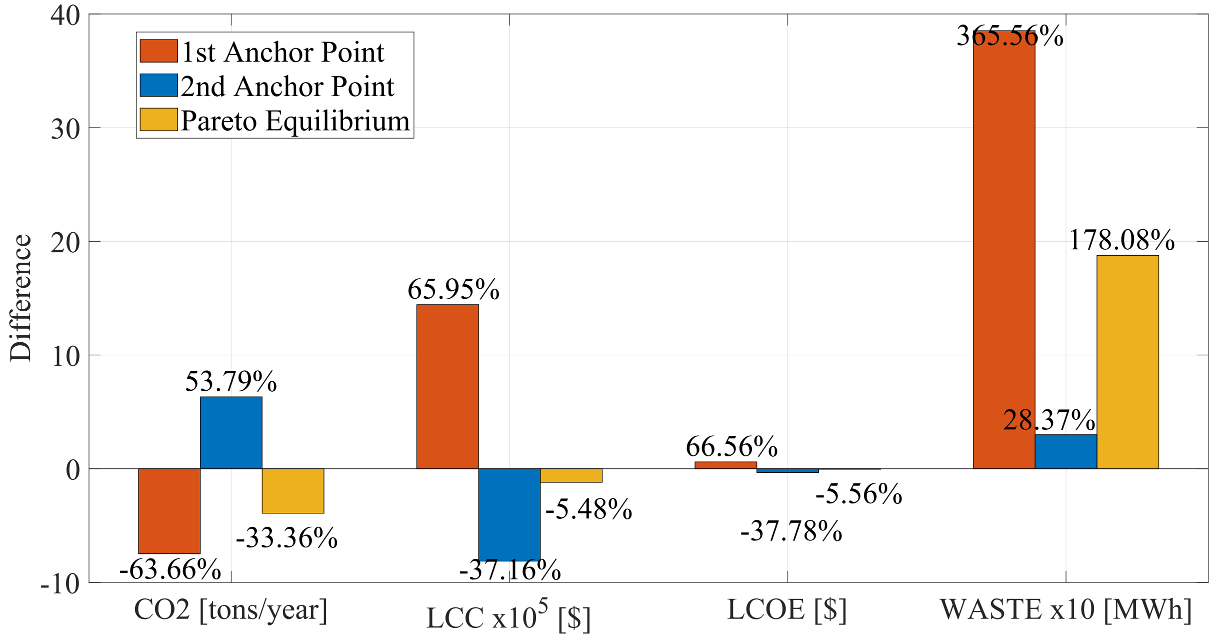


**Figure 6.14:** Performance of the New Pareto Solutions Under the Snow Conditions.

The performance of the Pareto anchor points and the new equilibrium, based on the current design, is summarized in the bar plot (Fig. 6.14). Each solution reflects a trade-off between minimizing carbon emissions and reducing Life Cycle Cost (LCC), influenced significantly by the seasonal variability in bifacial module production.

The low carbon emissions solution achieves a 63.66% reduction in $CO_2$ emissions but incurs a 65.95% increase in LCC. This outcome is driven by the need for an expanded renewable energy infrastructure, including 15 batteries and 139 bifacial modules, to reduce reliance on diesel generation. However, the system's overdesign leads to a 365% increase in wasted energy, as the bifacial modules generate surplus power during high-production periods, such as summer or clear-sky conditions. This waste arises due to the significant discrepancy between bifacial module production in winter, especially under snow coverage, and their higher output during summer. The low-cost solution reduces the LCC by 37.16% but results in a 53.8% increase in $CO_2$ emissions. This configuration requires only 2 batteries and 49 bifacial modules, minimizing investment and operating costs. However, the smaller system struggles to meet energy demand during low solar production periods, such as winter, increasing reliance on diesel generation and thereby elevating emissions.

The Pareto equilibrium solution balances the trade-offs between environmental and economic objectives. It reduces $CO_2$ emissions by 33.6% and LCC by 5.48%, avoiding the extremes of overdesign or underinvestment. By employing a more proportional design, it mitigates the waste associated with seasonal production variability while maintaining a reasonable cost.

### 1.5 Impact of Snow Conditions on the Performance of Previous Solutions

Upon examining carbon emissions, we found that the previous pareto equilibrium solution resulted in higher emissions, specifically 8.54 tons per year, compared to the new equilibrium, which emitted only 7.83 tons per year. This indicates a reduction in carbon emissions. The cause of these emissions can be traced to the winter season, when the panels fail to generate sufficient energy to meet the load, necessitating the use of a diesel generator. The first solution overestimated the power production of the bifacial modules, which led us to discover that the optimal design only requires 88 modules, whereas the second solution requires approximately 104 modules. Despite these differences, both solutions have nearly the same Levelized Cost of Energy (LCOE) and Levelized Cost of Carbon (LCC) at 0.85$\$/kWh$ and 20.8$\times$ $10^4$ \$,respectively.
The Pareto equilibrium represents an interesting point of analysis. However, in this study, we assessed the performance of all previously identified optimal solutions under new snow conditions in relation to the objectives and constraints. The first figure 6.15 illustrates that approximately 47% of the previous optimization results exhibit negative performance in terms of CO2 emissions when compared to the new solution under real snow conditions, with an average negative performance of -139.72%. Conversely, about 53% of the solutions show positive performance, with an average improvement of 39.69%. It is important to note that the key constraint in our optimization is system reliability, which is ensured by maintaining the Loss of Power Supply Probability (LPSP) below 0.001%. Among the positive solutions, 9% do not meet this reliability criterion.
Regarding the LCC objective (Fig. 6.16), we found that 54% of the previous solutions exhibited negative performance compared to the new solution, while 46% demonstrated positive performance. The average performance of the positive solutions was -40.9%, while the negative solutions had an average performance of 25.74%. For the LPSP constraint, we found that 15.4% of the positive solutions failed to meet this condition, while 8.7% of the negative solutions also did not comply with the constraint.

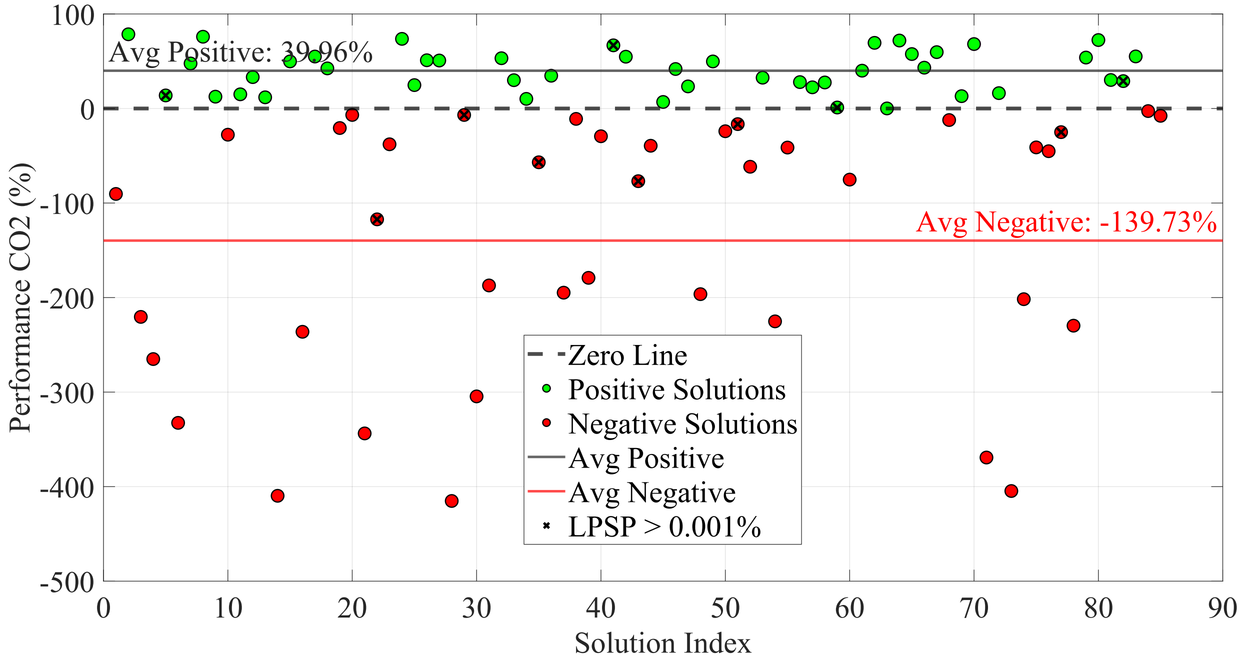


**Figure 6.15:** Performance of Previous Pareto Solutions Under Snow Conditions.

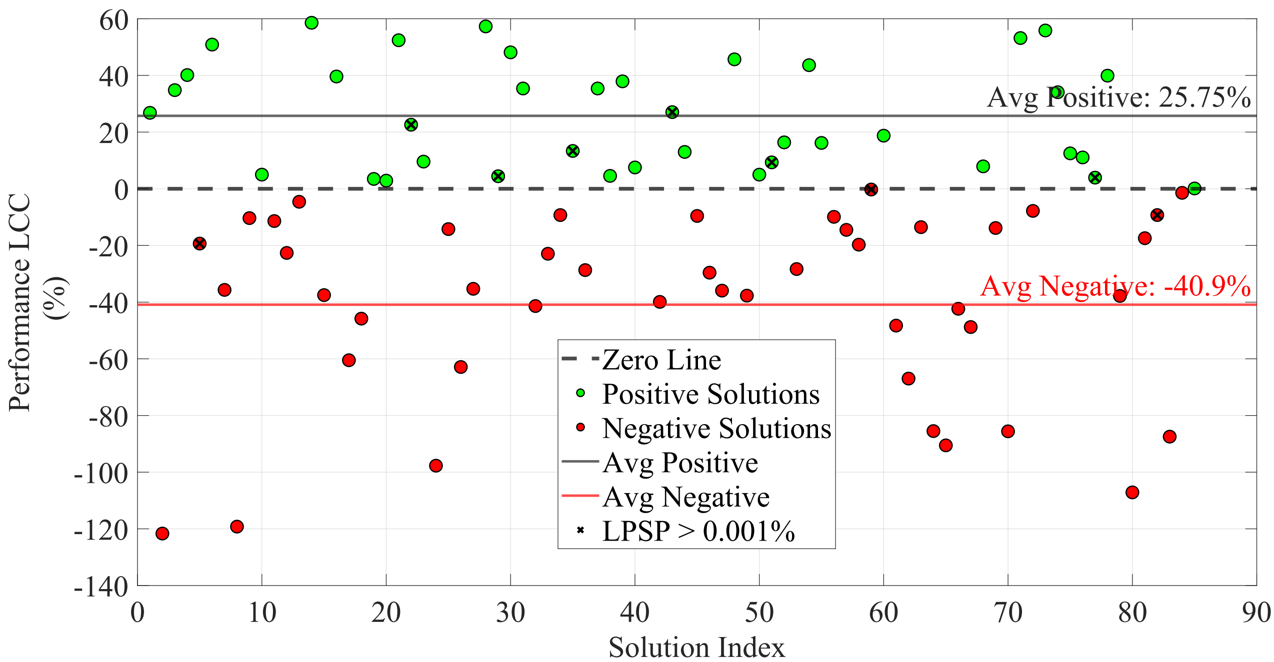


**Figure 6.16:** Performance of Previous Pareto Solutions Under Snow Conditions.

### 1.6 Conclusion

This chapter focuses on the design and optimization of nanogrids for off-grid telecommunication base stations (BTS) that predominantly rely on diesel generators, especially in snow-prone regions. The proposed nanogrid integrates bifacial photovoltaic modules, lithium iron phosphate (LFP) batteries, and a diesel generator to ensure a reliable and environmentally conscious energy supply.
The optimization process employed the Controlled Elistic Genetic Algorithm with two primary objectives: minimizing the life cycle cost (LCC) and reducing annual carbon emissions, while ensuring system reliability through a constraint on the Loss of Power Supply Probability. Initial simulations under snow-free conditions generated a Pareto Front of solutions, from which three representative points were analyzed. One anchor point reduced carbon emissions by 91.99%, while the other minimized LCC by 37.72%. The equilibrium point offered a balanced trade-off, achieving a 40.4% reduction in emissions and a 5.9% reduction in LCC.
Subsequent analysis incorporated the effects of snow on the performance of bifacial modules, refining the optimized design. A new equilibrium point was identified, which further reduced annual carbon emissions from 8.54 tons (the snow-free equilibrium) to 7.83 tons. However, this adjustment revealed significant challenges: 47% of the previously optimized solutions exhibited increased $CO_2$ emissions, with an average rise of 139.72%, while 54% displayed reduced cost-effectiveness, averaging a 40.9% LCC decrease. Additionally, 11.76% of the solutions under snow-free conditions failed to meet reliability criteria when snow impacts were considered.
An important finding of this study is that accounting for snow conditions in the optimization process, while addressing emissions and reliability, can lead to substantial energy waste. For example, the low-emission solution increased energy waste by 365%, amounting to 49 MWh annually. This highlights a critical avenue for future work: enhancing the management strategy of the proposed solutions.
Overall, this research emphasizes the necessity of integrating environmental factors, such as snow impacts, into the optimization of off-grid energy systems.

## 2 Joint Optimization

### 2.1 Introduction

Having addressed the first and second research questions, this final chapter focuses on responding to the third and fourth research questions by integrating control variables into the optimization framework and proposing novel design solutions. We maintain the same objectives established in the preceding chapter while emphasizing practical, market-compatible solutions. The previous chapter provided a theoretical analysis of snow's impact on nanogrid optimal design; this chapter proceeds directly to quantifying these effects and incorporating the findings into the optimization process.

### 2.1.1 Bifacial Modules Production Under Snowy Conditions

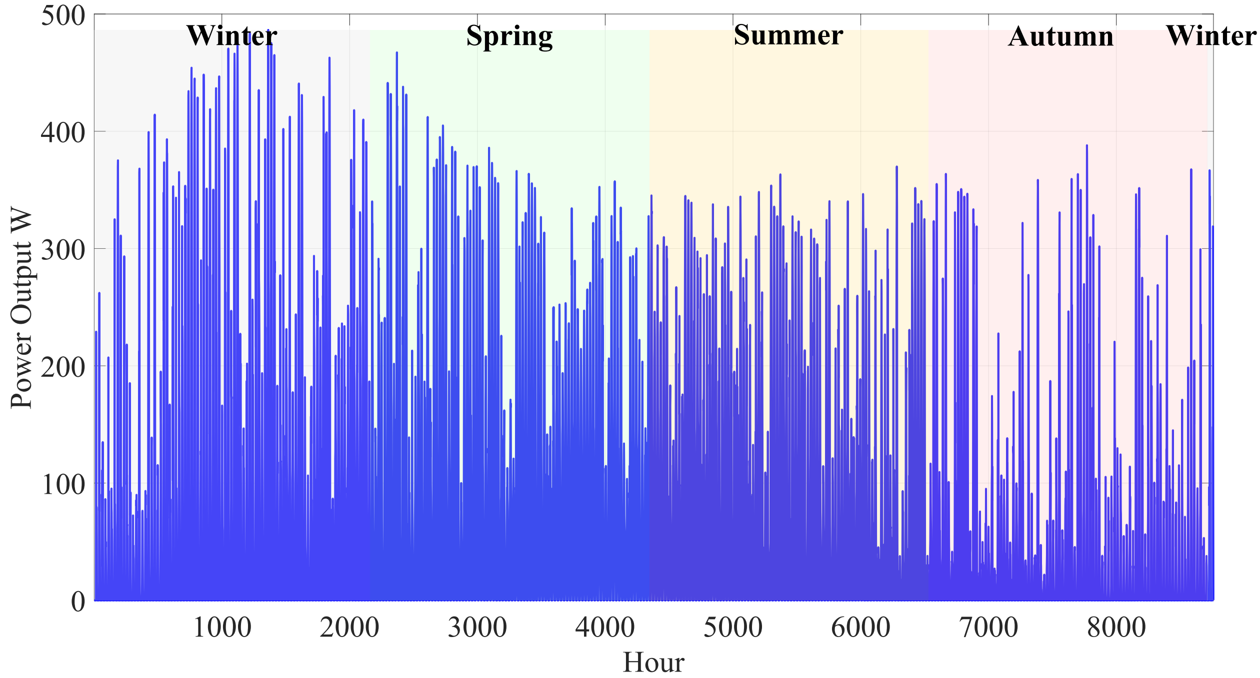


**Figure 6.17:** Power Production of One Module for the TMY

Figure 6.17 reveals a noteworthy trend in power production: energy output during winter surpasses that of other seasons. This phenomenon can be attributed to the high albedo values typically observed in winter, which can reach an estimated 0.7, leading to a 24% increase in module power production. However, during snowfall, the front surface of the modules can become fully covered, leaving the rear surface as the sole contributor to power generation. To accurately account for this effect, we employed the Marion Model [2], which offers an interesting accuracy of 1.5% (absolute). The adjusted power output of the module, incorporating this phenomenon, is presented in Figure .

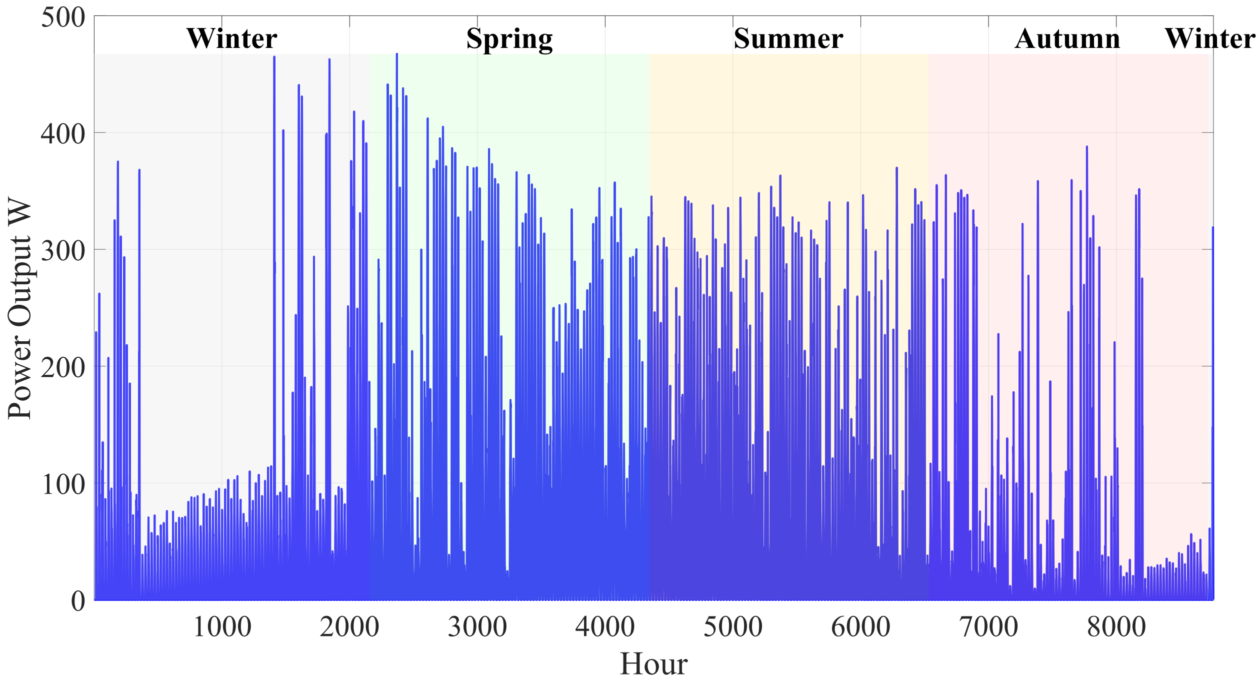


**Figure 6.18:** Power Production of One Bifacial Module Accounting for the Impact of the Snow for a TMY

## 2.2 Analysis of Objective Functions and Algorithm Selection

The optimization problem outlined in the previous section is classified as a mixed-integer optimization problem. This classification arises because certain decision variables, such as the number of panels, the rated power of the diesel generator, and the number of batteries, are restricted to integer values. In contrast, the control variables are continuous, with values constrained between 0 and 1.

### 2.2.1 LPSP Constraint

A systematic analysis was performed to assess the convexity of the functions under study. Convex functions allow for the selection of efficient algorithms that guarantee the identification of the global minimum. From the variation of the LPSP constraint function, as shown in Figure 6.19a, with respect to the two control variables, $Thr_{min}$ and $Thr_{max}$, it is evident that the function is non-convex. This is indicated by the presence of both concave and convex regions. A similar observation holds true when examining the function's variation with respect to the design variables, as shown in Figure 6.19b.

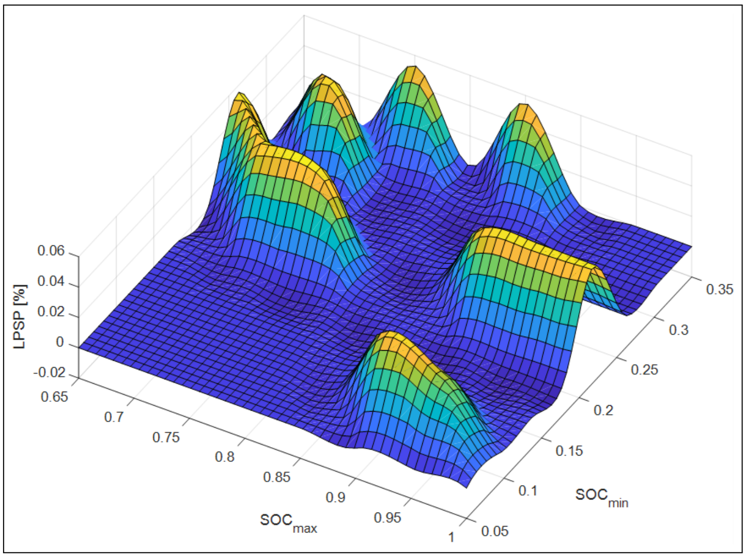


(a) Non-Convexity of the Constraint (Control).

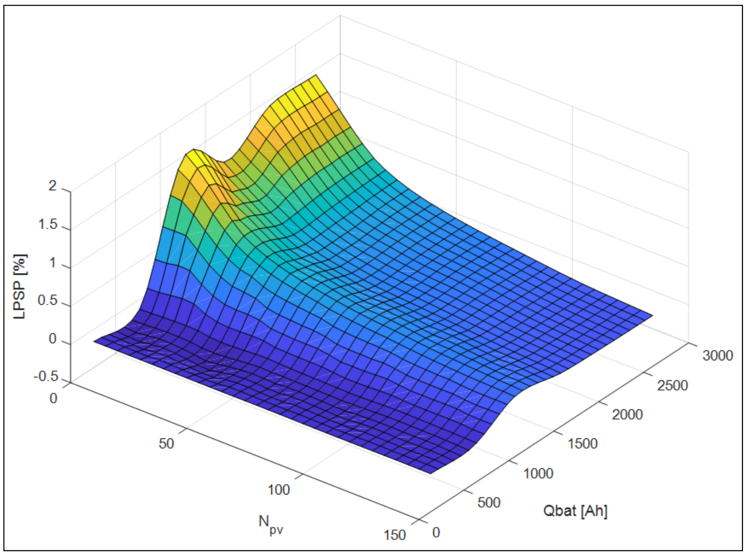


(b) Non-Convexity of the Constraint (Design Variables).

**Figure 6.19:** Convexity of the LPSP Constriant Function with Respect to Control and Design Variables.

### 2.2.2 $CO_2$ Objective Function

An analysis of the $CO_2$ objective function reveals its non-convex nature. Variations with respect to the control variables, $Thr_{min}$ and $Thr_{max}$, display regions alternating between concavity and convexity. A comparable pattern emerges when examining the function in relation to the design variables, $P_{gen}$ and $Q_{bat}$, further confirming its non-convex behavior.

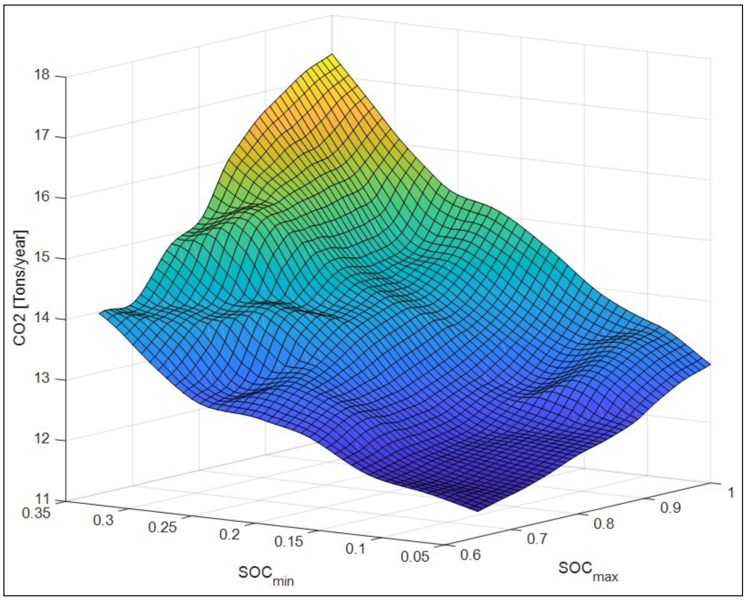


**(a)** Non-Convexity of the Objective (Control).

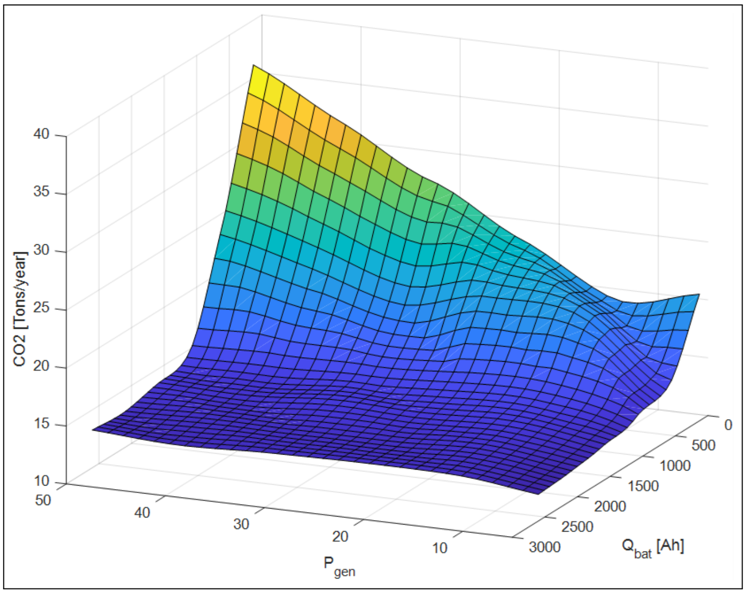


**(b)** Non-Convexity of the Objective (Design).

**Figure 6.20:** Convexity of the LCC Objective Function with Respect to Control and Design Variables.

### 2.2.3 Algorithm Selection

For the optimization process, we utilize the MATLAB Optimization Toolbox, which offers a range of algorithms. Based on our analysis, we have selected a Genetic Algorithm, specifically the Controlled Elitist Genetic Algorithm, a variant of NSGA-II. This algorithm is well-suited for the problem at hand, as it is designed to improve both convergence and diversity. Additionally, it is particularly appropriate due to the non-complex nature of the objective and constraint functions and its ability to handle the non-linearity of these functions.

The flow chart of the approach applied in this study is detailed in Figure 6.21.

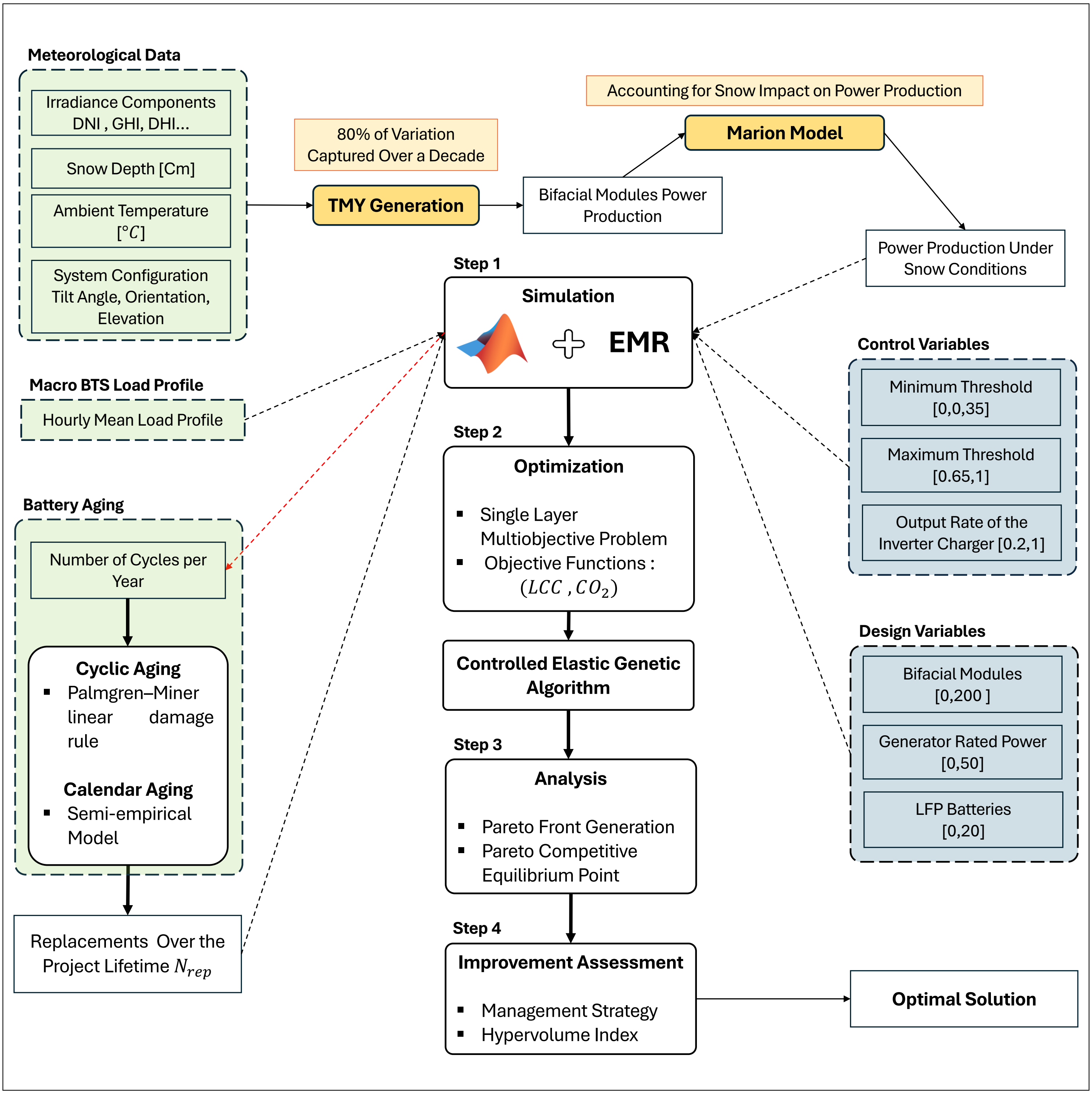


**Figure 6.21:** Flowchart Detailing the Methodological Approach of the Research Study

## 2.3 Results and Discussion

### 2.3.1 Optimal Design

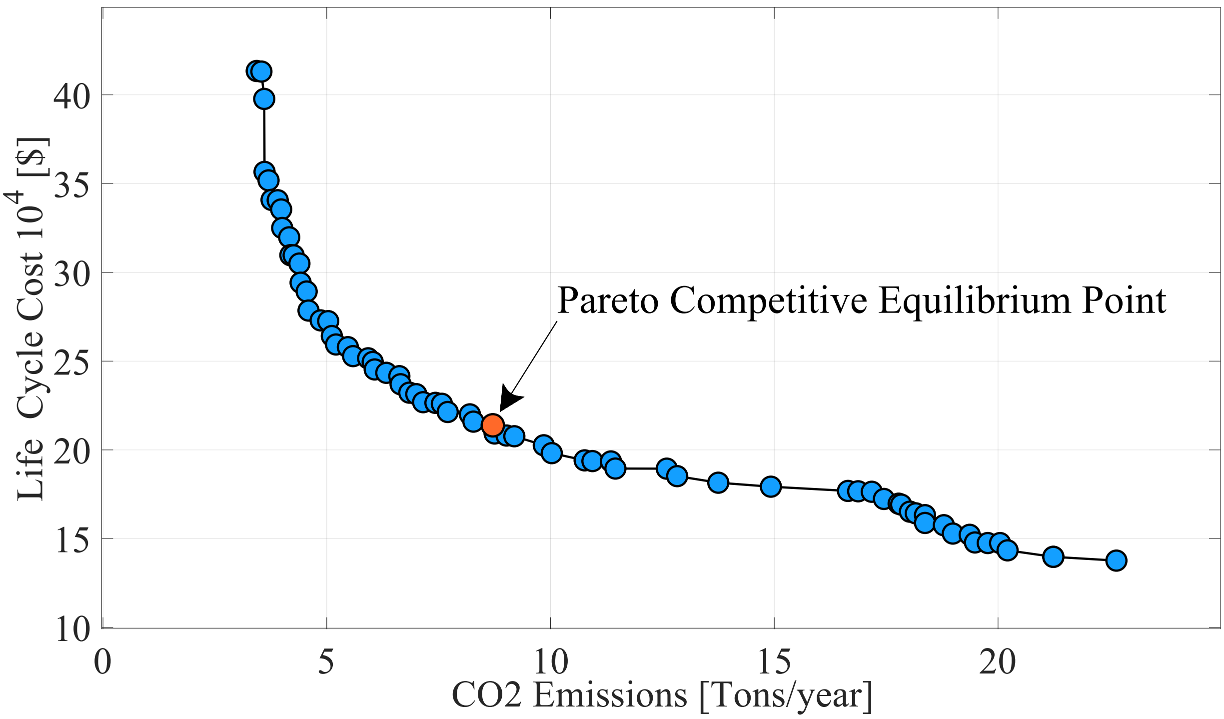


**Figure 6.22:** Pareto Front for Optimal Design: Balancing $CO_2$ Emissions and Life Cycle Cost

The optimization process begins with identifying an optimal design, which serves as the starting point for iterative improvement. At each step, additional control variables are incorporated, and the resulting changes are evaluated systematically. This process is guided by two objective functions, with the algorithm's output represented by the Pareto front. For the initial setup, the population size is set at 100 individuals, and the Pareto set score is initialized at 0.7. Consequently, the Pareto front comprises 70 solutions, which collectively exhibit a high degree of diversity, as illustrated in Figure 6.22. An economic analysis of the proposed nanogrid configurations has been conducted Figure 6.23, revealing that the minimum achievable $CO_2$ emissions amount to 3.45 tons per year. This environmentally optimal configuration incurs a total cost of approximately $41.34 \times 10^4$ \$, making it the most expensive solution. The associated capital expenditure is about $39.98 \times 10^4$ \$, with the storage system accounting for $27.9 \times\ 10^4$\$. Based on Table 6.5, this configuration requires 18 batteries and the maximum number of photovoltaic (PV) modules that can be installed in the area—150 bifacial modules. The estimated capital cost of the PV panels is approximately $11.53 \times 10^4$\$ . In this setup, the battery bank is primarily charged by the bifacial modules, while a 5 kW diesel generator, as indicated in Table 6.5, is used primarily during periods of low solar radiation, as shown in 6.24. In contrast, the economically optimal solution reduces the total cost to $13.21 \times 10^4$ \$, albeit at the expense of increased environmental impact. Under this configuration, $CO_2$ emissions rise significantly to 21.25 tons per year. This cost-effective design relies more heavily on the diesel generator, resulting in an operational cost of $8.39 \times 10^4$ \$ and a CAPEX of $4.82 \times 10^4$ \$. The lower investment cost is attributable to the proposed nanogrid configuration, which includes 81 bifacial modules, five LFP batteries, and a 5 kW diesel generator. To address the trade-off between ecological and economic objectives, A transformation method was applied to determine the Pareto competitive equilibrium point [1]. This balanced configuration results in $CO_2$ emissions of 8.93 tons per year and a corresponding life-cycle cost of approximately $21.47 \times 10^4$\$. The trade-off solution requires 6 batteries, 110 bifacial modules, and a 5 kW diesel generator, achieving a compromise between environmental sustainability and economic feasibility.

This analysis highlights the inherent tension between minimizing environmental impact and reducing costs, underscoring the importance of multi-objective optimization in nanogrid design.

| Solution/ Equipement Size | LFP Batteries | PV Modules | Diesel Generator |
|---|---|---|---|
| Min CO2 | 18 | 150 | 5 |
| Min LCC | 5 | 81 | 5 |
| Pareto Equilibrium | 6 | 110 | 5 |

**Table 6.5:** Optimal Design Variable Values for Anchor Points and Pareto Equilibrium

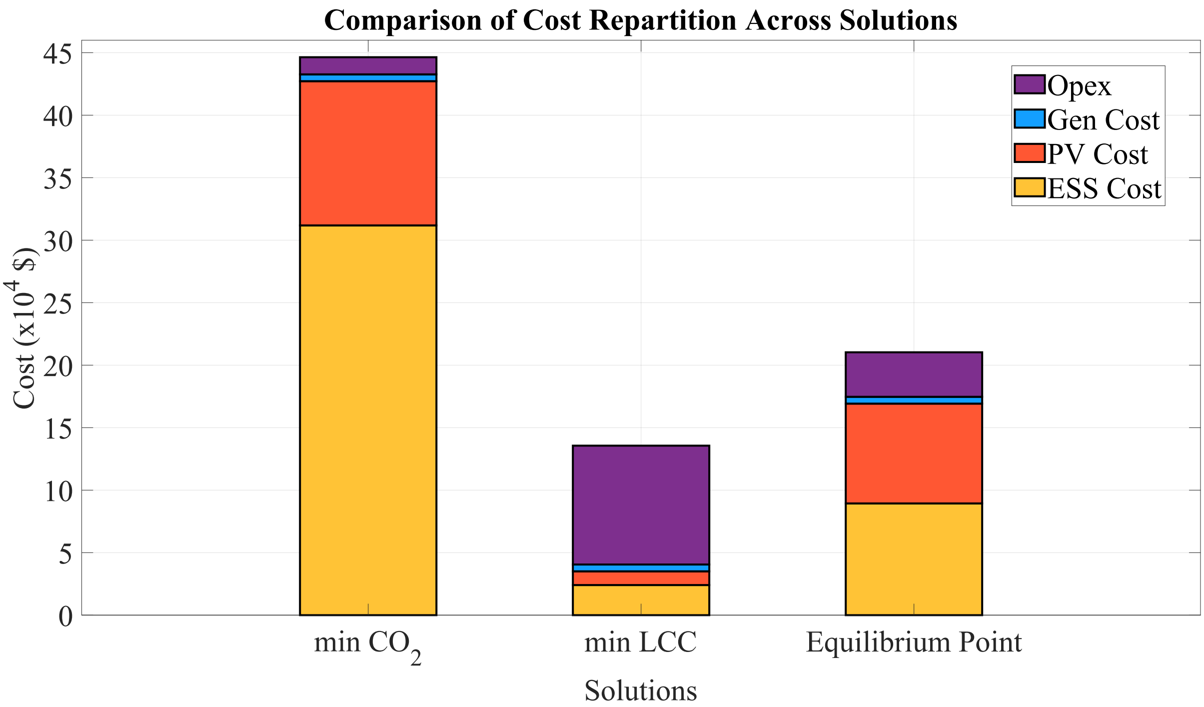


| Cost/Solution | min CO2 | min LCC | Pareto Equilibrium |
|---|---|---|---|
| Total Cost | **41.34** | **13.21** | 21.47 |
| CAPEX | 39.98 | 4.82 | 17.94 |
| OPEX | 1.36 | 8.39 | 3.53 |
| Storage System Cost | 27.90 | 2.40 | 8.93 |
| PV System Cost | 11.53 | 1.867 | 8.46 |
| DG System Cost | 0.55 | 0.55 | 0.55 |
| $CO_2$ Emissions | **3.45** | **21.25** | 8.93 |

**Figure 6.23:** Economic Analysis of Optimization Solutions: Comparative Evaluation of Anchor Points and Pareto Equilibrium (Costs in $\times 10^4$ [$])

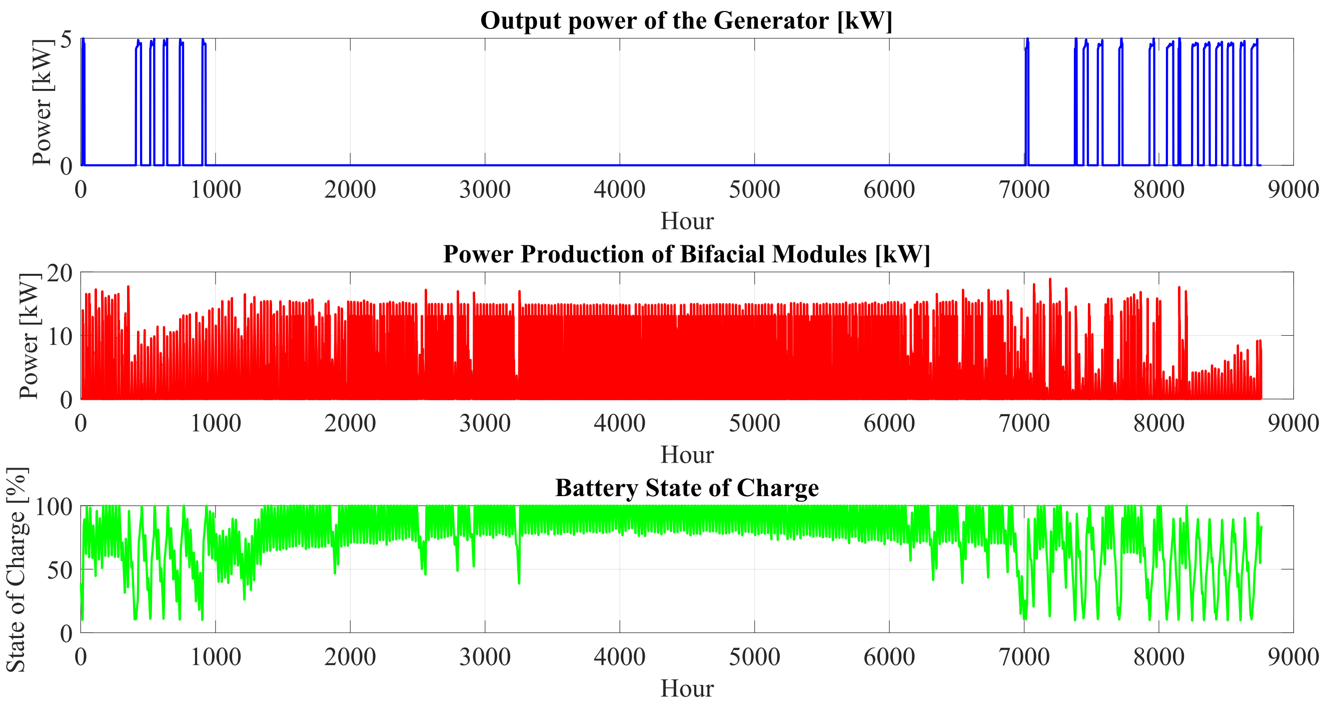


**Figure 6.24:** Operation of Nanogrid Subsystems: Diesel Generator Output, Bifacial Panel Output, and Battery State of Charge in the Most Ecological Design Optimization Solution.

## 2.4 Joint Optimization with Fixed Control Variables

In this section, we introduce three control variables: $Thr_{\text{min}}$, $Thr_{\text{max}}$, and $\alpha_{\text{rate}}$. In the previous design configuration, these variables were assigned values of 0.1, 0.9, and 1, respectively. The primary goal of this setup was to ensure that the generator remained active until the battery's state of charge reached 90%, thereby prioritizing system reliability. The current approach retains the same two objective functions and optimization algorithm as in the previous design. However, the inclusion of the control variables modifies the decision vector, which is now expressed as:

$$\mathbf{x}_{\text{decision}} = \{N_{\text{pv}}, N_{\text{bat}}, P_{\text{gen}}, SOC_{\text{min}}, SOC_{\text{max}}, \alpha_{\text{rate}}\},$$

where $N_{\text{pv}}$ represents the number of photovoltaic panels, $N_{\text{bat}}$ the number of batteries, and $P_{\text{gen}}$ the generator's power output. By incorporating these control variables, the updated decision vector enables more precise control over system operations, balancing energy generation and storage while adhering to defined constraints.

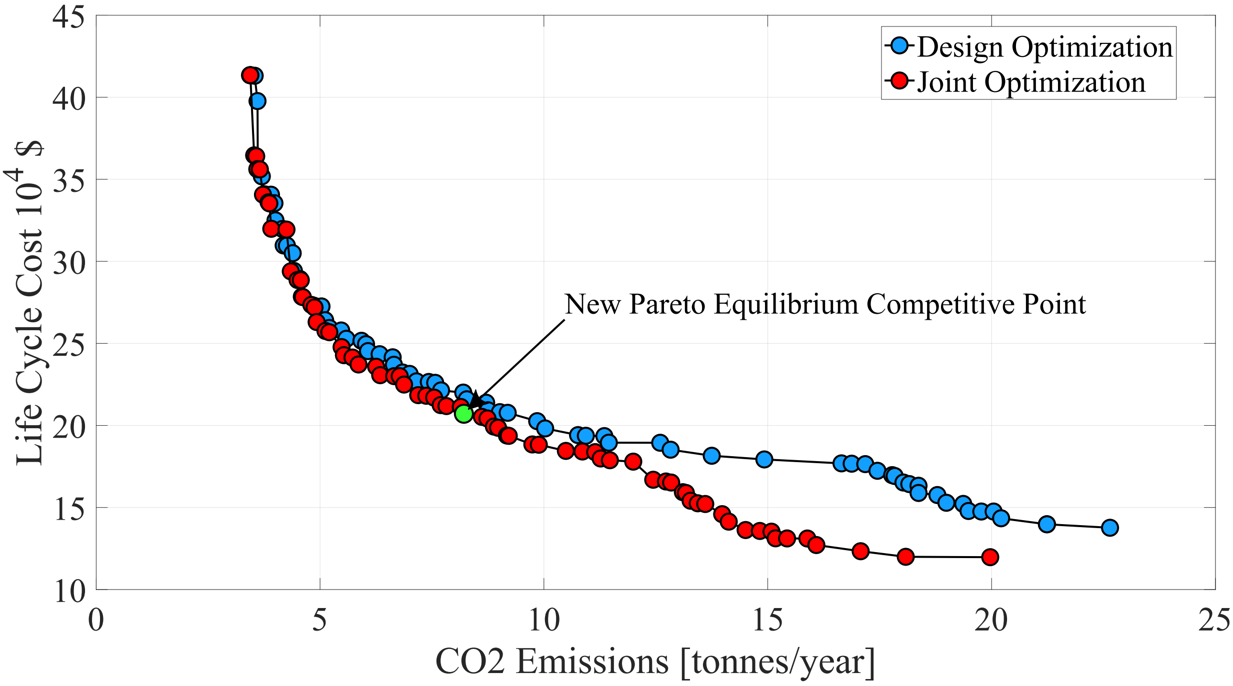


**Figure 6.25:** Pareto Front for Optimal Design: Balancing $CO_2$ Emissions and Life Cycle Cost

To evaluate the impact of incorporating the new control variables, we utilize the hypervolume indicator [3], as defined in Equation 6.26. This indicator quantifies the volume of the objective space that is weakly dominated by the points on the Pareto front. By comparing the hypervolume values of two Pareto fronts (or two sets of optimal solutions), we can assess the improvement. Specifically, an improvement is considered when the hypervolume of the updated Pareto front exceeds that of the previous one, indicating that the new solution set dominates a r region of the objective space.

$$HVI(S, \mathbf{r}) = \text{Vol}\left(\bigcup_{i=1}^{n} [\mathbf{r}, \mathbf{x}_i]\right) \tag{6.26}$$

The reference point is defined as the worst point than all solutions on the Pareto front, in the case of two pareto fronts, the point is defined as follows :

$$r_x = max(max(X_{PF,1}), max(X_{PF,2}))$$
$$r_y = max(max(Y_{PF,1}), max(Y_{PF,2}))$$

| Hyper Volume Indicator | Value |
|---|---|
| Pareto Front 1 | 413.09 |
| Pareto Front 2 | 457.65 |

**Table 6.6:** Hypervolume Indicator Values for the Two Pareto Fronts

Table 6.6 presents the Hypervolume Indicator values for each Pareto front. The newly obtained Pareto solutions exhibit a higher Hypervolume Indicator (457.65) compared to the previous set (413.09), indicating a substantial enhancement in the optimization process. This improvement suggests that the new solutions dominate the previous ones within the objective space, leading to the identification of new anchor points and a revised Pareto equilibrium. From Figure 6.25, we observe a notable reduction in the economic cost of the solution sets. The new minimum economic cost is approximately $11.97 \times 10^4$\$, compared to the previous cost of $13.21 \times 10^6$\$, representing a 9.39% improvement in economic efficiency. In contrast, there is negligible improvement in carbon emissions, as the minimum ecological solution remains unchanged at 3.44 tons per year. Regarding the Pareto equilibrium solution, carbon emissions are 8.21 tons per year, while the Life Cycle Cost is $20.71 \times 10^4$\$. This corresponds to an 8.06% improvement in emissions and a 3.54% reduction in total cost relative to the previous solution, which had emissions of 8.93 tons per year and an LCC of $21.47 \times 10^4$\$. These results demonstrate an overall optimization in economic and environmental performance, though the cost savings are lower than previously estimated. The Table 6.7 below provides a detailed summary of the values associated with the three key solutions on the second Pareto front.

| Solution/ Size | LFP Batteries | PV Modules | Diesel Generator | $SOC\_min$ | $SOC\_max$ | $\backslash\alpha\_rate$ |
|---|---|---|---|---|---|---|
| Min CO2 | 18 | 150 | 5 | 0.1 | 0.88 | 0.87 |
| Min LCC | 2 | 19 | 5 | 0.1 | 0.65 | 0.2 |
| Pareto Equilibrium | 6 | 108 | 5 | 0.1 | 0.65 | 0.2 |

**Table 6.7:** Optimal Design Variable Values for Anchor Points and Pareto Equilibrium of the New Pareto Front

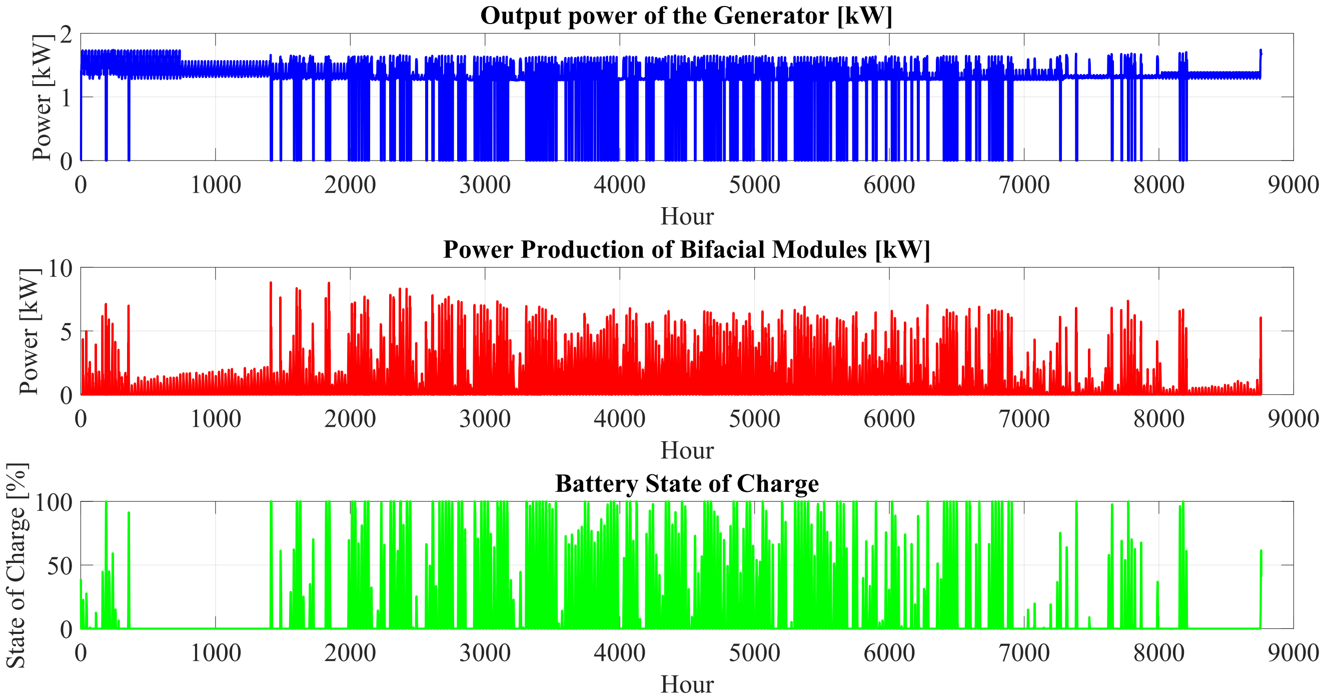


**Figure 6.26:** Operation of Nanogrid Subsystems: Diesel Generator Output, Bifacial Panel Output, and Battery State of Charge in the Most Economical Design Optimization Solution.

Figure 6.26 illustrates the energy flow between subsystems for the newly proposed economical solution. This nanogrid design consists of a 5kW diesel generator, 19 bifacial photovoltaic modules, and 2 batteries. The control variables are set as follows: $x_{\text{control}} = (\text{Thr}_{\text{min}}, \text{Thr}_{\text{max}}, \alpha_{\text{rate}}) = (0.1, 0.65, 0.2)$, resulting in a low investment cost.
It is observed that the generator activates when the battery's state of charge drops to 10%. The generator remains operational until a period of high solar radiation allows the bifacial modules to achieve high power output levels, subsequently recharging the batteries. This management strategy significantly increases the operational hours of the diesel generator, ensuring continuous energy supply while maximizing the use of renewable energy sources, thereby enhancing the overall cost-effectiveness of the system.

## 2.5 Joint Optimization with Monthly Management Strategy

To address monthly meteorological variability, we propose a novel approach that transitions from using fixed control variable values to employing monthly-specific vectors for each control variable. These vectors are defined as follows:

$$Thr_{\text{min}} = \{Thr_{\text{min, m1}}, \ldots, Thr_{\text{min, m12}}\}$$
$$Thr_{\text{max}} = \{Thr_{\text{max, m1}}, \ldots, Thr_{\text{max, m12}}\}$$
$$\alpha_{\text{rate}} = \{\alpha_{\text{rate, m1}}, \ldots, \alpha_{\text{rate, m12}}\}.$$

These monthly-specific control variables are integrated into the existing set of design variables, expressed as:

$$X_{\text{design}} = \{N_{\text{pv}}, N_{\text{bat}}, P_{\text{gen}}\}.$$

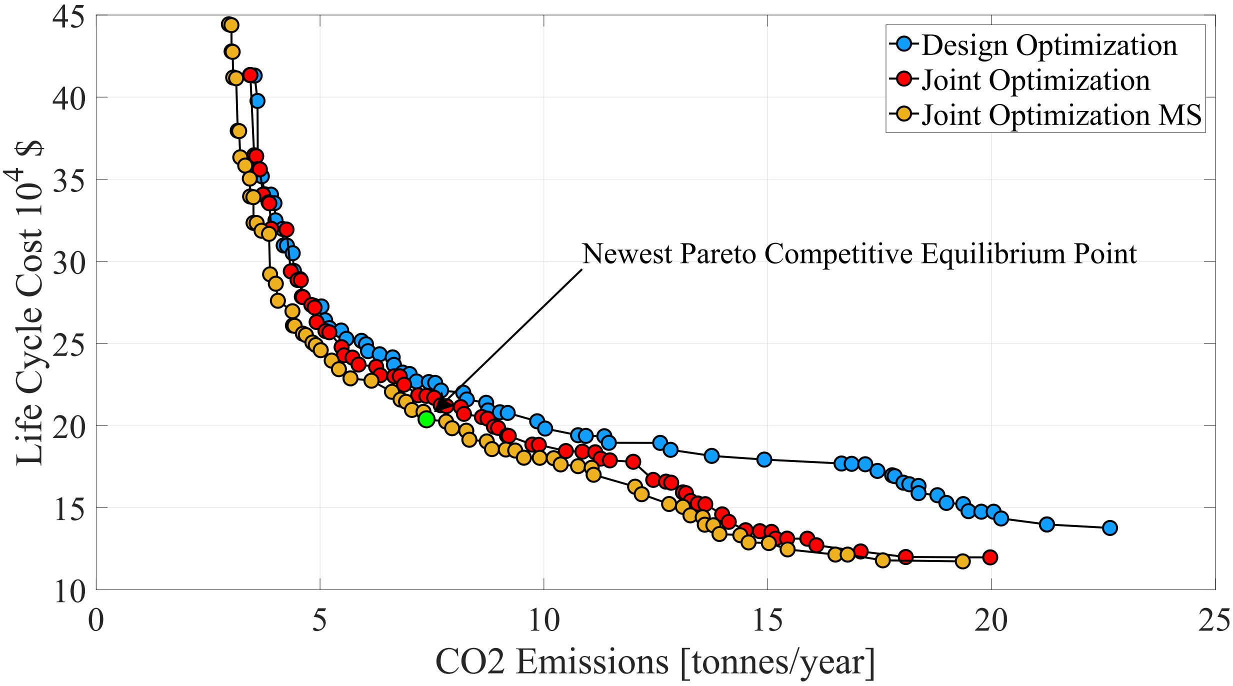


**Figure 6.27:** Pareto Front for Optimal Design: Balancing $CO_2$ Emissions and Life Cycle Cost

By incorporating these adjustments, a new Pareto front was generated and subsequently compared with the previously derived Pareto fronts to assess the improvements (Figure 6.27). To quantify this, the hypervolume indicator (HVI) was calculated, using a reference point determined by both the second and the newly generated Pareto fronts. The HVI for the second Pareto front was computed as 429.78, while the HVI for the new Pareto front was determined to be 453.57. This result demonstrates that the new Pareto front dominates the second, which itself dominates the first, confirming a further improvement in the optimization process. The new most economical solution achieves a total cost of $19.35 \times 10^4$, representing an improvement of approximately 3.05% compared to the previous total cost of $19.96 \times 10^4$. Additionally, for this solution, a reduction of 0.4 tons per year in $CO_2$ emissions is observed, resulting in a new annual emissions value of 3.02 tons per year. This represents an improvement of approximately 11.7% compared to the previous value. However, this environmental benefit comes with an increase in cost, rising from $41.34 \times 10^4$ to $44.38 \times 10^4$.

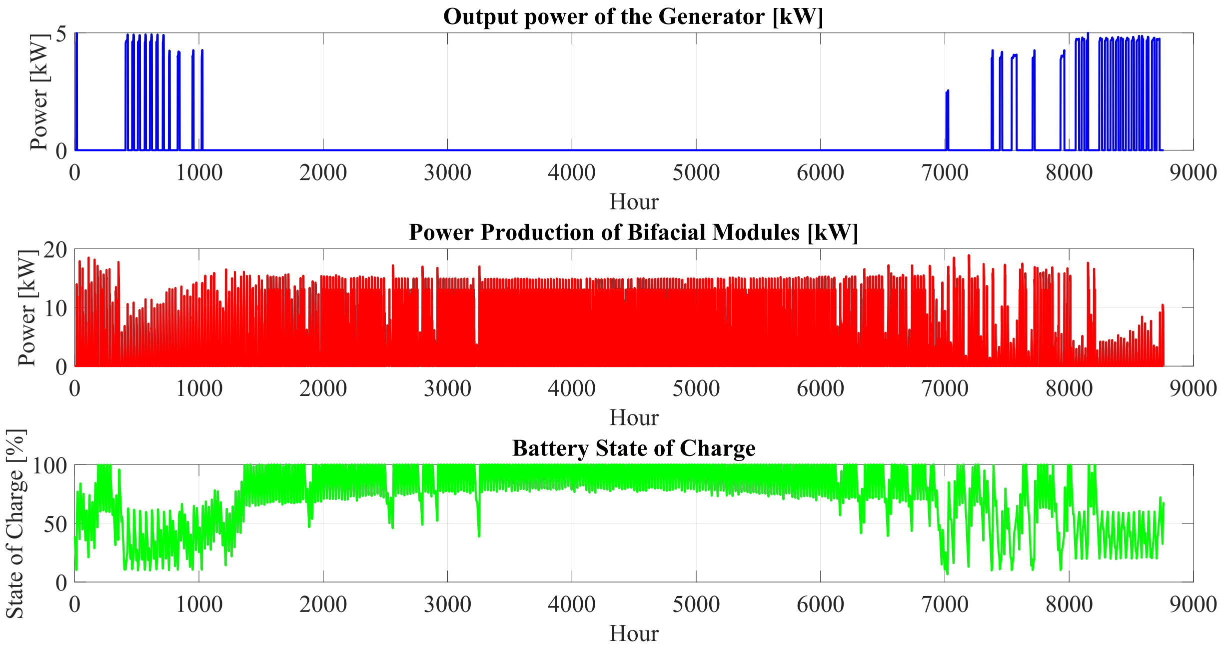


**Figure 6.28:** Operation of Nanogrid Subsystems: Diesel Generator Output, Bifacial Panel Output, and Battery State of Charge in the Most Ecological Optimization Solution.

To evaluate the notable improvements introduced by the new optimization approach, it is important to consider that the design configuration of the proposed solution remains identical to the initial design generated by the first optimization. Specifically, both configurations consist of 150 bifacial photovoltaic modules, 18 LFP batteries, and a 5 kW diesel generator. However, a key distinction lies in the environmental performance. While the original optimization resulted in annual $CO_2$ emissions of approximately 3.44 tons, the revised approach achieves a reduced emission level of about 3.02 tons per year. This improvement can be attributed to the implementation of a monthly control strategy, which optimizes energy distribution and subsystem interactions within the nanogrid. Figure 6.28 reveals that the system prioritizes the use of renewable energy, thereby increasing the contribution of bifacial photovoltaic modules while maintaining a high state of charge (SOC) for the battery. During the winter season, the diesel generator is utilized more frequently, as the maximum SOC of the battery is intentionally reduced to limit reliance on the generator.

Figure 6.29 illustrates the monthly variations of three critical control parameters: the minimum threshold, the maximum threshold, and the charge rate.

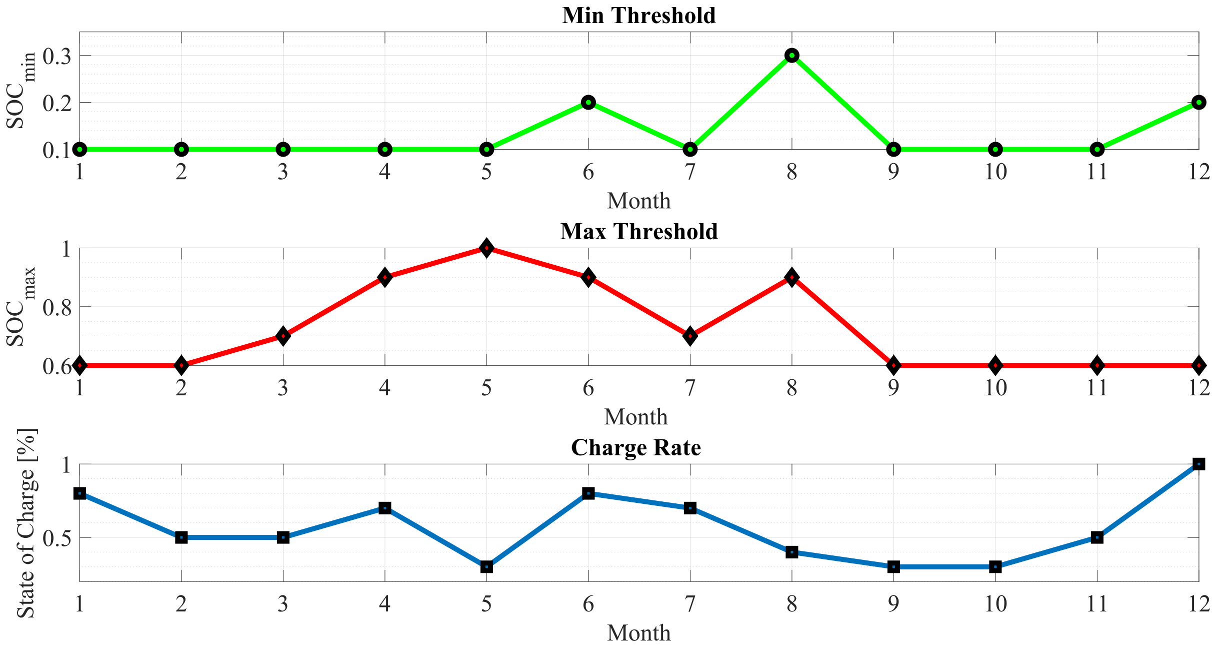


**Figure 6.29:** Monthly Variation in Control Variables for the Latest Ecological Solution

An economic analysis was conducted on the final refined optimization results. Figure 6.31 illustrates the cost distribution of each solution, focusing on the two anchor points and the newly identified Pareto equilibrium. Additionally, the corresponding carbon emissions for each solution are highlighted. The most economical solution achieved a total cost of $13.10 \times 10^4$ USD. As shown in Figure 6.31, this solution is characterized by a low CAPEX but a high OPEX due to the excessive reliance on the diesel generator, which results in an estimated annual fuel consumption of 6,533 liters. Compared to the initial optimization results, this solution yields an economic gain of 0.83% relative to $13.21 \times 10^4$ USD. The most environmentally friendly solution, while increasing costs, significantly reduces OPEX to $1.36 \times 10^4$ USD and limits annual fuel consumption to 856 liters. This reduction in fuel usage leads to a decrease in carbon emissions from 3.45 tons to 2.93 tons, representing an improvement of 15.07%. The most balanced solution is the Pareto equilibrium (LCC $= 20.34 \times 10^4$ USD, $CO_2 = 7.27\ tons$), which represents an improvement over previous solutions. Compared to the second Pareto equilibrium point, with LCC $= 20.71 \times 10^4$ USD and $CO_2 = 8.21$ tons, this solution shows a 1.79% reduction in total cost and an 11.45% decrease in emissions. Additionally, compared to the first Pareto equilibrium point, with LCC $= 21.47 \times 10^4$ USD and $CO_2 = 8.93$ tons, it achieves a larger reduction, with a 5.26%

decrease in total cost and an 18.59% decrease in emissions. This progression demonstrates the continuous improvements made in each step, refining the balance between economic and environmental considerations.

This final solution is recommended as it strikes a balance between economic and environmental considerations while minimizing dependency on the diesel generator( Figure 6.30), thereby reducing the risk of frequent failures.

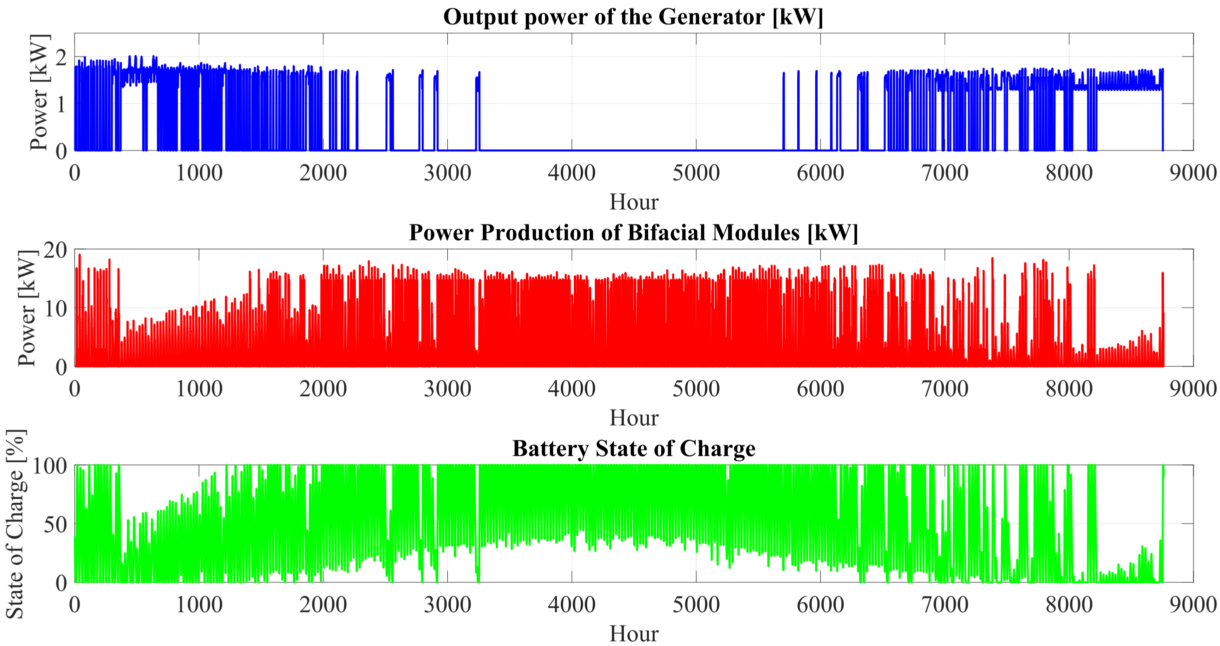


**Figure 6.30:** Operation of Nanogrid Subsystems: Diesel Generator Output, Bifacial Panel Output, and Battery State of Charge for the Pareto Equilibrium Solution.

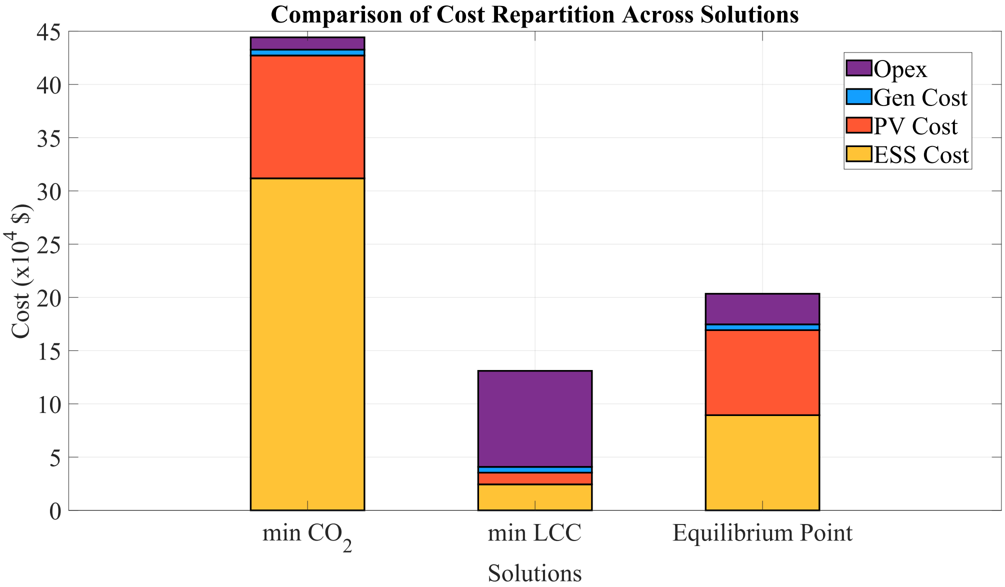


| Cost/Solution | min CO2 | min LCC | Pareto Equilibrium |
|---|---|---|---|
| Total Cost | 44.42 | 13.10 | 20.34 |
| CAPEX | 43.26 | 4.08 | 17.46 |
| OPEX | 1.15 | 9.01 | 2.87 |
| Storage System Cost | 31.18 | 2.44 | 8.93 |
| PV System Cost | 11.53 | 1.09 | 7.98 |
| DG System Cost | 0.55 | 0.55 | 0.55 |
| $CO_2$ Emissions | 2.93 | 22.83 | 7.27 |

**Figure 6.31:** Economic Analysis of Optimization Solutions: Comparative Evaluation of Anchor Points and Pareto Equilibrium (Costs in $\times 10^4$ [$])

## 2.6 Conclusion

The multi-objective optimization approach for nanogrid design demonstrated significant progress through three successive optimization stages. The initial optimization established baseline performance metrics, with the most environmentally conscious configuration achieving 3.45 tons/year of $CO_2$ emissions at a cost of $41.34 \times 10^4$ , while the most economical solution reduced costs to $13.21 \times 10^4$ but increased emissions to 21.25 tons/year. The introduction of fixed control variables ($Thr_{min}, Thr_{max}, \alpha_{rate}$) in the second optimization phase yielded notable improvements, particularly in economic performance, with a 9.39% reduction in minimum system cost. This phase also produced a more favorable Pareto equilibrium solution, reducing emissions by 8.06% and costs by 3.54% compared to the initial optimization. The final optimization phase, implementing monthly-specific control strategies, proved most effective. This approach achieved the best overall results, with the Pareto equilibrium solution reducing $CO_2$ emissions by 18.59% and costs by 5.26% compared to the initial optimization. The most environmentally friendly configuration under this strategy achieved a remarkable 15.07% reduction in emissions while maintaining economic viability. Figure 6.32 comprehensively illustrates these optimization results, displaying the progressive improvement in Pareto fronts across all three optimization phases and highlighting the superior performance of the monthly adjusted control strategy.

These results conclusively demonstrate that dynamic, monthly adjusted control strategies outperform fixed control approaches in nanogrid optimization. Progressive improvement in all optimization phases underscores the importance of sophisticated control strategies in achieving both environmental and economic objectives. The final recommended solution, with its balanced performance metrics and reduced dependence on diesel generation, represents a practical and sustainable approach to nanogrid design that could serve as a model for similar applications.

| | CO2 [Tonnes/ Année] | LCC [$] x10^4 |
|---|---|---|
| DA | **11,7** | **21,9** |

**- 70.09%** ⇩ **+ 36.99%**

| Solution | CO2 [Tonnes/ Année] | LCC [$] x10^4 |
|---|---|---|
| PA 1 | 3,5 | 41,3 |
| PA 2 | 22,6 | 13,8 |
| PE | 8,7 | 21,4 |

**- 0.85%** ⇩ **+ 8.7 %**

| Solution | CO2 [Tonnes/ Année] | LCC [$] x10^4 |
|---|---|---|
| PA 1 | 3,4 | 41,3 |
| PA 2 | 20 | 11,9 |
| PE | 8,21 | 20,7 |

**- 4.27%** ⇩ **+ 0.92 %**

| Solution | CO2 [Tonnes/ Année] | LCC [$] x10^4 |
|---|---|---|
| PA 1 | 2,9 | 44,4 |
| PA 2 | 19,2 | 11,7 |
| PE | 7,27 | 20,3 |

**Figure 6.32:** Summary of Multi-Objective Optimization Results Across Sequential Phasess

## References for Chapter 6

[1] Donald E. Grierson. "Pareto multi-criteria decision making". In: *Advanced Engineering Informatics* 22 (3 July 2008), pp. 371–384. ISSN: 14740346. DOI: 10.1016/j.aei.2008.03.001.

[2] "Measured and modeled photovoltaic system energy losses from snow for Colorado and Wisconsin locations". In: *Solar Energy* 97 (Nov. 2013), pp. 112–121. ISSN: 0038-092X. DOI: 10.1016/J.SOLENER.2013.07.029.

[3] Yongtao Cao, Byran J. Smucker, and Timothy J. Robinson. "On using the hypervolume indicator to compare Pareto fronts: Applications to multi-criteria optimal experimental design". In: *Journal of Statistical Planning and Inference* 160 (May 2015), pp. 60–74. ISSN: 03783758. DOI: 10.1016/j.jspi.2014.12.004.

# Conclusion and Perspectives

The telecommunications sector, responsible for approximately 3% of global energy consumption and 1% of total $CO_2$ emissions, faces significant challenges in achieving its net zero emissions targets by 2050. Base stations, particularly in remote locations, represent a substantial portion of this energy demand. The industry's progress toward sustainability varies across regions, with some areas demonstrating greater advancement than others particularly in addressing the complex challenges of remote infrastructure deployment. These challenges are particularly pronounced in regions with challenging geographical conditions, such as Canada, where the digital divide intersects with significant environmental and infrastructural barriers. Remote communities require telecommunications infrastructure that often relies on diesel generators for power, creating a stark conflict with national and industry sustainability commitments. The transition to renewable energy sources in these areas is further complicated by extreme geographical constraints, unpredictable weather conditions, and substantial economic considerations.

Our research into nanogrid systems for remote telecommunications infrastructure reveals promising potential alongside significant implementation challenges. The Dorval Lodge site in Quebec and the UdeS prototype in Sherbrooke provide valuable case studies for real-world application and laboratory testing of these systems. The analyzed nanogrid architecture—incorporating bifacial solar panels, lithium iron phosphate batteries, and diesel generators—demonstrates the feasibility of hybrid renewable energy systems for telecommunications applications. However, our critical assessment of existing modeling tools reveals significant limitations in current software solutions. These include inadequate modeling of bifacial photovoltaic performance, insufficient accounting for snow accumulation impacts, and limited integration of joint optimization techniques. These limitations affect the accuracy of system planning and optimization, particularly in northern climates where snow significantly impacts solar generation.

Building upon these findings, our preliminary simulation study using HOMER Pro reveals a notable trade-offs between economic and environmental priorities. Economically optimized systems achieved energy costs of 0.395$/kWh but with only 26% renewable penetration.

Conversely, environmentally optimized systems reached 99.9% renewable penetration but at substantially higher costs of 1.63$/kWh. Sensitivity analysis confirms that increasing renewable energy fraction significantly raises system costs, highlighting the need for innovative solutions that balance these competing priorities.

These simulation results underscored several critical areas requiring further investigation. Enhanced modeling tools must accurately represent bifacial photovoltaic performance and snow accumulation effects.Additionally, comprehensive studies on extreme weather impacts on renewable energy reliability in remote telecommunications installations are necessary, along with refinement of rule-based management strategies for optimal system operation.

To address these identified modeling gaps, we conducted a comprehensive year-long experiment in Sherbrooke, Canada, focusing on bifacial photovoltaic modules with particular emphasis on quantifying snow's influence on energy yield. Our findings revealed substantial impacts, with snow accumulation causing energy losses of up to 79%, critically affecting nanogrid design considerations in northern climates. We evaluated multiple modeling approaches, comparing the computationally intensive ray tracing method against the more efficient view factor method. While ray tracing provided excellent summer accuracy (3.1%-4.7% error), its winter performance deteriorated significantly (16.1%-19% error) due to snow coverage. The view factor method offered a superior balance of speed and accuracy, completing annual simulations in 15 seconds versus 3 hours for ray tracing. By incorporating snow accumulation and temperature data into our models, we improved winter accuracy by 51%. This led to the development of BifacialPowerEstimator, an open-source tool that provides several features for bifacial systems instaled in snowy-prone regions.

We extended our research to create comprehensive models for other critical components of the nanogrid. For base stations, we presented a mathematical model estimating power consumption based on traffic load and transceiver count. Our $LiFePO_4$ battery modeling incorporated both cyclic aging analysis using the Rainflow algorithm and calendar aging estimation. The diesel generator model achieved 7-8% accuracy compared to manufacturer specifications and integrated ISO 8528 standards for load requirements and maintenance parameters.

The next critical phase of our research focuses on developing a refined Typical Meteorological Year generation method using Principal Component Analysis. By analyzing key parameters including temperature, irradiance, and snow depth, we aim to create a more accurate meteorological dataset for optimizing nanogrid design. Preliminary results show the potential to reduce energy production variability from 8% to 5.3%, addressing the critical modeling limitations identified in our previous analyses. This approach will enable

more precise system planning for remote telecommunications infrastructure.
The subsequent optimization analysis utilizing the refined TMY methodology exposed critical insights into snow's impact on hybrid energy system design for remote telecommunications infrastructure. Our findings revealed significant performance variations, with snow causing annual energy losses of 23.4% and increasing diesel generator reliance by 60.8%. The Pareto front analysis demonstrated that 47% of previously identified design solutions become less effective under snow conditions, underscoring the necessity of integrating comprehensive environmental considerations into system optimization.
The final stage of our research integrated sophisticated control variables into the optimization framework, demonstrating significant potential for enhancing nanogrid system performance. By implementing dynamic control strategies, particularly monthly-adjusted approaches, we achieved a 18.59% reduction in $CO_2$ emissions and a 5.26% cost reduction. The Pareto front analysis revealed critical trade-offs between economic and environmental objectives, with the most balanced solution achieving 7.27 tons of $CO_2$ emissions at a life cycle cost of $20.34\times10^4$ \$. These findings underscore the importance of adaptive control strategies.
The results of our research project have not only addressed critical challenges in remote telecommunications infrastructure design but also unveiled promising avenues for future investigation. Our findings suggest three key perspectives for advancing nanogrid optimization:

- First, we propose implementing an advanced Model Predictive Control (MPC) strategy integrated into the joint optimization framework. Such an approach has significant potential to further refine both economic and environmental performance metrics of nanogrids, potentially reducing operational costs and emissions beyond our current results.

- Second, exploring seasonal energy storage solutions represents a critical research direction. By developing strategies to minimize energy waste and optimize storage capabilities, we can address the intermittency challenges inherent in renewable energy systems, particularly in snow-prone regions.

- Finally, the strategic combination of lithium-ion battery storage with hydrogen-based systems presents an innovative approach to long-term energy storage and sustainability. This hybrid technological framework could deliver enhanced energy density, extended operational lifecycles, and reduced environmental impact while leveraging the complementary strengths of both storage technologies..

These perspectives not only extend the boundaries of our current research but also chart a strategic roadmap for technological innovation in telecommunications infrastructure deployed in challenging, underserved, and resource-constrained environments.

# Publications

The following publications have resulted from this thesis :

## International Conferences :

- **Electrimacs 2022 (Published)** : Ghafiri, S., Darnon, M., Davigny, A., F.Trovão, J., Abbes, D. (2023). A Comparative Study of Existing Approaches for Modeling the Incident Irradiance on Bifacial Panels. In: Pierfederici, S., Martin, JP. (eds) ELECTRIMACS 2022. ELECTRIMACS 2021. Lecture Notes in Electrical Engineering, vol 993. Springer, Cham. doi.org/10.1007/978-3-031-24837-5_42
- **Electrimacs 2024 (Published)** : Ghafiri, S., Darnon, M., Abbes, D., Davigny, A., Trovão, J.P.F. (2025). Refined TMY Data Generation Method for Accurate Sizing of Bifacial PV Module-Based Micro-Grids in Snowfall-Prone Climates. In: Belenguer, E., Beltran, H. (eds) ELECTRIMACS 2024. ELECTRIMACS 2024. Lecture Notes in Electrical Engineering, vol 1275. Springer, Cham. doi.org/10.1007/978-3-031-73921-7_48

## National Conferences :

- **Symposium de Génie Électrique SGE 2023 (Published)** : Optimisation du Dimensionnement d'un Micro-Réseau avec Batteries pour Une Station de Transmission de Base (4G Macro BTS) 10.13140/RG.2.2.32737.28004

## Scientific Journals :

- **EPJ Photovoltaics (Published)** : Soufiane Ghafiri, Maxime Darnon, Arnaud Davigny, João Pedro F. Trovão, Dhaker Abbes, A comprehensive performance evaluation of bifacial photovoltaic modules: insights from a year-long experimental study conducted in the Canadian climate, EPJ Photovoltaics 15, 28 (2024) doi.org/10.1051/epjpv/2024025
- **Energy Systems (Submitted)** : Ghafiri, S., Abbes, D., Trovão, J. P. F., Davigny, A., & Darnon, M. (2025). Evaluating Snow Impact on Optimized Nanogrid Design for Remote Telecom Stations in Canada: A Multi-Objective Optimization Approach.
- **Energy (Submitted):** Ghafiri, S., Abbes, D., Trovão, J. P. F., Davigny, A., & Darnon, M. (2025). Accelerating Telecommunication Base Stations Deployment to Bridge the Digital Divide: A Joint Multi-Objective Optimization Framework for Optimally Sizing and Controlling Nanogrids in Remote Canadian Regions.